Understanding the role of the rigid amorphous fraction in polyesters

Clément Fosse

Normandie Université

THESE

Pour obtenir le diplôme de doctorat

Spécialité : Physique

Préparée au sein de l'Université de Rouen Normandie

Compréhension du rôle de la fraction amorphe rigide dans les polyesters

Présentée et soutenue par
Clément FOSSE

Thèse soutenue publiquement le 15 Décembre 2020 devant le jury composé de		
Mme. Madalena DIONISIO	Pr. Université de Lisbonne	Rapporteur
M. Frédéric AFFOUARD	Pr. UMET Université de Lille 1	Rapporteur
Mme. Valérie GAUCHER	Pr. UMET Université de Lille 1	Examinateur
M. Sébastien PRUVOST	Pr. IMP Université de Lyon – INSA Lyon	Examinateur
M. Laurent DELBREILH	Dr. HDR GPM Université de Rouen Normandie	Directeur de thèse
Mme. Antonella ESPOSITO	Dr. GPM Université de Rouen Normandie	Co-encadrant de thèse

Thèse dirigée par Dr. Laurent DELBREILH et Co-encadrée par Dr. Antonella ESPOSITO, Groupe de Physique des Matériaux (GPM)

UNIVERSITÉ DE ROUEN NORMANDIE

ED PSIME

GPM Groupe de Physique des Matériaux

Contents

List of Figures

List of Tables

Dedication

YOU KNOW HOW IT IS. You pick up a book, flip to the dedication, and find that, once again, the author has dedicated a book to someone else and not you.

Not this time.

Because we haven't yet met/have only a glancing acquaintance/are just crazy about each other/haven't seen each other in much too long/are in some way related/will never meet, but will, I trust, despite that, always think fondly of each other...

This one's for you.

With you know what, and you probably know why.

Acknowledgements

It is my pleasure to acknowledge several individuals who played an important role in the completion of this PhD thesis.

First of all, I would like to express my deep and sincere gratitude to my supervisors Dr. Laurent Delbreilh and Dr. Antonella Esposito for their support and the richful discussions/moments that we had together. It has been a long and difficult path but we ended up with something that, I hope, we can be proud of.

I would also like to acknowledge the helpful suggestions made by the members of the thesis committee Pr. Madalena Dionisio, Pr. Frédéric Affouard, Pr. Valérie Gaucher and Pr. Sébastien Pruvost.

These aknowledgements would not be complete without mentioning my research lab colleagues. It was a great pleasure working with them and I really enjoyed the warm/funny moments we had together.

Finally, my deepest gratefulness belongs to my family and friends whom without which I would not have gone that far.

Give a man a fish and you feed him for a day.
Teach a man how to fish and you feed him for a lifetime.
- Lao Tzu

Introduction

When it comes to the microstructural depiction of semi-crystalline polymers, the simplest way to describe their microstructures is to use the so-called "two-phase model". In this model, the amorphous and crystalline domains can be clearly distinguished, quantified and identified as the "amorphous phase" and "crystalline phase", respectively. The amorphous phase is defined by the absence of long-range order, while polymer crystals result from a partial arrangement of the macromolecules in lamellae in which the polymer chains are able to fold and form a crystal lattice.

However, in most cases, this model is better replaced by a more complex "three-phase model"[1, 2]. The three-phase model involves an additional "phase" named "rigid amorphous fraction" (RAF), which is introduced to represent the fraction of polymer chains connecting the amorphous phase to the crystalline domains and is known to be a result of the length of the macromolecules that is much higher than the characteristic dimensions of the crystalline lamellae [3, 4]. By definition, the RAF is highly constrained by the neighboring crystalline domains and can therefore be distinguished from the unconstrained "mobile amorphous fraction" (MAF). Several studies have shown how this "interphase" can help explaining the macroscopic properties of semi-crystalline polymers (thermal[5, 6], mechanical, barrier[7, 8]...), which means that understanding the mechanisms of RAF formation and how to control the RAF amount are important steps in the characterization of semi-crystalline materials and the design of new materials. Numerous PhD works performed in the EIRCAP team of the GPM laboratory (former AMME-LECAP laboratory) have focused on semi-crystalline polyesters, investigating the formation of RAF and its consequences on the molecular mobility and/or the final properties. Firstly, Eric Dargent studied the impact of different thermo-mechanical treatments on the semi-crystalline microstructures of one of the most widespread fossil-based polyester, i.e. poly(ethylene-terephthalate)[9]. Then, Mickaël Arnoult investigated the molecular mobility in the amorphous phase of semi-crystalline poly(L-lactic acid)(PLLA) using Monte Carlo simulation [10]. At the same time, Nicolas Delpouve investigated the confinement effects induced on the amorphous phase of semi-crystalline PLA by the surrounding crystals[11]. Later on, Florian Hamonic investigated the structural anisotropy due to strain induced crystallization in semi-crystalline polyesters with different aptitudes to crystallize, such as PET and glycol-modified PET (PETg)[12]. Recently, Xavier Monnier studied the molecular dynamics in semi-crystalline PLA samples with different degrees of structural anisotropy induced by thermal treatments (quiescent and flow-induced crystallization)[13]. Lastly, Aurélie Bourdet characterized the complex semi-crystalline microstructures developed by a wide range of furan-based homopolyesters and copolyesters[14].

In a recent study carried out in the EIRCAP team of the GPM laboratory (former AMME-LECAP laboratory), Esposito et al.[15] proposed a combination of calorimetric and dynamic

approaches, to describe the microstructure of semi-crystalline polymers and the molecular mobility of the RAF. The concept behind this approach is that, for some polymers crystallized in specific conditions, the crystalline and amorphous phases are strongly coupled, and therefore the mobile and rigid amorphous fractions are hardly separated. In these conditions, the amorphous phase is better described as a continuum characterized by a gradient of mobility (the lowest mobility being represented by the crystalline phase, the highest mobility being represented by the total absence of crystals).

If PLA has probably been the most studied bio-based polyesters so far, in the last years many new bio-based polyesters are being synthesized based on different sustainable resources (vegetable feedstock [16, 17], bacteria[18, 19]...), which dramatically increases the panel of possible surrogates to fossil-based materials. Bio-polyesters can have very different chemical compositions, microstructures and final properties. In fact, they can be obtained by combining an acid and a dioln and many methods exist to extract acids and diols from the biomass, which gives access to an almost infinite number of possible combinations. The chemical composition and structure of a polyester have a major impact on the final properties of the material, therefore both the acid and the diol should be carefully selected [20, 21, 22].

Polyhydroxyalkanoates (PHAs) are one of the most promising, however challenging, family of bio-based polyesters. The growing interest for these polymers is due to the fact that their behavior and properties depend on both the nature and content of the repeating units introduced into the macromolecular chains during the biosynthesis[18, 23]. Indeed, these polymers can be synthesized by bacteria and a large panel of different homopolymers and copolymers can be obtained by controlling the conditions of the biosynthesis[19, 24]. However these polymers are tricky, because their biosynthesis is not widely spread and it sometimes difficult to control their properties. This research topic is being developed thanks to a collaboration established several years ago with bio-technologists from the Institut de Recherche Dupuy de Lôme (IRDL), Université de Bretagne-Sud, as well as from the School of Biological Sciences, Universiti Sains Malaysia.

Among all the new bio-based polyesters, the ones produced from furandicarboxylic acid (FDCA) are of one of the most promising, as they can be entirely produced from renewable resources and show very interesting properties (mechanical, barrier...), sometimes even better than the commonly adopted PET. Due to it's chemical structure, FDCA exists in the forms of three different position isomers, which further expands the range of possibilities. For this reason, numerous studies have been carried out in the last years to get a deeper insight into the relation between the chemical structure, the microstructure and the properties of this very interesting family of polyesters family. Aurélie Bourdet [14] has recently defended her Phd thesis, which is the starting point of this kind of investigations about furan-based polyesters in the EIRCAP team of the GPM laboratory. This research topic is being developed thanks to a collaboration

established in 2015 with chemists from the Food and Biobased Research (FBR) center at the Wageningen University and Research (WUR), The Netherlands. This collaboration is rapidly expanding, and today it involves chemists from the University of Bologna, Italy.

This PhD manuscript is organized as follows:

- Chapter 1 introduces the general concepts used in this work. In a first part, some general knowledge on the glassy state and the molecular mobility of glass-forming liquids are presented, as they allow to understand the relaxation phenomena occurring in glass-forming liquids. Then, the crystalline state and the associated theories of crystal growth are discussed to highlight the environmental and structural effects on the molecular dynamics in the amorphous phase. Different models allowing the description of semi-crystalline microstructures are presented and discussed. Finally, a brief presentation of the bio-based polymers investigated in this work is provided to contextualize the Phd work.
- Chapter 2 presents the materials and experimental techniques used in this work.
- The third chapter of this work focuses on the determination of the equilibrium melting enthalpy ΔH_m^0 as it is a key parameter towards the quantification of the RAF amount. Different methods are therefore presented and the reliability of these methods is discussed. In a second part, a model to determine the temperature dependency of the enthalpy of melting based of the Kirchoff's law is discussed and applied to a PEF sample. Lastly, the impact of different parameters (crystallization temperature, crystallization time, sample mass...) onto the formation of RAF in fast scanning calorimetry (FSC) is discussed.
- Chapter 4 approaches the effects of the content and nature of the repeating units on the semi-crystalline microstructure of several PHA samples. Firstly, the results obtained by DSC and Wide-Angle X-ray Diffraction (WAXD) are presented and the effects of the co-monomer content and nature on the crystallization and crystalline phase are discussed. Secondly, the effects of the co-monomer content and nature on the molecular mobility of the amorphous phase are investigated according to different models (Donth, Hong...). Finally, the impact of the co-monomer content and nature on the formation of RAF is studied according to the three-phase model.
- Chapter 5 deals with the effects of the glycolic subunit's length onto the properties of furan-based polyesters. In a first part, the impact of the glycolic subunit's length on the crystallization and melting properties is investigated through Differential Scanning Calorimetry (DSC). Then, in a second part, the effects of the glycolic subunit's length on the molecular mobility of the amorphous phase are discussed according to different models (Donth, Hong...). Finally, a discussion about the impact of the glycolic subunit's length on the formation of RAF in furan-based polyesters is made according to the three-phase model.

References

[1] B. Wunderlich, "Reversible crystallization and the rigid–amorphous phase in semicrystalline macromolecules," *Progress in Polymer Science*, vol. 28, pp. 383–450, Mar. 2003.

[2] H. Chen and P. Cebe, "Vitrification and Devitrification of Rigid Amorphous Fraction of PET during Quasi-Isothermal Cooling and Heating," *Macromolecules*, vol. 42, pp. 288–292, Jan. 2009.

[3] B. Wunderlich and A. Mehta, "Macromolecular nucleation," *J. Polym. Sci. Polym. Phys. Ed.*, vol. 12, pp. 255–263, Feb. 1974.

[4] R. Androsch and B. Wunderlich, "The link between rigid amorphous fraction and crystal perfection in cold-crystallized poly(ethylene terephthalate)," *Polymer*, vol. 46, pp. 12556–12566, Dec. 2005.

[5] J. Menczel and B. Wunderlich, "Heat capacity hysteresis of semicrystalline macromolecular glasses," *J. Polym. Sci. B Polym. Lett. Ed.*, vol. 19, pp. 261–264, May 1981.

[6] Q. Ma, G. Georgiev, and P. Cebe, "Constraints in semicrystalline polymers: Using quasi-isothermal analysis to investigate the mechanisms of formation and loss of the rigid amorphous fraction," *Polymer*, vol. 52, pp. 4562–4570, Sept. 2011.

[7] I. Kolesov and R. Androsch, "The rigid amorphous fraction of cold-crystallized polyamide 6," *Polymer*, vol. 53, pp. 4770–4777, Sept. 2012.

[8] M. L. Di Lorenzo and M. C. Righetti, "The three-phase structure of isotactic poly(1-butene)," *Polymer*, vol. 49, pp. 1323–1331, Mar. 2008.

[9] E. Dargent, "Evolution de la microstructure de films polyester soumis à un traitement thermomécanique.," 1994.

[10] M. Arnoult, "Contribution à l'étude des dynamiques moléculaires associées aux cinétiques de relaxation sous contrainte dans les polymères semicristallines: étude expérimentale et simulation numérique.," 2007.

[11] N. Delpouve, "Etude de la microstructure et des phénomènes de relaxation dans un biopolyester: le poly(acide lactique).," 2009.

[12] F. Hamonic, "Etude de la mobilité moléculaire dans des polyesters synthétiques: mise en évidence de l'anisotropie," 2012.

[13] X. Monnier, "Etude de la mobilité moléculaire dans des systèmes polymères complexes anisotropes et confinés," 2017.

[14] A. Bourdet, "Relations structure/propriétés physiques de polymères à base d'acide furandicarboxylique obtenu de la biomasse," 2020.

[15] A. Esposito, N. Delpouve, V. Causin, A. Dhotel, L. Delbreilh, and E. Dargent, "From a Three-Phase Model to a Continuous Description of Molecular Mobility in Semicrystalline Poly(hydroxybutyrate- *co* -hydroxyvalerate)," *Macromolecules*, vol. 49, pp. 4850–4861, July 2016.

[16] A. Bourdet, A. Esposito, S. Thiyagarajan, L. Delbreilh, F. Affouard, R. J. I. Knoop, and E. Dargent, "Molecular Mobility in Amorphous Biobased Poly(ethylene 2,5-furandicarboxylate) and Poly(ethylene 2,4-furandicarboxylate)," *Macromolecules*, vol. 51, pp. 1937–1945, Mar. 2018.

[17] G. Z. Papageorgiou, V. Tsanaktsis, D. G. Papageorgiou, S. Exarhopoulos, M. Papageorgiou, and D. N. Bikiaris, "Evaluation of polyesters from renewable resources as alternatives to the current fossil-based polymers. Phase transitions of poly(butylene 2,5-furandicarboxylate)," *Polymer*, vol. 55, pp. 3846–3858, Aug. 2014.

[18] Z. Li, J. Yang, and X. J. Loh, "Polyhydroxyalkanoates: opening doors for a sustainable future," *NPG Asia Mater*, vol. 8, pp. e265–e265, Apr. 2016.

[19] D. Moorkoth and K. M. Nampoothiri, "Production and characterization of poly(3-hydroxy butyrate-co-3 hydroxyvalerate) (PHBV) by a novel halotolerant mangrove isolate," *Bioresource Technology*, vol. 201, pp. 253–260, Feb. 2016.

[20] K. Kunal, C. G. Robertson, S. Pawlus, S. F. Hahn, and A. P. Sokolov, "Role of Chemical Structure in Fragility of Polymers: A Qualitative Picture," *Macromolecules*, vol. 41, pp. 7232–7238, Oct. 2008.

[21] J. Dudowicz, K. F. Freed, and J. F. Douglas, "Fragility of glass-forming polymer liquids," *The Journal of Physical Chemistry B*, vol. 109, no. 45, pp. 21350–21356, 2005. PMID: 16853769.

[22] J. Dudowicz, K. F. Freed, and J. F. Douglas, "The glass transition temperature of polymer melts," *The Journal of Physical Chemistry B*, vol. 109, no. 45, pp. 21285–21292, 2005.

[23] B. S. Kushwah, A. V. S. Kushwah, and V. Singh, "RETRACTED ARTICLE: Towards understanding polyhydroxyalkanoates and their use," *Journal of Polymer Research*, vol. 23, p. 153, Aug. 2016.

[24] A. J. Cal, W. D. Sikkema, M. I. Ponce, D. Franqui-Villanueva, T. J. Riiff, W. J. Orts, A. J. Pieja, and C. C. Lee, "Methanotrophic production of polyhydroxybutyrate-co-hydroxyvalerate with high hydroxyvalerate content," *International Journal of Biological Macromolecules*, vol. 87, pp. 302–307, June 2016.

Chapter 1

State of the art

Contents

1.1 The glassy state

The word "glass" has been traditionally used to name products or inorganic materials that have been melted and cooled down without the possibility of crystallizing. This designation is widely used in glass technology and standards (ISO, ASTM...). Several definitions have been proposed to describe this state of condensed matter; in glass science, a glass is generally defined as a material that exhibits glass transition. In 2017, Zanotto et al. [1] proposed the following definition:

"Glass is a non-equilibrium, non-crystalline condensed state of matter that exhibits a glass transition. The structure of glasses is similar to that of their parent supercooled liquids (SCL), and they spontaneously relax towards the SCL state. Their ultimate fate, in the limit of infinite time, is to crystallize."

However, the "glassy state" is much more complex than its definition, and has unique features requiring a more detailed description. Conventionally, glasses are defined as materials with no long-range order [1, 2, 3] and a structure similar to that of a liquid [4], but mechanically behaving like solids. In theory, it is assumed that any liquid is able to form a glass when cooled down at sufficiently high cooling rates [4], i.e. fast enough to avoid crystallization. Liquids like this are conventionally called "glass-forming liquids" and can have very different chemical structures, e.g. chalcogenides [5], organic compounds [6, 7], polymers [8, 9], and metal alloys [10, 11]. For most glass-forming materials, an increase in viscosity is experimentally observed as temperature decreases with sufficiently high cooling rates, which is generally referred to as the "viscous slowing down" of SCL. Viscosity reaches values of about 10^{13} Poise (10^{12} Pa.s) at a temperature defined as the "glass transition temperature" T_g [4, 12]. This viscosity increase upon cooling prevents the liquid from reaching a thermodynamic equilibrium, resulting in the formation of the so-called "glassy state". Consequently, the glassy state is inherently a non-equilibrium state [1].

Figure 1.1 illustrates the temperature dependence of enthalpy, volume, and entropy. For glass-forming liquids that are also able to arrange in a crystalline state, these thermodynamic properties slowly and steadily increase as temperature increases; at the melting temperature T_m, their values instantly increase. This increase is due to the melting process, which brings the crystals from the solid state to a "liquid-like state" through a first-order transition. In the liquid-like state, the molecules have a higher mobility and the material is in thermodynamic equilibrium. If this liquid is subsequently cooled down using a cooling rate sufficiently high to avoid crystallization, it will reach the so-called "supercooled liquid state". During cooling, the viscosity gradually increases and the molecular movements consequently slow down [1]. Unlike melting, glass transition is spread over a wide temperature range and is generally defined as the intersection between the lines representing the liquid-like and the glassy state defined by the thermodynamic properties plotted as a function of temperature [4], as depicted in Figure

1.1.

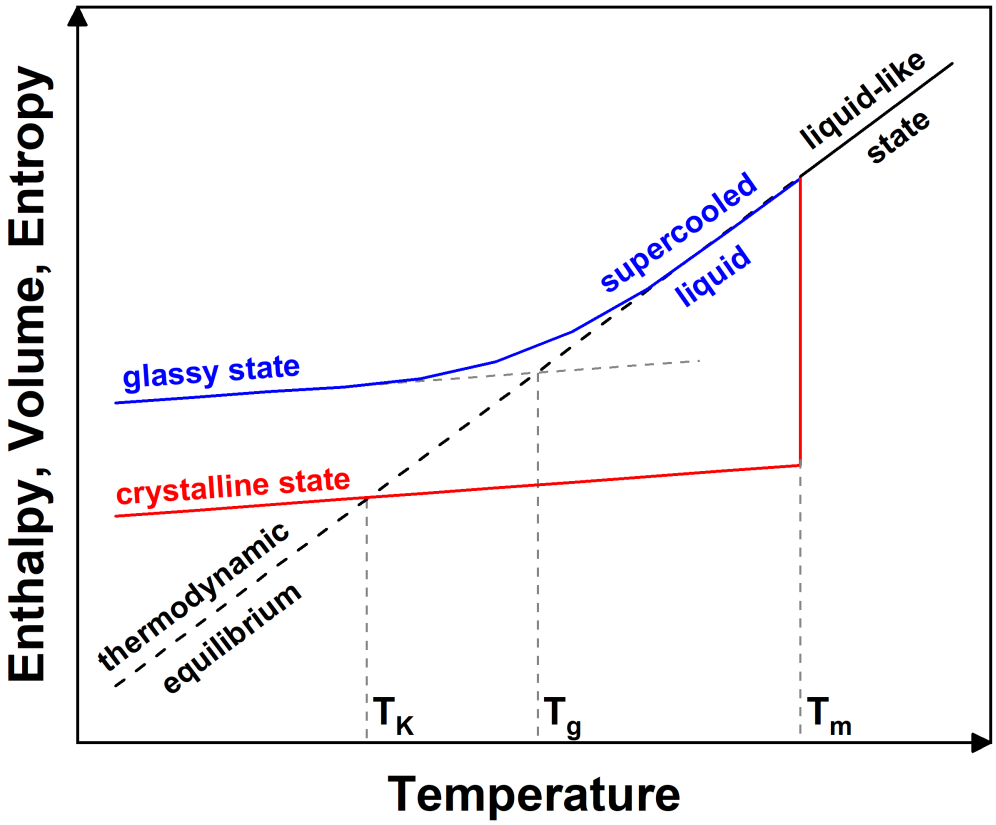

Figure 1.1: Illustration of the temperature dependence of thermodynamic properties (enthalpy, volume, entropy) in glass forming liquids, T_K is the Kauzmann temperature, T_g is the glass transition temperature and T_m is the melting temperature.

Upon cooling, the entropy difference between the liquid-like and the solid states progressively decreases. The Kauzmann temperature T_K is defined as the temperature at which this difference becomes zero. Below this temperature, the entropy difference between the liquid-like and the solid states would become negative, which is a violation of the third principle of thermodynamics. This phenomenon is known as the Kauzmann's paradox [13] and has been the focus of many debates that are still ongoing. Although being not yet observable due to experimental limitations, it has been argued that at this temperature an "ideal glass transition" of the second-order should be observed [14].

As previously mentioned, the glassy state results from the liquid's inability to reach the thermodynamic equilibrium in a given lapse of time; i.e the time imposed by the selected cooling rate. The cooling rate β_c is conventionally determined as the first derivative of the temperature change with time:

$$\beta_c = \frac{dT}{dt} \tag{1.1}$$

The higher is the cooling rate, the shorter is the time to reach the thermodynamic equilibrium. The so-called "relaxation time" τ refers to the time required by any externally perturbed system to reach the equilibrium. Thus, if the cooling rate is sufficiently high and the cooling time is

shorter than the relaxation time, the liquid goes out of equilibrium and forms a glass.

1.2 Molecular mobility

The formation of the glassy state has been attributed to the slowing down of the molecular motions in a liquid cooled at a sufficiently high cooling rate. However, many studies are still focused on the molecular dynamics and the corresponding relaxation phenomena, because some features remain unsolved.

1.2.1 General features of glass forming liquids

In glass-forming liquids, the molecular motions related to the glass transition are often associated with the so-called α-relaxation process. One of the most important features of glass-forming liquids is the change from an Arrhenius to a non-Arrhenius temperature dependence of the relaxation times when approaching the glass transition [4]. On a laboratory scale, it may seem that the material has reached an equilibrium, but molecular motions keep ongoing even when temperature falls below the glass transition temperature. This means that, provided an infinitely long time, a glass flows and relaxes until reaching the thermodynamic equilibrium or eventually the crystalline state [1, 4]. This general feature of glass-forming liquids is the origin of the process known as "physical aging" [15]. The molecular motions associated with the α-relaxation process are very slow below the glass transition temperature, and the corresponding relaxation times are longer than the experimental time-scale, which makes it difficult to observe. However, fast localized motions also take place inside the material on different scales. These motions are characterized by an Arrhenius temperature dependence of the relaxation times, and are associated with the vibrations and rotations of atoms, side groups and molecules, and are sequentially named β, γ and δ-relaxations, and so on.

1.2.2 The particular case of polymers

Polymers are peculiar glass-forming liquids; their molecular mobility in the glassy state displays some specific features resulting from the complex arrangement of very long macromolecular chains. Glassy polymers contain entanglements involving both inter-molecular and intra-molecular interactions. As a result, molecular motions are highly affected by parameters such as chain flexibility, polarity, molecular weight, steric hindrance, crystallization, plasticization, and so on. The complexity of molecular motions in polymers arises from the co-existence of both strong bonds (covalent bonds) and weaker interactions (Van der Waals interactions). Schematically, molecular motions can be differentiated in two main categories: the motions of macromolecular segments (portions of polymer backbone), and the local motions of smaller groups of atoms belonging to the macromolecular chain (pendant groups or side chains).

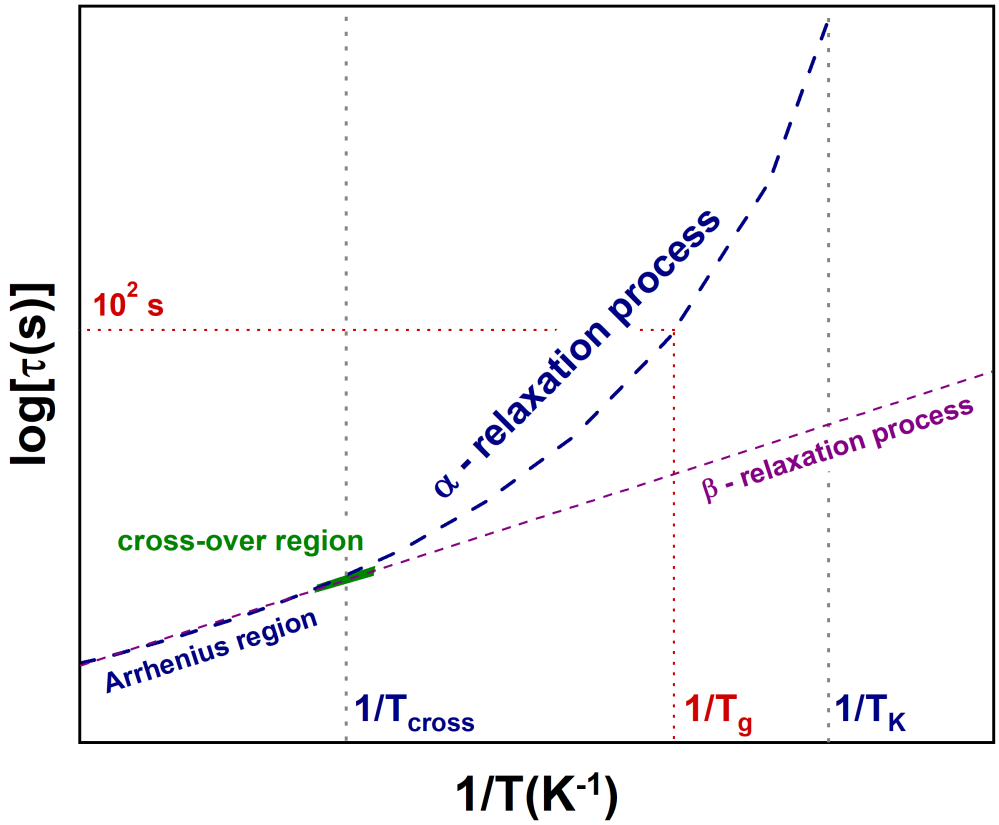

Figure 1.2: Schematic illustration of the temperature dependence of the relaxation times in glassy polymers: T_{cross} is the cross-over temperature (i.e the temperature at which the relaxation times associated with the α relaxation go from an Arrhenius to a non-Arrhenius behavior), T_g is the glass transition temperature (i.e the temperature at which a relaxation time of 100s is measured), and T_K is the Kauzmann temperature.

1.2.3 Temperature dependence of the relaxation times

Several theories and concepts have been proposed in an attempt to describe the glass transition phenomenon [16, 17, 18], yet some features remain unexplained. Among the unresolved challenges, the Arrhenius/non-Arrhenius behavior of the temperature dependence of the relaxation times is not yet fully understood. Many experimental techniques have been used to investigate the relaxation dynamics of glass-forming liquids over different temperature ranges and timescales (differential scanning calorimetry, dielectric relaxation spectroscopy, dynamic mechanical analysis...). In particular, the relaxation spectroscopic techniques (dielectric or mechanical) allow to study the relaxation dynamics over a wide range of temperatures and frequencies, as depicted in Figure 1.2. Going from very high temperatures down to the so-called "cross-over temperature" T_{cross} [12], relaxation times follow an Arrhenius temperature dependence that can be expressed as follows:

$$\tau(T) = \tau_\infty * exp\left(\frac{E_a}{k_B T}\right) \tag{1.2}$$

Where τ_∞ is the limit value of the relaxation time observed at high temperature (with a typical value of $\tau_\infty = 10^{-14}$ s), E_a is the activation energy of the relaxation process (i.e the energy barrier that should be overcome to activate the molecular motions), and k_B is the Bolztmann constant. Figure 1.2 shows that, in the cross-over region, the α and β-relaxation processes split

into two distinct behaviors. The β-relaxation times keep on following an Arrhenius temperature dependence, while the α-relaxation times deviates to a non-Arrhenius temperature dependence. The non-Arrhenius temperature dependence of the α-relaxation is often described by the Vogel-Tamman-Fulcher (VTF) equation [19]:

$$\tau_\alpha(T) = \tau_\infty * exp\left(\frac{A}{T - T_V}\right) \tag{1.3}$$

Where A is a fitting parameter and T_V is a characteristic temperature, also called the Vogel temperature. Depending on the chemical composition and structure of the glass-forming liquid, the deviation from an Arrhenius to a non-Arrhenius behavior is more or less pronounced. Angell proposed the concept of "fragility" to classify glass-forming liquids according to the degree of deviation from the Arrhenius behavior [20, 21].

This parameter characterizes the temperature dependence of viscosity/relaxation time as temperature approaches the glass transition, and shows how the molecular motions slow down as the glass-forming liquid goes from liquid-like to glassy. The "fragility index", also known as "steepness index", can be estimated as [22, 23]:

$$m = \left[\frac{d(log\tau)}{d(\frac{T_g}{T})}\right]_{T=T_g} \tag{1.4}$$

Using the values of fragility index, glass-forming liquids can be classified as either "strong" or "fragile" glass formers. Small values of the fragility index ($m \leq 30$) indicate that the temperature dependence of the α-relaxation process is quite close to an Arrhenius-like behavior (a perfect Arrhenius behavior corresponds to a value of $m = 16$). This behavior is typical of "strong" glass-forming liquids. When the α-relaxation process drastically deviates from the Arrhenius behavior, the glass-forming liquid is considered as "fragile", with values of the fragility index that are much higher ($m \geq 100$). For intermediate values of the fragility index ($30 \leq m \leq 100$), the liquid is considered as an intermediate glass former. The Angell's plot in Figure 1.3 is the graphical illustration of the fragility concept.

Dielectric relaxation spectroscopy (DRS) is an effective tool when it comes to the study of the temperature dependence of the relaxation times. The VTF equation is often rewritten under the form:

$$\tau_{max} = \tau_0 * exp\left(\frac{DT_0}{T - T_0}\right) \tag{1.5}$$

where τ_0 is a pre-exponential factor, D a dimensionless parameter related to the slope variation ("steepness strength"), and T_0 is a reference temperature generally corresponding to the glass transition temperature of an ideal glass, i.e a glass formed at an infinitely slow cooling rate. The fragility index can then be obtained by measuring the slope of the experimental VTF curve at the temperature for which a relaxation time of $\tau = 100$ s is observed, which is referred to as the

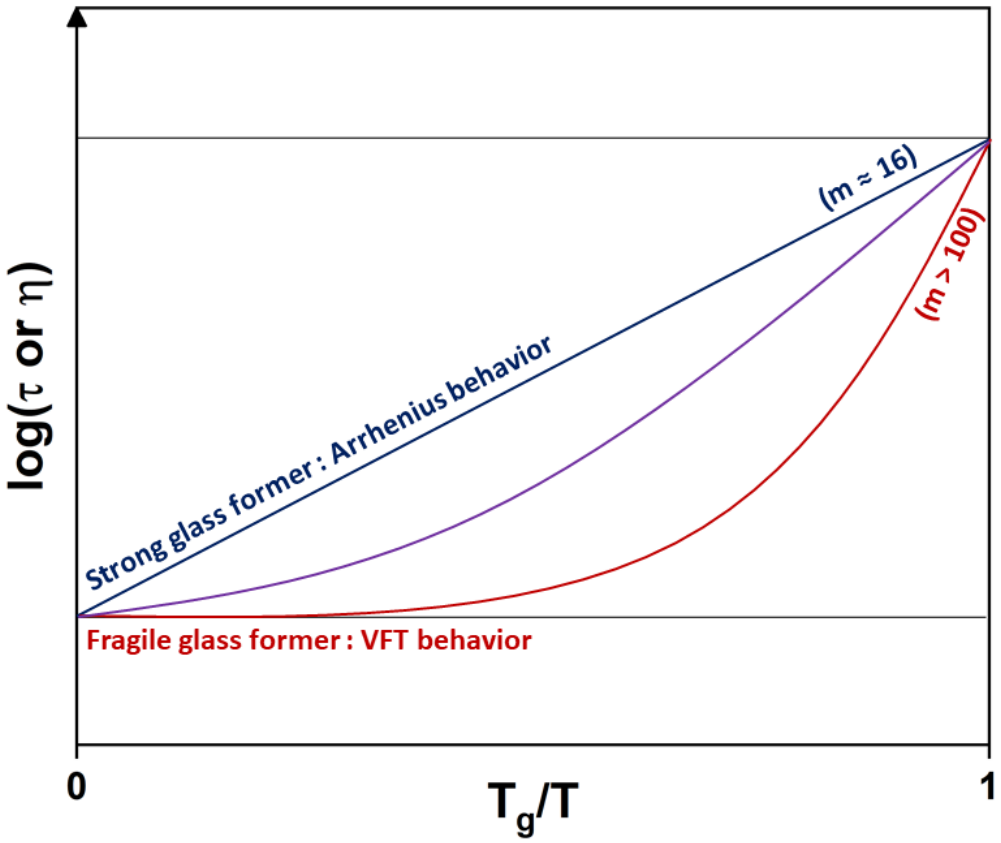

Figure 1.3: Schematic illustration of the "strong" and "fragile" behaviors according to Angell's fragility concept. Strong glass formers follow an Arrhenius temperature dependence of the relaxation times (m $\leq$ 30). On the opposite, fragile glass formers follow a Vogel-Tamman-Fulcher (VTF) temperature dependence of the relaxation times (m $\geq$ 100).

"dielectric glass transition temperature" $T_g(\tau = 100s)$. The dielectric glass transition temperature $T_g(\tau = 100s)$ is approximately equivalent to the calorimetric glass transition temperature T_g.

1.2.4 Adam and Gibbs approach

In 1965, Adam and Gibbs proposed a new approach to explain the slowing down of the molecular motions upon cooling towards glass transition [17]. They proposed that the α-relaxation process observed in glass-forming liquids takes place through the cooperative rearrangements of groups of atoms or molecular groups; the basic assumption is that the motion of these molecular groups is only possible if a number of neighboring molecular groups are also in motion. It is therefore expected that the number of molecular groups cooperatively rearranging increases as temperature decreases. A "cooperative rearranging region" (CRR) can therefore be defined as the smallest subsystem in which the main α-relaxation process occurs independently of the neighboring subsystems dynamics. Each CRR is characterized by its own relaxation dynamics and thermodynamic variables (average relaxation time and temperature fluctuation δT). Based on the theory from Adam and Gibbs, Donth proposed an experimental approach [24, 25] allowing to estimate the average size of a CRR from calorimetric measurements with the following

equation:

$$\xi_{T\alpha}^3 = \frac{1/(C_p)_{solid} - 1/(C_p)_{liquid}}{\rho(\delta T)^2} k_B (T_\alpha)^2 \tag{1.6}$$

Where $(C_p)_{solid}$ and $(C_p)_{liquid}$ are respectively the specific heat capacity at constant pressure in the solid and in the liquid states extrapolated at the glass transition temperature, ρ is the density, δT is the temperature fluctuation associated with the dynamic glass transition, and T_α is the average dynamic glass transition temperature. Donth's approach allows to estimate the average CRR size at the glass transition temperature exclusively from calorimetric experiments. Studies have further been achieved to develop other experimental methods allowing the determination of the CRR size on a wider range of temperatures, which can then be used to obtain the complete spectrum of structural relaxations. Saiter et al. [26, 27] proposed a method combining dielectric relaxation spectroscopy (DRS) and modulated-temperature differential scanning calorimetry (MT-DSC) to estimate the CRR size in an extended temperature range, i.e. from the cross-over region to the dynamic glass transition temperature.

Cooperativity has been proved to depend not only on temperature, but also on structural constraints (crystallization[28, 29], processing[26, 30, 31]...). It has also been shown in numerous studies that the cooperativity length $\xi_{T\alpha}$ can be modified by changes in the intermolecular interactions, as in the case of plasticization, or changes in the length of the side chains [32, 33, 34]. Nakanishi et al. [35] developed a simplified model of hydrogen bonding network to unveil the structure of a CRR using the Adam and Gibbs approach; they successfully explained the general features of the glass transition in polyhydric alcohols, showing that the CRR size increases with intermolecular interactions.

1.2.5 Correlation between fragility and cooperativity length

Some attempts have been made to link the changes in the CRR size to the evolution of the relaxation time. Hong et al. [36, 37], for instance, explored a wide range of glas-forming liquids including polymers, however no evident correlation between the cooperativity length and the fragility index has been observed. They tried to explain this discrepancy by splitting the fragility index in two main contributions: m_v (the fragility measured in isochoric conditions) and $m - m_v$ (the volume contribution to fragility). Under this assumption, fragility can be expressed as:

$$m = (m - m_v) + m_v = \frac{\Delta V^\#}{ln(10) k_B} \frac{\alpha_\tau}{\kappa} + m_v \tag{1.7}$$

Where α_τ is the thermal expansion coefficient of the supercooled liquid at the glass transition temperature, κ is the compressibility and $\Delta V^\#$ is approximately equal to 4% of the cooperativity volume. For a wide range of glass-forming liquids including polymers, $\frac{\alpha_\tau}{\kappa}$ is comprised between 0.5 to 3 $MPa.s^{-1}$. From this equation, only the parameter $(m - m_v)$ is assumed to be straightly correlated to the cooperativity at the glass transition. Therefore, fragility and co-

operativity are expected to be correlated only when the isochoric fragility m_v remains constant.

Recently, Araujo et al. [38] proposed a structural interpretation of the two contributions governing the fragility index measured in the liquid-like state for polymer systems approaching the glass transition upon cooling. The investigation of interpenetrated polymer networks made of two macromolecular systems with very different properties (soft and flexible acrylate, with rigid and stiff epoxy) revealed that $(m - m_v)$ depends on the interchain interactions, while the isochoric fragility m_v is mainly dependent on the backbone stiffness. Analogously, it is reasonable to think that any modification of the interchain interactions (due to structural changes and with no impact on the backbone stiffness) should lead to a concomitant evolution of fragility and cooperativity. This has been proved in a more recent study [32] on plasticized polylactic acid, where the modification of the interchain interactions induced by the incorporation of a plasticizer resulted in a correlated evolution of cooperativity and dynamic fragility. This finding supports the idea that $(m - m_v)$ and CRR size are highly correlated and that they both depend on intermolecular interactions.

1.2.6 Sub-glass relaxation processes

As previously mentioned, fast localized motions take place also at temperatures far beyond the glass transition temperature. These secondary relaxation processes are associated with the vibrations and rotations of atoms and molecular groups. The temperature dependence of these sub-glass relaxation processes follows an Arrhenius behavior that can be fitted with to the following equation:

$$\tau(T) = \tau_{0,A} * exp\left(\frac{E_a}{RT}\right) \tag{1.8}$$

Where $\tau_{0,A}$ is a pre-exponential factor, R is the gas constant and E_a is the activation energy of the relaxation process.

1.3 The crystalline state

Through the previous sections, the concept of glassy state has been discussed from both the theoretical and experimental points of view. However, as well as being able to form a glass when submitted to sufficiently high cooling rates, polymers are also able to crystallize into different crystalline forms.

1.3.1 Theories of crystal growth

The crystallization of polymers is generally described through the Lauritzen-Hoffman concept [39], which is based on the nucleation theory. A stable crystal nucleus is formed in the liquid state, which then grows up into a stable crystalline phase. In polymers, the crystallization process occurs in the presence of entangled macromolecular chains. The crystals are formed from the folding of these macromolecular chains into structures made of crystalline lamellae

with an average thickness of 10 nanometers. The crystalline lamellae are embedded in an amorphous matrix; a portion of the resulting microstructure can be schematically represented as in Figure 1.4. Due to the size of their molecules (much larger than the size of the formed crystalline structures) and to the presence of entanglements, polymers are not able to fold into a perfect crystalline lattice, so they are never found in a fully crystalline state. Polymers can crystallize from different pathways that are generally classified into two categories, called conventional and unconventional crystallization. "Conventional crystallization" is the thermally activated crystallization process that follows the Lauritzen-Hoffman concept. On the other hand, "unconventional crystallization" is the crystallization process that is activated through other mechanisms (cross-nucleation [40], memory effect [41]...). During conventional crystallization, the crystalline lamellae grow in a direction that corresponds to a defined crystallographic plane. This crystallization proceeds radially from the nucleus, generating a spherical structure called "spherulite".

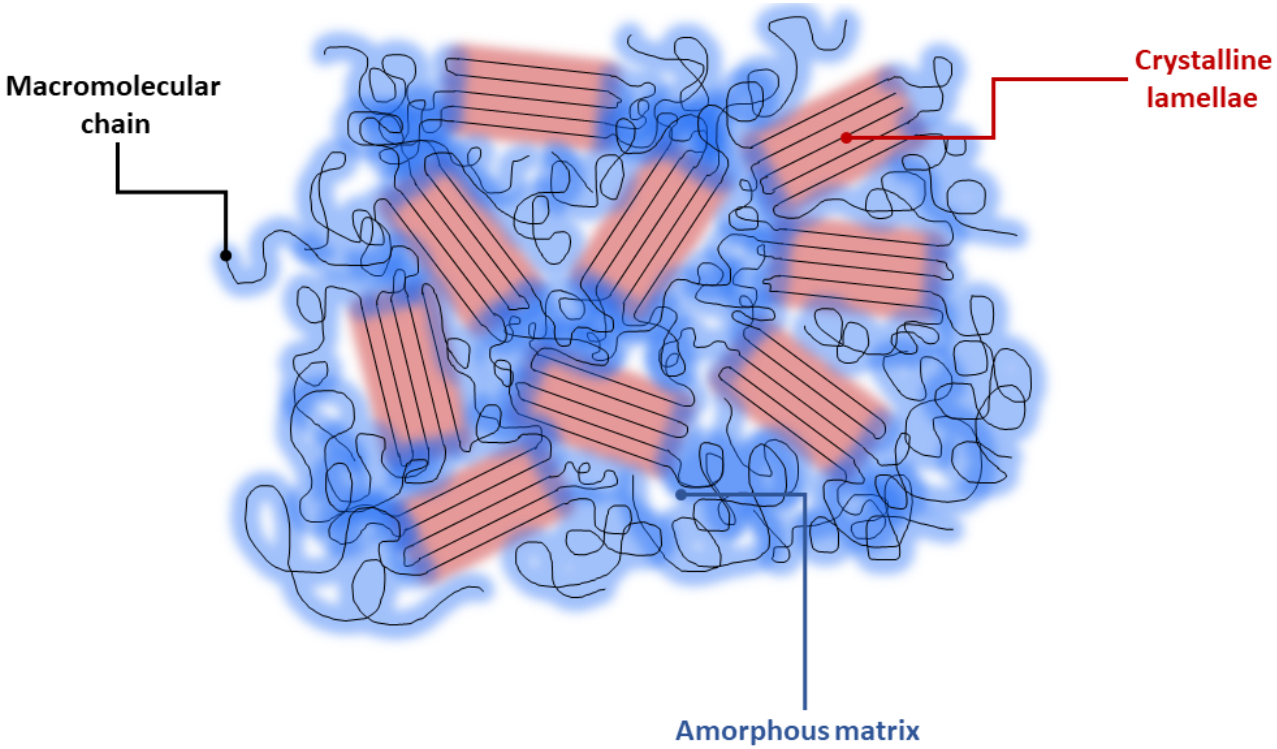

Figure 1.4: Illustration of the semi-crystalline microstructure than can be observed in polymer systems. Black lines represent the macromolecular chains, red areas depict the crystalline domains (lamellar stackings), and the blue areas represent the amorphous matrix.

Conventional crystallization can be achieved following two different pathways, i.e. by cooling a polymer from the molten state or by heating it from the glassy state, as shown in Figure 1.5. Whatever the pathway, according to the nucleation-growth theory [39], crystallization is only possible when two processes ("nucleation" and "growth") occur. The nucleation process relies on the ability to form stable nuclei, whereas the growth process corresponds to the capability to grow a crystalline structure from the existing nuclei.

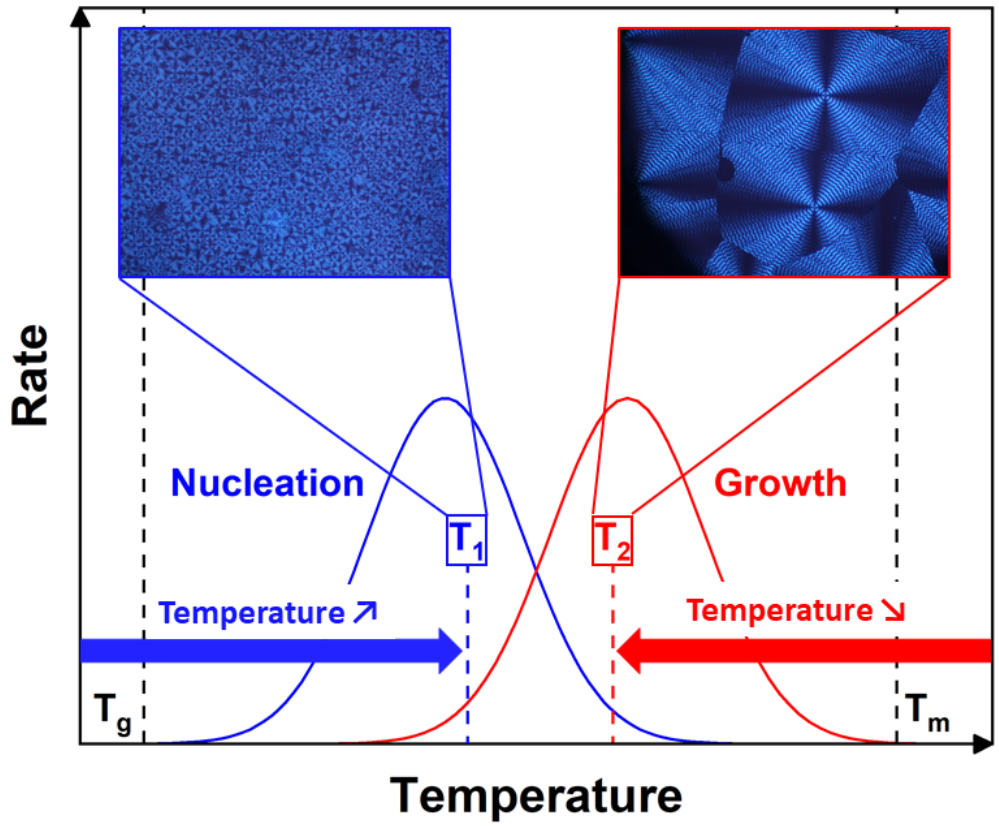

Figure 1.5: Schematic illustration of the nucleation-growth processes in polymers. Conventional crystallization can be achieved by cooling from the melt, which generally leads to a small number of big spherulites (red arrow), but also by heating from the glassy state, which results in a higher number of smaller spherulites (blue arrow). The two pictures are experimental results obtained by polarized optical microscopy on a polymer sample crystallized either from the melt or from the glassy state.

1.3.2 Crystallization from the molten state vs. crystallization from the glassy state

It has been previously mentioned that conventional crystallization can be obtained through two main pathways. The first one requires to cool the sample from the molten state down to a given crystallization temperature, as shown by the red arrow in Figure 1.5. When a sample is progressively cooled down from the molten state, it will first experience a growth process. However, in the absence of nuclei, the crystal growth is impossible. In order to initiate crystal growth, it is therefore necessary to cool the sample down to a temperature at which the nucleation process occurs (T_2 in Figure 1.5). Yet, at this temperature the nucleation rate is lower than the crystal growth rate. This difference between the nucleation and growth rates leads to the formation of a microstructure containing small amounts of big crystals, as shown by the inset on the right side of Figure 1.5. These crystals are formed in a highly energetic environment, where the folding mechanisms of the macromolecular chains are favoured, which eventually leads to highly perfected crystals.

Conventional crystallization can also be achieved by heating an amorphous polymer sample from the glassy state. Unlike what happens during the crystallization from the molten state,

when a polymer sample is heated from the glassy state up to the crystallization temperature, it will experience a nucleation process. However, if the temperature remains too low for the growth process to start, crystallization is not observed. In this case, the number of stable nuclei is much higher, yet no crystals are forming. As soon as the temperature is increased until reaching the growth-process temperature range, crystal growth starts (T_1 in Figure 1.5). At this crystallization temperature, however, the nucleation rate is still higher than the growth rate, which leads to the formation of a microstructure containing a large number of very small crystals, as shown by the inset on the left side of Figure 1.5. Moreover, in this case, the crystallization occurs in a low energetic environment, where chain folding is hindered, resulting in imperfect crystals. Sometimes this situation can lead to polymorphism; in the case of poly(lactic acid) (PLA), for instance, a poorly organized and unstable crystalline phase (α') is formed at low crystallization temperatures, which reorganizes into a more perfect crystalline phase (α) as temperature increases.

1.4 Semi-crystalline microstructures

The semi-crystalline structures observed in polymers are generally made of crystalline lamellae embeded in an amorphous matrix. These microstructures can be described through different models.

1.4.1 Two-phase model

The simplest way to describe the microstructure of semi-crystalline polymers is the so-called "two-phase model", which assumes that crystalline and amorphous domains can be clearly distinguished, quantified and globally identified as the "crystalline phase" and the "amorphous phase", respectively. In a two-phase model, a simple and straightforward distinction is made based on the fact that the crystalline domains are ordered, whereas the amorphous domains are disordered. On one hand, the amorphous phase is defined by the absence of a long-range order [1, 2, 3] and is quantified and characterized through different techniques, such as calorimetry [8, 28, 42, 43], dielectric spectroscopy [44, 45, 46] and dynamic mechanical analysis [47, 48]. In particular, Differential Scanning Calorimetry (DSC) reveals the presence of an amorphous phase as a heat capacity step measured at the glass transition temperature, i.e. the temperature at which the glassy domains formed by the randomly entangled polymer chains go from the glassy to the liquid state. On the other hand, polymer crystals result from a partial arrangement of the macromolecules in lamellae, where most of the polymer chains are able to fold and form a crystal lattice [49] but some of them remain entangled and locally disrupt the long-range order. These complex structures, which are intrinsically semi-crystalline and more or less regular, are known to go from the solid to the liquid state at a temperature called the "melting temperature" T_m, which in fact corresponds to a more or less extended temperature range rather than a single temperature value. Both the growth (crystallization) and the disappearance (melting) of polymer crystals can be observed and characterized by techniques such as calorimetry [43],

polarized optical microscopy (POM) [33, 50], and X-ray diffractometry (XRD) [28, 42].

1.4.2 Three-"phase" model

The two-phase model describes the microstructure of semi-crystalline as follows:

$$X_{amorphous} + X_{crystalline} = 1 \tag{1.9}$$

Where $X_{amorphous}$ is the amorphous phase and $X_{crystalline}$ is the crystalline phase. However, in most cases, the microstructural description provided by the two-phase model is not accurate and is better replaced by a more complex three-"phase" model [49, 51]. The latter involves an additional "phase" introduced to represent the fraction of polymer chains connecting the amorphous phase to the crystalline domains. Indeed, it is difficult for a macromolecule to regularly fold into crystals, because the length of a polymer chain is much higher than the characteristic dimensions of the crystalline lamellae [52, 53]. This sort of "interphase" is amorphous but also highly constrained by the nearby crystalline regions; for this reason, it is called "rigid amorphous fraction" (RAF). From an experimental point of view, the RAF is distinguished from the unconstrained "mobile amorphous fraction" (MAF) because it does not contribute to the heat capacity change at the glass transition [54, 55]. Equation 1.9 can then be rewritten as follows:

$$X_{MAF} + X_{crystalline} + X_{RAF} = 1 \tag{1.10}$$

Where X_{MAF} is the unconstrained mobile amorphous fraction,$X_{crystalline}$ is the fraction of crystalline phase, and X_{RAF} is the fraction of amorphous phase constrained by the nearby crystalline phase. Several studies showed that the RAF can be used to explain some macroscopic properties of semi-crystalline materials [56, 57], which means that understanding this interphase should be considered as a major step in the characterization of semi-crystalline polymers [58]. During the past years, different techniques have been used to investigate the RAF in semi-crystalline polymers, such as calorimetry [59], dielectric spectroscopy [60] or infrared spectroscopy [61, 62]. However, the amount of RAF cannot be directly measured, it can only be estimated through equation 1.10. It is then mandatory to get a fairly accurate quantification of both the MAF and the crystalline fraction. The MAF is the only amorphous fraction that devitrifies in the glass transition temperature range, and in most cases X_{MAF} can be quantified by Differential scanning Calorimetry (DSC) as follows:

$$X_{MAF} = \frac{(\Delta C_p)^{DSC}_{crystallized}}{(\Delta C_p)^{DSC}_{amorphous}} \tag{1.11}$$

Where $(\Delta C_p)^{DSC}_{crystallized}$ is the change in specific heat capacity measured at the glass transition for a crystallized sample, and $(\Delta C_p)^{DSC}_{amorphous}$ is the change in specific heat capacity measured at the glass transition for its fully amorphous counterpart.

The crystalline fraction $X_{crystalline}$ is generally determined by DSC and Wide-Angle X-ray

Diffraction (WAXD). The measurement of $X_{crystalline}$ by DSC is obtained according to the following equation:

$$X_{crystalline} = \frac{(\Delta H_m)^{DSC}}{(\Delta H_m^0)} \tag{1.12}$$

Where $(\Delta H_m)^{DSC}$ is the melting enthalpy measured on a crystallized sample, and (ΔH_m^0) is the enthalpy that would have been measured on a theoretically 100% crystallized sample. Nonetheless, for some polymers debates are ongoing regarding the (ΔH_m^0) value that has to be used to make the calculation as different values can be found in the literature for a same polymer. These differences in $(\Delta H_m^0$ values reported in the literature are most of the time due to the fact that this value is determined through extrapolative methods (see chapter 3 for more details).

The determination of $X_{crystalline}$ by WAXD is most of the time achieved by calculating a ratio between the area under the crystalline peaks and the total area under the diffraction spectrum, as shown by equation 1.12.

$$X_{crystalline} = \frac{A_{crystalline}}{A_{total}} \tag{1.13}$$

Where $A_{crystalline}$ is the area under the crystalline peaks, and A_{total} is the total area under the diffraction spectrum (crystalline peaks plus the amorphous halo, as graphically shown in Figure 1.6).

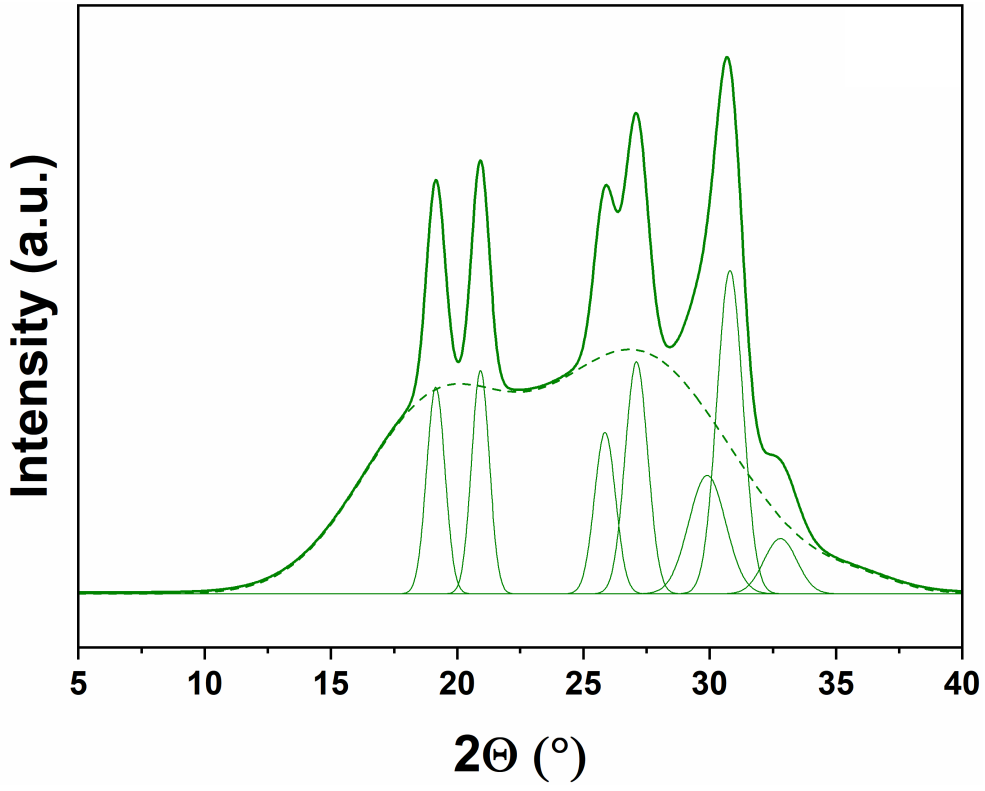

Figure 1.6: Example of XRD diffraction pattern of a semi-crystalline polymer.

This method does not give access to the absolute crystalline degree of the sample, and the Ruland's method [63] (which considers the conservation of the total intensity by a set of atoms, independently on their structural order) should be used to get a more accurate estimation of the crystalline fraction. However, the Ruland's method is a heavy analitycal method, and in most cases the method based on the ratio of areas is considered as sufficient to get a fairly accurate estimation of the crystalline fraction. If equations 1.10, 1.11, 1.12 and 1.13 are merged, the RAF can be determined as:

$$X_{RAF} = 1 - \frac{(\Delta C_p)^{DSC}_{crystallized}}{(\Delta C_p)^{DSC}_{amorphous}} - \frac{(\Delta H_m)^{DSC}}{(\Delta H^0_m)} = 1 - \frac{(\Delta C_p)^{DSC}_{crystallized}}{(\Delta C_p)^{DSC}_{amorphous}} - \frac{A^{WAXD}_{crystalline}}{A^{WAXD}_{total}} \tag{1.14}$$

In the past few years, many studies have discussed the complexity behind the formation of the RAF in different semi-crystalline polymers [58, 64]; nonetheless, the role and the consequences of this interphase is still under investigation, as many features have not been fully comprehended yet.

1.4.3 General knowledge about the rigid amorphous fraction

As previously mentioned, in the literature it has been shown that the RAF can be used to explain many macroscopic properties of semi-crystalline polymers (mechanical properties [56, 65], gas permeability [66, 67]) as well as their evolution with time (embrittlement [58]). From a thermodynamic point of view, an increase in the RAF amount can have a non-negligible effect on the glass transition. In most cases, it leads to an overall increase in the glass transition temperature [58, 68]. With regards to the mechanical properties, it has been shown that the RAF behaves similarly to the crystalline phase, and can therefore have a strong influence on the elastic modulus [56, 65]. It has also been pointed out that the RAF has an important effect on the gas barrier properties [66, 67]. However, in this case, its behavior is different from the crystalline phase, and is closer to the behavior of an unconstrained amorphous phase in the glassy state. This behavior has been attributed to a higher free volume as compared to the crystalline phase. Because the RAF amount can have a non-negligible effect on the macroscopic properties of semi-crystalline polymers, it is of great interest to understand the behavior of this interphase as well as the conditions that are favorable (or not) to its formation.

MAF and RAF are fractions of the same amorphous phase. As any other amorphous phase, they both go from a glassy state to a liquid-like state upon heating (this transition is also known as "devitrification"). The presence of crystalline domains constrains the amorphous fraction in the closest surroundings; for this reason, the devitrification of the RAF generally occurs over a wide temperature range between the glass transition temperature T_g (devitrification of the MAF) and the melting temperature T_m. This behavior makes it difficult to observe the devitrification of the RAF, which is widespread and often overlaps with other thermal events, such as the crystallization and melting of the crystals.

Studies have been carried out [53, 58, 69] to understand the mechanisms driving the development of the RAF. It has been shown, on a limited amount of semi-crystalline polymers, that this mechanism is mainly impacted by the crystallization conditions. Therefore, crystal growth and RAF development, as well as melting and RAF devitrification, are strongly correlated. From these studies, it has been observed that at low crystallization temperatures (i.e. slightly above the glass transition temperature, T_1 in Figure 1.5) the development of the RAF takes places concomitantly with crystallization [49, 69]. On the other hand, at high temperatures (i.e. slightly below the melting temperature, T_2 in Figure 1.5) the development of the RAF takes place during the final stages of crystallization, sometimes simultaneously to the growth of secondary crystals [51, 70]. For some polymers, such as poly(hydroxybutyrate) (PHB)[71], poly(ethylene terephthalate) (PET)[59] and poly(L-lactic acid) (PLLA)[72], the devitrification of the RAF has been observed at temperatures close the temperature at which RAF has been formed upon crystallization. This confirms that the development of the RAF can be directly correlated to the crystallization process. The appearance of the RAF is thus dependent on the crystallization conditions, and the higher is the crystallization temperature, the lower is the RAF amount. This general trend suggests that RAF amount is dependent on both crystal morphology and degree of perfection.

As pointed out in section (1.3), at low crystallization temperatures, the high nucleation density and the relatively low chain mobility lead to the growth of a high number of small imperfect crystals. Therefore, the crystal-amorphous interface is thicker, which results in a higher amount of RAF. On the opposite, at higher temperatures, the chain mobility is favoured and the crystal growth occurs in a more suitable environment, leading to the growth of a small number of more perfected crystals. In this case, the crystal-amorphous interface is reduced, and the RAF amount is smaller. It is then possible to control the amount of RAF developed in the microstructure of a semi-crystalline polymer by controlling the crystallization temperature.

1.4.4 An improved version of the two-phase model

The microstructure of semi-crystalline polymers were historically described using a quite "simple" two-phase model. This model was then replaced by a "quantitatively more accurate" three-phase model, which considers the amorphous phase as composed of an unconstrained fraction (MAF) and a constrained fraction (RAF).

More recently, Esposito et al. [58] proposed a new approach to describe the microstructure of semi-crystalline polymers. This approach uses an "improved version" of the two-phase model instead of the previous two-phase or three-phase models. In this complex version of the two-phase model, the interface between the crystalline domains and their surroundings amorphous regions is rather described as a "continuum of mobility". This concept is based on the fact that, for some polymers crystallized in specific conditions, the crystalline and amorphous phases are strongly coupled, and therefore the mobile and rigid fractions of the amorphous phase are

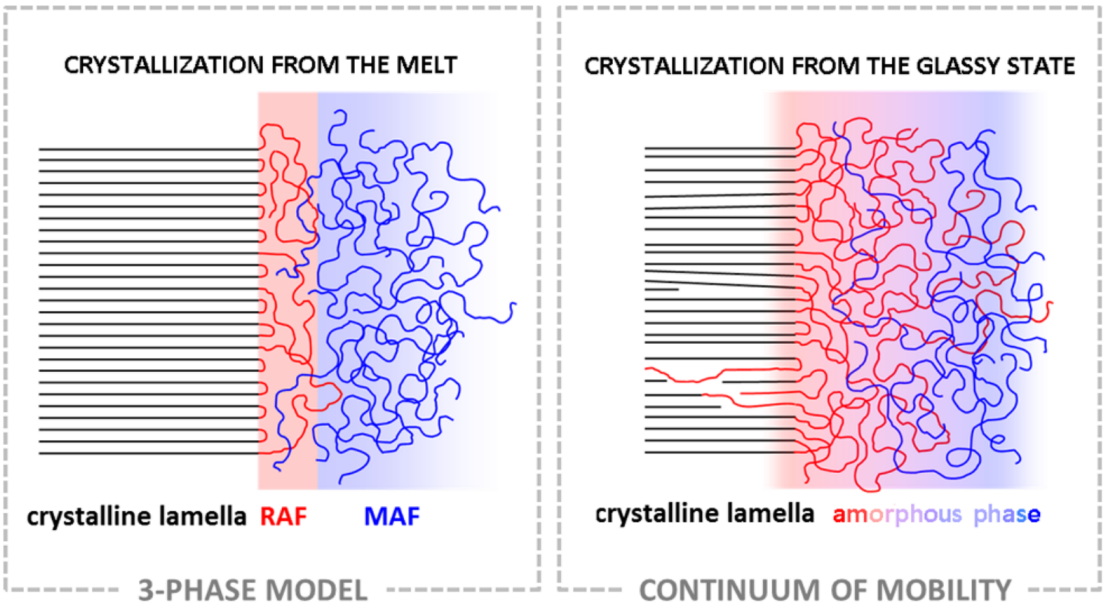

Figure 1.7: Schematic illustration of the concept of "continuum of mobility" introduced by Esposito et al. Reprinted with permission from [58].

hardly separated. When the coupling between phases is very strong, splitting the amorphous phase in two fractions is not only difficult, but also less pertinent than described the entire amorphous phase as a continuum characterized by a gradient of mobility (the lowest mobility being represented by the crystalline phase, the highest mobility being represented by the total absence of crystals). In other words, from the point of view of molecular relaxations, it is sometimes better to considered an extended distribution of the relaxation times (i.e. a single amorphous phase with modified relaxation dynamics) rather than two distinct amorphous fractions having their respective relaxation dynamics. This concept is schematized in Figure 1.7.

1.5 From fossil to sustainable resources

Nowadays, new polymers are constantly synthesized from sustainable resources (vegetable feedstock [73, 74], bacteria [75, 76]...), increasing the panel of possible alternatives to fossil-based materials. Polyesters are one of the largest family of polymers; they can be obtained by combining an acid with a diol. Many possibilites exist to extract both acids and diols from renewable ressources, which provides an almost unlimited number of possible combinations. Both the acid and the diol for polymer synthesis should be carefully selected, because their chemical composition and atomic arrangement can dramatically affect the properties of the final polyester. Indeed, depending on the selected monomers, the polymer backbone may contain either aromatic rings (e.g. benzene in poly (ethylene terephthalate) (PET), furan rings in poly (ethylene furanoate) (PEF)), alicyclic compounds (e.g. cyclohexanoate), or linear aliphatic segments (e.g. polylactic acid (PLA), polyhydroxyalkanoates (PHAs)); moreover, many different diols with different lengths and possible position isomers can be used in combination with any given

acid [77], which further pushes the boundaries of what is possible.

However, when the aim of the investigations is to deep understand the features of newly developed materials, a major drawback rapidly rises: the lack of information in the literature. The preliminary characterizations of brand new materials aiming at determining their fundamental properties (such as the equilibrium melting temperature T_m^0 or the equilibrium enthalpy of melting ΔH_m^0, the temperature ranges, the main thermal transitions, the aptitude to crystallize...) are critical to dive deeper into their microstructural characterization, for instance, and thus to fully understand their behaviours.

1.5.1 Polyhydroxyalkanoates

Of all the new bio-based polymers that have been synthesized to find sustainable alternatives to fossil ressources, the large family of polyhydroxyalkanoates (PHAs) is one of the most promising and challenging. The behavior and properties of these polyesters depend on both the nature and content of the repeating units in the macromolecular chains, which explains the growing interest for these materials [75, 78]. PHAs are natural polyesters, for they are synthesized by bacteria in incubators. By controlling the parameters of the biosynthesis, it is possible to obtain a large panel of different homopolymers and copolymers [76, 79]. The simplest homopolyester belonging to the PHAs family is poly [(R)-3-hydroxybutyrate] (PHB), which is also one of the most studied. PHB generally develops high crystallinities, and has a poorer thermal stability with respect to other polyesters, which makes it rather complicated to use is for industrial applications [80]. The problems related to high crystallinity can be generally overcome by the use of nucleation agents, or by the association of different repeating units in the same macromolecule, e.g. by associating hydroxyvalerate (HV) or hydroxyhexanoate (HHx) units to the hydroxybutyrate (HB) units. This approach gives access to a series of possible copolyesters, which could meet the expectations of a broader range of applications compared to PHB.

1.5.2 Furanoate-based polymers

Currently, one of the most promising bio-chemicals is furandicarboxylic acid (FDCA), which can be produced from vegetable feedstock and used to synthesize polyesters, such as poly(ethylene furandicarboxylate) (PEF), poly(propylene furandicarboxylate) (PPF) and poly(butylene furandicarboxylate) (PBF). FDCA exists in the form of three position isomers; the most commonly used is 2,5-FDCA. Among all the furanoate-based polymers, 2,5-PEF is the most studied due to some interesting mechanical and barrier properties, which makes it the best sustainable surrogate to poly(ethylene terephthalate) (PET) for packaging applications [81]. 2,5-PPF is also an interesting polymer with excellent gas barrier properties [82], which makes it a promising substitute for its petroleum-based homologues poly(trimethylene terephthalate) (PTT) and poly(trimethylene naphthalate) (PTN) in packaging applications. Another polymer belonging to the family of furanoate-based polyesters and worth investigating is 2,5-PBF. This poly-

mer has good thermal, mechanical [83] and barrier properties [83], which can be suitable for food-packaging applications in replacement of its terephthalic counterpart.

References

[1] E. D. Zanotto and J. C. Mauro, "The glassy state of matter: Its definition and ultimate fate," *Journal of Non-Crystalline Solids*, vol. 471, pp. 490–495, Sept. 2017.

[2] M. C. Wilding, M. Wilson, and P. F. McMillan, "Structural studies and polymorphism in amorphous solids and liquids at high pressure," *Chem. Soc. Rev.*, vol. 35, no. 10, p. 964, 2006.

[3] I. M. Kalogeras and H. Hagg Lobland, "The nature of the glassy state: Structure and glass transitions," *Journal of Materials Education*, vol. 34, pp. 69–94, 2012.

[4] C. A. Angell, "Formation of Glasses from Liquids and Biopolymers," *Science*, vol. 267, pp. 1924–1935, Mar. 1995.

[5] M. Tatsumisago, B. L. Halfpap, J. L. Green, S. M. Lindsay, and C. A. Angell, "Fragility of Ge-As-Se glass-forming liquids in relation to rigidity percolation, and the Kauzmann paradox," *Phys. Rev. Lett.*, vol. 64, pp. 1549–1552, Mar. 1990.

[6] B. Schammé, M. Mignot, N. Couvrat, V. Tognetti, L. Joubert, V. Dupray, L. Delbreilh, E. Dargent, and G. Coquerel, "Molecular Relaxations in Supercooled Liquid and Glassy States of Amorphous Quinidine: Dielectric Spectroscopy and Density Functional Theory Approaches," *J. Phys. Chem. B*, vol. 120, pp. 7579–7592, Aug. 2016.

[7] B. Atawa, N. Couvrat, G. Coquerel, E. Dargent, and A. Saiter, "Impact of chirality on the Glass Forming Ability and the crystallization from the amorphous state of 5-ethyl-5-methylhydantoin, a chiral poor glass former," *International Journal of Pharmaceutics*, vol. 540, pp. 11–21, Apr. 2018.

[8] E. Hempel, G. Hempel, A. Hensel, C. Schick, and E. Donth, "Characteristic Length of Dynamic Glass Transition near T_g for a Wide Assortment of Glass-Forming Substances," *J. Phys. Chem. B*, vol. 104, pp. 2460–2466, Mar. 2000.

[9] P. de Gennes, "Glass transitions in thin polymer films," *Eur. Phys. J. E*, vol. 2, pp. 201–205, July 2000.

[10] A. L. Greer, "Metallic Glasses," *Science*, vol. 267, pp. 1947–1953, Mar. 1995.

[11] W. Wang, C. Dong, and C. Shek, "Bulk metallic glasses," *Materials Science and Engineering: R: Reports*, vol. 44, pp. 45–89, June 2004.

[12] W. Gotze and L. Sjogren, "Relaxation processes in supercooled liquids," *Rep. Prog. Phys.*, vol. 55, pp. 241–376, Mar. 1992.

[13] W. Kauzmann, "The Nature of the Glassy State and the Behavior of Liquids at Low Temperatures.," *Chem. Rev.*, vol. 43, pp. 219–256, Oct. 1948.

[14] F. H. Stillinger, "Supercooled liquids, glass transitions, and the Kauzmann paradox," *The Journal of Chemical Physics*, vol. 88, pp. 7818–7825, June 1988.

[15] I. M. Hodge, "Physical Aging in Polymer Glasses," *Science*, vol. 267, pp. 1945–1947, Mar. 1995.

[16] R. E. Powell, W. E. Roseveare, and H. Eyring, "Diffusion, Thermal Conductivity, and Viscous Flow of Liquids," *Ind. Eng. Chem.*, vol. 33, pp. 430–435, Apr. 1941.

[17] G. Adam and J. H. Gibbs, "On the Temperature Dependence of Cooperative Relaxation Properties in Glass-Forming Liquids," *The Journal of Chemical Physics*, vol. 43, pp. 139–146, July 1965.

[18] U. Bengtzelius, W. Gotze, and A. Sjolander, "Dynamics of supercooled liquids and the glass transition," *J. Phys. C: Solid State Phys.*, vol. 17, pp. 5915–5934, Nov. 1984.

[19] G. S. Fulcher, "Analysis of recent measurements of the viscosity of glasses," *J American Ceramic Society*, vol. 8, pp. 339–355, June 1925.

[20] C. Angell, "Spectroscopy simulation and scattering, and the medium range order problem in glass," *Journal of Non-Crystalline Solids*, vol. 73, pp. 1–17, Aug. 1985.

[21] C. Angell, "Relaxation in liquids, polymers and plastic crystals — strong/fragile patterns and problems," *Journal of Non-Crystalline Solids*, vol. 131-133, pp. 13–31, June 1991.

[22] D. J. Plazek and K. L. Ngai, "Correlation of polymer segmental chain dynamics with temperature-dependent time-scale shifts," *Macromolecules*, vol. 24, pp. 1222–1224, Sept. 1991.

[23] R. Böhmer and C. A. Angell, "Correlations of the nonexponentiality and state dependence of mechanical relaxations with bond connectivity in Ge-As-Se supercooled liquids," *Phys. Rev. B*, vol. 45, pp. 10091–10094, May 1992.

[24] E. Donth, "Characteristic length of the glass transition," *Journal of Polymer Science Part B: Polymer Physics*, vol. 34, pp. 2881–2892, Dec. 1996.

[25] E. Donth, "The size of cooperatively rearranging regions at the glass transition," *Journal of Non-Crystalline Solids*, vol. 53, pp. 325–330, Dec. 1982.

[26] A. Saiter, D. Prevosto, E. Passaglia, H. Couderc, L. Delbreilh, and J. M. Saiter, "Cooperativity length scale in nanocomposites: Interfacial and confinement effects," *Phys. Rev. E*, vol. 88, p. 042605, Oct. 2013.

[27] B. Rijal, L. Delbreilh, and A. Saiter, "Dynamic Heterogeneity and Cooperative Length Scale at Dynamic Glass Transition in Glass Forming Liquids," *Macromolecules*, vol. 48, pp. 8219–8231, Nov. 2015.

[28] C. Schick and E. Donth, "Characteristic length of glass transition: experimental evidence," *Phys. Scr.*, vol. 43, pp. 423–429, Apr. 1991.

[29] N. Varol, N. Delpouve, S. Araujo, S. Domenek, A. Guinault, R. Golovchak, A. Ingram, L. Delbreilh, and E. Dargent, "Amorphous rigidification and cooperativity drop in semi-crystalline plasticized polylactide," *Polymer*, vol. 194, p. 122373, Apr. 2020.

[30] C. Zhang, Y. Guo, and R. D. Priestley, "Characteristic Length of the Glass Transition in Isochorically Confined Polymer Glasses," *ACS Macro Lett.*, vol. 3, pp. 501–505, June 2014.

[31] S. F. Nassar, S. Domenek, A. Guinault, G. Stoclet, N. Delpouve, and C. Sollogoub, "Structural and Dynamic Heterogeneity in the Amorphous Phase of Poly(l, l-lactide) Confined at the Nanoscale by the Coextrusion Process," *Macromolecules*, vol. 51, pp. 128–136, Jan. 2018.

[32] S. Araujo, N. Delpouve, S. Domenek, A. Guinault, R. Golovchak, R. Szatanik, A. Ingram, C. Fauchard, L. Delbreilh, and E. Dargent, "Cooperativity Scaling and Free Volume in Plasticized Polylactide," *Macromolecules*, vol. 52, pp. 6107–6115, Aug. 2019.

[33] J. A. S. Puente, A. Esposito, F. Chivrac, and E. Dargent, "Effects of Size and Specific Surface Area of Boron Nitride Particles on the Crystallization of Bacterial Poly(3-hydroxybutyrate- *co* -3-hydroxyvalerate)," *Macromol. Symp.*, vol. 328, pp. 8–19, June 2013.

[34] X. Monnier, N. Delpouve, N. Basson, A. Guinault, S. Domenek, A. Saiter, P. Mallon, and E. Dargent, "Molecular dynamics in electrospun amorphous plasticized polylactide fibers," *Polymer*, vol. 73, pp. 68–78, Sept. 2015.

[35] M. Nakanishi and R. Nozaki, "Model of the cooperative rearranging region for polyhydric alcohols," *Phys. Rev. E*, vol. 84, p. 011503, July 2011.

[36] L. Hong, V. Novikov, and A. Sokolov, "Is there a connection between fragility of glass forming systems and dynamic heterogeneity/cooperativity?," *Journal of Non-Crystalline Solids*, vol. 357, pp. 351–356, Jan. 2011.

[37] A. P. Sokolov, "Cooperativity and heterogeneity in dynamics of glass-forming systems," (Sendai, Japan), pp. 104–109, 2013.

[38] S. Araujo, F. Batteux, W. Li, L. Butterfield, N. Delpouve, A. Esposito, L. Tan, J.-M. Saiter, and M. Negahban, "A structural interpretation of the two components governing the kinetic fragility from the example of interpenetrated polymer networks: A Structural Interpretation of the Two Components Governing the Kinetic Fragility from the Example of Interpenetrated Polymer Networks," *J. Polym. Sci. Part B: Polym. Phys.*, vol. 56, pp. 1393–1403, Oct. 2018.

[39] J. Lauritzen and J. D. Hoffman, "Theory of formation of polymer crystals with folded chains in dilute solution.," 1960.

[40] D. Cavallo, L. Gardella, G. Portale, A. J. Müller, and G. C. Alfonso, "On cross- and self-nucleation in seeded crystallization of isotactic poly(1-butene)," *Polymer*, vol. 54, pp. 4637–4644, Aug. 2013.

[41] B. O. Reid, M. Vadlamudi, A. Mamun, H. Janani, H. Gao, W. Hu, and R. G. Alamo, "Strong Memory Effect of Crystallization above the Equilibrium Melting Point of Random Copolymers," *Macromolecules*, vol. 46, pp. 6485–6497, Aug. 2013.

[42] R. Androsch, M. L. Di Lorenzo, C. Schick, and B. Wunderlich, "Mesophases in polyethylene, polypropylene, and poly(1-butene)," *Polymer*, vol. 51, pp. 4639–4662, Oct. 2010.

[43] C. Schick, "Differential scanning calorimetry (DSC) of semicrystalline polymers," *Anal Bioanal Chem*, vol. 395, pp. 1589–1611, Nov. 2009.

[44] M. Tress, M. Erber, E. U. Mapesa, H. Huth, J. Müller, A. Serghei, C. Schick, K.-J. Eichhorn, B. Voit, and F. Kremer, "Glassy Dynamics and Glass Transition in Nanometric Thin Layers of Polystyrene," *Macromolecules*, vol. 43, pp. 9937–9944, Dec. 2010.

[45] A. Serghei, H. Huth, C. Schick, and F. Kremer, "Glassy Dynamics in Thin Polymer Layers Having a Free Upper Interface," *Macromolecules*, vol. 41, pp. 3636–3639, May 2008.

[46] S. Weyer, A. Hensel, J. Korus, E. Donth, and C. Schick, "Broad band heat capacity spectroscopy in the glass-transition region of polystyrene," *Thermochimica Acta*, vol. 304-305, pp. 251–255, Nov. 1997.

[47] D. Chen and H. Zachmann, "Glass transition temperature of copolyesters of PET, PEN and PHB as determined by dynamic mechanical analysis," *Polymer*, vol. 32, pp. 1612–1621, Jan. 1991.

[48] J. Rieger, "The glass transition temperature Tg of polymers—Comparison of the values from differential thermal analysis (DTA, DSC) and dynamic mechanical measurements (torsion pendulum)," *Polymer Testing*, vol. 20, pp. 199–204, Oct. 2001.

[49] B. Wunderlich, "Reversible crystallization and the rigid–amorphous phase in semicrystalline macromolecules," *Progress in Polymer Science*, vol. 28, pp. 383–450, Mar. 2003.

[50] R. Androsch, M. Soccio, N. Lotti, D. Cavallo, and C. Schick, "Cold-crystallization of poly(butylene 2,6-naphthalate) following Ostwald's rule of stages," *Thermochimica Acta*, vol. 670, pp. 71–75, Dec. 2018.

[51] H. Chen and P. Cebe, "Vitrification and Devitrification of Rigid Amorphous Fraction of PET during Quasi-Isothermal Cooling and Heating," *Macromolecules*, vol. 42, pp. 288–292, Jan. 2009.

[52] B. Wunderlich and A. Mehta, "Macromolecular nucleation," *J. Polym. Sci. Polym. Phys. Ed.*, vol. 12, pp. 255–263, Feb. 1974.

[53] R. Androsch and B. Wunderlich, "The link between rigid amorphous fraction and crystal perfection in cold-crystallized poly(ethylene terephthalate)," *Polymer*, vol. 46, pp. 12556–12566, Dec. 2005.

[54] J. Menczel and B. Wunderlich, "Heat capacity hysteresis of semicrystalline macromolecular glasses," *J. Polym. Sci. B Polym. Lett. Ed.*, vol. 19, pp. 261–264, May 1981.

[55] Q. Ma, G. Georgiev, and P. Cebe, "Constraints in semicrystalline polymers: Using quasi-isothermal analysis to investigate the mechanisms of formation and loss of the rigid amorphous fraction," *Polymer*, vol. 52, pp. 4562–4570, Sept. 2011.

[56] I. Kolesov and R. Androsch, "The rigid amorphous fraction of cold-crystallized polyamide 6," *Polymer*, vol. 53, pp. 4770–4777, Sept. 2012.

[57] S. Martín, M. T. Expósito, J. F. Vega, and J. Martínez-Salazar, "Microstructure and properties of branched polyethylene: Application of a three-phase structural model," *J. Appl. Polym. Sci.*, pp. 1871–1878, 2012.

[58] A. Esposito, N. Delpouve, V. Causin, A. Dhotel, L. Delbreilh, and E. Dargent, "From a Three-Phase Model to a Continuous Description of Molecular Mobility in Semicrystalline Poly(hydroxybutyrate- *co* -hydroxyvalerate)," *Macromolecules*, vol. 49, pp. 4850–4861, July 2016.

[59] M. C. Righetti, M. Laus, and M. L. Di Lorenzo, "Rigid amorphous fraction and melting behavior of poly(ethylene terephthalate)," *Colloid and Polymer Science*, vol. 292, pp. 1365–1374, June 2014.

[60] A. Nogales, T. A. Ezquerra, F. Batallán, B. Frick, E. López-Cabarcos, and F. J. Baltá-Calleja, "Restricted Dynamics in Poly(ether ether ketone) As Revealed by Incoherent Quasielastic Neutron Scattering and Broad-Band Dielectric Spectroscopy," *Macromolecules*, vol. 32, pp. 2301–2308, Apr. 1999.

[61] P. Huo and P. Cebe, "Effects of thermal history on the rigid amorphous phase in poly(phenylene sulfide)," *Colloid and Polymer Science*, vol. 270, pp. 840–852, Sept. 1992.

[62] S.-F. Yao, X.-T. Chen, and H.-M. Ye, "Investigation of Structure and Crystallization Behavior of Poly(butylene succinate) by Fourier Transform Infrared Spectroscopy," *J. Phys. Chem. B*, vol. 121, pp. 9476–9485, Oct. 2017.

[63] W. Ruland, "The separation of coherent and incoherent Compton X-ray scattering," *Br. J. Appl. Phys.*, vol. 15, pp. 1301–1307, Nov. 1964.

[64] M. C. Righetti, E. Tombari, M. Angiuli, and M. L. D. Lorenzo, "Enthalpy-based determination of crystalline, mobile amorphous and rigid amorphous fractions in semicrystalline polymers," *Thermochimica Acta*, vol. 462, pp. 15–24, Oct. 2007.

[65] M. L. Di Lorenzo and M. C. Righetti, "The three-phase structure of isotactic poly(1-butene)," *Polymer*, vol. 49, pp. 1323–1331, Mar. 2008.

[66] B. G. Olson, J. Lin, S. Nazarenko, and A. M. Jamieson, "Positron Annihilation Lifetime Spectroscopy of Poly(ethylene terephthalate): Contributions from Rigid and Mobile Amorphous Fractions," *Macromolecules*, vol. 36, pp. 7618–7623, Oct. 2003.

[67] A. Guinault, C. Sollogoub, V. Ducruet, and S. Domenek, "Impact of crystallinity of poly(lactide) on helium and oxygen barrier properties," *European Polymer Journal*, vol. 48, pp. 779–788, Apr. 2012.

[68] I. Okazaki and B. Wunderlich, "Modulated differential scanning calorimetry in the glass transition region, V. activation energies and relaxation times of poly(ethylene terephthalate)s," *Journal of Polymer Science Part B: Polymer Physics*, vol. 34, pp. 2941–2952, Dec. 1996.

[69] C. Schick, A. Wurm, and A. Mohammed, "Formation and disappearance of the rigid amorphous fraction in semicrystalline polymers revealed from frequency dependent heat capacity," *Thermochimica Acta*, vol. 396, pp. 119–132, Feb. 2003.

[70] C. Schick, A. Wurm, and A. Mohamed, "Vitrification and devitrification of the rigid amorphous fraction of semicrystalline polymers revealed from frequency-dependent heat capacity," *Colloid & Polymer Science*, vol. 279, pp. 800–806, Aug. 2001.

[71] M. L. Di Lorenzo, M. Gazzano, and M. C. Righetti, "The Role of the Rigid Amorphous Fraction on Cold Crystallization of Poly(3-hydroxybutyrate)," *Macromolecules*, vol. 45, pp. 5684–5691, July 2012.

[72] M. C. Righetti and E. Tombari, "Crystalline, mobile amorphous and rigid amorphous fractions in poly(L-lactic acid) by TMDSC," *Thermochimica Acta*, vol. 522, pp. 118–127, Aug. 2011.

[73] A. Bourdet, A. Esposito, S. Thiyagarajan, L. Delbreilh, F. Affouard, R. J. I. Knoop, and E. Dargent, "Molecular Mobility in Amorphous Biobased Poly(ethylene 2,5-furandicarboxylate) and Poly(ethylene 2,4-furandicarboxylate)," *Macromolecules*, vol. 51, pp. 1937–1945, Mar. 2018.

[74] G. Z. Papageorgiou, V. Tsanaktsis, D. G. Papageorgiou, S. Exarhopoulos, M. Papageorgiou, and D. N. Bikiaris, "Evaluation of polyesters from renewable resources as alternatives to the current fossil-based polymers. Phase transitions of poly(butylene 2,5-furandicarboxylate)," *Polymer*, vol. 55, pp. 3846–3858, Aug. 2014.

[75] Z. Li, J. Yang, and X. J. Loh, "Polyhydroxyalkanoates: opening doors for a sustainable future," *NPG Asia Mater*, vol. 8, pp. e265–e265, Apr. 2016.

[76] D. Moorkoth and K. M. Nampoothiri, "Production and characterization of poly(3-hydroxy butyrate-co-3 hydroxyvalerate) (PHBV) by a novel halotolerant mangrove isolate," *Bioresource Technology*, vol. 201, pp. 253–260, Feb. 2016.

[77] S. Thiyagarajan, M. A. Meijlink, A. Bourdet, W. Vogelzang, R. J. I. Knoop, A. Esposito, E. Dargent, D. S. van Es, and J. van Haveren, "Synthesis and Thermal Properties of Bio-Based Copolyesters from the Mixtures of 2,5- and 2,4-Furandicarboxylic Acid with Different Diols," *ACS Sustainable Chem. Eng.*, vol. 7, pp. 18505–18516, Nov. 2019.

[78] B. S. Kushwah, A. V. S. Kushwah, and V. Singh, "Towards understanding polyhydroxyalkanoates and their use," *J Polym Res*, vol. 23, p. 153, Aug. 2016.

[79] A. J. Cal, W. D. Sikkema, M. I. Ponce, D. Franqui-Villanueva, T. J. Riiff, W. J. Orts, A. J. Pieja, and C. C. Lee, "Methanotrophic production of polyhydroxybutyrate-co-hydroxyvalerate with high hydroxyvalerate content," *International Journal of Biological Macromolecules*, vol. 87, pp. 302–307, June 2016.

[80] Y.-M. Corre, S. Bruzaud, J.-L. Audic, and Y. Grohens, "Morphology and functional properties of commercial polyhydroxyalkanoates: A comprehensive and comparative study," *Polymer Testing*, vol. 31, pp. 226–235, Apr. 2012.

[81] S. K. Burgess, J. E. Leisen, B. E. Kraftschik, C. R. Mubarak, R. M. Kriegel, and W. J. Koros, "Chain Mobility, Thermal, and Mechanical Properties of Poly(ethylene furanoate) Compared to Poly(ethylene terephthalate)," *Macromolecules*, vol. 47, pp. 1383–1391, Feb. 2014.

[82] F. Nederberg, R. Bell, and J. M. Torradas, "Furan-based polymeric hydrocarbon fuel barrier structures," 2016.

[83] M. Soccio, M. Costa, N. Lotti, M. Gazzano, V. Siracusa, E. Salatelli, P. Manaresi, and A. Munari, "Novel fully biobased poly(butylene 2,5-furanoate/diglycolate) copolymers containing ether linkages: Structure-property relationships," *European Polymer Journal*, vol. 81, pp. 397–412, Aug. 2016.

Chapter 2

Experimental Section

Contents

2.1 Materials and thermal treatments

2.1.1 Alkanoates

The alkanoate-based polymers investigated in this thesis are listed in Table 2.1 and their repeating units are depicted in Figure 2.1. Different samples of poly (hydroxybutyrate-*co*-hydroxyvalerate) (PHBV) and poly (hydroxybutyrate-*co*-hydroxyhexanoate) (PHHx) were investigated, containing four different ratios of randomly arranged HV and HHx monomer units. Some samples were provided by our academic collaborators from the Institut de Recherche Dupuy de Lôme (IRDL) in France and from the University Sains Malaysia (USM), some were provided by industrial partners (Table 2.1).

Table 2.1: List of PHBV and PHHx copolymers with their source (*commercial grades) and some information about their biosynthesis: relative content of hydroxyvalerate (HV) or hydroxyhexanoate (HHx) units, number-average molecular weight ($\overline{M}_n$) and weight-average molecular weight ($\overline{M}_w$).

SAMPLE	**SOURCE**	% $[HV]or$ $[HHx](mol\%)$	$\overline{M}_n$ $(g.mol^{-1})$	$\overline{M}_w$ $(g.mol^{-1})$
PHBV3%	Tianan (China)*	0.03	n.d	350 000
PHBV15%	IRDL (France)	0.15	344 000	492 000
PHBV23%	IRDL (France)	0.23	354 000	478 000
PHBV27%	IRDL (France)	0.27	442 000	535 000
PHHx3%	USM (Malaysia)	0.03	400 000	740 000
PHHx8%	Kaneka (Japan)*	0.08	300 000	590 000
PHHx12%	Kaneka (Japan)*	0.12	400 000	760 000
PHHx35%	USM (Malaysia)	0.35	80 000	120 000

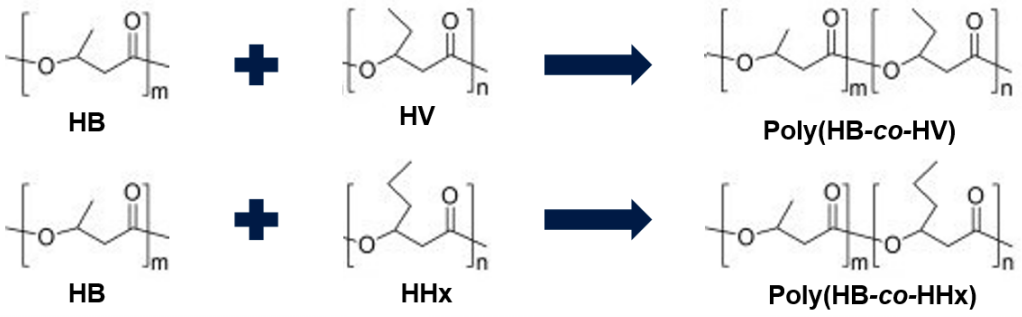

Figure 2.1: Schematic representation of the repeating units of the PHA copolymers used in this work.

2.1.2 Furanoates

The furanoate-based polymers investigated in this thesis are listed in Table 2.1 and a schematic representation of their repeating units is displayed in Figure 2.2. The samples of poly(ethylene 2,5-furandicarboxylate) (PEF) and poly(butylene 2,5-furandicarboxylate) (PBF) were synthesized in the laboratories of Wageningen Food and Biobased Research (FBR), located in the Netherlands. PEF was synthesized according to the procedure reported by Thiyagarajan et

al. [1] and PBF was obtained with the synthesis procedure described in a previous work [2]. Poly(propylene 2,5-furandicarboxylate) (PPF) was synthesized in the laboratories of the University of Bologna (Italy) according to the procedure reported in a paper that we are currently preparing for submission. Prior to measurement, all the samples were stored in a desiccator with P_2O_5 for at least 24h.

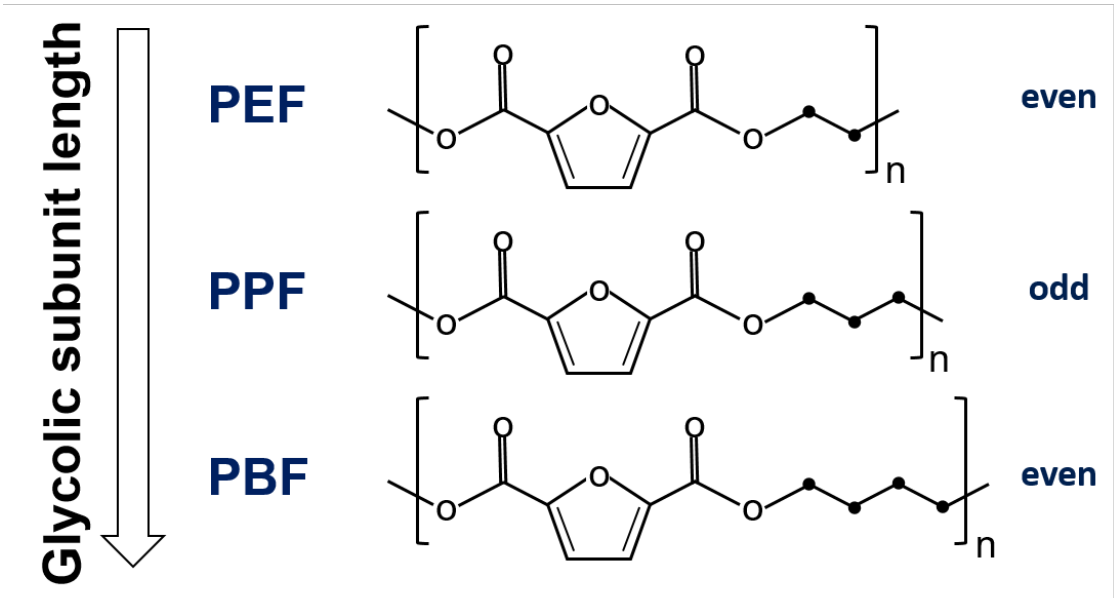

Figure 2.2: Schematic representation of the repeating units of the furan-based polymers used in this work.

Table 2.2: List of furanoate samples with their source, number-average molecular weight ($\overline{M}_n$) and weight-average molecular weight ($\overline{M}_w$).

SAMPLE	SOURCE	$\overline{M}_n$ ($g.mol^{-1}$)	$\overline{M}_w$ ($g.mol^{-1}$)
PEF	Wageningen FBR The Netherlands	15 300	18 200
PPF	University of Bologna Italy	n.d	62 000
PBF	Wageningen FBR The Netherlands	36 000	74 500

2.1.3 Thermal treatments

Different thermal treatments were performed to obtain specific microstructures, as explained in section (1.3).

Quenching

Quenching was performed to obtain fully amorphous samples. In this protocol, the samples were first heated up to a temperature above their respective melting temperature, and then

cooled down as fast as possible (ballistic cooling) using either liquid nitrogen, cold water or a cold metal plate, depending on the aptitude of each sample to crystallize. A schematic representation of the quenching protocol is provided in Figure 2.3 (green solid line).

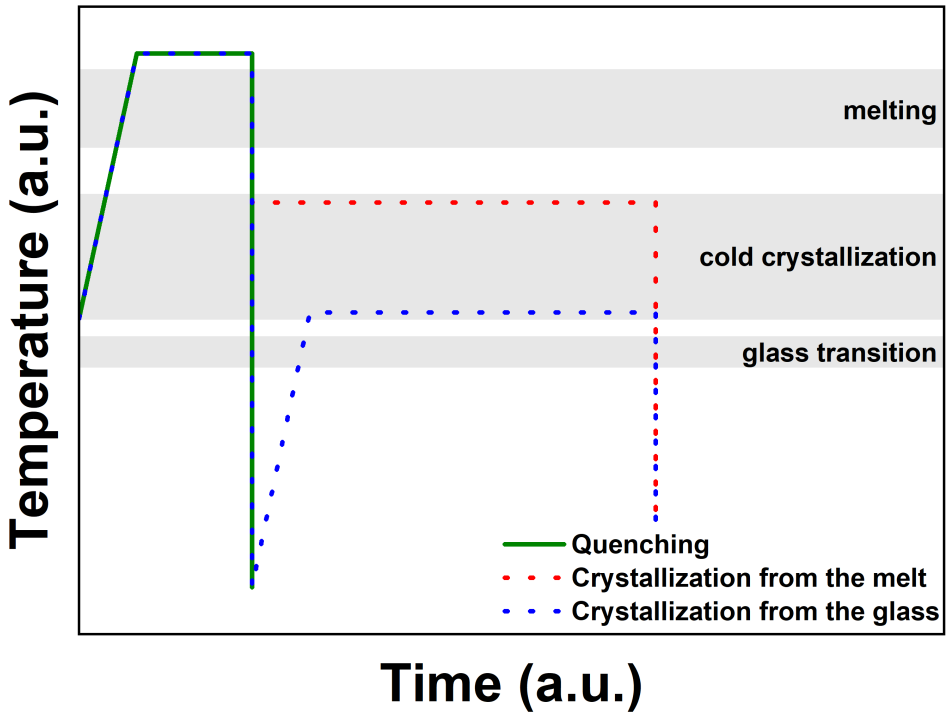

Figure 2.3: Scheme of the protocols used for different thermal treatments. The green solid line represents quenching, the red dotted line represents crystallization from the melt, and the blue dotted line represents crystallization from the glassy state. The grey horizontal stripes represent the temperature ranges where the main thermal events are expected to occur for each polymer, and therefore differ from one another.

Crystallization from the melt

This protocol was used to obtain microstructures containing small amounts of RAF, as described in section (1.3). The samples were melted, cooled down to a selected crystallization temperature, and held for a given time in isothermal conditions. The samples were then quenched to freeze the microstructure. A schematic representation of this protocol is provided in Figure 2.3 (red dotted line).

Crystallization from the glass

This protocol was used to obtain microstructures containing large amounts of RAF, as described in section (1.3). The samples were first submitted to the quenching protocol in order to obtain a fully amorphous glassy state; then, they were heated up to a selected crystallization temperature, held for a given time in isothermal conditions, and quenched again to freeze the microstructure. A schematic representation of this protocol is provided in Figure 2.3 (blue dotted line).

2.2 Characterization methods

2.2.1 Differential Scanning Calorimetry (DSC)

DSC is a family of experimental techniques that can be used to investigate thermal events such as the glass transition, crystallization or melting, as well as the evolution of a material with time, as in the case of physical ageing of glasses. This characterization technique is based on the fact that, when a material is heated and undergoes some thermal event, it can either absorb (endothermic event) or release (exothermic events) heat. The basic principle of a heat-flux DSC instrument consists in measuring the heat flow generated by a difference in temperature between the sample (undergoing thermal events) and a reference (linearly following the temperature set by the protocol). Any change in the heat flow associated with a thermal event due to the sample is then represented as a function of temperature. In this work, DSC measurements were achieved using a TA2920 heat-flux calorimeter (TA Instruments).

Conventional DSC experiments are performed on samples having masses of a few milligrams. Both the sample and the reference are held in isothermal conditions, or submitted to heating (cooling) ramps during which the temperature increases (decreases) linearly. Therefore, the temperature ramp can be expressed as:

$$T(t) = T_i + \beta t \tag{2.1}$$

Where $T(t)$ is the temperature at the time t, T_i is the initial temperature and β is the scanning rate (constant). The heat flow ϕ generated by the heat transfer Q is then estimated as:

$$\phi = \frac{dQ}{dt} = C\frac{dT}{dt} \tag{2.2}$$

Where C is the heat capacity of the thermodynamic system as a whole (furnace, pans and sample). In a heat-flux calorimeter, the sample and the reference are placed in the same furnace. The temperature ramp is applied to the furnace (i.e. to both the sample and the reference), therefore a heat is transferred to the sample (Q_S) and to the reference (Q_R). The thermal events (exothermic and endothermic) occurring to the sample result in a difference of temperature $\Delta T = T_S - T_R$ between the sample and the reference. The heat flow expressed in equation 2.2 can then be rewritten as follows:

$$\phi = Q_S - Q_R = \frac{\Delta T}{R} \tag{2.3}$$

Where R is the thermal resistance of the system.

Prior to measurement, energy and temperature were calibrated using indium standards. For every measurement, a constant nitrogen flow of 50 $mL.min^{-1}$ was applied to avoid any oxidative degradation of the samples and the furnace. In order to ensure a good signal-to-noise ratio,

the measurements were performed on samples whose mass ranged between 5 mg and 10 mg. The heating rate was set at 20 $K.min^{-1}$.

2.2.2 Modulated-Temperature Differential Scanning Calorimetry (MT-DSC)

Upon heating and cooling, samples are submitted to thermal reactions that are eventually changing their physical and/or chemical properties, such as glass transition, melting, crystallization, cross-linking, and so on. Some of these thermal reactions occur over temperature ranges that partially or completely overlap. It is impossible to distinguish overlapping events by conventional DSC. The heat flow ϕ measured by conventional DSC is expressed as:

$$\phi = \frac{dQ}{dt} = C * \beta + f(t, T) \tag{2.4}$$

Where $f(t, T)$ represents the part of heat flow related to the kinetic events, usually called "non-reversing heat flow" ϕ_{NR}. The other contribution is related to the thermodynamics events, is generally called "reversing heat flow" ϕ_R, and can be expressed as the product of the complex heat capacity and the scanning rate $C * \beta$. As previously mentioned, conventional DSC applies linear temperature ramps; Reading et al. [3] further developed DSC, proposing to superimpose a sinusoidal oscillation to the linear ramp in order to dissociate the thermodynamic and kinetic events, as shown in Figure 2.4.

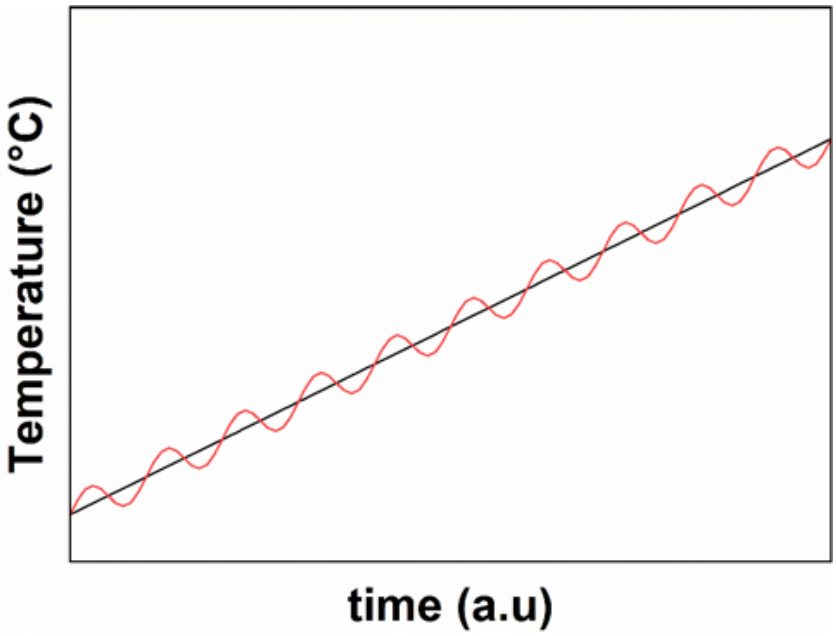

Figure 2.4: Illustration of a sinusoidal oscillation superimposed to a linear heating ramp, as proposed by Reading et al. [3]

Equation 2.1 can then be rewritten as follows:

$$T = T_i + \beta t + Asin(\omega t) \tag{2.5}$$

Where A is the amplitude of the sinusoidal oscillation, ω is the angular frequency, and $p = 2\pi/\omega$ is the period. The modulated heat flow ϕ is thus expressed as follows:

$$\phi = \frac{dQ}{dt} = C^*(\beta + A\omega cos(\omega t)) \tag{2.6}$$

With the complex heat capacity C^* defined as:

$$C^* = \frac{A_{HF}}{A_\beta} = \frac{\omega A C^*}{\omega A} \tag{2.7}$$

Where A_β and A_{HF} are the modulation amplitudes of the heating rate and of the heat flow, respectively. Thermodynamics events are related to the vibrational and translational motions of the molecules within the sample. These motions are very fast and can easily follow slights modulations of the sample temperature. On the opposite, kinetic events are not able to follow these temperature variations and do not contribute to the modulated part of the heat flow. The reversing heat flow ϕ_R and non-reversing heat flow ϕ_{NR} can then be estimated through the following equations:

$$\phi_R = C^*\beta = \frac{A_{HF}}{A_\beta}\beta \tag{2.8}$$

$$\phi_{NR} = \phi - \phi_R = C^* A\omega cos(\omega t) \tag{2.9}$$

Experimentally, a phase lag φ is measured between the heating modulation and the "total heat flow", which is the global response of the calorimeter. Considering this phase lag, two components of the apparent heat capacity C^*, the "reversing heat capacity" C' and the "non-reversing heat capacity" C'', respectively related to the reversing heat flow ϕ_R and the non-reversing heat flow ϕ_{NR}, can be distinguished. These two components are calculated as follows:

$$C' = |C^*| \cos(\phi) \tag{2.10}$$

$$C'' = |C^*| \sin(\phi) \tag{2.11}$$

MT-DSC experiments were performed on a DSC Q100 (TA instruments) using the T_{zero} technology. Temperature and energy were calibrated using indium standards, and heat capacity was calibrated using sapphire standards. The calibration for heat capacity uses sapphire standards because they do not undergo any kind of transition within the temperature ranges typically used for polymer thermal analysis. Moreover, the heat capacity of sapphire as a function of the temperature is stable and well known. This calibration step was repeated any time the modulation parameters were changed. From the calibration curve, a calibration factor K_{Cp} is calculated by comparing the experimental and theoretical values of the heat capacity. The calibration factor is obtained at each temperature, averaged on the temperature range selected for measurement, and used to correct the apparent heat capacity of the sample:

$$K_{Cp}(T) = \frac{(C_p)_{sapphire,theoretical}}{(C_p)_{sapphire,experimental}} \tag{2.12}$$

MT-DSC measurements can be performed with four different temperature-modulation modes:

- Quasi-Isothermal ($\beta = 0$)
- Heat-Only ($A* \omega < \beta$)
- Heat-Iso ($A* \omega = \beta$)
- Heat-Cool ($A* \omega > \beta$)

Each thermal event may require a different temperature-modulation mode. In this work, the Heat-Only mode with an heating rate of 2 $K.min^{-1}$, an amplitude of $\pm$0.318K and a period of 60s was used, as reported in the literature [4]. The Heat-Only protocol is particularly suitable to investigate coupled thermal events (as in semi-crystalline polymers, where melting and re-crystallization processes are sometimes concomitant).

2.2.3 Fast Scanning Calorimetry (FSC)

As mentioned in the previous section, during the heating ramp a sample can sometimes undergo concomitant thermal events. In MT-DSC, these events can be separated through the use of a temperature-modulated heating ramp. Another approach has been recently proposed by Schick and Mathot [5] in which very high scanning rates are applied to very small samples to delay or totally inhibit kinetic thermal reactions. This approach can be used not only to separate concomitant events, but also to observe very fast thermal reactions. The FSC equipement is a power-compensated DSC apparatus, in which the sample and the reference are placed in separated furnaces. A linear temperature ramp is applied to both the sample and the reference. Because of the thermal events occurring to the sample, a different power is required to keep the sample and the reference at the same temperature; this difference is measured and converted to a heat flow signal.

In this work, FSC measurements were performed using a Flash DSC 1 apparatus (Mettler-Toledo) equipped with a Huber TC100 intracooler. The experiments were carried out using a power-compensation twin-chip sensor, based on MEMS technology (Figure 2.5), containing a sample and a reference side working as independent furnaces. Prior to use, each Multistar UFS1 MEMS empty chip was calibrated following the recommendations of the manufacturer. As suggested in the literature [6], two thermal lags were considered (the "dynamic thermal lag" ΔT_D and the "static thermal lag" ΔT_S), and each FSC measurement was corrected accordingly to both these thermal lags. The dynamic thermal lag ΔT_D was calculated as half the distance between the glass transition temperatures measured upon heating and cooling at the same rates. The dynamic thermal lag depends on the selected heating (and cooling) rate [6]; in this work it was measured at $\beta^+ = |\beta^-| = 1000K.s^{-1}$. The static thermal lag ΔT_S mostly depends on the sample thickness and was calculated as a third of the distance between the melting temperatures of two indium pieces, one placed on the reference sensor and the other placed on top of the sample [6]. To prevent thermal gradients and ensure small values of static

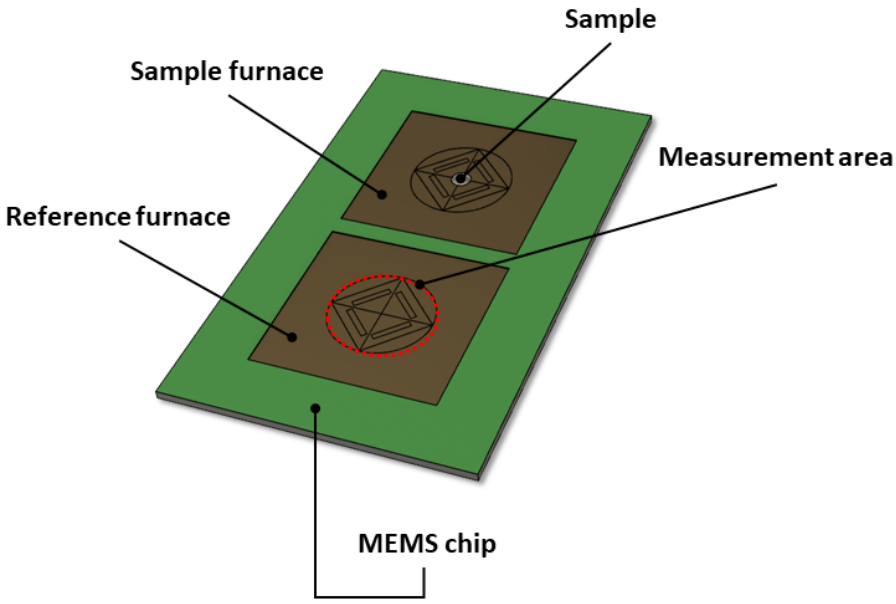

Figure 2.5: Scheme of a UFS1 MEMS chip sensor for FSC measurements.

thermal lag, all the samples were prepared with a thickness of $10 \pm 3\mu m$ as recommended by Toda et al. [7], and placed in the middle of the sensor as advised by Schick et al.[8].

A constant nitrogen flow of $20mL.min^{-1}$ was used to purge the measurement cell and avoid any possible oxidative degradation of the samples. Prior to measurement, the samples were melt-quenched to their reference amorphous state by performing several heating and cooling steps at scanning rates ranging from $1000K.s^{-1}$ to $3000K.s^{-1}$ over a temperature range going from -60°C to the melt. This step was meant to erase the thermo-mechanical history of the sample and ensure a good thermal contact between the sample and the chip sensor. The sample mass was measured according to equation 2.13:

$$m = \frac{(\Delta C_p)_{am}{}^{FSC}}{(\Delta C_p)_{am}{}^{MT-DSC}} \tag{2.13}$$

Where $(\Delta C_p)_{am}{}^{FSC}$ is the heat capacity step at the glass transition estimated by FSC ($\beta^+ = 1000K.s^{-1}$) and $(\Delta C_p)_{am}{}^{MT-DSC}$ is the heat capacity step at the glass transition measured by MT-DSC ($\beta^+ = 2K.min^{-1} \approx 0.033K.s^{-1}$) on the sample in its reference amorphous state. For the samples that could not be quenched to the fully amorphous state in MT-DSC experiments, the sample mass was estimated according to the method reported by Cebe et al.[9]. The calculation was done according to equation 2.14:

$$m = \frac{(C_p)^{FSC}(T_1)}{(C_p)^{MT-DSC}(T_1)} \tag{2.14}$$

Where $(C_p)^{FSC}(T_1)$ is the heat capacity obtained from FSC measurements at the temperature T_1 and $(C_p)^{MT-DSC}(T_1)$ is the heat capacity measured by MT-DSC at the same temperature T_1. The temperature T_1 was selected in the liquid state, and the calculation was made several

times over a wide temperature range to get an average value of the sample mass.

2.2.4 Dielectric Relaxation Spectroscopy (DRS)

As previously discussed, DRS is a very useful tool when it comes to the study of molecular mobility in glass-forming liquids, as it allows measuring the relaxation times over a wide range of temperature and frequencies (10^{-6} to 10^{11}Hz).

During dielectric measurements, an alternating electric field generated by the application of a controlled voltage is applied on a material which is non-conductive but contains dipoles. The consequence is a symmetric distribution of positive and negative charges known as "electric polarization" P. This phenomenon arises from two major processes known as the "induced polarization" P_∞ and the "orientational polarization" $P_{or}(t)$ [10]. The induced polarization P_∞ involves the "electronic polarization" P_e and the "atomic polarization" P_a. The orientational polarization $P_{or(t)}$ is the direct consequence of the rotational motions of permanent dipoles when an external electric field is applied to the sample. When no electric field ($E = 0$) is applied to the system, the dipoles are randomly orientated according to thermal agitation, as pictured in Figure 2.6 (left). When an electric field E is applied to a system in which the dipoles are initially randomly orientated, a preferred direction is imposed to the dipoles, which creates both induced and orientational polarization, as depicted in Figure 2.6 (right).

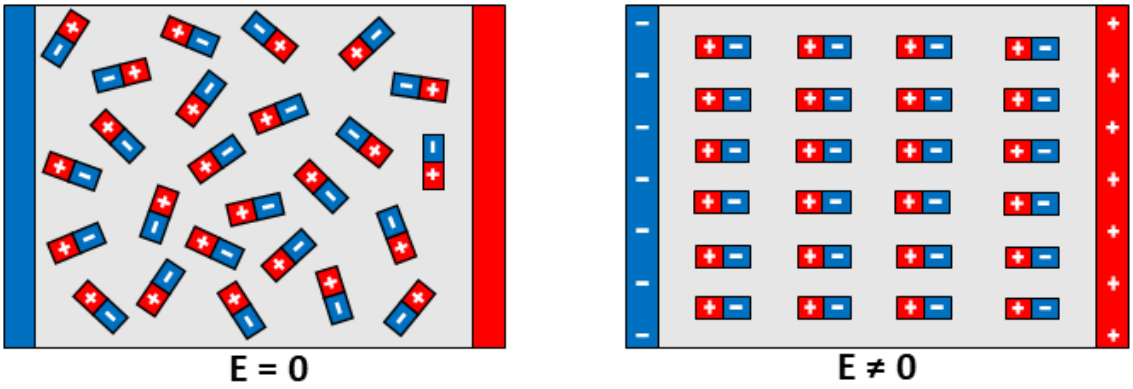

Figure 2.6: Illustration of dipole orientations in presence and absence of an external electric field E.

When a static electric field is applied to a dielectric sample, the total polarization can be estimated according to the following equation [11]:

$$P(t) = P_\infty + \varepsilon_0 \int_{-\infty}^{t} \varepsilon(t - t') \frac{dE(t')}{dt'} dt' \tag{2.15}$$

After the electric field is turned on at a time $t = t_1$, the induced polarization P_∞ instantly increases until reaching the following value:

$$P_\infty = \varepsilon_0(\varepsilon_\infty - 1)E \tag{2.16}$$

Where ε_0 is the dielectric permittivity of vacuum and ε_∞ is the dielectric permittivity of the sample in the high-frequency range. On the other hand, the orientational polarization $P_{or}(t)$ slowly increases with time as a consequence of intermolecular frictions. The maximum (saturation value) of orientational polarization P_s is observed at a time $t = t_2$:

$$P_s = \varepsilon_0(\varepsilon_s - 1)E \tag{2.17}$$

Where ε_s is the static permittivity of the sample. The saturation value of the orientation polarization observed at $t = t_2$ can then be expressed as follows:

$$P_o = \varepsilon_0(\varepsilon_s - \varepsilon_\infty)E \tag{2.18}$$

When the electric field is turned off, the induced polarization immediately drops, while the orientational polarization $P_0(t)$ requires an adequately long time to fully decay. This time-dependent phenomenon of progressive increase and decrease of the orientational polarization $P_0(t)$ is conventionally named "dielectric relaxation" and can be mathematically expressed by the following differential equation [10]:

$$\tau_D \frac{dP_{or}(t)}{dt} = P_0 - P_{or}(t) \tag{2.19}$$

In the previous equation, τ_D represents a "relaxation time" which is characteristic of the analyzed material. A solution to equation 2.19 is found for:

$$P_{or}(t) = P_0[1 - exp(-t/\tau_D)] \tag{2.20}$$

Instead of using a static electric field, it is possible to use an alternating (sinusoidal) electric field and rewrite equation 2.20 as follows:

$$\tau_D \frac{dP^*_{or}(t)}{dt} = \varepsilon_0(\varepsilon_s - \varepsilon_\infty)E_0 e^{i\omega t} - P^*_{or}(t) \tag{2.21}$$

A solution of this differential equation is:

$$P^*_{or}(t) = \frac{\varepsilon_0(\varepsilon_s - \varepsilon_\infty)}{1 + i\omega\tau_D} E_0 e^{i\omega t} \tag{2.22}$$

The total polarization can then be rewritten as:

$$P^*(t) = \varepsilon_0(\varepsilon_\infty - 1)E^*(t) + \frac{\varepsilon_0(\varepsilon_s - \varepsilon_\infty)}{1 + i\omega\tau_D} E^*(t) \tag{2.23}$$

The response of a dielectric material submitted to an external alternating electric field can then be expressed as a "complex dielectric permittivity":

$$\varepsilon^*(\omega) = \varepsilon'(\omega) - i\varepsilon''(\omega) = \varepsilon_\infty + \frac{\varepsilon_s - \varepsilon_\infty}{1 + i\omega\tau_D} \tag{2.24}$$

Where $\varepsilon'(\omega)$ and $\varepsilon'(\omega)$ are respectively the real and imaginary parts of the complex dielectric permittivity. This model describing dipole relaxation is known as the "Debye model". In the Debye model, $\varepsilon'(\omega)$ and $\varepsilon'(\omega)$ can be respectively expressed as:

$$\varepsilon'(\omega) = \varepsilon_\infty + \frac{\varepsilon_s - \varepsilon_\infty}{1 + (\omega\tau_D)^2} \tag{2.25}$$

$$\varepsilon''(\omega) = (\varepsilon_s - \varepsilon_\infty)\frac{\omega\tau_D}{1 + (\omega\tau_D)^2} \tag{2.26}$$

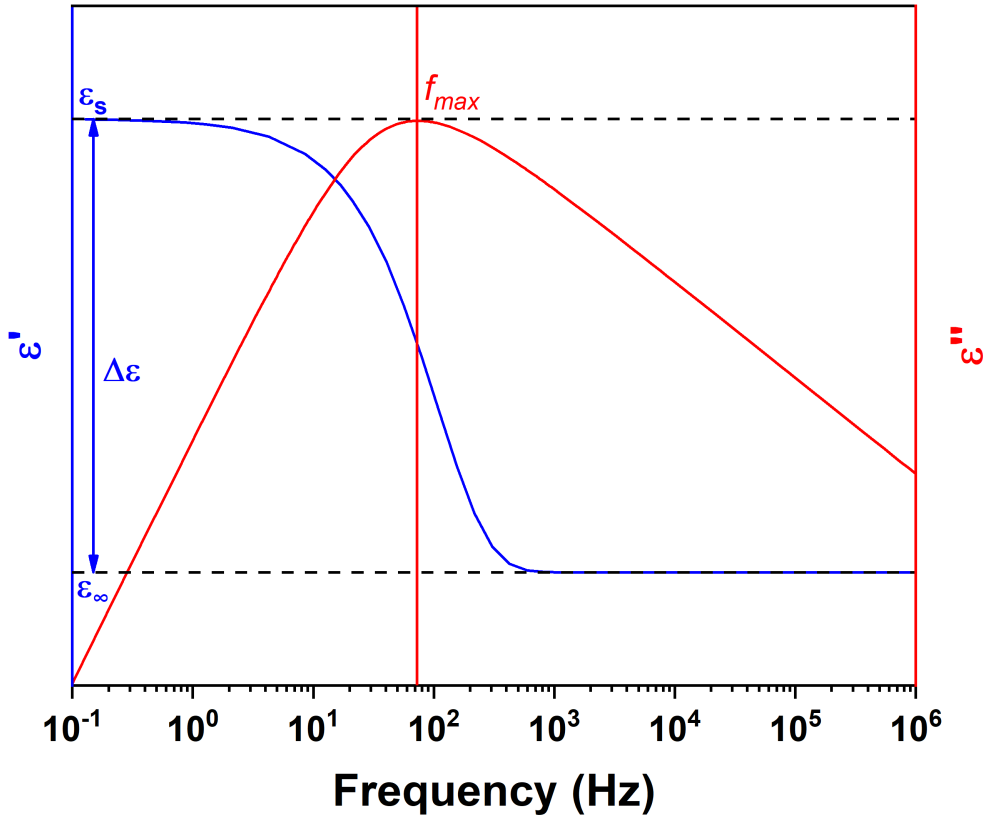

Figure 2.7: Example of signal measured by dielectric relaxation spectroscopy (DRS). The blue line represents the real dielectric permittivity, the red line represents the imaginary dielectric permittivity, and $\Delta\epsilon$ is called the "dielectric strength".

Figure 2.7 illustrates the real and imaginary parts of the complex dielectric permittivity measured by DRS. The magnitude of the relaxation process, also known as "dielectric strength", can be estimated from the real permittivity as $\Delta\varepsilon = \varepsilon_s - \varepsilon_\infty$. The dielectric strength of a material can be linked to the density of relaxing dipoles through the Kirkwood-Fröhlich relation:

$$\Delta\varepsilon = \frac{1}{3\varepsilon_0} g_K \frac{\mu^2}{k_B T} \frac{N}{V} \tag{2.27}$$

Where ε_0 is the vacuum permittivity, g_K is the Kirkwood correlation factor, μ^2 is the time-correlation of the total dipole moment, k_B is the Boltzmann constant and $\frac{N}{V}$ is the volume density of dipoles. The imaginary permittivity presents a peak, also referred to as the "dielectric

loss peak". The frequency at which the maximum value of ε'' is observed is labelled f_{max} and can be directly related to the characteristic relaxation time of the relaxing dipoles τ_D as follows:

$$\tau_D = \frac{1}{2\pi f_{max}} \tag{2.28}$$

DRS experiments were performed using interdigitated electrodes (BDS 1410-20-150) from Novocontrol Technologies GmbH (accuracy in $\tan\delta \approx 0.001$, sensor diameter 20mm, gold-plated copper combs with fingers 150 μm wide and 35 μm thick spaced by 150 μm). Prior to sample deposition, the electrodes were calibrated by determining their respective geometric (empty) capacity (C_0) and substrate capacity (C_{su}) through measurements of a reference material of known dielectric permittivity (hydroxy-terminated PPMS, Sigma Aldrich). After sample deposition, the electrodes were heated on a hot plate to melt the sample, and then transferred to a cold plate to possibly quench the sample to a fully amorphous glassy state. The measurements were carried out in a frequency range of 10^{-1} to 10^6 Hz by an Alpha-A analyzer from Novocontrol Technologies GmbH. A Quatro Cryosystem (Novocontrol Technologies GmbH) was used to control the temperature with a stability of ±0.5 °C. The temperature was gradually increased from -150°C to 150°C using appropriate steps. The Havriliak-Negami (HN) [12] complex function was then used to analyze the experimental data:

$$\varepsilon^*(\omega) = \varepsilon_\infty + \frac{\Delta\varepsilon_{HN}}{[1 + (i\omega\tau_{HN})^{\alpha_{HN}}]^{\beta_{HN}}} \tag{2.29}$$

This equation allows to fit the real and imaginary parts of the complex dielectric permittivity, which is useful to estimate parameters such as the dielectric strength $\Delta\varepsilon_{HN}$, the relaxation time τ_{HN}, as well as the symmetric and asymmetric broadening factors α_{HN} and β_{HN}.

2.2.5 X-Ray Diffraction (XRD)

XRD is a non-destructive experimental technique providing information about the spatial arrangement in crystalline and semi-crystalline materials having more or less complex microstructures. In polymer science, this technique is mainly used to characterize and quantify the crystalline phase in semi-crystalline microstructures. Wide-Angle X-ray Diffraction (WAXD) exploits the X-rays that are diffracted to different angles after elastic interactions with regular and/or irregular spatial arrangements of atoms and molecules. The crystalline domains of a sample are detected through the presence of diffraction peaks, which are generally analyzed with the Bragg's law [13]:

$$n\lambda = 2d\sin(\theta) \tag{2.30}$$

WAXD measurements can be performed either in reflection or in transmission mode. In reflection mode, the surface of the sample is hit by the X-ray beam emitted by a source placed at an angle θ with respect to the surface of the sample holder (Figure 2.8). The X-ray beam is then diffracted by the sample and the resulting beam is collected by an X-ray detector placed at an angle 2θ with respect to the incident X-ray beam. For this reason, the intensity of the scattered

beam is usually plot as a function of the scattering angle 2θ. The transmission mode is based on the same measurement principle, but the X-ray beam is diffracted trough the sample instead of being diffracted by its surface.

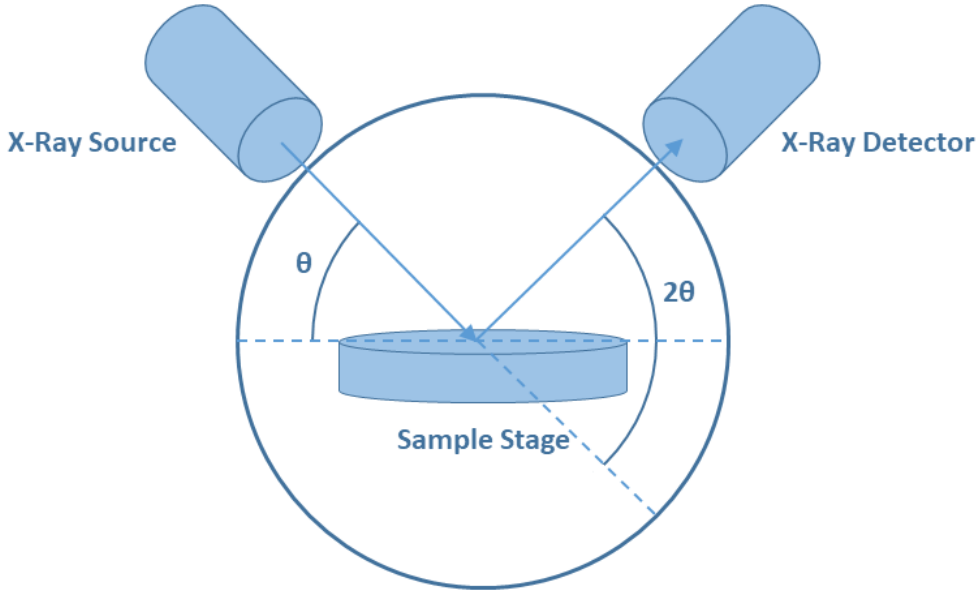

Figure 2.8: Scheme of a Wide Angle X-ray Diffraction (WAXD) apparatus in a θ:2θ configuration (reflection mode).

In this work, WAXD spectra were recorded at room temperature on (16 mm x 16 mm) samples by a Bruker D8 X-ray diffractometer within the angular range 2 θ = 5-40°, with a scanning step of 0.05 °and a counting time of $1s$/step, using a Co Kα radiation ($\lambda = 2.29$Å) as X-ray source. The XRD patterns were obtained by subtracting the background signal and averaging at least three spectra recorded on the same spot of the sample. The XRD spectra were fitted with as many Gaussian functions as necessary to take into account all the crystalline diffraction peaks and the amorphous halos, to determine crystallinity according to equation 1.13. The average size of the crystalline domains were estimated using the following Scherrer's equation [14]:

$$size = \frac{K\lambda}{\beta cos(\theta)} \tag{2.31}$$

Where K is a dimensionless shape factor and β is the full width at half maximum of the diffraction peak.

References

[1] S. Thiyagarajan, W. Vogelzang, R. J. I. Knoop, A. E. Frissen, J. van Haveren, and D. S. van Es, "Biobased furandicarboxylic acids (FDCAs): effects of isomeric substitution on polyester synthesis and properties," *Green Chem.*, vol. 16, no. 4, pp. 1957–1966, 2014.

[2] C. Fosse, A. Bourdet, E. Ernault, A. Esposito, N. Delpouve, L. Delbreilh, S. Thiyagarajan, R. J. Knoop, and E. Dargent, "Determination of the equilibrium enthalpy of melting of two-phase semi-crystalline polymers by fast scanning calorimetry," *Thermochimica Acta*, vol. 677, pp. 67–78, July 2019.

[3] M. Reading, B. Hahn, and B. Crowe, "Method and apparatus for modulated differential analysis," 1994.

[4] A. A. Lacey, D. M. Price, and M. Reading, "Theory and Practice of Modulated Temperature Differential Scanning Calorimetry," in *Modulated Temperature Differential Scanning Calorimetry* (M. Reading and D. J. Hourston, eds.), vol. 6, pp. 1–81, Springer Netherlands, 2006.

[5] C. Schickh and V. Mathot, eds., *Fast scanning calorimetry*. Cham: Springer, 2016. OCLC: 960840409.

[6] J. E. Schawe, "Measurement of the thermal glass transition of polystyrene in a cooling rate range of more than six decades," *Thermochimica Acta*, vol. 603, pp. 128–134, Mar. 2015.

[7] A. Toda, R. Androsch, and C. Schick, "Insights into polymer crystallization and melting from fast scanning chip calorimetry," *Polymer*, vol. 91, pp. 239–263, May 2016.

[8] K. Jariyavidyanont, A. Abdelaziz, R. Androsch, and C. Schick, "Experimental analysis of lateral thermal inhomogeneity of a specific chip-calorimeter sensor," *Thermochimica Acta*, vol. 674, pp. 95–99, Apr. 2019.

[9] P. Cebe, D. Thomas, J. Merfeld, B. P. Partlow, D. L. Kaplan, R. G. Alamo, A. Wurm, E. Zhuravlev, and C. Schick, "Heat of fusion of polymer crystals by fast scanning calorimetry," *Polymer*, vol. 126, pp. 240–247, Sept. 2017.

[10] K. Grzybowska, K. Adrjanowicz, and M. Paluch, "Application of Broadband Dielectric Spectroscopy to Study Molecular Mobility in Pharmaceutical Systems," in *Disordered Pharmaceutical Materials* (M. Descamps, ed.), pp. 301–360, Weinheim, Germany: Wiley-VCH Verlag GmbH & Co. KGaA, Apr. 2016.

[11] F. Kremer and A. Schönhals, eds., *Broadband dielectric spectroscopy*. Berlin ; New York: Springer, 2003.

[12] S. Havriliak and S. Negami, "A complex plane representation of dielectric and mechanical relaxation processes in some polymers," *Polymer*, vol. 8, pp. 161–210, Jan. 1967.

[13] W. H. Bragg and W. L. Bragg, "The reflection of X-rays by crystals," *Proc. R. Soc. Lond. A*, vol. 88, pp. 428–438, July 1913.

[14] P. Scherrer *Göttinger Nachrichten Gesell*, vol. 2.

Chapter 3

The equilibrium melting enthalpy : a key towards rigid amorphous fraction quantification

Contents

Part of this chapter is issued from the following publication: C. Fosse, A. Bourdet, E. Ernault, A. Esposito, N. Delpouve, L. Delbreilh, S. Thiyagarajan, R.J. Knoop, and E. Dargent, "Determination of the equilibrium enthalpy of melting of two-phase semi-crystalline polymers by fast scanning calorimetry", Themorchim. Acta 2019, 677, 67–78. [1]

As presented in Chapter 1, section 1.4, the presence of a rigid amorphous fraction (RAF) is classically detected as a deviation from the two-phase model, which describes the microstructure of a semi-crystalline polymer as made of a crystalline phase (represented by the fraction X_c) and an amorphous phase (represented by the fraction X_{MAF}). In other words, the presence of a RAF is associated with the condition $X_c + X_{MAF} < 1$. Therefore, it must be possible to graphically evidence the presence of a RAF by plotting the crystalline fraction X_c as a function of the mobile amorphous fraction X_{MAF}. In Figure 3.1, the black line represents the linear evolution expected according to a two-phase model, and the blue area represents the range in which the two-phase model should be better replaced by a three-phase model. Any deviation from the linear trend corresponding to $X_c = 1 - X_{MAF}$ falling in the blue area could be attributed to the presence of a RAF. This being said, it is quite straightforward that the quantification of RAF cannot be correct without an accurate quantification of X_c and X_{MAF}. A few alternatives exist to the graph in Figure 3.1, where X_c and X_{MAF} are replaced by other quantities related to the measurement or calculation of these fractions, e.g. the heat capacity step at the glass transition ΔC_p or the sample mass, but this does not change the basic principle of the procedure itself, which consists in drawing plots where the trend corresponding to a two-phase model is clearly identified and any deviation is consequently associated to the presence of RAF.

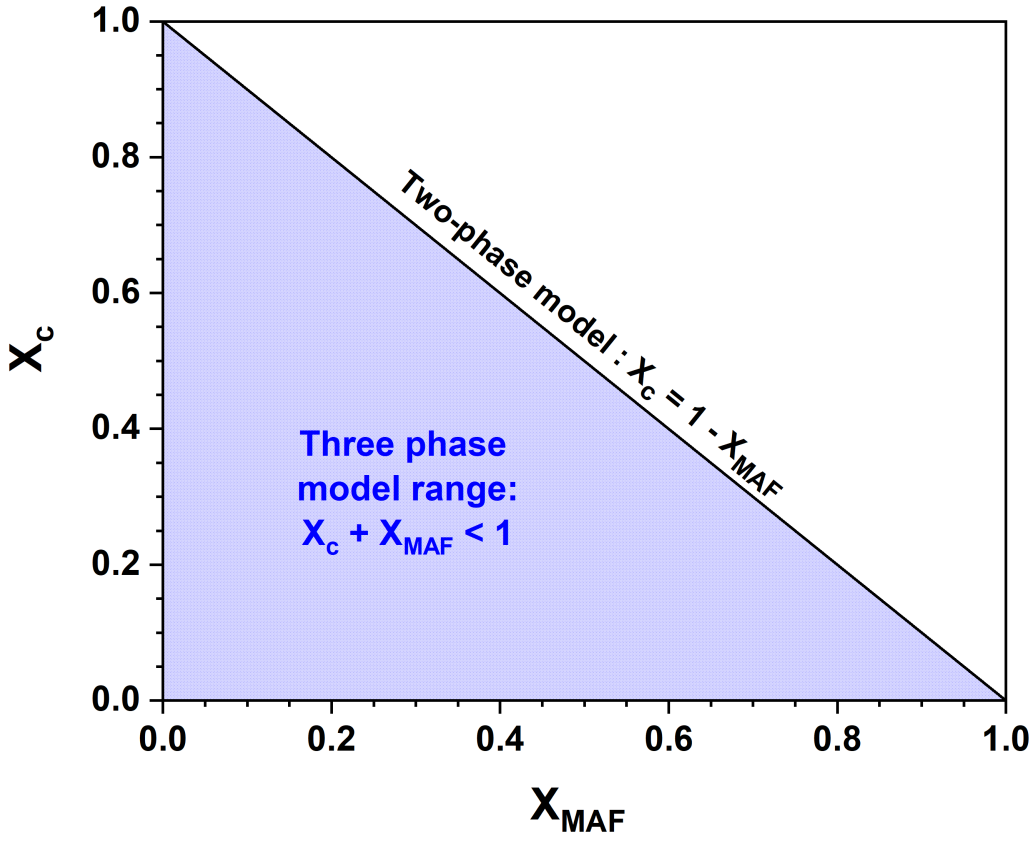

Figure 3.1: Schematic representation of the plot that can be drawn to highlight the presence of RAF in the microstructure of a semi-crystalline polymer. The black line represents the linear trend associated with a two-phase model, and the blue area represents the range of application of a three-phase model.

The quantification of X_c is generally done by either differential scanning calorimetry (DSC) and/or wide angle X-ray diffraction (WAXD) according to equation (1.12); this method requires to know a reference quantity, the "equilibrium enthalpy of melting" ΔH_m^0, that is specific to each material. ΔH_m^0 is defined as the melting enthalpy that would be measured if the material were 100% crystalline in conditions of thermodynamic equilibrium. For widespread (commercially available) polymers, this value can usually be found in handbooks or in the literature; however, when it comes to brand new (possibly bio-based) polymers, most properties (including ΔH_m^0) are unknown. In some cases, even for well-known polymers, the literature reports very different values of ΔH_m^0 (see Table 3.1). The good news is that this value can be obtained (or at least approached) with different experimental methods that have their own strengths and weaknesses.

Table 3.1: Values of the equilibrium enthalpy of melting ΔH_m^0 $[J \cdot g^{-1}]$ found in the literature for a selection of crystallizable polymers.

Polymer	**Abbreviation**	ΔH_m^0 $[J \cdot g^{-1}]$
Poly(ethylene)	PE	289[2], 282[3], 307[4], 281[5]
Isotactic poly(styrene)	iso-PS	86[6], 80[7], 96[8]
Isotactic poly(propylene)	iso-PP	260[6], 65[9], 147[10], 188[11], 138[12]
Polyamide 6	PA6	188[13], 155[14]
Poly(ethylene terephtalate)	PET	140 [15], 125[16]
Poly(butylene terephtalate)	PBT	145[17], 141[18]
Poly(L-lactic acid)	PLLA	135[19], 91[20], 146[21], 96[22], 143[23]
Poly(phenylene sulfide)	PPS	80[24], 146, 112[25]
Poly(ethylene 2,5-furandicarboxylate)	PEF	137[26], 146[27], 112[28]
Poly(butylene 2,5-furandicarboxylate)	PBF	129[29]

3.1 Cross-comparison of DSC and XRD

One of the most popular methods to obtain ΔH_m^0 is based on the direct comparison of the melting enthalpy measured by DSC with the crystalline fractions estimated by XRD techniques on different samples of the same material supposedly having the same microstructure [21, 23]. Most of the time, this comparison is made on several samples having different crystalline fractions, which allows to calculate an average value of the equilibrium enthalpy of melting. This method generally provides a fairly good estimation of ΔH_m^0 and can be applied to most samples. The main advantage of this method is that it is simple and does not require any heavy analytic treatment of the experimental results. Yet, this method suffers from several weaknesses that have to be considered.

The errors induced by this method mainly come from the comparison of two different techniques having their own limits and uncertainties. In the case of DSC, the sample is characterized through a heating ramp; depending on the heating rate, its microstructure can sometime evolve upon heating, which means that the measured melting enthalpy does not always correspond to

the initial crystalline structures. In fact, the literature reports that semi-crystalline polymers often undergo more or less pronounced melting/recrystallization processes upon heating [30]. These phenomena are generally faster than the heating rates used in conventional DSC; for this reason, it may be interesting to perform ramp at much higher heating rates, as in the case of FSC [31, 32, 33, 34]. Depending on the heating rate and on the intrinsic behavior of the material under investigation, the uncertainties due to melting/recrystallization processes can be non-negligible. Another possible source of uncertainties related to DSC is observed for crystalline materials that gradually melts; in this case, the beginning of the melting process is hardly distinguished from the baseline drift associated with the devitrification of the RAF [35, 36, 37].

XRD uncertainties are mainly dues to the fitting process. In most studies, the crystalline fraction/percentage is obtained by using equation 1.13 reported in section 1.4. This method does not provide the absolute crystallinity of the sample. Ruland's method [38] would provide a better estimation, but it is rarely used because it is an heavy analytical method. On a whole, uncertainties are also (and fundamentally) dues to the assumption that two samples of the same material, prepared in two different ways according to the same thermal protocol, having different dimensions, masses and thicknesses, and finally characterized with different experimental techniques, provide results that represent the same system, with the same microstructure.

The uncertainties dues to DSC and XRD, combined all together when the respective experimental results are cross-compared, can eventually lead to non-negligible errors on the estimation of the equilibrium enthalpy of melting. For this reason, it is essential to compare the results obtained by the cross-comparison of DSC and XRD with the results obtained by other methods.

3.2 A two-phase model approach based on MT-DSC

As discussed in section 1.4, the development of a RAF is mainly dependent on the crystallization conditions. As a consequence, it must be possible to control the amount of RAF by optimizing the crystallization conditions. Starting from here, Pyda et al. [39] decided to optimize the crystallization conditions of poly(L-lactic acid) (PLLA) in an attempt to create a microstructure with a minimized amount of RAF. The description of a microstructure where the amount of RAF is negligible is legitimately done by a two-phase model, and equations 1.9 and 1.11 can be combined into equation 3.1:

$$X_{crystalline} = \frac{(\Delta H_m)^{DSC}}{(\Delta H_m^0)} = 1 - \frac{(\Delta C_p)^{DSC}_{crystallized}}{(\Delta C_p)^{DSC}_{amorphous}} \tag{3.1}$$

Equation (3.1) can then be used to calculate the equilibrium enthalpy of melting ΔH_m^0 by generating several microstructures with different crystalline fractions and then extrapolating to the ideal case of a fully crystalline sample of the same material. The extrapolation should be

done on a graph plotting the values of melting enthalpy $(\Delta H_m)^{DSC}$ as a function of the heat capacity step at the glass transition $(\Delta C_p)^{DSC}_{crystallized}$, both obtained by DSC. In their work on PLLA, Pyda et al. [20] found a value of $\Delta H^0_m = 91 J \cdot g^{-1}$, which is in good agreement with the values previously reported in the literature, obtained with other methods.

This method is interesting because it only requires DSC (eventually MT-DSC for a better estimation of the heat capacity step at the glass transition), which reduces the uncertainties dues to the comparison of different samples characterized by different experimental techniques. Yet, this method still suffers from the sneaky processes of melting/recrystallization that are frequently observed in semi-crystalline polymers (with regard to this issue, MT-DSC may be even worse than DSC, because slower heating rates are required for modulated-temperature heating ramps). Last but not least, uncertainties can come from the assumption that the analyzed microstructure contains no RAF (which is not totally realistic, because it corresponds to a situation that can only be approached not reached). Nevertheless, a combination of this "two-phase model approach" with the "cross-comparison method" detailed in the previous section is interesting, because it is likely to provide a more accurate estimation of the ΔH^0_m value.

In a two-phase model, the dependency of ΔH_m plotted against ΔC_p should be linear with a slope equal to 1. In the presence of RAF, this dependency deviates from the two-phase model trend. This observation is nowadays fully explained by the three-phase model proposed by Pyda et al. [20], which indeed was originally developed to point out the presence of RAF in semi-crystalline polymers.

3.3 Methods based on FSC

The methods presented so far are affected by non-negligible uncertainties. They suffer from intrinsic errors due to the selected experimental technique and/or to the theoretical assumptions. In both cases, an error is most likely introduced by the use of heating rates that are not fast enough to suppress the melting/recrystallization processes possibly observed during DSC measurements. This error can be reduced by using higher heating rates, whose limits have been pushed by a technique developed a few years ago, called Fast Scanning Calorimetry (FSC) [31, 32, 33, 34].

3.3.1 Cross-comparison of FSC and XRD

When the results obtained by DSC and XRD (or any other non-calorimetric technique providing an estimation of the crystalline fraction) are cross-compared, errors can be made due to more or less extensive melting/recrystallization processes; but this is not the only disadvantage of conventional and temperature-modulated DSC. The degradation of the sample is another problem that can be encountered when relatively slow heating rates are used during calorimetric investigations. Degradation may start at temperatures which are dangerously close to the

melting temperature, making it difficult to obtain a correct estimation of the melting enthalpy. This situation is frequently observed when thermally unstable biodegradable materials are investigated, such as PHA or silk [35, 40, 41].

In 2017, Cebe et al. [5] proposed a method allowing to determine the value of ΔH_m^0 using a FSC apparatus. The ultimate purpose of their work was to determine the value of ΔH_m^0 for silk fibroin biomaterials, which degrade upon melting. But they claimed other advantages, including reduction of error, applicability to all types of samples (polymers, copolymers, and blends) regardless of their degree of crystallinity, and of course applicability to biomaterials which may require fast scanning rates to prevent degradation. This method is very close to the DSC-XRD cross-comparison method, where the melting enthalpy is plotted as a function of crystallinity; instead of using several samples with different crystalline fractions, the melting enthalpy (measured by FSC) is plotted against the product of the sample mass times its crystallinity (determined by complementary techniques, such as XRD and infrared spectroscopy) for samples with variable masses and/or crystallinities. This means that equation 1.12 can be rewritten as follows:

$$(\Delta H_m)^{FSC}[J] = (\Delta H_m^0)[J \cdot g^{-1}] * (mass[g] * X_c) \tag{3.2}$$

The value of ΔH_m^0 is the slope of a linear regression obtained with the values of melting enthalpy ΔH_m^{FSC} plotted as a function of $(mass[g] * X_c)$, with crystallinity expressed as a fraction. This method was first tested on poly(ethylene) (PE), which is a well-known polymer, and a value of ΔH_m^0 in very good agreement with the literature was obtained; after validation, the same procedure was successfully used on silk fibroin. Cebe's method is interesting because it applies to a wide range of materials (even the ones that are thermally unstable or prone to melting/recrystallization processes) and could eventually be used in comparison with other methods, helping to get a more accurate estimate of the equilibrium enthalpy of melting.

3.3.2 Two-phase model approach using FSC

As previously proved in the case of the cross-comparison method, replacing DSC with FSC allows to reduce the error and extend the approach to materials that would be otherwise impossible to characterize. Nonetheless, the method proposed by Cebe et al. [5] still suffers from the uncertainties dues to the fact that FSC results have to be compared to the crystallinity measured by some other technique (XRD, IR spectroscopy...). This means that FSC and XRD results are obtained on different samples of the same material, prepared in two different ways, with different dimensions (mass, thickness). Supposing that FSC and XRD samples develop exactly the same microstructure is a quite strong assumption. Uncertainties can be further reduced by transposing the two-phase model approach proposed by Pyda et al.[39] to FSC measurements. With this method, the value of ΔH_m^0 can be calculated with results extracted all from the same sample and using the same experimental technique. This method was first

applied to well-known polymers and then extended to recently developed biobased polymers, for which the literature is not abundant. The results were then discussed and compared to the ones obtained with the classical cross-comparison method combining DSC and WAXD.

Materials and methods

Commercial grades of poly(ethylene terephthalate) (PET), poly(L-lactic acid) (PLLA) and poly(phenylene sulfide) (PPS) were purchased in the form of pellets, with the exception of PET that was purchased as a film. Poly(ethylene 2,5-furandicarboxylate) (PEF) and poly(butylene 2,5-furandicarboxylate) (PBF) were synthesized in the laboratories of the Wageningen Food and Biobased Research (FBR), the Netherlands. PEF was synthesized according to the procedure reported by Thiyagarajan et al. [42] and PBF was synthesized according to the procedure reported in [1]. All the samples were dried prior to measurement: PET and PLLA were dried at $T_g + 10°C$ for at least 4h, whereas PPS, PEF and PBF were stored in a desiccator with P_2O_5 for at least 24h. The list of samples used is reported in Table 3.2. Nanoscale samples were crystallized *in situ* on FSC sensors and subsequently characterized by FSC. Bulk samples were crystallized in an oven and then characterized by WAXD, DSC, MT-DSC and FSC. More details about the instrumental calibration and set up can be found in Chapter 2.

Table 3.2: List of samples with their respective source, number-average molecular weight ($\overline{M}_n$) and weight-average molecular weight ($\overline{M}_w$).

SAMPLE	SOURCE	$\overline{M}_n$ ($g.mol^{-1}$)	$\overline{M}_w$ ($g.mol^{-1}$)
PET	Carolex France	31 000	62 000
PLLA	PLI 0005, Natureplast France	53 000	97 000
PPS	FORTRON 0214, Celanese France	n.a	n.a
PEF	Wageningen FBR The Netherlands	15 300	18 200
PBF	Wageningen FBR The Netherlands	36 000	74 500

Sample preparation and thermal treatments

Pyda et al. [39] showed that the amount of RAF in semi-crystalline polymers can be reduced by optimizing the crystallization conditions. In their work, this optimization was done by selecting relatively high crystallization temperatures, i.e. temperatures close to the melting temperature (T_2 in section (1.3)). The samples used for FSC measurements are intrinsically nanoscale. Nassar et al. [43] recently observed that crystallizing nanoscale samples with a thickness reduced to a few nanometers dramatically reduces the chances of developing RAF, even when the temperature selected for isothermal crystallization does not favor phase decoupling. Thus, it is reasonable to assume that the *in situ* crystallization directly performed on FSC sensors, with

appropriate crystallization conditions, leads to the development of microstructures with considerably reduced amounts of RAF. Under these circumstances and the consequent assumptions, the approach proposed by Pyda et al. [39] based on the two-phase model was applied to FSC measurements to determine ΔH_m^0.

In this work, the crystallization conditions were optimized both in terms of crystallization temperature T_c and crystallization time t_c. The samples were melted, cooled down to a crystallization temperature located in the sample's crystallization range, held in isothermal conditions for 60 min, quenched and finally heated again up to their melting temperature to observe the melting endotherm characteristic of a semi-crystalline microstructure. Both heating and cooling rates were set at $\beta^+ = \beta^- = 1000\ K.s^{-1}$. This protocol was repeated at increasing crystallization temperatures (with steps of 5 °C) until no melting endotherm could be observed. The crystallization temperature T_c was then set as the temperature at which the crystallization started within 60 minutes from the beginning of the isothermal step (i.e. crystallization induction time $\leq$ 60 min was observed). This choice, which is arbitrary, results from a compromise between a reasonable crystallization time and a sufficiently high crystallization temperature for crystal perfection.

Figure 3.2 illustrates the experimental design of the cycles used to optimize the crystallization conditions. Several cycles were performed at the selected crystallization temperature T_c for progressively increasing durations, until a microstructure was formed that showed no further increase in the intensity of the melting endotherm, i.e. until crystallinity reached its maximum. The corresponding time was taken as $(t_c)_{max}$. The final heating scans of selected cycles were used to quantify the amorphous and crystalline phases required by the two-phase model, and then the value of ΔH_m^0 was determined by extrapolating the linear regression built on the experimental data to the ideal case of a 100% sample.

The results obtained by FSC on nanoscale samples (weighing a few nanograms) were then compared to the results obtained by cross-comparing XRD, DSC and MT-DSC, which require bigger samples (weighing from a few milligrams to a few grams). To this purpose, semi-crystalline bulk samples (so-called to make a difference with semi-crystalline nanoscale samples) were prepared by melting the polymer between two Teflon sheets, then quickly transferring the assembly to an oven previously set at the selected crystallization temperature T_c and holding the isothermal conditions for a crystallization time at least equal to $(t_c)_{max}$. Maximum crystallized bulk samples were obtained by holding the selected crystallization temperature T_c for a crystallization time varying between 2 and 5h. The fully amorphous counterparts were obtained by melting the samples between two Teflon sheets, followed by quenching in cold water.

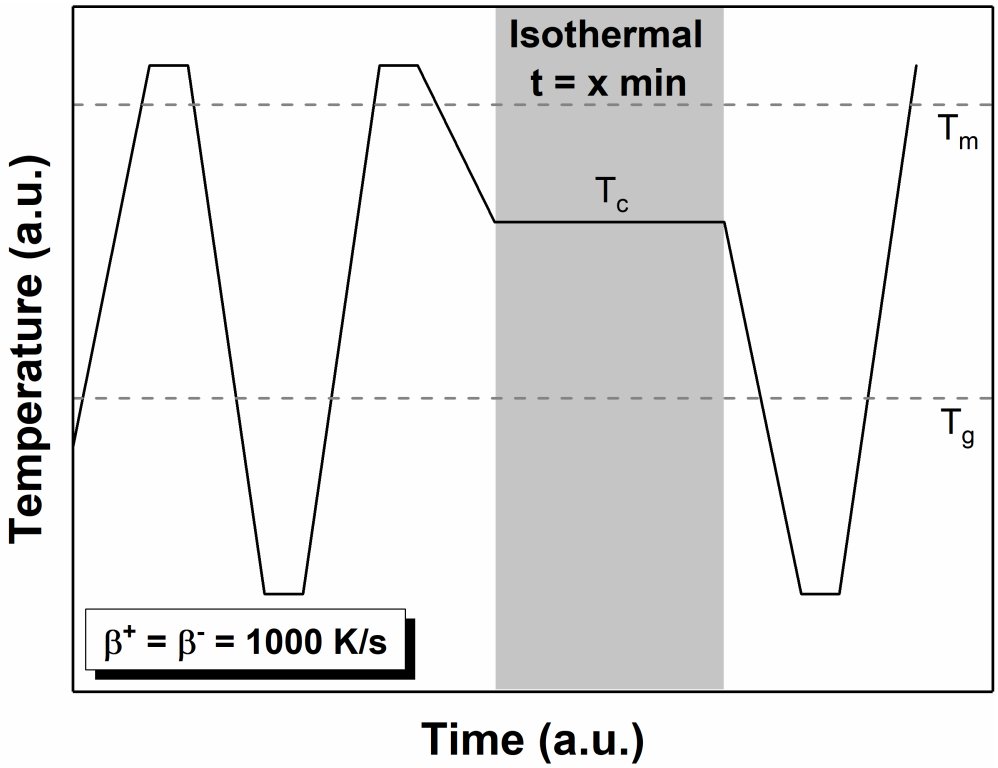

Figure 3.2: Experimental design of the thermal cycles used to create microstructures with different crystalline fractions by *in situ* crystallization on FSC sensors. T_c is the crystallization temperature, T_m is the melting temperature and T_g is the glass transition temperature.

Determination of the equilibrium enthalpy of melting ΔH_m^0

Based on the works by Pyda et al.[20] and Cebe et al. [5], equations (3.1) and (3.2) can be combined and rewritten as follows:

$$(\Delta H_m)^{FSC}[J \cdot g^{-1}] = \frac{-(\Delta H_m^0)[J \cdot g^{-1}]}{(\Delta C_p)_{am}^{FSC}[J \cdot g^{-1}.K^{-1}]} * (\Delta C_p)_{cryst}^{FSC}[J \cdot g^{-1}.K^{-1}] + (\Delta H_m^0)[J \cdot g^{-1}] \quad (3.3)$$

As shown in Figure 3.3 in the case of poly(ehtylene terephthalate)(PET), ΔH_m^0 was calculated from the intercept of a plot representing the enthalpy of melting ΔH_m^{FSC} versus the heat capacity step at the glass transition $(\Delta C_p^{FSC})_{cryst}$. ΔH_m^{FSC} is obtained by integrating the endothermic peak observed on the FSC curves normalized to the sample mass (according to equation (2.13)) with a linear baseline going from the end of the glass transition up to the melt. $(\Delta C_p^{FSC})_{cryst}$ is obtained by extrapolating the baselines of the FSC curves in the glassy state ($T < T_g$) and in the liquid state ($T > T_g$) through the glass transition T_g (midpoint), and then calculating the difference between $baseline_{liquid}^{FSC}(T = T_g)$ and $baseline_{solid}^{FSC}(T = T_g)$. Values equivalent to a change in the heat capacity at the glass transition are obtained from the values of heat flow [mW] converted to [J] and normalized to the sample mass [g].

Results obtained for a selection of polymers

Figure 3.4 shows the FSC curves recorded on nanoscale samples upon heating at $\beta^+ = 1000 K.s^{-1}$ after *in situ* isothermal crystallization from the melt at the crystallization temperature T_c dur-

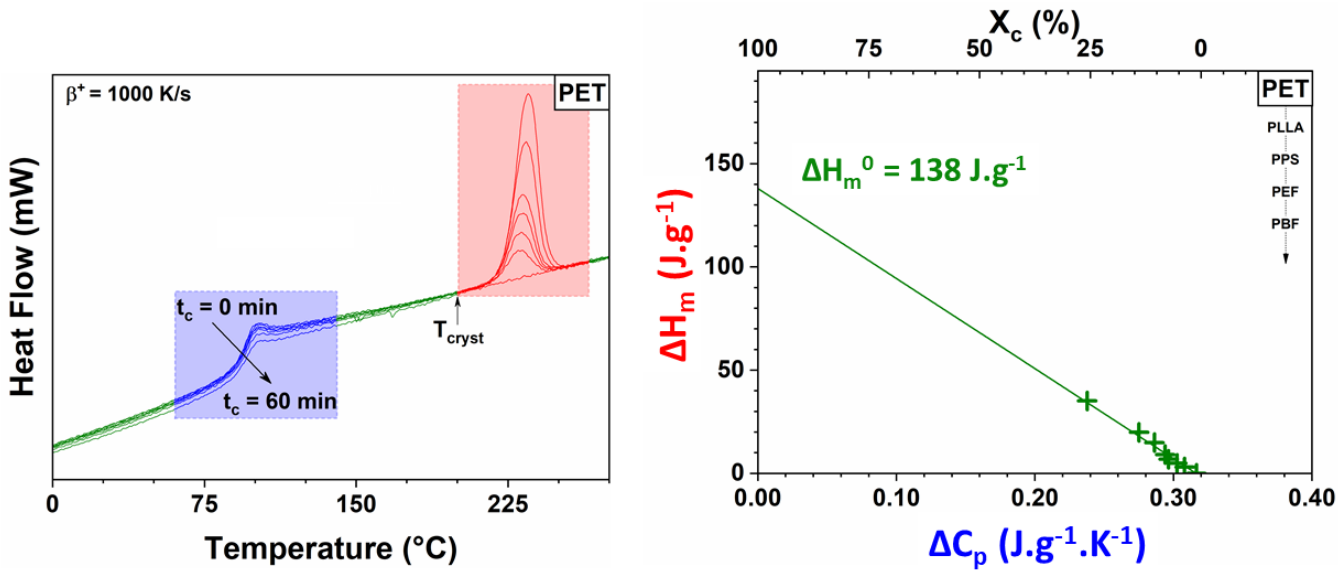

Figure 3.3: Example of ΔH_m^0 determination on a PET sample using the method based on the works of Pyda et al. [20] and Cebe et al. [5].

ing different crystallization times t_c followed by cooling down to −60 °C at $\beta^+ = 1000 K.s^{-1}$. Some of the samples investigated in this study are known to be potentially subjected to the formation of a metastable crystalline phase (PLLA[23, 44], PEF[28, 45] and PBF[46]). Thus, the selection of T_c was made with special care so that only the most stable crystalline phase was formed. In the case of PLLA, the crystallization from the melt at temperatures higher than 130 °C leads to the formation of α crystals (helical chain segments aligned in an orthorhombic unit cell), whereas at temperatures lower than 100 °C the formation of conformationally disordered α' crystals is observed [23]. At intermediate temperatures, i.e. 100 °C $< T_c <$ 130 °C, both α and α' crystals are formed. The presence of metastable crystalline phases increases the risk of crystalline reorganization, which in turn affects the calculation of the enthalpy of melting. Besides, one may wonder whether the α and α' crystals are supposed to have the same value of ΔH_m^0. For these reasons, the PLLA samples were crystallized at T_c=145 °C, i.e. in conditions excluding the formation of α' crystals. For similar reasons, T_c was set at 175 °C in the case of PEF and 135 °C in the case of PBF (whose thresholds between different crystalline phases were respectively found at 170 °C [45] and 130 °C [46]).

Under these conditions, all the samples show a single and relatively sharp melting peak (Figure 3.4), which excludes the possibility of melting/recrystallization processes during heating. As the crystallization time increases, the intensity of the melting endotherm increases. Since no cold crystallization occurs during the heating ramp, the values of ΔH_m^{FSC} obtained by integrating the endothermic peaks in Figure 3.4 can be reliably and exclusively associated to the melting of the crystalline domains progressively created during the previous isothermal treatments. For some polymers (e.g. for PET and PPS), the maximum of the melting endotherm slightly shifts to higher temperatures as the crystallization time increases. This suggest that, as the crystallization progresses, the crystalline lamellae grow thicker, which is in agreement

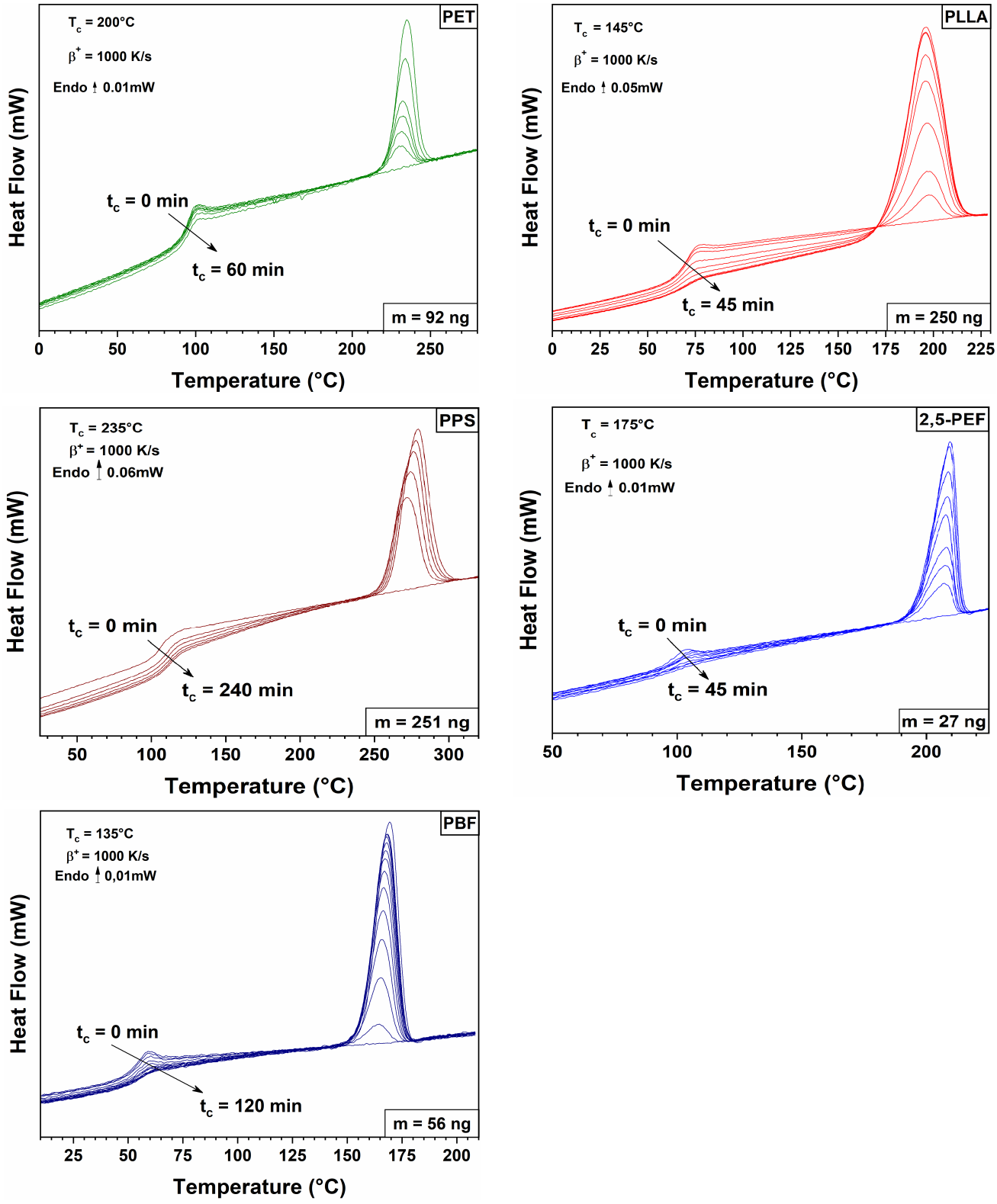

Figure 3.4: FSC curves recorded upon heating at $\beta^+ = 1000 K.s^{-1}$ on nanoscale samples of PET, PLLA, PPS, PEF and PBF after *in situ* isothermal crystallization from the melt at the crystallization temperature T_c during different crystallization times t_c.

with the Gibbs-Thomson equation [47].

One may also note that the baseline of the FSC curves in Figure 3.4 slightly changes as the crystallinity of the samples increases. This dependency is observed in the solid state (from the glassy state up to the onset of melting) but never observed in the molten state, and is particularly visible when the sample mass is relatively large (e.g. for PLLA and PPS). These changes may be due to some interfacial effects associated with stress transfers between the polymer sample and the SiN membrane of the FSC sensor. Stress transfers could be the consequence of a mismatch in thermal conductivity, but also to the shrinkage associated with crystallization. The second hypothesis is most likely, because the shrinkage of a polymer sample is expected to be proportional to the extent of crystallization, proportional to the sample mass, and only visible when the sample is semi-crystalline (in the molten state the polymer is supposed to relax and release stresses). These effects are not due to a sample mass change, because precautions were taken to make sure that the mass of polymer in contact with the sensor remained constant during the whole experimental protocol.

XRD scans were recorded on maximum crystallized bulk samples to confirm that the crystalline phases grown during the isothermal crystallization at T_c are the most stable ones (Figure 3.5). Results are consistent with the information previously reported in the literature about PLA [23, 44], PEF [28] and PBF[46]. The XRD patterns in Figure 3.5 were also used to estimate the apparent degree of crystallinity, as reported in section (1.4). In this work, all the samples crystallized to the maximum extent in the bulk showed a complex amorphous halo that required two Gaussian functions for fitting. In the past, Huo et al. [25] pointed out that the presence of RAF affects XRD patterns; being part of the amorphous phase, the RAF is expected to be included in the amorphous halo along with the MAF. The literature reports that the amorphous halo of PET can be deconvoluted in two Gaussian contributions [48]: the first one attributed to the interchain distances perpendicular to the plans of the aligned aromatic rings, the second one attributed to the interchain distances within the plane of the aligned aromatics rings. Similarly to PET, two Gaussian contributions were used to deconvolute the amorphous halos of PLLA and PPS according to information reported in the literature [49, 50]. Two Gaussian contributions were also used for PEF and PBF, even if no information is reported in the literature.

Figure 3.6 shows the values of enthalpy of melting ΔH_m^{FSC} plotted against the values of heat capacity step at the glass transition in the semi-crystalline samples $(\Delta C_p^{FSC})_{cryst}$, both measured on the FSC curves reported in Figure 3.4. According to its definition and to the method proposed by Pyda et al. [20], ΔH_m^0 could be straightforwardly calculated with the datasets reported in Figure 3.6. It is worth reminding that this calculation is correct only if the hypothesis of a two-phase microstructure is verified. Indeed, the comparison between the values of ΔH_m^{FSC} (with respect to its reference ΔH_m^0) and $(\Delta C_p)_{cryst}$ (with respect to its reference $(\Delta C_p)_{am}$) obtained from the same DSC curve is generally used to discuss the pertinence of a two-phase

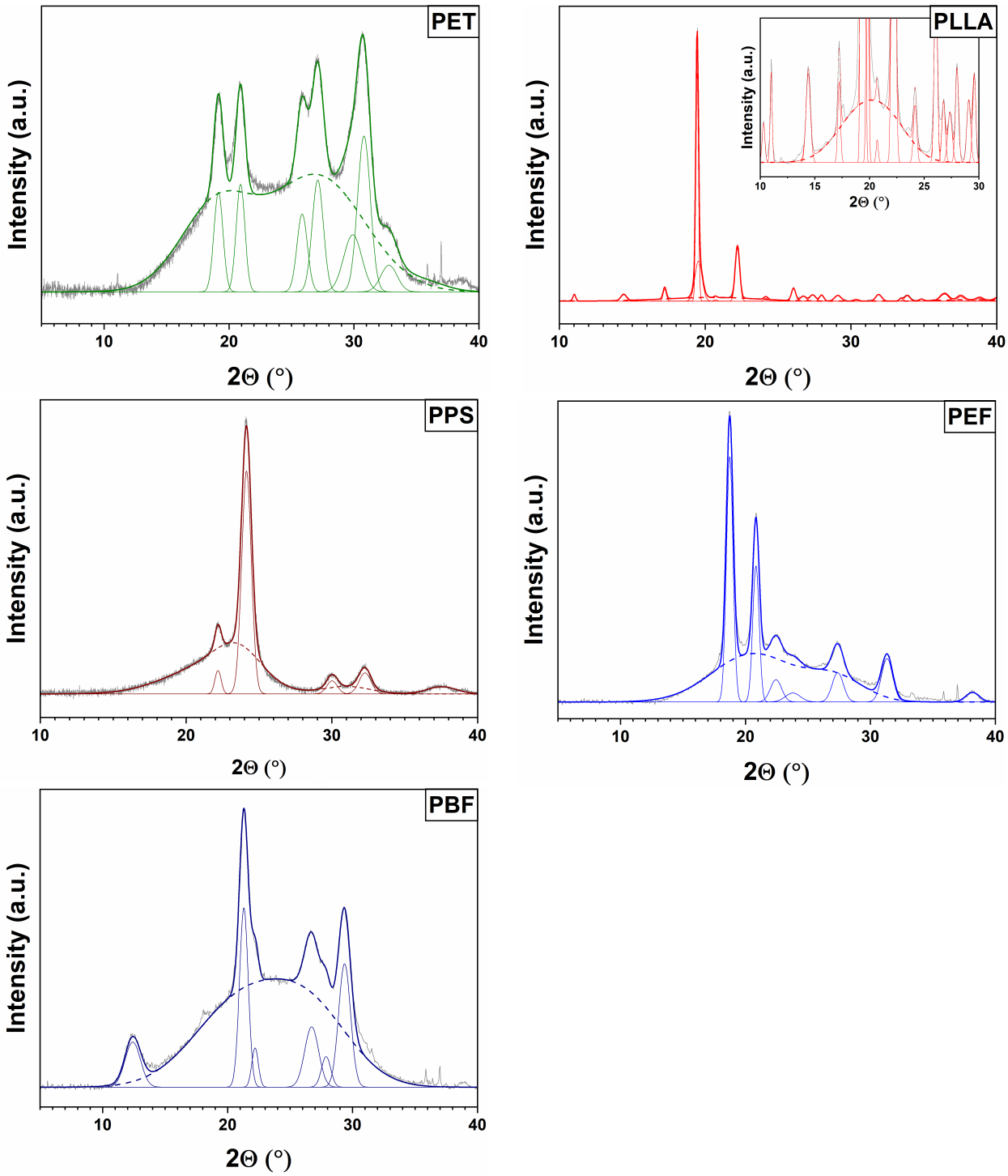

Figure 3.5: XRD patterns recorded at room temperature on maximum crystallized bulk samples of PET, PLLA, PPS, PEF and PBF after isothermal crystallization from the melt at the crystallization temperature T_c (solid lines). The raw data are in grey. The thick solid lines represent the fitting result. Thinner solid and dashed lines are reported to represent the crystalline and amorphous contributions to each pattern (Origin multi-peak fitting with Gaussian functions). The amorphous halos were fitted by two Gaussian functions; the dashed lines represent the sum of the peaks used for fitting. In the case of PLLA, an inset with suitable rescaling is provided to better visualize the amorphous halo.

model to describe the microstructure of semi-crystalline polymers. Whenever a discrepancy is revealed in the information provided by ΔH_m (crystalline fraction X_c calculated according to equation (1.12)) and $(\Delta C_p)_{cryst}$ (residual amorphous fraction relaxing at the glass transition), a three-phase model is adopted in the place of equation (3.1) and the RAF is introduced to solve the discrepancy as shown in equation (1.10).

As previously pointed out, growing polymer crystals in a confined nanoscale environment reduces the development of RAF, even when the crystallization temperature is supposed to favor the connections between the crystalline domains and the surrounding amorphous phase [43]. The samples used for FSC experiments are intrinsically nanoscale (the biggest weighs 250 ng), which may limit the formation of RAF for similar reasons, i.e. for a sort of finite-size effect. With this being said, the choice of a two-phase model to determine the crystallinity using equation (3.1) applied to FSC curves sounds encouraging. Besides, the crystallization conditions were also optimized to minimize the development of RAF. The fact that the baselines of the FSC curves in Figure 3.4 is straight in the temperature range between the glass transition and the melt, suggests that a two-phase model could actually apply to all the semi-crystalline microstructures obtained. As reported in the literature and in section (1.4), the amount of RAF formed during the crystallization process typically decreases as the size and thermal stability of the crystalline phase increases[51], and it is well known that the size and thermal stability of the crystalline lamellae increases with the crystallization temperature[52]. The literature also reports that the development of RAF is typically associated with an increase in the glass transition temperature [53] (revealing a mobility restriction of the RAF on the MAF), as well as a modification of its shape [35](due to a different distribution of the relaxation times, revealing a stronger coupling between phases). No clear changes in glass transition temperature and shape were observed in the FSC curves recorded for this study, which supports the assumption that negligible amounts of RAF were formed during the crystallization process.

When equation (3.3) is used to fit the data in Figure 3.6, the linear regression gives a slope that corresponds to ΔH_m^0 $[J \cdot g^{-1}\ ]/\ (\Delta C_p)_{am}$ $[J \cdot g^{-1}K^{-1}\ ]$ and an intercept that directly provides the value of ΔH_m^0. The dispersion of the experimental values around the linear fit (grey hatched areas in Figure 3.6) corresponds to $\pm$ 5 % uncertainty on the estimation of the degree of crystallinity. If this uncertainty were introduced in the calculation, the value of ΔH_m^0 would be affected by an uncertainty of $\pm$ 10 $J \cdot g^{-1}$ (which is acceptable when compared to the error introduced by a wrong estimation of the enthalpy of melting, e.g. in the case of massive crystalline reorganizations during the DSC measurement ramps at conventional heating rates). Indeed, as previously mentioned in this chapter, there are several possible sources of uncertainties, and the scattering in the values of ΔH_m^0 found in the literature is therefore quite explicit (see Table 3.1), as illustrated by the grey horizontal areas in Figure 3.6, which cover all the values previously reported in the literature. One of the main sources of uncertainty in determining the equilibrium enthalpy of melting is due to the fact that this is an extrapolative method.

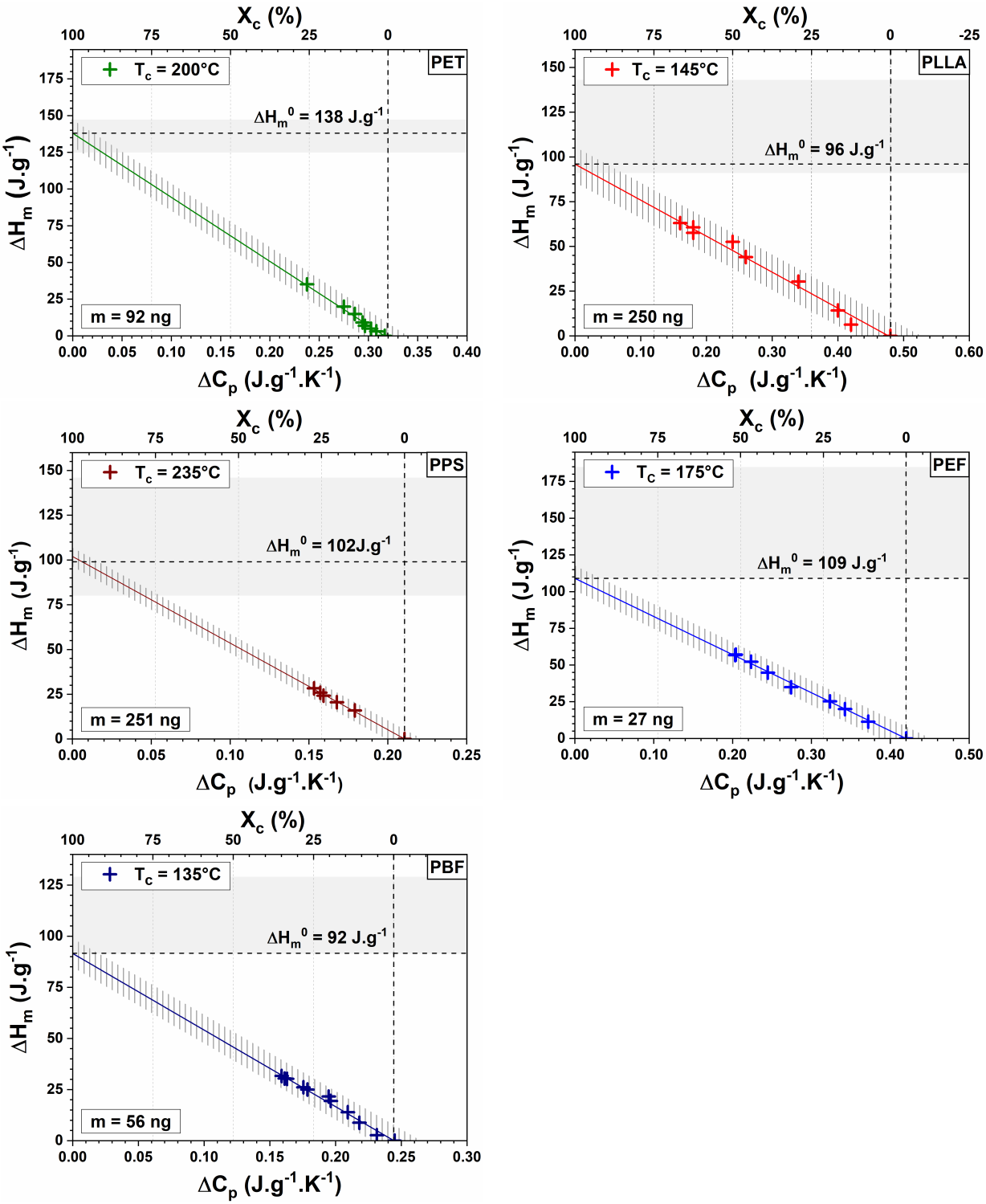

Figure 3.6: Enthalpy of melting vs. heat capacity change at the glass transition obtained from FSC curves normalized to the sample mass and the heating rate (Figure 3.4) for nanoscale samples of PET, PLLA, PPS, PEF and PBF crystallized *in situ* at the crystallization temperature T_c for different crystallization times t_c. The linear regression of the experimental data (solid lines) extrapolated to $X_c = 100\%$ and $C_p = 0\ J{\cdot}g^{-1}.K^{-1}$ reveals the equilibrium enthalpy of melting ΔH_m^0 under the assumption of a two-phase model. The grey hatched areas around the solid lines represent the uncertainty of ± 5 % on the estimation of the apparent degree of crystallinity. The grey horizontal areas represent the domain covered by the values of ΔH_m^0 that can be found in the literature (Table 3.1) plus the values obtained in this work.

Moreover, it is quite difficult to obtain a polymer with a highly crystalline microstructure for which the two-phase assumption can be assuredly made. Most of the polymers investigated in this paper have a degree of crystallinity that barely reaches 30%. For these polymers, the uncertainty associated with the slope of the ΔH_m vs ΔC_p plots is much relevant. This being said, the values of ΔH_m^0 obtained in this study fall in the same range as the values previously reported in the literature by several authors (grey areas in Figure 3.6).

In the case of PET, for instance, for which no substantial divergences are found in the literature, the FSC protocol provides a value of 138 $J \cdot g^{-1}$, which is in agreement with the value previously reported by Wunderlich and Androsch (140 $J \cdot g^{-1}$) [51, 15]. As a consequence, when it comes to relatively new polymers for which no data are found in the literature, such as PEF and PBF, one may assume that this method provides at least preliminary estimation of ΔH_m^0 that is fairly reliable, yet debatable if different values are successively found by other experimental techniques. Table 3.3 summarizes the experimental conditions used for the *in situ* isothermal crystallization performed on the FSC sensors, as well as the main outcomes of the crystallization process measured by FSC on the maximum crystallized nanoscale samples (exploitation of Figure 3.4) and the corresponding values of ΔH_m^0.

Table 3.3: Crystallization temperature (T_c) and crystallization time (t_c^{max}) selected to reach the maximum crystallinity degree during *in situ* isothermal crystallization aiming to reduce coupling between phases. T_g and T_m are the glass transition temperature and the melting temperature of the maximum crystallized nanoscale samples measured by FSC. The equilibrium enthalpy of melting ΔH_m^0 was obtained according to equation (3.3) based exclusively on FSC results. For comparison's purposes, the crystallinities of maximum crystallized bulk and nanoscale samples, which were obtained by XRD and FSC respectively, are also reported ($(X_c^{XRD})_{max}$ and $(X_c^{FSC})_{max}$).

SAMPLE	T_c [°C]	t_c^{max} [min]	T_g [±1°C]	T_m [±1°C]	ΔH_m^0 [$\pm 10 J \cdot g^{-1}$]	$(X_c^{XRD})_{max}$ [±5%]	$(X_c^{FSC})_{max}$ [±5%]
PET	200	60	92	235	138	37	25
PLLA	145	45	68	196	96	82	67
PPS	235	240	108	279	102	39	27
PEF	175	45	96	210	109	52	52
PBF	135	120	51	169	92	33	30

Comparison with other methods

The experimental procedure proposed in this work can be compared to the ones commonly found in the literature that are based on the cross-comparison of two different techniques (see sections 3.1, 3.2 and 3.3.1 for further details on the methods). PET is a good example to illustrate the possible sources of uncertainty when different methods are used to estimate ΔH_m^0. The XRD patterns recorded on maximum crystallized bulk samples (Figure 3.5) were used to calculate the apparent degree of crystallinity $(X_c^{XRD})_{max}$. The value obtained for PET is 37 ± 5%. Ruland method (based on the conservation of the total scattered intensity by a set of atoms, independent on their structural order) could have been used to obtain the absolute

degree of crystallinity [38], but most of the works reported in the literature use the method based on the ratio of areas. When equation (1.12) is used to cross-compare $(X_c^{XRD})_{max}$ with the enthalpy of melting measured by conventional DSC, a value of 162 $J \cdot g^{-1}$ is obtained. When FSC results are used instead of DSC in equation (1.12), the cross-comparison with $(X_c^{XRD})_{max}$ provides a value of 165 $J \cdot g^{-1}$. These values are quite different with respect to the values found in the literature (140 $J \cdot g^{-1}$ [15], 125 $J \cdot g^{-1}$ [16]), independently on the technique used to measure the enthalpy of melting. The value obtained by the FSC method is much closer to the values of the literature (138 $J \cdot g^{-1}$).

Comparing different values of ΔH_m^0 is definitely a multifactor problem that requires a deeper understanding of both the advantages and drawbacks of the experimental procedures used to obtain them. The differences may be acceptable or very large, depending on the nature of the sample (some polymers crystallize faster, easier and more regularly than other polymers, generating different amounts of RAF), on the design of the experimental protocol used for crystallization (which includes the size of the sample and the crystallization conditions, i.e. the crystallization temperature and time), as well as on the calculation procedure. Since ΔH_m^0 is estimated by extrapolating the experimental data (crystallinity degree X_c vs. enthalpy of melting ΔH_m) obtained on samples with different crystallinity degrees, it is mandatory to ensure the accuracy on the calculation of these quantities.

In general, techniques such as XRD and DSC are used to cross-compare the results obtained on bulk samples crystallized in controlled conditions (see section 3.1). Bulk samples are subjected to bigger thermal gradients, resulting in less controlled crystallization conditions and less regular microstructures. Besides, using conventional DSC to determine the enthalpy of melting of semi-crystalline polymers expands the level of uncertainty because of crystalline reorganization that is sometimes observed during the heating ramps, and that is hardly distinguished from the baseline drift related to the devitrification of the RAF.

Using FSC improves the accuracy of measurement thanks to the extremely fast heating rates, which exclude any possible crystalline reorganization and suppress the effects eventually due to polymorphism. Last but not least, in suitable and controlled crystallization conditions, FSC allows the concomitant measurement of X_{MAF} = 1 - X_c and ΔH_m, considerably reducing the uncertainties due to the cross-comparison of samples whose microstructures are not necessarily the same because of sampling heterogeneities. Yet, the FSC method proposed here is related to the fact that ΔH_m^0 is estimated under the assumption that a two-phase microstructure is obtained during the in situ crystallization protocol which can induce some errors on the calculation. For this reason, an accurate selection of the crystallization temperature T_c should be done with the purpose of growing regular crystalline domains with reduced connections between phases, i.e. with a negligible amount of RAF.

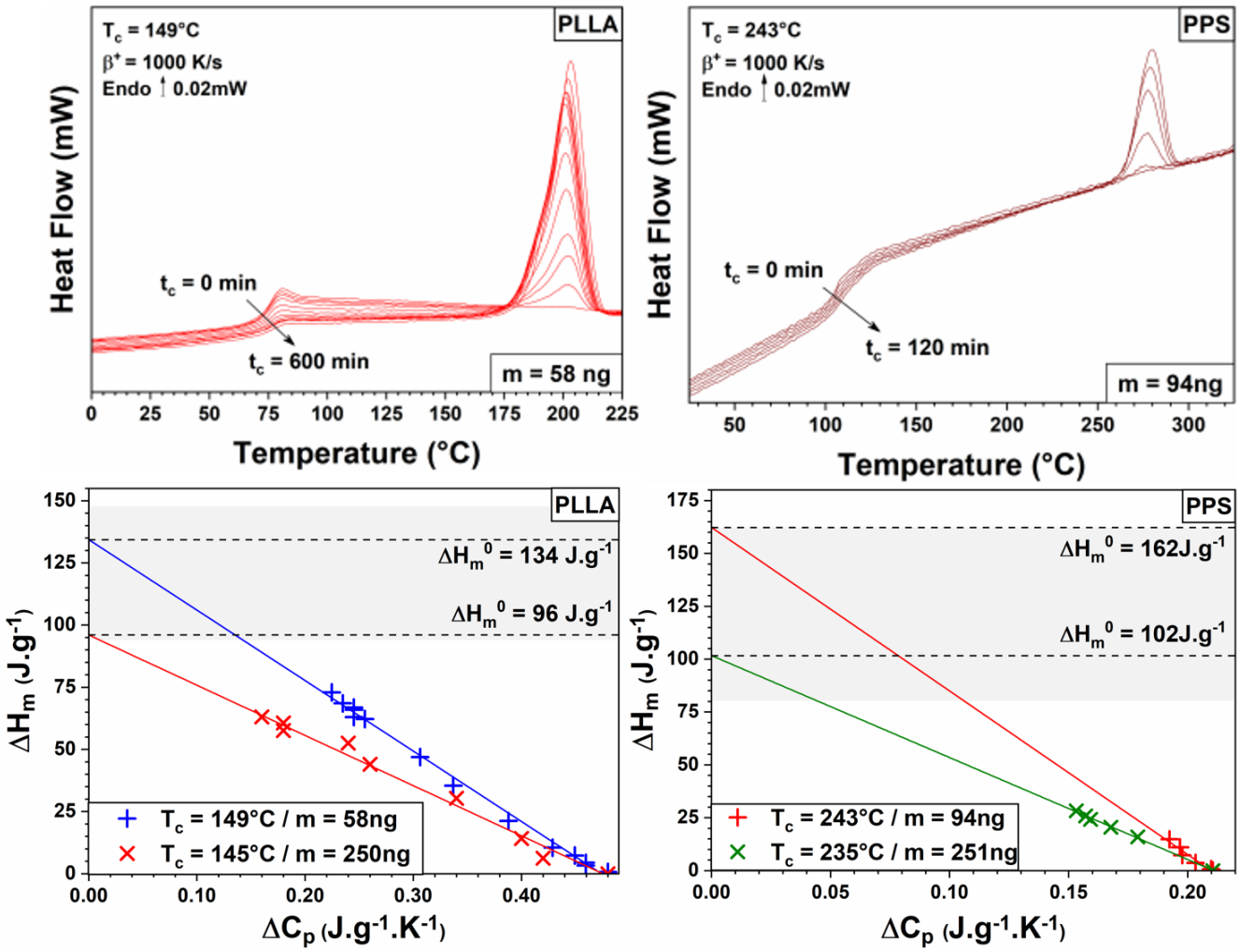

Figure 3.7: (top) FSC curves recorded upon heating at $\beta^+ = 1000 K.s^{-1}$ on nanoscale samples of PLLA and PPS after in situ isothermal crystallization from the melt at two different crystallization temperatures (145 °C and 149 °C for PLLA, 235 °C and 243 °C for PPS) during different crystallization times. Smaller samples were used with respect to Figure 3.4 (58 ng vs. 250 ng for PLLA, 94 ng vs. 251 ng for PPS). (bottom) Enthalpy of melting vs. heat capacity change at the glass transition obtained from the FSC curves normalized to the sample mass and to the heating rate. The linear regression (solid lines) of the experimental data (crosses) extrapolated to $X_c = 100$ % and $\Delta C_p = 0\ J \cdot g^{-1} K^{-1}$ reveals the equilibrium enthalpy of melting ΔH_m^0 under the assumption of a twophase model. The grey horizontal areas represent the domain covered by the values of ΔH_m^0 that can be found in the literature plus the values obtained in this work.

Uncertainty sources

Among the samples shown in Figure 3.4, PLLA and PPS are the ones with the largest masses (∼250 ng). Sample mass and crystallization temperature are two parameters that possibly affect the results of FSC measurements and the following data treatment. However, it is quite difficult to distinguish how these parameters respectively contribute to the combined uncertainty on ΔH_m^0 because it is very hard to prepare FSC sensors with samples having exactly the same mass and shape, and placed exactly in the same position on the membrane. Figure 3.7 shows the results obtained on smaller samples of PLLA and PPS (58 ng and 94 ng respectively) at higher crystallization temperatures (149 °C and 243 °C respectively) with respect to Figure 3.4. The ΔH_m vs ΔC_p plots reveal that, for these polymers, the extrapolated value of ΔH_m^0 is indeed quite dependent on the sample mass and/or on the choice of T_c. Yet these results are not sufficient and further studies are required to evaluate the influence of these parameters. It should be reminded that all extrapolative methods have intrinsic limitations that are sources of uncertainties, and this is particularly true when the extrapolation is done on a large range of values starting with few points unevenly distributed (the case of PPS crystallized at 243 °C is a good example). From this point of view, the extrapolation done on the basis of FSC measurements is neither better nor worse than any other extrapolative method, but provides values in agreement with the literature.

Besides, there are polymers (such as PET) that are quite insensitive to the choice of a different crystallization temperature. The same PET sample was crystallized at three different temperatures (190 °C, 200 °C, and 210 °C) and the values of ΔH_m^0 obtained (141 $J \cdot g^{-1}$, 138 $J \cdot g^{-1}$ and 133 $J \cdot g^{-1}$ respectively) are quite similar and in perfect agreement with the literature (140 $J \cdot g^{-1}$ [15] and 125 $J \cdot g^{-1}$ [16]) (Figure 3.8).

Other samples may be more sensitive to the choice of T_c, especially if they have peculiar crystallization features such as polymorphism. PLLA, for instance, exhibits several types of crystal modifications (α, α', β, and γ phases) that are sometimes difficult to isolate, even if the crystallization temperature is accurately selected. The ΔH_m vs ΔC_p plots reported in Figure 3.7 (bottom) suggest that PLLA is extremely sensitive to the choice of T_c. Table 3.3 reported a value of $\Delta H_m^0 = 96 \pm 10\ J \cdot g^{-1}$ for PLLA crystallized at T_c=145 °C, but a much different value is obtained for T_c=149 °C (ΔH_m^0= 134 ± 10 $J \cdot g^{-1}$). None of these values is in disagreement with the literature, because Pyda et al. [20] and Kalish et al. [22] reported values of 91 $J \cdot g^{-1}$ (at T_c =145 °C) and 96 $J \cdot g^{-1}$ (at T_c =150 °C) respectively, whereas Miyata et al. [19] and Badrinarayanan et al. [21] reported values of 135 $J \cdot g^{-1}$ and 146 $J \cdot g^{-1}$ respectively; the most accurate approach seems to be the one proposed by Righetti et al. [23], which suggests to take into account the temperature dependency of ΔH_m^0. These preliminary results indicate that polymers are not equally sensitive to parameters such as the sample mass and the crystallization temperature. As potential sources of uncertainty on the extrapolated value of the equilibrium enthalpy of melting, these parameters definitely deserve further investigations.

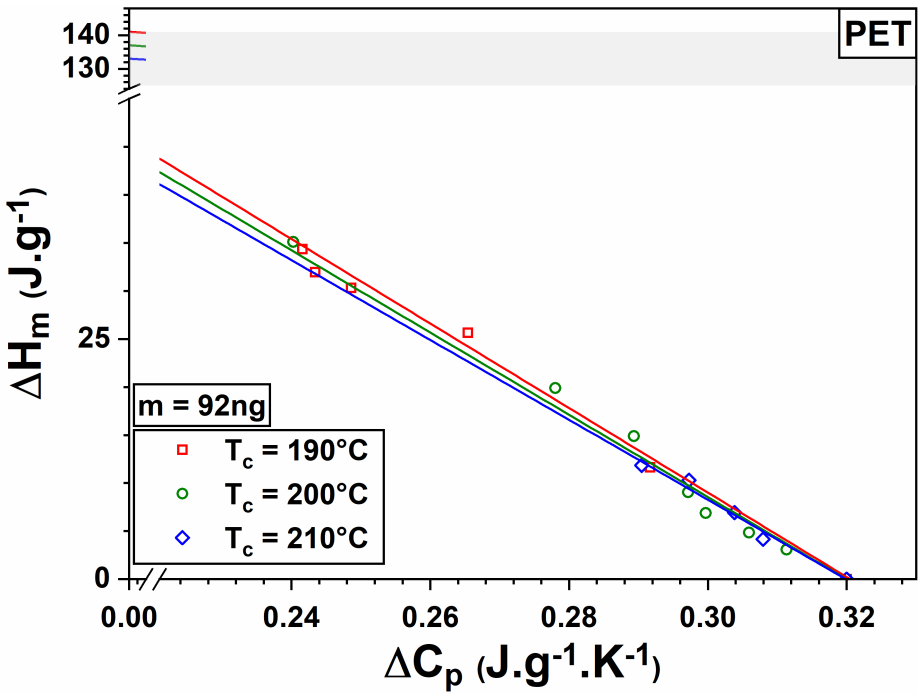

Figure 3.8: Extrapolation based on the FSC measurements on a nanoscale sample of PET (92 ng) isothermally crystallized from the melt at three different crystallization temperatures (190 °C, 200 °C and 210 °C) during different crystallization times. The linear regression (solid lines) of the experimental data (crosses) extrapolated to $X_c = 100$ % and $\Delta C_p = 0\ J \cdot g^{-1}.K^{-1}$ provides a values of $\Delta H_m^0 = 137 \pm 4\ J \cdot g^{-1}$. The grey horizontal area represents the domain covered by the values of ΔH_m^0 found in the literature.

As a perspective, it would also be interesting to measure the crystallinity degree by recording XRD patterns directly on the FSC sensor, according to the technical solutions proposed by Ivanov, Cavallo, Vlassak and their-coworkers [54, 55, 56, 57], who worked out some feasible solutions to combine XRD with FSC.

Conclusion

Equilibrium enthalpy of melting ΔH_m^0 can then be approached by using only fast scanning calorimetry (FSC), provided that suitable crystallization conditions are selected to reduce the connection between phases. The metrological concept relies, as usual, on the characterization of samples having microstructures with different degrees of crystallinity and the extrapolation of the experimental data to the theoretical situation of a 100% crystalline polymer. Contrarily to the methods commonly found in the literature, which are based on the cross-comparison of different experimental techniques (such as XRD and DSC) performed on different samples, this method is as for the method proposed by Pyda et al. [39] only calorimetric.

The main advantages of this method is that it significantly reduces the uncertainties related to (1) thermal gradients (FSC measurements are performed on nanoscale samples), (2) polymorphism and/or crystalline reorganization (FSC ramps are recorded at very high heating rates), and (3) sample heterogeneities (all the information required to calculate ΔH_m^0 is obtained from

the same curve, recorded on the same sample). This method applies to any crystallizable polymer that is quenchable and for which a two-phase microstructure with a negligible amount of rigid amorphous fraction and reduced connections between phases is obtained under controlled crystallization conditions. The protocol of isothermal crystallization is performed in situ on nanoscale samples placed on the FSC sensor. The optimization of the crystallization parameters (temperature and time) should be preliminarily done according to the selected samples, especially for polymers that are subjected to polymorphism and/or particularly sensitive to the choice of the crystallization temperature.

This method was used to estimate the equilibrium enthalpy of melting ΔH_m^0 of well-known polymers, such as PET and PPS, as well as of more recent biopolymers, such as PLLA, PEF and PBF and was the focus of a paper published during the PhD thesis [1].

The method was also applied on other newly developed materials for which no values were found in the literature. Poly(propylene 2,5-furandicarboxylate) (PPF) and Poly(neopentyl 2,5-furandicarboxylate) (PNF) as well as Poly(propylene-cyclo-hexanedicarboxylate) (PPCE) and Poly(pentylene-cyclohexanedicarboxylate) (PPentCE) were kindly provided by collaborators of the University of Bologna (Italy). Values of ΔH_m^0 for these materials are reported in the following Table 3.4.

As previously explained, a particular care has to be taken when working on samples that are able to form more than one crystallographic form (polymorphism). This is even more important when working with samples such as PLLA for which the concomitant presence of two different crystallographic forms (α and α') has been reported. Moreover, according to Righetti et al. [23] the equilibrium melting enthalpy of the two crystallographic forms of PLLA have a different temperature dependency and thus different equilibrium melting enthalpy values. As a consequence, an attempt was made to determine the equilibrium melting enthalpy value of the metastable α' crystallographic form of PLLA using the method detailed in this section. In order to do so, the crystallization temperature has been carefully chose in the temperature range at which no α crystals develops. Result of this calculation is reported in Table 3.4.

Table 3.4: List of the materials on which the two phase model based method for ΔH_m^0 has been applied along with the ΔH_m^0 values found.

SAMPLE	ΔH_m^0 [$\pm 10 J \cdot g^{-1}$]
Poly(propylene 2,5-furandicarboxylate) (PPF)	135
Poly(neopentyl 2,5-furandicarboxylate) (PNF)	161
Poly(propylene-cyclohexanedicarboxylate) (PPCE)	117
Poly(pentylene-cyclohexanedicarboxylate) (PPentCE)	108
Poly(L-lactic acid) (PLLA) (α' phase)	67

3.4 Temperature dependency of the enthalpy of melting

Let's consider a polymer that (1) can crystallize, (2) is not polymorphic, (3) has a glass transition well above room temperature, and (4) can easily be quenched into the glassy state from the melt. If this polymer is crystallized from the melt at a temperature T_c as close as possible to the melting temperature T_m, it will likely develop a two-phase microstructure, with extended domains of well-grown crystals surrounded by the residual amorphous phase. The size of the crystalline lamellae will depend on the crystallization time t_c, the amorphous phase will contain only few non-crystallizable loops, and the number of tie molecules will be reduced to the minimum. The same polymer, previously quenched from the melt and subsequently heated from the glassy state, can eventually crystallize at a temperature T_{cc} slightly above the glass transition temperature T_g (a situation referred to as "cold-crystallization"). In this case, it will likely develop a more complex microstructure, with smaller, impinged, and less perfect crystals, strongly coupled to the surrounding amorphous phase [35, 37, 58]. The crystals grown at relatively high crystallization temperatures T_c will be less prone to reorganization as compared to the crystals grown at T_{cc} [59]. Besides, crystalline reorganization is most likely to occur when the temperature gap between the glass transition and the melting point is large.

It is customary to perform DSC scans to estimate the crystallinity of semi-crystalline samples in their initial state, i.e. prior to measurement. To this purpose, the melting enthalpy of the sample ΔH_m is measured and compared to a reference value ΔH_m^0 corresponding to the hypothetical case of 100 % crystallinity. If the sample is initially amorphous, or semi-crystalline but only partially crystallized, cold crystallization is observed upon heating, and the melting enthalpy actually corresponding to the initial crystals is calculated as the difference between ΔH_m and the enthalpy associated with cold crystallization ΔH_{cc}:

$$X_{crystalline} = \frac{\Delta H_m - \Delta H_{cc}}{\Delta H_m^0} \tag{3.4}$$

This calculation is done under the assumptions that the melting and crystallization enthalpies have the same absolute value, and that they do not depend on temperature. Even when T_{cc} and T_m are several degrees apart from each other, ΔH_{cc} and ΔH_m are both compared to the same value of ΔH_m^0, which is generally taken as the "equilibrium enthalpy of melting", i.e. the melting enthalpy of the "equilibrium crystalline state", whose melting temperature is referred to as the "equilibrium melting temperature" T_m^0. This is a rough assumption that can be source of large errors in the calculation of the cristallinity degree, and can potentially account for the discrepancies observed between DSC and other techniques (XRD, density measurements...) [60].

As previously stressed, whatever the temperature selected for crystallization (crystallization from the melt at T_c close to T_m vs. cold crystallization at T_{cc} slightly above T_g), and no matter how long the crystallization time t_c, there is no polymer (intended as a macromolecular material with a molecular weight well above its entanglement molecular weight) that can completely

crystallize in the bulk, i.e. $X_c = 1$ is never reached experimentally. However, for any given T_c, it is possible to grow semi-crystalline microstructures with increasingly thick lamellae (and therefore increasing melting temperatures T_m according to Gibbs-Thomson [61]) by gradually extending the crystallization time t_c until crystallinity reaches its maximum.

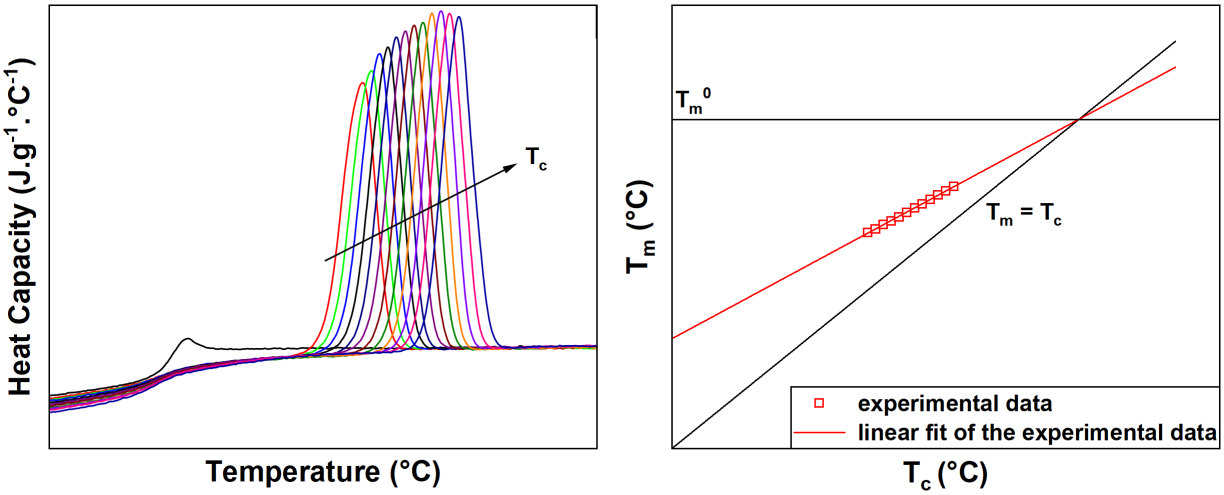

Figure 3.9: Schematic representation of the Hoffman-Weeks [62] method used to determine the equilibrium melting temperature T_m^0.

As depicted in Figure 3.9, the equilibrium melting temperature T_m^0 is generally obtained by plotting the melting temperatures T_m measured for samples crystallized to their maximum extent ($t_c \to \infty$) at different crystallization temperatures T_c, and then extrapolating this trend to the intersection with the straight line $T_m = T_c$ corresponding to the equilibrium crystal (Hoffman-Weeks [62]). Experimentally, only polymer crystals with $T_m < T_m^0$ are obtained in the bulk [63], therefore an approximation is made any time the value of ΔH_m^0 is used to estimate the crystallinity degree of a sample by calorimetric measurements.
In fact, the melting enthalpy of a polymer is intrinsically temperature-dependent because of the differences in the temperature dependencies of the solid and liquid heat capacities [60, 64]. This dependency can be expressed according to Kirchoff's law:

$$\Delta H_m(T_2) - \Delta H_m(T_1) = \int_{T_1}^{T_2} \Delta C_p dT \tag{3.5}$$

Where $\Delta H_m(T_1)$ and $\Delta H_m(T_2)$ are the melting enthalpies measured at the temperatures T_1 and T_2, and ΔC_p is the difference between $C_p^{liquid}(T)$ and $C_p^{solid}(T)$, since during melting the polymer goes from the solid state at $T = T_1$ to the molten state at $T = T_2$. A schematic representation of the Kirchoff's Law is displayed in Figure 3.10. According to this equation, ΔH_m can be calculated at any temperature between $T_{g,endset}$ and T_m^0, and ΔH_m^0 can be subsequently obtained by extrapolating $\Delta H_m(T)$ to $T = T_m^0$.

An example of such a calculation has been previously proposed by Wunderlich et al. [64] for polyethylene, which displays a very broad range of melting temperatures depending on the

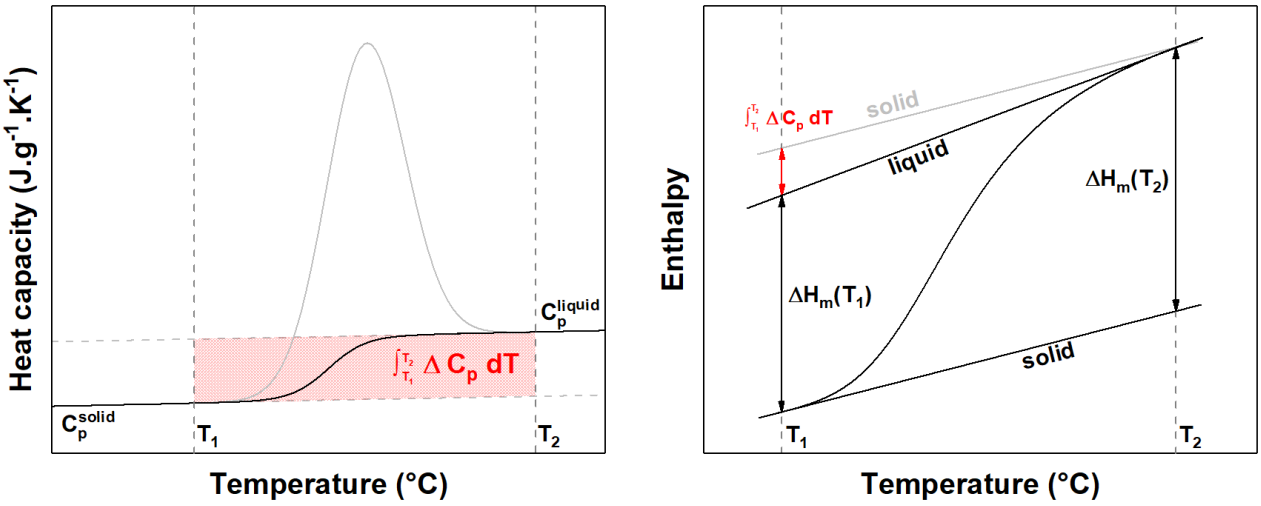

Figure 3.10: Schematic representation of the Kirchoff's law (equation 3.5) applied to melting of a 100% crystalline polymer. On the left, the black line represents the heat capacity curve that goes from the solid state ($C_p^{solid}(T)$) to the liquid state ($C_p^{liquid}(T)$) during the melting process. The grey curve is the heat flow trace measured upon melting using DSC on the same temperature range and the red area represents the integration of the heat capacity difference ΔC_p over the temperature range T_1 to T_2. On the right, the enthalpy is schematically represented as a function of the temperature as well as the extrapolated lines of the solid and liquid state (black lines). $\Delta H_m(T_1)$ and $\Delta H_m(T_2)$ are the melting enthalpies measured respectively at the temperatures T_1 and T_2. The grey line represents the solid state line shifted to the top to represent the enthalpy associated with the integration of the heat capacity curves displayed on the left.

sample molecular weight. They reported that the phase-transition enthalpy of highly defective PE crystals melting around room temperature drops by about 15% compared to nearly perfect PE crystals melting close to the thermodynamic equilibrium melting point. This description is also supported by the experimental results obtained by Blundell et al. [65] on PET ($\Delta H_m = 95 J.g^{-1}$ at $T = 100\ °C$ and $\Delta H_m = 136 J.g^{-1}$ at $T = 290\ °C$), and later on by Séguéla et al. [60] on PET and PEEK. The temperature dependency of the melting enthalpy for PET was expressed as follows [60]:

$$\Delta H_{m,PET} = -166.57 + 1.1624 * T - 0.001099 * T^2 \tag{3.6}$$

In the case of PET, the 8% depression of the melting enthalpy between the thermodynamic equilibrium melting point T_m^0 and the cold-crystallization temperature has a relatively weak impact on the calculation of the crystalline fraction. In their study about PE, Wunderlich and Czornyj [64] observed that the plot of ΔH_m vs. T has a parabolic shape with a maximum, which was further confirmed by Séguéla [60] in the case of PET and PEEK. The practical consequence is that the larger is the gap between T and T_m^0, the rougher is the assumption that ΔH_m^0 can be compared to ΔH_m whatever the temperature, and the larger are the errors made in the calculation of cristallinity.

As previously mentioned, the question about the temperature dependency of the melting enthalpy may be of great interest for samples such as poly(L-lactic acid) (PLLA), whose crystal-

lization strongly depends on temperature. Indeed, both the α and α' PLLA crystals arrange in orthorombic lattices; however, the α' crystals grown at low temperatures have conformational defects that are not found in the α crystals grown at high temperatures. This situation corresponds to a "packing polymorphism" that admits the existence of crystals with the same crystalline lattice but very different degrees of perfection, thermal stability, and thermodynamic properties [66]. In a recent work, Righetti et al. [23] investigated PLLA samples isothermally crystallized at $T_c = 85\ ^\circ C$ and $T_c = 145\ ^\circ C$ (i.e. containing only α' or α crystals, respectively). They measured the enthalpy of crystallization Δh_c by DSC, and compared it to the degree of crystallinity X_c obtained by XRD. The temperature dependency of the melting enthalpy was then expressed by rewriting equation (3.5) as follows:

$$\Delta h_m^0(T) = \Delta h_m^0(T_c) + \int_{T_c}^{T} [c_p^l(T') - c_p^s(T')]dT' \tag{3.7}$$

Where Δh_m^0 represents the melting enthalpy extrapolated to the hypothetical case of a 100% crystalline sample. This equation takes into account the temperature evolution of the solid and liquid specific heat capacities, and was used to obtain the temperature dependency of the melting enthalpy for both the α and α' crystalline forms of PLLA. At identical temperature, the difference between the two values was found to be constantly about $25 J.g^{-1}$. [67], 247°C [68] and 265°C [26]).

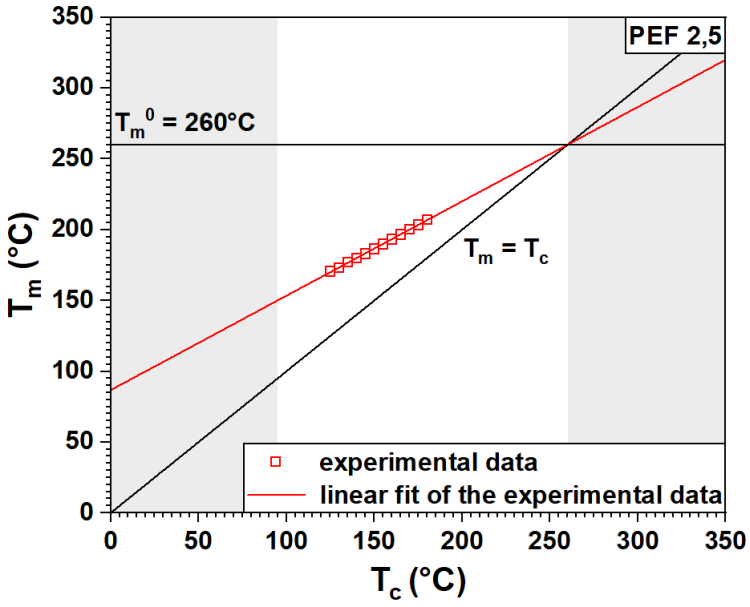

Figure 3.11: Melting temperature T_m vs. crystallization temperature T_c for a sample of poly(ethylene furanoate) (PEF) crystallized at different T_c. The red line represents the best fit, and the black line corresponds to $T_m = T_c$; the equilibrium melting temperature T_m^0 is obtained as the intersection of the two lines, according to Hoffman-Weeks procedure [62].

It is inevitable to wonder whether the protocol described in section 3.3.2 for the estimation of ΔH_m^0 can be further improved by determining the temperature dependency of the melting enthalpy using the Kirchoff's law. The value of ΔH_m^0 would then be obtained by extrapolating

$\Delta H_m(T)$ to $T = T_m^0$. The method based on Kirchoff's law was applied to a PEF sample using the FSC technique. As previously mentioned, it is first necessary to get a fairly accurate estimation of the equilibrium melting temperature T_m^0, which is most of the time achieved using the Hoffman-Weeks procedure. The Hoffman-Weeks protocol was applied to a PEF sample isothermally crystallized to the maximum possible extent on a FSC sensor chip at different T_c. The measured melting temperatures were then plotted against the crystallization temperature, and the value of T_m^0 was determined as the intersection between the $T_m = f(T_c)$ trend and the $T_m = Tc$ curve (see Figure 3.11), obtaining a value of 260°C. This value is in agreement with the T_m^0 values previously reported in the literature (226°C [27], 240°C [68]).

Now, let's consider a sample of PEF isothermally crystallized at a temperature T_c during increasing crystallization times t_c, and having a melting temperature T_m. Using the extrapolating procedure reported in section 3.3.2, it is possible to determine the melting enthalpy $\Delta H_m(T_m)$ that would be observed on a sample with a crystalline fraction $X_c = 1$. Equation 3.5) can be rewritten as:

$$\Delta H_m(T_2) - \Delta H_m(T_m) = \int_{T_m}^{T_2} [c_p^l(T) - c_p^s(T)]dT \tag{3.8}$$

This equation allows to determine the melting enthalpy that would be observed at any given melting temperature T_m, and in particular at the ideal melting temperature T_m^0, which indeed corresponds to the equilibrium melting enthalpy ΔH_m^0:

$$\Delta H_m(T_m^0) - \Delta H_m(T_m) = \int_{T_m}^{T_m^0} [c_p^l(T) - c_p^s(T)]dT \tag{3.9}$$

Only equation 3.9 actually provides the value of the melting enthalpy that would be recorded for a fully crystalline material ($X_c = 1$) at the equilibrium melting temperature; any other method can only provide a value of melting enthalpy extrapolated to $X_c = 1$, which is generally quite close to the equilibrium value if the crystallization conditions are carefully selected. Equation 3.9 requires to know the temperature dependencies of the solid and liquid heat capacities, which can be achieved experimentally by MT-DSC. In the case of PEF, their difference was obtained as: $[c_p^{liquid}(T) - c_p^{solid}(T)] = 1.389 - 0.00267 * T(J \cdot g^{-1} \cdot K^{-1})$ (see Figure 3.12). With this information, equation 3.9 can be rewritten as follows:

$$\begin{aligned}\Delta H_m(T_m^0) - \Delta H_m(T_m) &= \int_{T_m}^{T_m^0} [1.389 - 0.00267 * T]dT \\ &= (1.389 * T_m^0 - 1.389 * T_m) + (0.001335 * (T_m)^2 - 0.001335 * (T_m^0)^2 \end{aligned} \tag{3.10}$$

Now let's consider a sample of PEF isothermally crystallized at $T_c = 125$°C during increasing crystallization times t_c, having a maximum melting temperature T_m=178°C. According to the procedure reported in 3.3.2, the melting enthalpy extrapolated to $X_c = 1$ is equal to

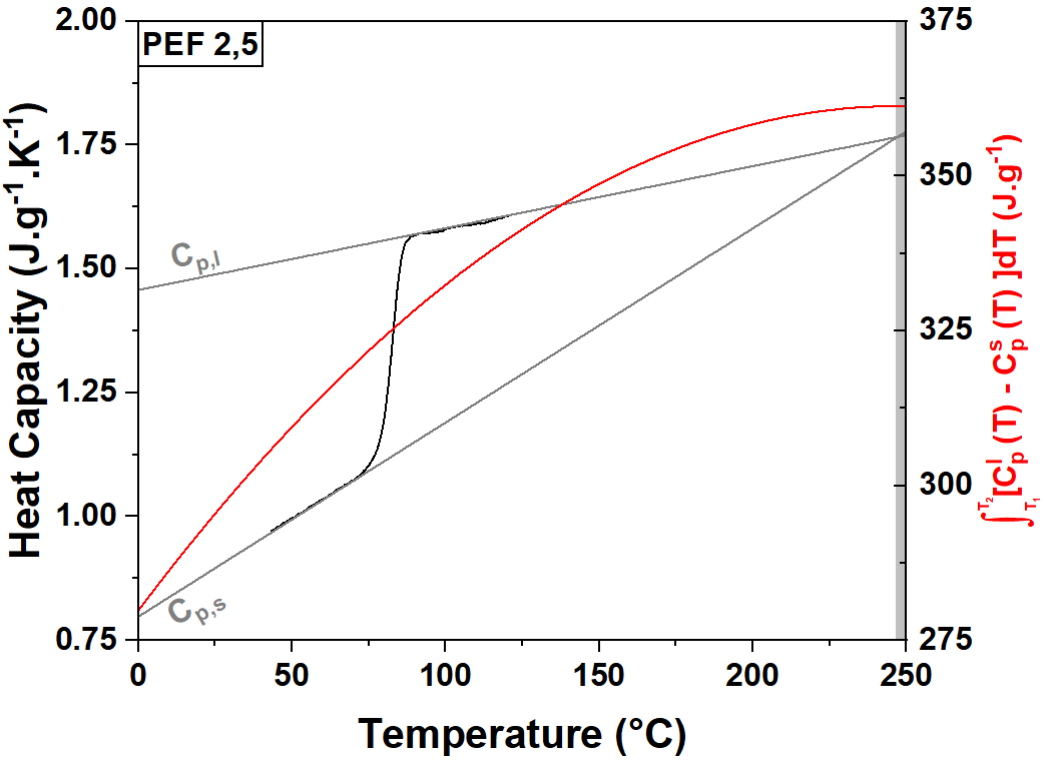

Figure 3.12: Heat capacity curves obtained from MT-DSC measurements on a fully amorphous PEF sample. The grey lines represents the heat capacity of the solid and liquid state extrapolated from the experimental curve (in black). The red line displays the integral of the solid and liquid heat capacities difference.

$\Delta H_m(T_m$=178°C) = $87 J \cdot g^{-1}$. Equation 3.10 can then be rewritten as follows:

$$\Delta H_m(T_m^0) = -268 + 1.389 * T_m^0 - 0.001335 * (T_m^0)^2 \tag{3.11}$$

As a reminder, $T^0_{m,PEF}$=260°C. With this value, $\Delta H^0_m = \Delta H_m(T_m = T^0_m)$ obtained from equation 3.11 is equal to 93 $J \cdot g^{-1}$. A depression of about 7% is observed between the melting enthalpy measured at T_m=178°C and the melting enthalpy that would be observed at $T_m = T^0_m$. This finding is in good agreement with the results previously reported by Wunderlich et al. [64] and Séguéla [60], who estimated a depression of 15% for polyethylene (PE) and 8% for poly(ethylene terephthalate) (PET).

The procedure reported in section 3.3.2 was repeated at different T_c ranging from 125 to 175°C to obtain a better estimation of the equilibrium enthalpy of melting for PEF. The value of ΔH^0_m was estimated for every T_c using equation 3.11, and an average value of 98 $J \cdot g^{-1}$ was obtained. Equation 3.10 was rewritten as follows:

$$\Delta H_m(T_m) = -263 + 1.389 * T_m - 0.001335 * T_m^2 \tag{3.12}$$

The melting enthalpy of PEF was plotted against the melting temperature, as shown in Figure 3.13. This graphical representation shows that equation 3.12 gives a fairly good fit of the experimental values of ΔH_m obtained from the procedure reported in section 3.3.2. However,

as shown by the inset in Figure 3.13, the value of T_m^0 previously reported in this work (vertical dotted lines) falls in the temperature range where $\Delta H_m(T_m)$ starts to decrease, which in turn indicates that the solid and liquid heat capacities have crossed and $C_p^{liquid}(T) < C_p^{solid}(T)$. This situation is a physical non-sense. Such discrepancy has two possible explanations: (1) the value of T_m^0 determined with the Hoffman-Weeks procedure has been overestimated due to overheating processes that have not been corrected [3]; (2) the temperature dependencies of the solid and liquid heat capacities, which have been experimentally determined from MT-DSC measurements, are submitted to uncertainties that led to an underestimation of the temperature at which C_p^{solid} crosses C_p^{liquid}. When compared to the values reported in the literature, it appears that the value of T_m^0 reported by Codou et al. [68] is quite close to the temperature at which the solid and liquid heat capacities cross, therefore this temperature seems to be a better estimation of T_m^0 and was chosen as the highest temperature limit for the application of the Kirchoff's law.

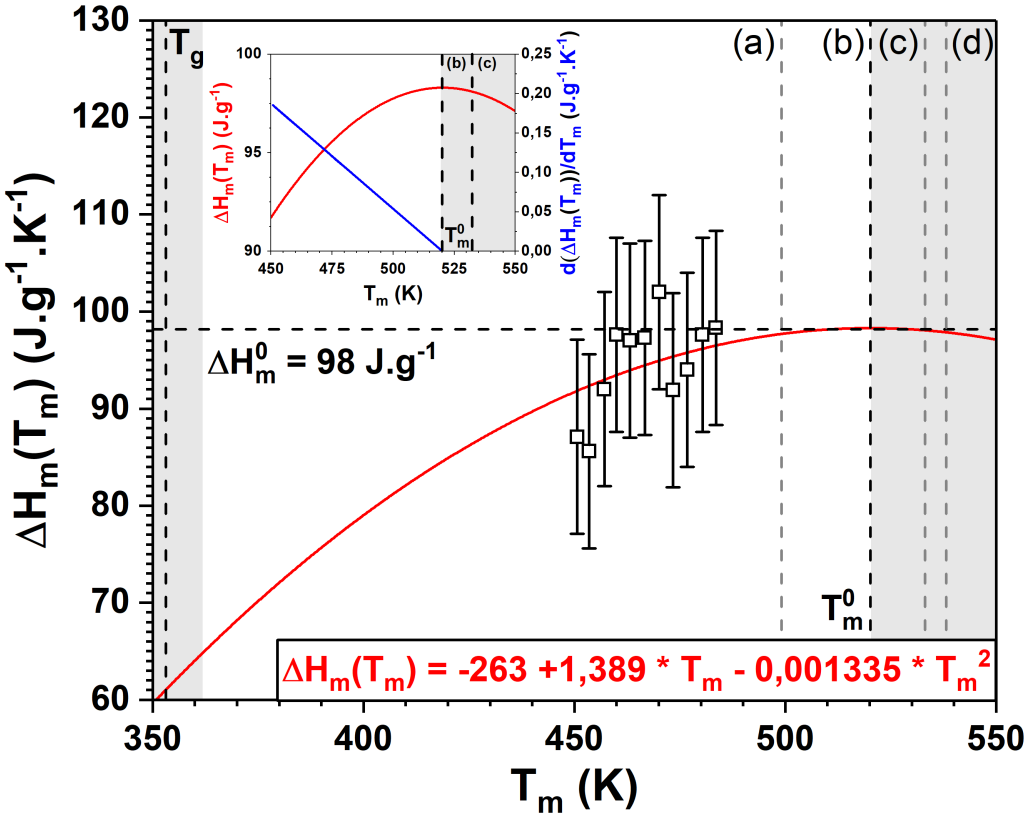

Figure 3.13: Enthalpies of melting obtained from the extrapolation protocol reported in section 3.3.2 for a PEF sample crystallized at different crystallization temperatures T_c comprised between 125°C and 175°C. The results are displayed against the maximum melting temperature measured on a PEF sample crystallized at each crystallization temperature. The red line corresponds to the best fit obtained using Kirchhoff's law [60]. The grey areas provides the temperature limits for fitting, i.e. $T_{g,endset}$ on the left and T_m^0 on the right. The inset displays the best fit (red) and its derivative (blue). The equilibrium melting temperature T_m^0 is obtained as the temperature at which the derivative of the $\Delta H_m(T_m)$ function is equal to $0J \cdot g^{-1} \cdot K^{-1}$, which is also the temperature at which the solid heat capacity line crosses the liquid heat capacity line. The equilibrium melting enthalpy ΔH_m^0 is determined as the enthalpy of melting measured at $T_m = T_m^0 = 520.15$K and is equal to 98 $J \cdot g^{-1}$. The vertical dotted lines (a), (b), (c) and (d) correspond to the values of T_m^0 obtained from the literature ((a) [27], (b) [68] and d[26]), from the Hoffman Weeks procedure (c) and from the crossing of the solid and liquid heat capacities (b).

Figure 3.13 shows that the value of ΔH_m^0 obtained using T_m^0= 260°C is very close to the value obtained using T_m^0= 247°C. Therefore, equation 3.12 is still valid and can be used over a temperature range going from $T_{g,endset}$= 90°C up to T_m^0= 247°C. Using this equation it is then possible to get a more rigorous estimation of the melting enthalpy that should be used as a reference value to determine the crystalline fraction with equation 3.4. Yet, it could be interesting to check what would be the difference between the crystalline fraction determined using the procedure based on the Kirchoff's law as compared to the crystalline fraction that would be classically obtained using equation 3.4, i.e. without considering the temperature dependency of the solid and liquid heat capacities as well as the crystal surface and internal degree of perfection of the crystalline phase.

Let's consider a sample of PEF crystallized at T_c= 175°C during different crystallization times; the melting enthalpy of the fully crystalline material (X_c = 1) can be determined using the FSC protocol reported in section 3.3.2. The melting enthalpy $\Delta H_m(T_m$ =211°C) is equal to 98 $J \cdot g^{-1}$. Now, let's consider the same sample crystallized at a lower crystallization temperature T_c= 125°C during t_c= 120 min; the melting temperature recorded upon heating is T_m= 178°C and ΔH_m= 56 $J \cdot g^{-1}$. The crystalline fraction provided by equation 3.4 (using the value of ΔH_m obtained for T_c= 175°C) would be X_c= 57%. However, if equation 3.12 is used to determine the melting enthalpy of the fully crystalline material crystallized at T_c= 125°C, the reference value to be used in equation 3.4 is $\Delta H_m(T_m$ =178°C)= 92 $J \cdot g^{-1}$ and a crystalline fraction X_c=61% is obtained, which corresponds to a difference of about 4%. This finding is in good agreement with the results reported by Séguéla et al. [60], and one may think that such a difference is not a big deal when it comes to the estimation of the crystallinity degree. However it is, especially when the crystalline fraction is used as a starting point to estimate the amount of RAF.

The melting enthalpy depends on the temperature dependencies of the solid and liquid heat capacities, which are different. Equation 3.12 is particularly useful when the melting temperature measured on the analyzed sample is much lower than the melting temperature of the sample previously used to estimate the melting enthalpy of the fully crystalline material (X_c=1) according to the methods detailed in sections 3.1, 3.2 and 3.3.

One of the most interesting features of the procedure detailed in this section is that it allows the determination of the melting enthalpy that would be observed at the equilibrium melting temperature T_m^0, i.e. the equilibrium melting enthalpy ΔH_m^0. If a rapid estimation of this value is needed with sufficient accuracy, Figure 3.13 shows that the melting enthalpy determined using the procedure reported in section 3.3.2 is ($\Delta H_m(T_m$ =211°C) = 98 $J \cdot g^{-1}$) is very close to the ΔH_m^0 value determined by extrapolating the temperature dependency of $\Delta H_m(T_m)$ to $T_m = T_m^0$. This means that, if the crystallization conditions are optimized to obtain crystals with a melting temperature as close as possible to the equilibrium melting temperature T_m^0,

the procedure reported in sections 3.1, 3.2 and 3.3 provides a sufficiently accurate estimation of the ΔH_m^0 value, for the experimental data falls in the range where the parabolic trend of $\Delta H_m(T_m)$ is close to its maximum.

3.5 Rigid amorphous fraction as evidenced by fast scanning calorimetry

In this chapter, different methods to determine the melting enthalpy of a 100% crystalline material as well as its temperature dependence have been discussed. When the methods are based on the two-phase model (section (3.2) and subsection (3.3.2)), the crystallization conditions should be optimized in order to reduce the amount of rigid amorphous fraction and therefore the coupling bewteen the crystalline and amorphous phases. Under these conditions, a two-phase model can be applied to determine a value of melting enthalpy that approaches fairly well the equilibrium melting enthalpy ΔH_m^0. The opposite is also true, i.e. the crystallization conditions can also be selected on purpose to develop different microstructures containing different amounts of rigid amorphous fraction.

According to a two-phase model, the $\Delta H_m^{FSC} = f((\Delta C_p^{FSC})_{cryst})$ trend is linear when the amount of RAF in the microstructure is negligible [5, 20, 39]. Thus, the appearance of RAF should result in a deviation from this trend. The development of RAF can then be investigated as a function of the crystallization conditions (temperature, time, but also sample size).

Starting from the crystallization temperature T_c that has been used in the previous study on the determination of ΔH_m^0 (i.e. a temperature at which a very small amount of RAF is formed), a bigger sample of PEF (m $\simeq$ 100 ng) was crystallized at decreasing crystallization temperatures. The appearance of RAF was then detected through the possible deviations from the $\Delta H_m^{FSC} = f((\Delta C_p^{FSC})_{cryst})$ linear trend (Figure 3.14).

Figure 3.14 shows that a slight deviation from the two-phase linear trend is observed for every crystallization temperature. Apparently, the development of RAF in PEF samples crystallized from the melt is not really dependent on the crystallization temperature, even when the crystallization temperature is low ($T_c = 125$ °C).

More interestingly, whatever the crystallization temperature, the $\Delta H_m^{FSC} = f((\Delta C_p^{FSC})_{cryst})$ trend is linear at short crystallization times, but then at longer crystallization times a plateau is reached, indicating that the amorphous fraction progressively disappears (ΔC_p decreases) as it converts from mobile to rigid, with no increase in crystallinity (ΔH_m is constant). The linear trend observed at short crystallization times suggests that the RAF development is not significant during the earlier stages of primary crystallization; the plateau shows that the RAF develops during the last stages of primary crystallization, as well as during secondary crystal-

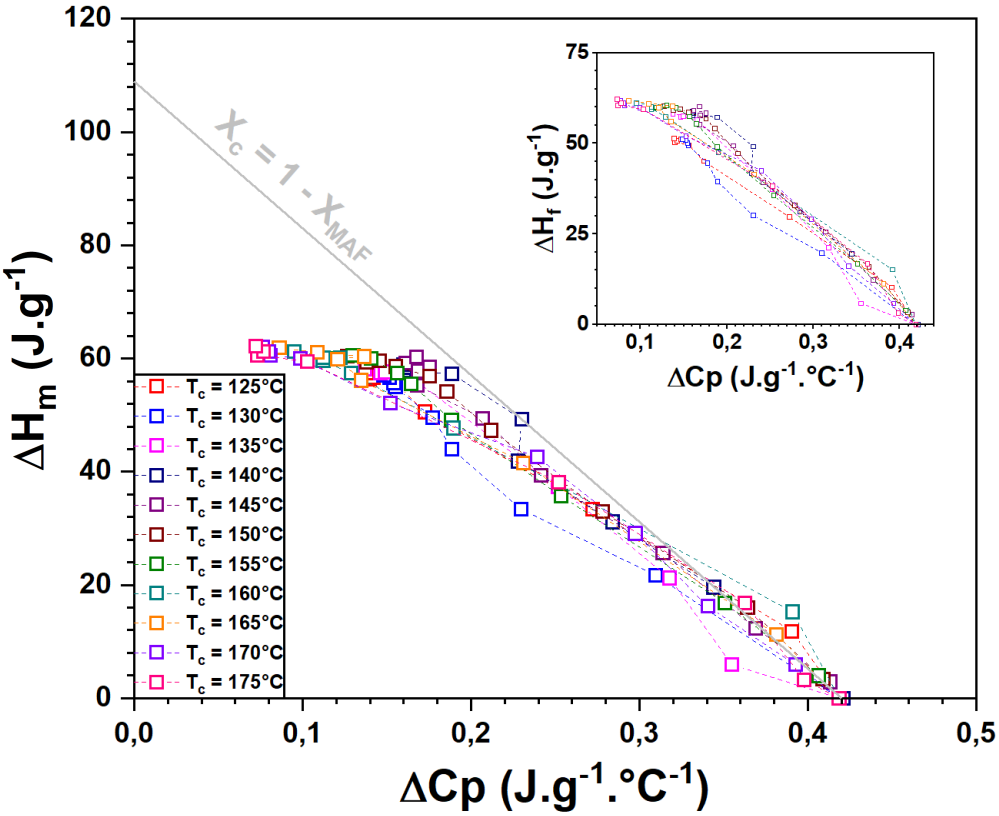

Figure 3.14: Melting enthalpy vs. heat capacity step at the glass transition for a sample of PEF crystallized at different temperatures T_c (ranging from 125°C to 180°C) for increasing times t_c. The grey line was obtained by applying the method reported in section 3.3.2 with the experimental data of a sample crystallized at T_c = 175°C, and is used here as the reference line corresponding to a two-phase model.

lization. The fact that the crystalline fraction reaches a plateau proves that the rigidification of the amorphous phase, i.e. the conversion of the mobile amorphous fraction into a rigid amorphous fraction, continues even after the primary crystallization process is achieved. The literature reports that the RAF is expected to develop simultaneously to the primary crystallization process at low crystallization temperatures [35, 69, 70]; at higher crystallization temperatures, the development of the RAF has been mainly observed during the final stages of crystallization, and particularly during the secondary crystallization process [69, 70, 71, 72].

Besides, one may notice that there is a difference between the results obtained in section 3.3 (ΔH_m^0= 109 $J \cdot g^{-1}$) and the results obtained in this section (ΔH_m^0= 98 $J \cdot g^{-1}$). In addition to the uncertainties that affect any measurement, this difference could also be attributed to two other parameters, the crystallization time and the sample size. In regards to the crystallization time, Figure 3.14 shows that the development of RAF significantly increases after a given time spent at the selected crystallization temperature, and continues after the primary crystallization process is achieved. Thus, it could be argued that the results reported in section 3.3 were obtained on a sample that was not sufficiently crystallized as compared to the sample presented herein. This comparison is interesting and could be a good explanation to the appearance of a plateau in Figure 3.14. As a perspective, it would be interesting to crystallize the

sample reported in section 3.3 to longer crystallization times to check this hypothesis. Anyway, the deviation from the linear trend observed in Figure 3.14 was not observed on the sample shown in Figure 3.6. This may suggest that a significant amount of RAF develops during the primary crystallization process in the bigger sample (m≈ 100 ng), while it only develops at longer crystallization times in the smaller samples (m≈ 25 ng). It is likely to conclude that the sample size has a non-negligible impact on the development of the RAF. This finding is in good agreement with the literature, where it has been reported that the formation of RAF is negligible in nanoscale samples [43].

Clearly, the development of RAF depends both on the sample size and the crystallization time. These aspects should be taken into account for the determination of the equilibrium enthalpy of melting, of course, and then obviously for the subsequent microstructural characterizations. In particular, in the selected crystallization conditions, it appears that the formation of RAF is mostly driven by the sample size which supports the previous observations made on PLLA and PPS samples in section 3.3. It would be interesting to repeat the measurements for samples with different sizes, and viceversa, samples with different sizes may be used in order to tailor the formation of different amounts of RAF. To this purpose, FSC is a particularly interesting apparatus, for it allows the development and analysis of microstructures containing controlled amounts of RAF.

3.6 Conclusions

In order to get an accurate estimation of the rigid amorphous fraction (RAF) amount, it is first necessary to quantify the crystalline and mobile amorphous fractions. The quantification of the crystalline fraction is most of the time made using WAXD and/or DSC through the use of equation (1.12), which requires to know the melting enthalpy of the 100% crystalline material. Several methods that can be used to determine the melting enthalpy of the 100% crystalline material have then been discussed and compared. The focus was made on the method based on the protocol reported by Pyda et al. [39] applied to the recently developed FSC technique [1]. As usual, the concept relies on the characterization of semi-crystalline samples containing different degrees of crystallinity and the extrapolation to the 100% crystalline polymer. Nonetheless, as opposed to the methods frequently used in the literature, this method is not based on the cross comparison of results obtained through different measurement techniques and performed on different samples but based on only one experimental technique. This method has many advantages and can be applied on a large panel of crystallizable materials.

Furthermore, based on previous works [23, 60, 64, 65] the temperature dependency of the melting enthalpy was discussed using the Kirchoff's law. As a consequence, the melting enthalpy of the 100% crystalline PEF sample was expressed as a function of the melting temperature. The equilibrium melting enthalpy ΔH_m^0 was then obtained as the melting enthalpy that would be

measured on a 100% crystalline material with a melting temperature equal to the equilibrium melting temperature T_m^0. This improvement of the methods previously described is of great interest as it is a more rigorous approach that take into account the differences in the crystalline fraction perfection degree as well as the differences in the temperature dependencies of the solid and liquid heat capacity curves.

Moreover, RAF formation in 2,5-PEF has been evidenced in FSC and the impact of different parameters (crystallization temperature, crystallization time and sample mass) has been discussed. From the results, it appears that crystallization temperature does not have a significant impact on RAF formation in the studied temperature range. On the other hand, crystallization time and sample mass seems to have a significant effect on the formation of RAF. In this particular crystallization conditions, the parameter which seems to have the most significant effect is the sample size. Thus, it is of uppermost importance to optimize the sample mass depending on the aim of the study, i.e. using a small sample to limit the amount of RAF or a big sample to maximize the amount of RAF.

References

[1] C. Fosse, A. Bourdet, E. Ernault, A. Esposito, N. Delpouve, L. Delbreilh, S. Thiyagarajan, R. J. Knoop, and E. Dargent, "Determination of the equilibrium enthalpy of melting of two-phase semi-crystalline polymers by fast scanning calorimetry," *Thermochimica Acta*, vol. 677, pp. 67–78, July 2019.

[2] R. Chiang and P. J. Flory, "Equilibrium between Crystalline and Amorphous Phases in Polyethylene [1]," *Journal of the American Chemical Society*, vol. 83, pp. 2857–2862, July 1961.

[3] B. Wunderlich and C. M. Cormier, "Heat of fusion of polyethylene," *Journal of Polymer Science Part A-2: Polymer Physics*, vol. 5, pp. 987–988, Sept. 1967.

[4] C. M. L. Atkinson and M. J. Richardson, "Thermodynamic properties of ideally crystalline polyethylene," *Transactions of the Faraday Society*, vol. 65, p. 1764, 1969.

[5] P. Cebe, D. Thomas, J. Merfeld, B. P. Partlow, D. L. Kaplan, R. G. Alamo, A. Wurm, E. Zhuravlev, and C. Schick, "Heat of fusion of polymer crystals by fast scanning calorimetry," *Polymer*, vol. 126, pp. 240–247, Sept. 2017.

[6] F. Danusso and G. Gianotti, "Fusion enthalpy and entropy of isotactic polypropylene," *European Polymer Journal*, vol. 4, pp. 165–171, Feb. 1968.

[7] R. Dedeurwaerder and J. F. M. Oth, "Enthalpie et entropie de fusion du polystyrolène isotactique," *Journal de Chimie Physique*, vol. 56, pp. 940–945, 1959.

[8] I. Abu-Isa and M. Dole, "Specific Heat of Synthetic High Polymers. XII. Atactic and Isotactic Polystyrene [1]," *The Journal of Physical Chemistry*, vol. 69, pp. 2668–2675, Aug. 1965.

[9] B. Ke, "Characterization of polyolefins by differential thermal analysis," *Journal of Polymer Science*, vol. 42, pp. 15–23, Jan. 1960.

[10] R. W. Wilkinson and M. Dole, "Specific heat of synthetic high polymers. X. Isotactic and atactic polypropylene," *Journal of Polymer Science*, vol. 58, pp. 1089–1106, Apr. 1962.

[11] E. Passaglia and H. K. Kevorkian, "Specific Heat of Atactic and Isotactic Polypropylene and the Entropy of the Glass," *Journal of Applied Physics*, vol. 34, pp. 90–97, Jan. 1963.

[12] J. Fatou, "Melting temperature and enthalpy of isotactic polypropylene," *European Polymer Journal*, vol. 7, pp. 1057–1064, Aug. 1971.

[13] P. Marx, C. W. Smith, A. E. Worthington, and M. Dole, "Specific Heat of Synthetic High Polymers. IV. Polycaprolactam.," *The Journal of Physical Chemistry*, vol. 59, pp. 1015–1019, Oct. 1955.

[14] S. Gogolewski and A. Pennings, "Crystallization of polyamides under elevated pressure: 2. Pressure-induced crystallization of nylon-6 (polycapramide) from the melt," *Polymer*, vol. 16, pp. 673–679, Sept. 1975.

[15] B. Wunderlich, *Thermal analysis of polymeric materials*. Berlin: Springer, 2005. OCLC: 262680683.

[16] H. F. Mark, ed., *Encyclopedia of polymer science and engineering. Suppl. Vol.. [Zur 2. Aufl.]: Acid base interactions to vinyl chloride polymers*. A Wiley Interscience publication, New York: Wiley, 1989. OCLC: 247222633.

[17] A. Conix and R. Van Kerpel, "Crystallization behavior and melting properties of m-phenylene group containing polyesters," *Journal of Polymer Science*, vol. 40, pp. 521–532, Nov. 1959.

[18] K. H. Illers, "Heat of fusion and specific volume of poly(ethylene terephthalate) and poly(butylene terephthalate," *Colloid and Polymer Science*, vol. 258, pp. 117–124, Feb. 1980.

[19] T. Miyata and T. Masuko, "Crystallization behaviour of poly(l-lactide)," *Polymer*, vol. 39, pp. 5515–5521, Oct. 1998.

[20] M. Pyda, R. Bopp, and B. Wunderlich, "Heat capacity of poly(lactic acid)," *The Journal of Chemical Thermodynamics*, vol. 36, pp. 731–742, Sept. 2004.

[21] P. Badrinarayanan, K. B. Dowdy, and M. R. Kessler, "A comparison of crystallization behavior for melt and cold crystallized poly (l-Lactide) using rapid scanning rate calorimetry," *Polymer*, vol. 51, pp. 4611–4618, Sept. 2010.

[22] J. P. Kalish, K. Aou, X. Yang, and S. L. Hsu, "Spectroscopic and thermal analyses of alpha' and alpha crystalline forms of poly(l-lactic acid)," *Polymer*, vol. 52, pp. 814–821, Feb. 2011.

[23] M. C. Righetti, M. Gazzano, M. L. Di Lorenzo, and R. Androsch, "Enthalpy of melting of alpha'- and alpha-crystals of poly(l-lactic acid)," *European Polymer Journal*, vol. 70, pp. 215–220, Sept. 2015.

[24] S. Z. D. Cheng, Z. Q. Wu, and B. Wunderlich, "Glass transition and melting behavior of poly(thio-1,4-phenylene)," *Macromolecules*, vol. 20, pp. 2802–2810, Nov. 1987.

[25] P. Huo and P. Cebe, "Effects of thermal history on the rigid amorphous phase in poly(phenylene sulfide)," *Colloid and Polymer Science*, vol. 270, pp. 840–852, Sept. 1992.

[26] G. Z. Papageorgiou, V. Tsanaktsis, and D. N. Bikiaris, "Synthesis of poly(ethylene furandicarboxylate) polyester using monomers derived from renewable resources: thermal behavior comparison with PET and PEN," *Phys. Chem. Chem. Phys.*, vol. 16, no. 17, pp. 7946–7958, 2014.

[27] G. Stoclet, G. Gobius du Sart, B. Yeniad, S. de Vos, and J. Lefebvre, "Isothermal crystallization and structural characterization of poly(ethylene-2,5-furanoate)," *Polymer*, vol. 72, pp. 165–176, Aug. 2015.

[28] J. G. van Berkel, N. Guigo, J. J. Kolstad, L. Sipos, B. Wang, M. A. Dam, and N. Sbirrazzuoli, "Isothermal Crystallization Kinetics of Poly (Ethylene 2,5-Furandicarboxylate): Isothermal Crystallization Kinetics of Poly (Ethylene 2,5-Furandicarboxylate)," *Macromolecular Materials and Engineering*, vol. 300, pp. 466–474, Apr. 2015.

[29] G. Z. Papageorgiou, V. Tsanaktsis, D. G. Papageorgiou, S. Exarhopoulos, M. Papageorgiou, and D. N. Bikiaris, "Evaluation of polyesters from renewable resources as alternatives to the current fossil-based polymers. Phase transitions of poly(butylene 2,5-furandicarboxylate)," *Polymer*, vol. 55, pp. 3846–3858, Aug. 2014.

[30] Y. Kong and J. Hay, "The measurement of the crystallinity of polymers by DSC," *Polymer*, vol. 43, pp. 3873–3878, June 2002.

[31] A. Toda, R. Androsch, and C. Schick, "Insights into polymer crystallization and melting from fast scanning chip calorimetry," *Polymer*, vol. 91, pp. 239–263, May 2016.

[32] A. A. Minakov, D. A. Mordvintsev, and C. Schick, "Melting and reorganization of poly(ethylene terephthalate) on fast heating (1000 K/s)," *Polymer*, vol. 45, pp. 3755–3763, May 2004.

[33] S. Adamovsky, A. Minakov, and C. Schick, "Scanning microcalorimetry at high cooling rate," *Thermochimica Acta*, vol. 403, pp. 55–63, June 2003.

[34] F. De Santis, S. Adamovsky, G. Titomanlio, and C. Schick, "Scanning Nanocalorimetry at High Cooling Rate of Isotactic Polypropylene," *Macromolecules*, vol. 39, pp. 2562–2567, Apr. 2006.

[35] A. Esposito, N. Delpouve, V. Causin, A. Dhotel, L. Delbreilh, and E. Dargent, "From a Three-Phase Model to a Continuous Description of Molecular Mobility in Semicrystalline Poly(hydroxybutyrate- *co* -hydroxyvalerate)," *Macromolecules*, vol. 49, pp. 4850–4861, July 2016.

[36] M. L. Di Lorenzo and M. C. Righetti, "The three-phase structure of isotactic poly(1-butene)," *Polymer*, vol. 49, pp. 1323–1331, Mar. 2008.

[37] Q. Ma, G. Georgiev, and P. Cebe, "Constraints in semicrystalline polymers: Using quasi-isothermal analysis to investigate the mechanisms of formation and loss of the rigid amorphous fraction," *Polymer*, vol. 52, pp. 4562–4570, Sept. 2011.

[38] W. Ruland, "The separation of coherent and incoherent Compton X-ray scattering," *Br. J. Appl. Phys.*, vol. 15, pp. 1301–1307, Nov. 1964.

[39] M. Pyda, A. Boller, J. Grebowicz, H. Chuah, B. V. Lebedev, and B. Wunderlich, "Heat capacity of poly(trimethylene terephthalate)," *Journal of Polymer Science Part B: Polymer Physics*, vol. 36, pp. 2499–2511, Oct. 1998.

[40] P. Cebe, X. Hu, D. L. Kaplan, E. Zhuravlev, A. Wurm, D. Arbeiter, and C. Schick, "Beating the Heat - Fast Scanning Melts Silk Beta Sheet Crystals," *Scientific Reports*, vol. 3, Dec. 2013.

[41] Y. Corvis, A. Wurm, C. Schick, and P. Espeau, "Vitreous State Characterization of Pharmaceutical Compounds Degrading upon Melting by Using Fast Scanning Calorimetry," *The Journal of Physical Chemistry B*, vol. 119, pp. 6848–6851, June 2015.

[42] S. Thiyagarajan, W. Vogelzang, R. J. I. Knoop, A. E. Frissen, J. van Haveren, and D. S. van Es, "Biobased furandicarboxylic acids (FDCAs): effects of isomeric substitution on polyester synthesis and properties," *Green Chem.*, vol. 16, no. 4, pp. 1957–1966, 2014.

[43] S. F. Nassar, S. Domenek, A. Guinault, G. Stoclet, N. Delpouve, and C. Sollogoub, "Structural and Dynamic Heterogeneity in the Amorphous Phase of Poly(l, l-lactide) Confined at the Nanoscale by the Coextrusion Process," *Macromolecules*, vol. 51, pp. 128–136, Jan. 2018.

[44] J. Zhang, Y. Duan, H. Sato, H. Tsuji, I. Noda, S. Yan, and Y. Ozaki, "Crystal Modifications and Thermal Behavior of Poly(l-lactic acid) Revealed by Infrared Spectroscopy," *Macromolecules*, vol. 38, pp. 8012–8021, Sept. 2005.

[45] L. Martino, N. Guigo, J. G. van Berkel, J. J. Kolstad, and N. Sbirrazzuoli, "Nucleation and Self-Nucleation of Bio-Based Poly(ethylene 2,5-furandicarboxylate) Probed by Fast Scanning Calorimetry," *Macromolecular Materials and Engineering*, vol. 301, pp. 586–596, May 2016.

[46] J. Ma, X. Yu, J. Xu, and Y. Pang, "Synthesis and crystallinity of poly(butylene 2,5-furandicarboxylate)," *Polymer*, vol. 53, pp. 4145–4151, Aug. 2012.

[47] A. Toda, K. Taguchi, G. Kono, and K. Nozaki, "Crystallization and melting behaviors of poly(vinylidene fluoride) examined by fast-scan calorimetry: Hoffman-Weeks, Gibbs-Thomson and thermal Gibbs-Thomson plots," *Polymer*, vol. 169, pp. 11–20, Apr. 2019.

[48] N. S. Murthy, S. T. Correale, and H. Minor, "Structure of the amorphous phase in crystallizable polymers: poly(ethylene terephthalate)," *Macromolecules*, vol. 24, pp. 1185–1189, Sept. 1991.

[49] J. F. Mano, "Structural evolution of the amorphous phase during crystallization of poly(l-lactic acid): A synchrotron wide-angle X-ray scattering study," *Journal of Non-Crystalline Solids*, vol. 353, pp. 2567–2572, Aug. 2007.

[50] N. Murthy and H. Minor, "General procedure for evaluating amorphous scattering and crystallinity from X-ray diffraction scans of semicrystalline polymers," *Polymer*, vol. 31, pp. 996–1002, June 1990.

[51] R. Androsch and B. Wunderlich, "The link between rigid amorphous fraction and crystal perfection in cold-crystallized poly(ethylene terephthalate)," *Polymer*, vol. 46, pp. 12556–12566, Dec. 2005.

[52] J. D. Hoffman, "Regime III crystallization in melt-crystallized polymers: The variable cluster model of chain folding," *Polymer*, vol. 24, pp. 3–26, Jan. 1983.

[53] I. Okazaki and B. Wunderlich, "Modulated differential scanning calorimetry in the glass transition region, V. activation energies and relaxation times of poly(ethylene terephthalate)s," *Journal of Polymer Science Part B: Polymer Physics*, vol. 34, pp. 2941–2952, Dec. 1996.

[54] C. Schick and V. Mathot, eds., *Fast Scanning Calorimetry*. Cham: Springer International Publishing, 2016.

[55] A. Melnikov, M. Rosenthal, A. Rodygin, D. Doblas, D. Anokhin, M. Burghammer, and D. Ivanov, "Re-exploring the double-melting behavior of semirigid-chain polymers with an in-situ combination of synchrotron nano-focus X-ray scattering and nanocalorimetry," *European Polymer Journal*, vol. 81, pp. 598–606, Aug. 2016.

[56] M. van Drongelen, T. Meijer-Vissers, D. Cavallo, G. Portale, G. V. Poel, and R. Androsch, "Microfocus wide-angle X-ray scattering of polymers crystallized in a fast scanning chip calorimeter," *Thermochimica Acta*, vol. 563, pp. 33–37, July 2013.

[57] "Simultaneous Synchrotron WAXD and Fast Scanning (Chip) Calorimetry: On the (Isothermal) Crystallization of HDPE and PA11 at High Supercoolings and Cooling Rates up to 200 $^{\circ}c.s{-}1$, volume = 36, issn = 10221336, shorttitle = Simultaneous Synchrotron WAXD and Fast Scanning (Chip) Calorimetry, url = http://doi.wiley.com/10.1002/marc.201500081, doi = 10.1002/marc.201500081, language = en, number = 12, urldate = 2018-11-26, journal = Macromolecular Rapid Communications, author = Baeten, Dorien and Mathot, Vincent B. F. and Pijpers, Thijs F. J. and Verkinderen, Olivier and Portale, Giuseppe and Van Puyvelde, Peter and Goderis, Bart, month = jun, year = 2015, pages = 1184–1191,"

[58] J. D. Hoffman, G. T. Davis, and J. I. Lauritzen, *The Rate of Crystallization of Linear Polymers with Chain Folding*, pp. 497–614. Boston, MA: Springer US, 1976.

[59] M. C. Righetti, P. Marchese, M. Vannini, A. Celli, C. Lorenzetti, D. Cavallo, C. Ocando, A. J. Müller, and R. Androsch, "Polymorphism and Multiple Melting Behavior of Bio-Based Poly(propylene 2,5-furandicarboxylate)," *Biomacromolecules*, p. acs.biomac.0c00039, Apr. 2020.

[60] R. Séguéla, "Temperature dependence of the melting enthalpy of poly (ethylene terephthalate) and poly(aryl-ether-ether-ketone)," *Polymer*, vol. 34, pp. 1761–1764, Apr. 1993.

[61] C. A. Johnson, "Generalization of the Gibbs-Thomson equation," *Surface Science*, vol. 3, pp. 429–444, Dec. 1965.

[62] J. Hoffman and J. Weeks, "Melting process and the equilibrium melting temperature of polychlorotrifluoroethylene," *Journal of research of the national bureau of standards-A, Physics and Chemistry*, vol. 66A, Jan. 1961.

[63] V. Mathot, "Temperature dependence of some thermodynamic functions for amorphous and semi-crystalline polymers," *Polymer*, vol. 25, pp. 579–599, May 1984.

[64] B. Wunderlich and G. Czornyj, "A Study of Equilibrium Melting of Polyethylene," *Macromolecules*, vol. 10, pp. 906–913, Sept. 1977.

[65] D. Blundell, D. Beckett, and P. Willcocks, "Routine crystallinity measurements of polymers by d.s.c.," *Polymer*, vol. 22, pp. 704–707, May 1981.

[66] R. Purohit and P. Venugopalan, "Polymorphism: An overview," *Reson*, vol. 14, pp. 882–893, Sept. 2009.

[67] R. J. I. Knoop, W. Vogelzang, J. van Haveren, and D. S. van Es, "High molecular weight poly(ethylene-2,5-furanoate); critical aspects in synthesis and mechanical property determination," *J. Polym. Sci. Part A: Polym. Chem.*, vol. 51, pp. 4191–4199, Oct. 2013.

[68] A. Codou, N. Guigo, J. van Berkel, E. de Jong, and N. Sbirrazzuoli, "Non-isothermal Crystallization Kinetics of Biobased Poly(ethylene 2,5-furandicarboxylate) Synthesized via the Direct Esterification Process," *Macromol. Chem. Phys.*, vol. 215, pp. 2065–2074, Nov. 2014.

[69] B. Wunderlich, "Reversible crystallization and the rigid–amorphous phase in semicrystalline macromolecules," *Progress in Polymer Science*, vol. 28, pp. 383–450, Mar. 2003.

[70] M. C. Righetti and E. Tombari, "Crystalline, mobile amorphous and rigid amorphous fractions in poly(L-lactic acid) by TMDSC," *Thermochimica Acta*, vol. 522, pp. 118–127, Aug. 2011.

[71] C. Schick, A. Wurm, and A. Mohamed, "Vitrification and devitrification of the rigid amorphous fraction of semicrystalline polymers revealed from frequency-dependent heat capacity," *Colloid & Polymer Science*, vol. 279, pp. 800–806, Aug. 2001.

[72] H. Chen and P. Cebe, "Vitrification and Devitrification of Rigid Amorphous Fraction of PET during Quasi-Isothermal Cooling and Heating," *Macromolecules*, vol. 42, pp. 288–292, Jan. 2009.

Chapter 4

Effect of co-monomer content and nature on the semi-crystalline microstructures of Polyhydroxyalkanoates samples

Contents

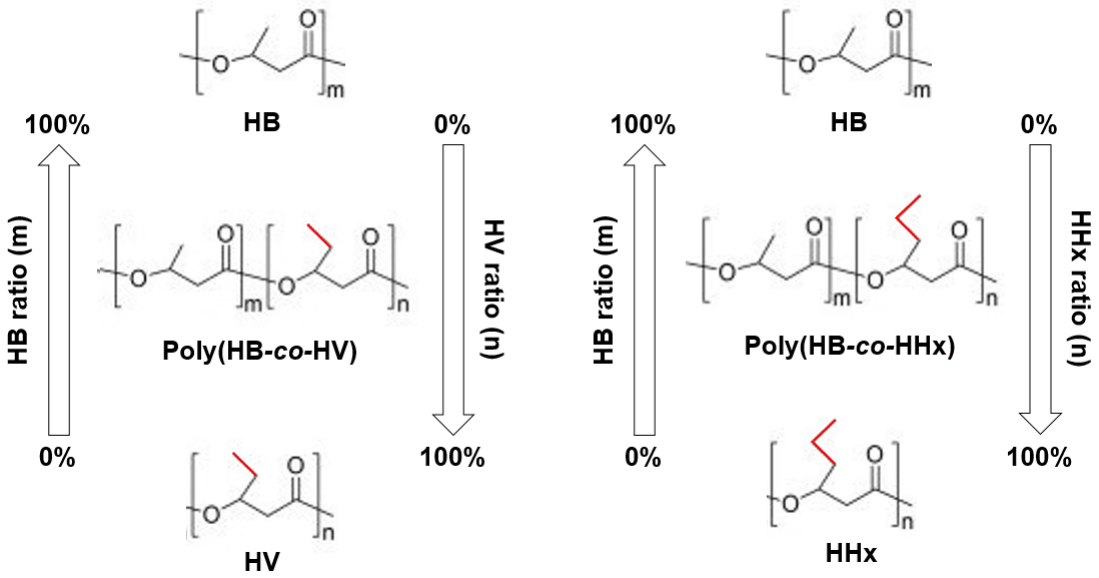

Figure 4.1: Schematic depiction of the copolymers investigated in this work, four of them are poly(HB-*co*-HV) copolymers (containing respectively n=3mol%,n=15mol%, n=23mol% and n=27mol%) and the four others are poly(HB-*co*-HHx) copolymers (containing respectively n=3mol%,n=8mol%, n=12mol% and n=35mol%).

Because of the growing interest for sustainable alternatives to fossil resources, biopolymers have recently become the focus of numerous investigations. Among all the available biopolymers, polyhydroxyalkanoates (PHAs) are particularly promising for their behavior can be tuned by controlling the content and nature of the monomers involved in the biosynthesis [1, 2] . Currently, poly(3-hydoxybutyrate) (PHB) is the most studied homopolyester but this polymer suffers from high crystallinity degrees concerns, which makes its processability rather complicated. This issue can be overcome by decreasing the crystallinity degree through the incorporation of different monomers such as hydroxyvalerate (HV) or hydroxyhexanoate (HHx). The resulting copolyesters have enhanced properties that can be finely tuned to fit a broader range of applications. As shown in Figure 4.1, the HV and HHx monomer units bear longer carboned side-groups as compared to the HB monomer unit; the HV monomer unit is one carbon longer whereas the HHx one is two carbon longer. Therefore, one may expect assumed that the copolymerization of HB co-monomer and HV or HHx co-monomer units leads to an increase in the free volume as a result of an increase in the side-group length. However, the effects of the chemical composition and arrangement of the repeating units on the microstructural properties of PHAs are not yet fully explored and understood, and further investigations are required to reveal their potentiality for future applications.

The aim of this chapter is to investigate the effects of the co-monomer unit content and nature on the microstructural properties of a series of PHA copolymers. To this purpose, eight PHA copolymers containing different amounts of HV or HHx co-monomer units (samples are listed in section 2.1.3) were characterized. First, the impact of the co-monomer content and nature on the crystallizability of the copolymers is investigated through modulated temperature differential scanning calorimetry (MT-DSC) and wide-angle X-Ray diffraction (WAXD).

Then, MT-DSC and dielectric relaxation spectroscopy (DRS) experiments were carried out to evaluate the impact of the co-monomer content and nature on the molecular mobility in the amorphous phase. Finally, MT-DSC, DRS and WAXD experiments were conducted to investigate how the co-monomer content/nature affects the semi-crystalline microstructures and the coupling between phases.

4.1 Crystallization and crystalline phase

Figure 4.2(a) shows the Total Heat Flow recorded by MT-DSC with an overall heating rate of 2 $K.min^{-1}$ after the *Quenching* protocol. All the samples display a well-defined glass transition in the temperature range between -10°C and 10°C, followed by cold crystallization. The cold crystallization temperature T_{cc} as well as the width of the glass transition peak δT_{cc} have been extracted from Figure 4.2 and are reported in Table 4.1. The cold-crystallization temperature range previously measured for the reference homopolymer poly(hydroxybutyrate) (PHB) (20-50°C according to [3]) is strictly maintained only if the content of co-monomer units is limited to 23 mol % in the case of hydroxyvalerate (HV), and 8 mol % in the case of hydroxyhexanoate (HHx). Not only the position, but also the shape of the cold-crystallization peak strongly depend on the nature of the co-monomer unit. As the degree of co-monomerization increases, the cold-crystallization peak is generally shifted to higher temperatures. This shift is more significant with the HHx co-monomer units as compared to the HV co-monomers units. Also the width of the cold-crystallization peak is much more affected by the presence of the HHx co-monomer units as compared to the HV co-monomer units.

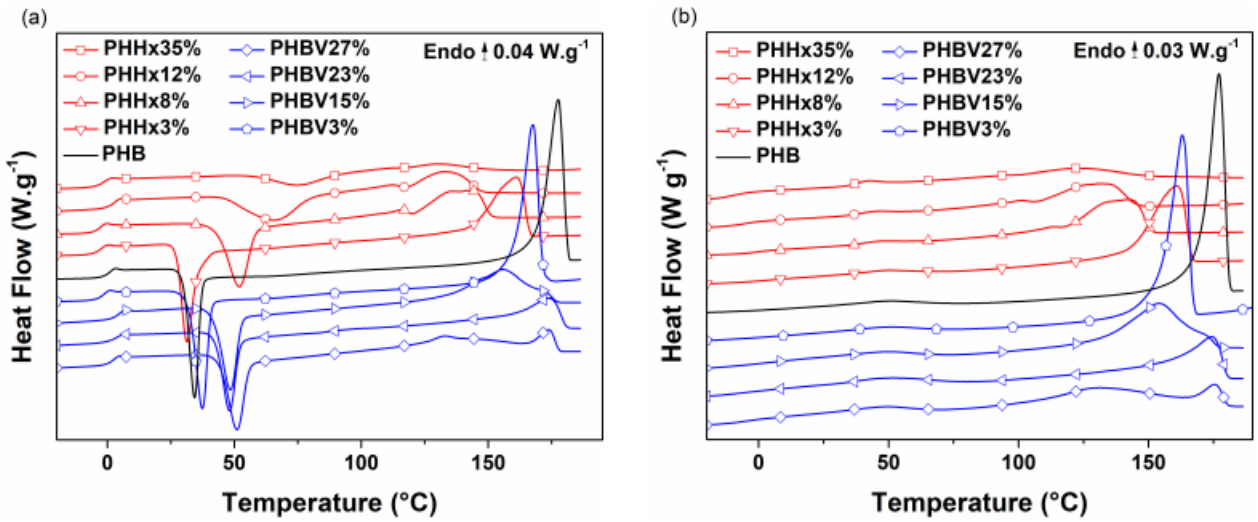

Figure 4.2: Total Heat Flow recorded by MT-DSC at 2 $Kmin^{-1}$, with an amplitude of a=±0.32K and a period of 60s, on the considered PHA samples ((HB-*co*-HV) copolymers with 3, 15, 23 and 27 mol % HV, and (HB-*co*-HHx) copolymers with 3, 8, 12 and 35 mol % HHx) after (a) *Quenching* and (b) *Crystallization from the glassy state* for $t_c = 1440min$. The curves obtained for the reference homopolymer PHB, after the same thermal treatments and in the same experimental conditions, are also shown for comparison.

The values reported in Table 4.1 clearly show how the presence of the co-monomer units delays (and sometimes considerably slows down) the cold-crystal- lization process. At the highest

extent, the temperature at which cold crystallization starts ($T_{cc,min}$) is shifted by 15°C in the (HB-*co*-HV) system containing 27 mol % HV, and 30°C in the (HB-*co*-HHx) system containing 35 mol % HHx, compared to the reference homopolymer PHB. The temperature range covered by the cold-crystallization process becomes wider as the content of HHx co-monomer units increases ($\delta T_{cc} = 46$°C in PHHx 35 mol %), whereas no significant differences are observed as a function of the content of HV co-monomer units ($\delta T_{cc} = 25$°C for all the (HB-*co*-HV) systems). On a whole, with both the co-monomer units, the width of the cold- crystallization peak is higher as compared to the $\delta T_{cc} = 17$°C observed for the reference homopolymer PHB.

Table 4.1: Characteristics of cold crystallization obtained from Figure 4.2 (as compared to PHB) along with the crystallinity degrees obtained by WAXD ($X_{C,WAXD}$) on (HB-co-HV) copolymers with 3, 15, 23 and 27% HV as well as on (HB-co-HHx) copolymers with 3, 8, 12 and 35% HHx after crystallization from the glass (Figure 4.2 (b)). The average size of the crystalline domains was estimated by Scherrer's equation [4] perpendicularly to the (020) and (110) crystallographic planes (K=1 on the hypothesis that there is no preferential crystal orientation and $\lambda = 2.29$Å).

SAMPLE	$T_{cc,min}$ ±1 [°C]	δT_{cc} ±1 [°C]	$X_{c,WAXD}$ [± 5%]	$(size)_{020}$ ±1 [nm]	$(size)_{010}$ ±1 [nm]
PHB	23	17	n.d	n.d	n.d
PHBV3%	23	22	50	30	25
PHBV15%	33	25	43	25	22
PHBV23%	35	25	36	28	17
PHBV27%	38	25	43	12	6
PHHx3%	23	22	44	18	18
PHHx8%	33	30	39	19	20
PHHx12%	40	44	42	13	11
PHHx35%	53	46	27	17	15

Esposito et al.[5] recently provided an explanation for the progressive embrittlement observed in PHBV 3 mol % stored at room temperature ($T_{room} > T_g$) after melt processing, even for samples crystallized to the maximum possible extent, and especially when crystallization is achieved from a fully amorphous glassy state. They observed a progressive rigidification (decrease in molecular mobility and increase in relaxation time) of the amorphous phase surrounding the crystalline lamellae, with the mobile amorphous fraction (MAF) gradually converting into rigid amorphous fraction (RAF). They described this phenomenon as a "continuum of mobility", characterized by a distribution of the relaxation times that is progressively modified. The shift of $T_{cc,min}$ to higher temperatures and the concomitant broadening of the cold-crystallization peak (increase in δT_{cc}), which are particularly relevant in the (HB-*co*-HHx) copolymers, suggest that the nature and content of co-monomer units significantly modifies the molecular mobility at T > T_g. Thus, it is reasonable to assume that different microstructures with different thermal stabilities can be obtained through copolymerization. This observation is confirmed by the complex sequence of endothermic phenomena observed at higher temperature, likely corresponding to the melting phenomena, which suggests that in most samples a massive crystalline reorganization occurs during the heating ramp; the extent of such a reorganization seems to increase with the content of co-monomer units. The presence of different repeating units

disrupt crystallization; during cold-crystallization, most of the samples grow highly defective crystalline domains, with thin and unevenly distributed crystalline lamellae; in the (HB-*co*-HHx) system with 35 mol % HHx co-monomer units, cold-crystallization and the subsequent melting phenomena are barely detectable.

Figure 4.2(b) shows the Total Heat Flow recorded by MT-DSC with an overall heating rate of 2 $K.min^{-1}$ after *Crystallization from the glassy state* for a duration of t_c = 1440min (see section 2.1.4 for further details about the protocols). As expected, the glass transition is hardly noticeable, which indicates that (1) the fraction of mobile amorphous polymer chains is dramatically reduced because a considerable portion of the sample is crystallized [5, 6], and/or (2) the temperature range over which the glass transition occurs is dramatically broadened by the presence of the crystalline domains, which constrain the molecular mobility in the amorphous phase by geometrical confinement [5, 7].

Figures 4.2 (a) and (b) are interesting to discuss, for their comparison allows pointing out how difficult it can be to characterize complex semi-crystalline microstructures that are thermally unstable because generated in quite unfavorable conditions. The massive crystalline reorganization detected after quenching (i.e. on a microstructure that develops concomitantly with the measuring heating ramp) is also observed after crystallization from the glassy state (i.e. on a microstructure that was first developed by isothermal crystallization at relatively low temperature and then measured upon heating). Estimating the crystallinity degree by integrating the DSC curves recorded with a low overall heating rates within a given temperature range ($T_1 - T_2$) and then dividing by the enthalpy of melting of 100% crystalline PHB at the equilibrium melting temperature (ΔH_m^0) would be, in this case, senseless.

First of all, the choice of the temperature range for integration is tricky because crystalline reorganization also affects the signal baseline. According to the literature [6, 8], the integration should always be done starting from the lowest temperature at which an excess heat capacity is observed that modifies the expected temperature dependence of the heat capacity, and stopping at a temperature above the completion of melting. When polymers are prone to crystalline reorganization, an excess heat capacity appears as soon as surface melting starts at the boundaries between the crystals and the surrounding amorphous fractions (reversing melting) [6, 9]. From a practical point of view, the consequence is that the baseline starts to deviate at temperatures well below the commonly admitted range of non-reversing melting. Such a thermodynamic excess is then gradually building up as melting progresses through the entire volume of crystallized material.

Besides, the choice of the value of reference enthalpy to calculate the crystallinity degree in PHB-based copolymers is also questionable. Many authors use the value reported for PHB (ΔH_m^0=146 $J.g^-1$) [10, 11]. This assumption is acceptable when the degree of copolymeriza-

tion is relatively low, as in the case of PHBV 3 mol % [5], and sometimes necessary because the information is not available for all the existing copolymers, as in the case of the (HB-*co*-HHx) copolymers [12]. However, the value of ΔH_m^0 for PHB-based copolymers may significantly change as a function of the degree of copolymerization, as illustrated by Scandola et al. [13] in the case of (HB-*co*-HV) copolymers. For all of these reasons, Table 4.1 only reports the values of cristallinity degrees obtained by WAXD ($X_{c,WAXD}$). Further investigations are required to estimate the value of ΔH_m^0 to be used for each polymer system (according to the protocols discussed in Chapter 3) and then calculate the crystallinity degree based on experimental curves leaving no place to crystalline reorganization upon melting (e.g. FSC scans).

Figure 4.3 shows the WAXD patterns recorded at room temperature (25°C) after *Crystallization from the glassy state* for 1440 minutes. According to the crystallographic description reported by Yokouchi et al. [14], PHB chains settle in the orthorhombic lattice by aligning to the *c* direction, and folds in the perpendicular plane (001). As previously found for cold-crystallized PHBV 3 mol% [5], two main peaks corresponding to the (020) and the (110) crystallographic planes ($2\theta = 13°$ and 16.7° respectively) of the orthorhombic crystal lattice are observed in all the samples [14, 15, 16]. This evidence is in agreement with the results previously reported by Scandola et al. [13]. In their study, they showed that in PHBV random copolymers the HB lattice accommodates the HV units for HV contents up to 34 mol %. This behavior seems to be verified also in PHHx random copolymers, nevertheless to the best of our knowledge it has not yet been reported in the literature.

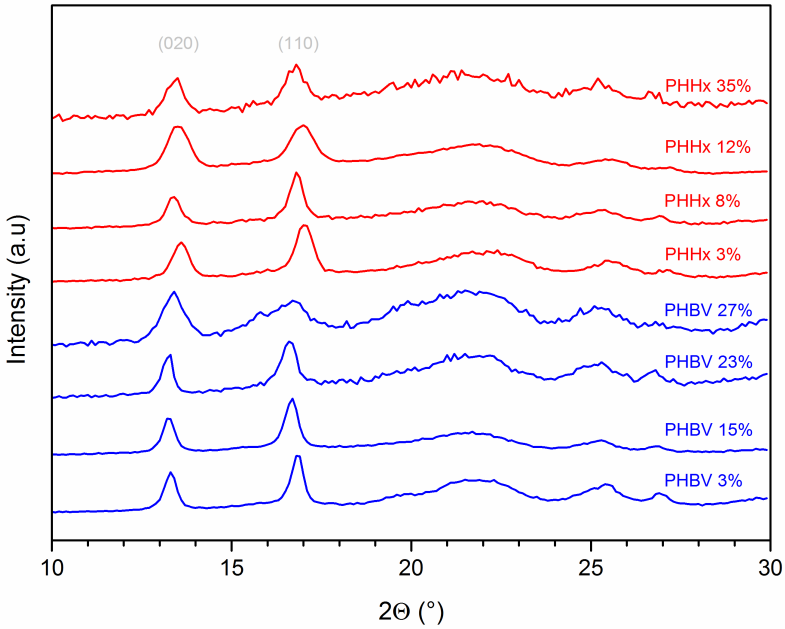

Figure 4.3: WAXD patterns recorded at room temperature (25°C) after crystallization from the glass (section 2.1.4) on (HB-co-HHx) copolymers with 3, 8, 12 and 35% HHx, and on (HB-co-HV) copolymers with 3, 15, 23 and 27% HV.

At $2\theta > 20°$ no sharp diffraction peaks are detected, which indicates that the semi-crystalline microstructure is highly defective compared to the WAXD patterns reported in the literature for PHBV 3 mol % isothermally crystallized from the melt [5]. The signal-to-noise ratio, which degrades as the degree of copolymerization increases in both (HB-*co*-HV) and (HB-*co*-HHx) systems, also suggests that the diffracting domains are reduced in size and regularity as the degree of copolymerization increases. Such a modification of the WAXD pattern is a sign of the gradual disruption of the crystalline network associated to the progressive deformation of the crystalline lattice, that cannot properly accommodate segments of polymer chains containing an increasing amount of different co-monomer units. This behavior has already been evidenced by Scandola et al. [13], who found that the co-monomer inclusion in PHBV systems changes both the a and b unit cell dimensions, whereas it has no effect on the c-axis. The consequences are particularly visible on the WAXD pattern recorded for PHBV 27 mol%, where the (020) diffraction peak is significantly reshaped by the inclusion of the co-monomer units, and the (110) diffraction peak appears almost dedoubled. Nonetheless, the (020) and (110) peaks were used to estimate the average size of the crystalline domains responsible for coherent scattering perpendicularly to each crystallographic plane.

The values obtained by the Scherrer's equation [4] for both the selected cristallographic plans are reported in Table 4.1 along with the crystallinity degrees calculated from the WAXD patterns ($X_{c,WAXD}$) with the method based on the ratio of areas. WAXD results show how the overall crystallinity degree decreases with the degree of copolymerization. In particular, the extent of crystalline disruption depends on the nature of the considered co-monomer units. The HHx co-monomer units, which bear a side-group that is only one carbon longer than the side-group in the HV units, have a stronger effect in disrupting the crystallization of the HB repeating units. Indeed, $X_{c,WAXD}$ decreases by almost 20% (from 44 to 27%) when the mol % of HHx repeating units increases from 3 to 35 mol% (11 times), whereas it only decreases by 14% (from 50 to 43%) when the mol % of HV repeating units increases from 3 to 27 mol% (9 times). Copolymerization also fragments the crystals, but only in the (HB-*co*-HV) systems, where the average size of the crystalline domains estimated by the Scherrer's equation for both the (020) and (110) crystallographic planes significantly decreases with the content of HV co-monomer units. In particular, the size of the crystalline domains is divided by 4 perpendiculary to the (110) planes as the HV content increases from 3 to 27 mol %. It is worth pointing out that the values obtained by applying the Scherrer's equation to the diffraction peaks of PHBV 27 mol% may be questionable because of the morphological change of both the considered diffraction peaks. As for the (HB-*co*-HHx) systems, the copolymerization seems to have no significant effects on the size of the crystalline domains.

4.2 Relaxation processes in the amorphous phase

4.2.1 Cooperativity as a measure of the intermolecular interactions

Figures 4.4 (a) and (b) respectively show the Reversing Heat Capacity (RevC_p) signals recorded by MT-DSC on the two series of (HB-*co*-HV) and (HB-*co*-HHx) copolymers after *Quenching* (see section 2.1.4 for further details about the protocols). The reference values of specific heat capacity in the solid and liquid states for PHB are reported from the literature

As previously discussed by Esposito et al. [5] in the case of (HB-*co*-HV) 3 mol%, using the values of solid and liquid heat capacities of PHB to make calculations (two-phase and three-phase models) about PHBV copolymers is reasonable only when the content of HV units is low. Figure 4.4 (a) illustrates how dangerous it could be to make the same assumption for higher degrees of copolymerization, because the experimental curves do not reach the reference $C_{p,liquid}$ line above the glass transition, but rather align to values that decrease as the content of HV co-monomer units increases. The same observation can be made about PHHx, as shown in Figure 4.4 (b), where the dependence of $C_{p,liquid}$ as a function of the content of HHx repeating units seems to be more gradual with respect to the (HB-*co*-HV) systems. Such a dependence was taken into account by using the experimental values of heat capacity obtained for each sample (rather than the "reference" values available for the corresponding homopolymer PHB) to make further calculations.

Besides, both Figures 4.4 (a) and (b) show that all the quenched copolymers in their glassy state contain only mobile (i.e. unconstrained) amorphous polymer chains, and they totally relax in a single-step process corresponding to the glass transition. Being fully amorphous, the quenched samples contain no crystals and therefore none of their amorphous phase is rigid ($X_{MAF} = 1$ whereas $X_c = X_{RAF} = 0$). The curves in Figures 4.4 (a) and (b) were used to obtain Figures 4.4 (c) and (d), respectively. The temperature dependencies of the total Solid Amorphous Fraction (mobile X_{MAF} and rigid X_{RAF}) were obtained as:

$$(X_{MAF} + X_{RAF})_{solid} = 1 - X_{c,WAXD} - \frac{RevC_p(T) - C_{p,solid}(T)}{C_{p,liquid}(T) - C_{p,solid}(T)} \tag{4.1}$$

where $X_{c,WAXD}$ is nil, the RevC_p (T) data are directly extracted from Figure 4.4 (a) or (b), and the reference data for heat capacity, i.e. $C_{p,solid}$ (T) and $C_{p,liquid}$ (T), were obtained experimentally according to the procedure reported by Schick et al. [6]. The curves $(X_{MAF} + X_{RAF})_{solid} = f(T)$ better illustrate the dependence of the glass transition on the degree of copolymerization. The values of glass transition temperature T_g and width of glass transition δT_g are reported in Table 4.2.
In quenched (HB-*co*-HV) copolymers, the glass transition temperature decreases by 5°C as the content of HV repeating units increases by 10 times; however, only the highest degree of copolymerization produces a significant increase in the width of the glass transition (approximately

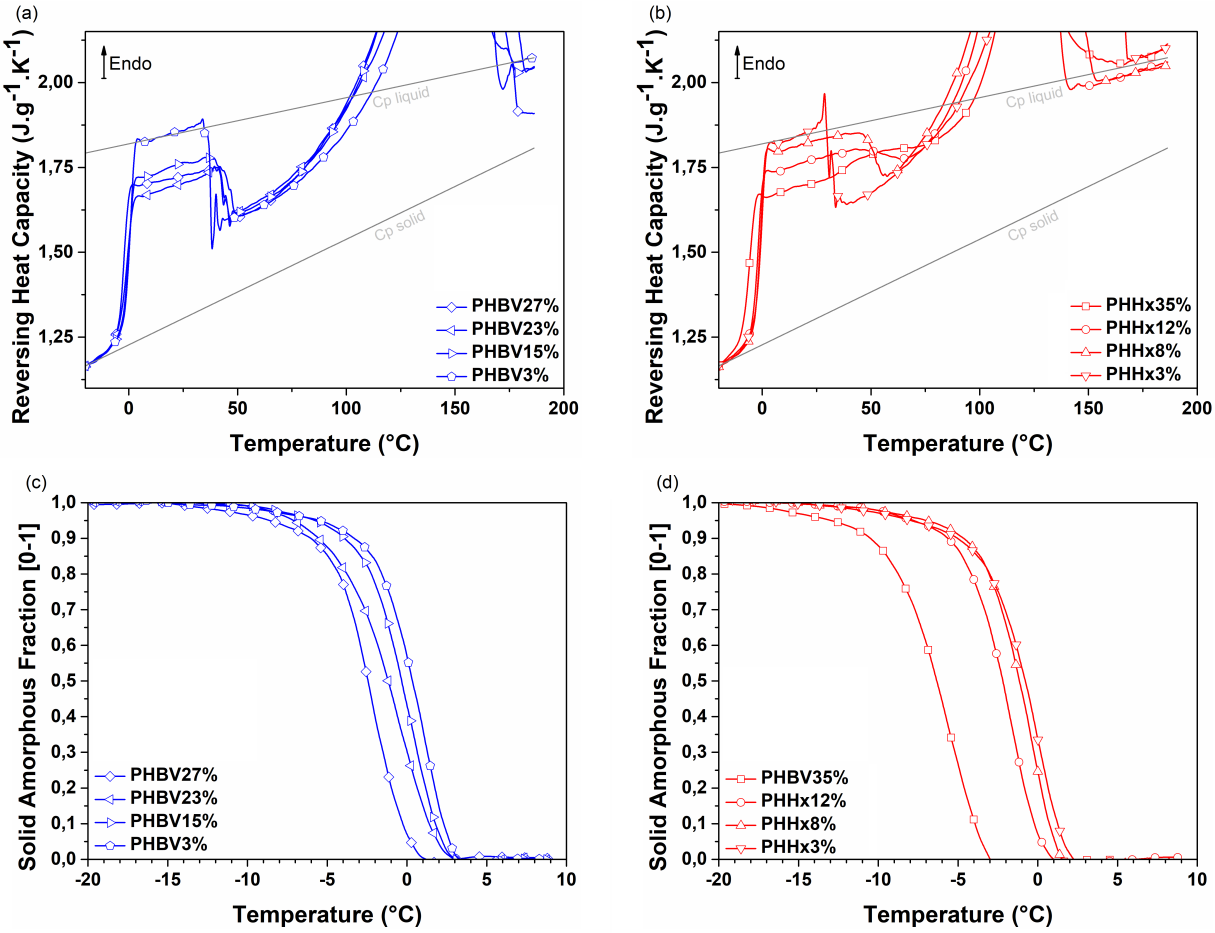

Figure 4.4: Reversing Heat Capacity extracted from MT-DSC signals in Heat-Iso conditions on (a) (HB-*co*-HV) copolymers with 3, 15, 23 and 27 mol% HV and (b) (HB-*co*-HHx) copolymers with 3, 8, 12 and 35 mol% HHx after *Quenching* (more details about the experimental protocol can be found in section 2.1.4 of chapter 2). The reference values of specific heat capacity in the solid and liquid states for PHB are reported from the literature [8]. Temperature dependence of the Solid Amorphous Fraction $(X_{MAF} + X_{RAF})_{solid}$ obtained from the MT-DSC curves (a) and (b) over the glass transition temperature range for the (c) (HB-*co*-HV) copolymers and the (d) (HB-*co*-HHx) copolymers, respectively. At $T < Tg$, $X_C = X_{RAF} = 0$ and $X_{MAF} = 1$.

1°C). In quenched (HB-*co*-HHx) copolymers, a minimum content of 12 mol% HHx repeating units is required to shift the glass transition by 1°C, then a large decrease of the glass transition temperature is observed as the degree of copolymerization triples (-6.3°C for PHHx 35 mol %). Such a dramatic shift of the glass transition temperature is also accompanied by a significant increase in δT_g.

As detailed in Chapter 1 (section 1.2.4), one of the experimental approaches used to evaluate and discuss the molecular mobility at the glass transition temperature is the model developed by Donth et al. [18, 19, 20], based on the concept of Cooperative Rearranging Regions (CRRs) previously introduced by Adam and Gibbs [21]. According to Adam and Gibbs, a CRR is a region that can be defined as the smallest subsystem in which the α-relaxation process occurs independently of the neighboring subsystems. The CRR size is generally estimated through the calculation of the so-called cooperative length ξ_α, which can be obtained experimentally using the following equation:

Table 4.2: Characteristics of molecular mobility at the glass transition for (HB-*co*-HV) copolymers with 3, 15, 23 and 27 mol% HV and (HB-*co*-HHx) copolymers with 3, 8, 12 and 35 mol% HHx after *Quenching* (Figure 4.2 (a)) and *Crystallization from the glassy state* (Figure 4.2 (b)). T_g and δT_g are the glass transition temperature and the width of the glass transition, respectively. ξ_α is the cooperativity length characteristic of the dynamic glass transition estimated with the 16-84% method by Hempel et al. [17]. $\xi_\alpha < 1$ nm for all the (HB-*co*-HV) and (HB-*co*-HHx) copolymers after *Crystallization from the glassy state*. More details about the experimental protocols can be found in section 2.1.4.

	Quenching			**Crystallization from the glassy state**	
SAMPLE	T_g ±1 [°C]	δT_g ±1[°C]	ξ ±0.1 [nm]	T_g ±1 [°C]	δT_g ±1 [°C]
PHB	1	4.2	4.1	n.d	n.d
PHBV3%	0.5	4.3	3.7	5	30
PHBV15%	-0.2	4.5	3.4	5	24
PHBV23%	-1.0	5.5	3.0	5	30
PHBV27%	-2.5	4.5	3.4	5	28
PHHx3%	-1.0	4.5	3.6	7	19
PHHx8%	-1.2	4.0	3.8	5	15
PHHx12%	-2.0	4.3	3.5	0	19
PHHx35%	-6.3	5.2	3.1	-5	12

$$\xi^3_{T\alpha} = \frac{1/(C_{p,solid} - 1/(C_{p,liquid} k_B (T_\alpha)^2}{\rho(\delta T)^2} \tag{4.2}$$

Where $C_{p,solid}$ and $C_{p,liquid}$ are respectively the specific heat capacities in the solid and liquid states extrapolated through glass transition and read at the glass transition temperature, ρ is the polymer density, δT is the temperature fluctuation associated with the dynamic glass transition, and T_α is the average dynamic glass transition temperature. The variations of the CRR size reported in the literature have been generally attributed to (1) chemical and/or physical modifications of the intermolecular interactions [17, 22, 23, 24, 25], or (2) confinement effects [26, 27, 28, 29].

Several studies have reported a correlation between the strength of the intermolecular interactions and the CRR size [23, 26, 30]. For example, in a study on poly(ethylene-vinyl acetate)(EVA) copolymers, Puente et al. [23] showed that a decrease in the vinyl acetate (VAc) content leads to a significant decrease in the CRR size. This finding was attributed to the fact that a decrease in the VAc content leads to a decrease in the dipole density, thus leading to a decrease in the intermolecular interactions.

Recently, Araujo et al. [25] investigated about the cooperativity size and free volume of plasticized poly(L-lactic acid). They showed a direct correlation between the CRR size and the free volume variations, in particular they showed than an increase in free volume leads to a significant decrease in the CRR size. This result is of great interest since the free volume is directly linked to the intermolecular interactions; the literature reports that an increase in the intermolecular interactions leads to a decrease in free volume [23, 25, 31]. Therefore, they assumed

that cooperativity and intermolecular interactions are correlated and that it is a decrease in intermolecular interactions that leads to a decrease in the CRR size in plasticized poly(L-lactic acid).

The literature also reports that CRR size variations can be observed as a consequence of a confinement effect, such as the one introduced by nanoparticles [27], nanolayers [28], intercalated nanocomposites [29] and crystals [32]. In a study on polycarbonate/poly(methylmetacrylate) multilayer films, Arabeche et al.[26] showed that polycarbonate (PC) and poly(methylmetacrylate)(PMMA) have a different sensitivity to the confinement effect due to a reduction of the layer thickness. In PMMA, confinement has a very weak influence on the intermolecular interactions, while it has a strong impact on the intermolecular interactions in PC. As a consequence, the CRR size variations and the associated fluctuations of intermolecular interactions can be impacted by confinement effects.

The cooperativity length ξ_α estimated for the homopolymer PHB as well as for the (HB-*co*-HV) and (HB-*co*-HHx) copolymers are reported in Table 4.2. For both copolymers, the incorporation and increase in the co-monomer content leads to a slight decrease of the cooperativity length. Herein, the cooperativity length slightly decreases as the co-monomer content increases; according to the literature, this could be due either to changes in the intermolecular interactions, or to a confinement effect. In this study, there is no confinement effect that could explain the experimental observations, as the cooperativity length was measured on fully amorphous samples, i.e. neither a crystalline phase nor some geometrical interfaces are present to produce a confinement effect. Thus, the decrease in cooperativity seems to be mainly due to a change in the intermolecular interactions. The same behavior has also been observed in other polymeric systems, such as poly(ethylene-vinyl acetate) copolymers [23].

The decrease of intermolecular interactions can also explain the decrease in the glass transition temperature. Indeed, having less intermolecular interactions generally leads to a higher free volume, which then results in a decrease of the glass transition temperature [23, 25, 31]. This kind of behavior is similar to the plasticizing effect; the presence of co-monomer units in PHAs seems to act as a sort of plasticizer. It is worth pointing out that this effect is more pronounced in the (HB-*co*-HHx) copolymers as compared to the (HB-*co*-HV) copolymers, probably due to the extra carbon atom in the side-chain groups.
Regarding the samples crystallized from the glassy state, it is clearly shown in Table 4.2 that crystallization leads to an important broadening of the glass transition, as well as to a shift of the glass transition temperature to higher temperatures. As reported for other semi-crystalline polymers, this observation can be ascribed to a confinement effect induced by the presence of the crystalline phase. This effect is the most noticeable in PHBV 3 mol%, and both the broadening and shift effects on the glass transition are less marked as the co-monomer content increases and an extra carbon atom is added to the side-chains. The literature reports that

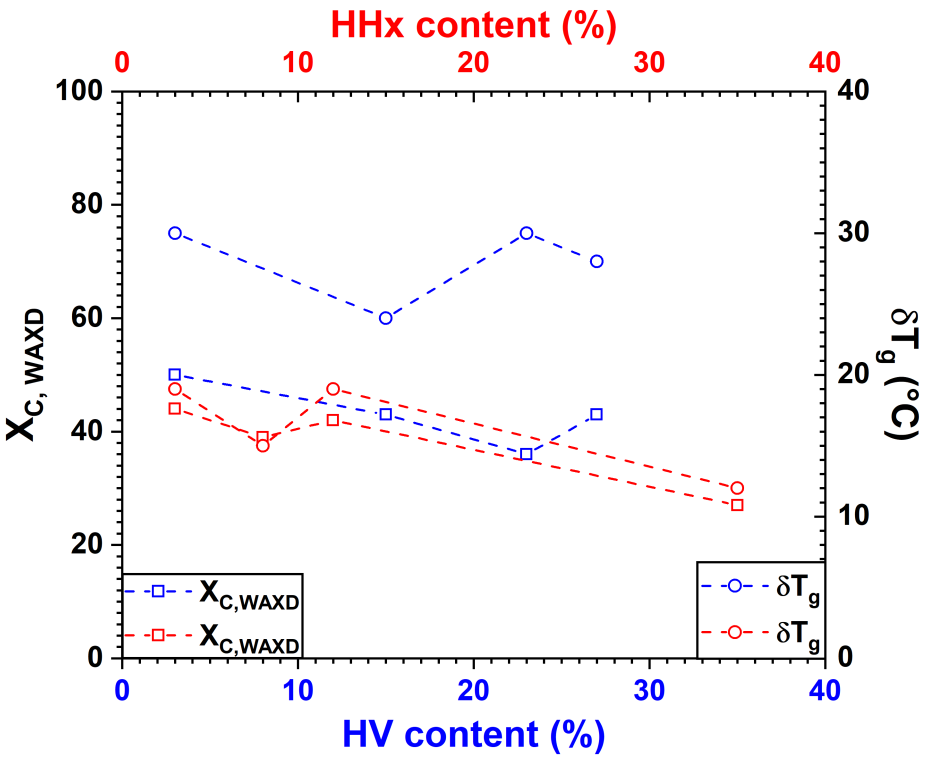

Figure 4.5: $X_{c,WAXD}$ (squares) and δT_g(circles) values measured on the (HB-*co*-HV)(blue) and (HB-*co*-HHx)(red) copolymers crystallized from the glassy state. The dashed lines have been added as a guide for the eye.

crystallization leads to a stronger coupling between phases, which in turns results in an increase in the dynamic heterogeneities; the glass transition, then, appears broadened and shifted to higher temperatures [5, 7, 33]. This work shows that an increase in the co-monomer content, as well as a change in the co-monomer units (from HV to HHx), leads to an overall decrease of the maximum crystallinity degree ($X_{c,WAXD}$). As shown in Figure 4.5, a direct correlation can be made between the maximum crystallinity degree measured by XRD ($X_{c,WAXD}$) and the glass transition width measured by MT-DSC (δT_g); the increase in crystallinity actually corresponds to a broadened glass transition.

4.2.2 Dielectric expression of the molecular interactions

The 3D plots of the dissipative signal (ϵ''(f,T)) of the complex permittivity ($\epsilon*$(f,T)) for the PHB sample after quenching (on the left) and crystallization from the glass (on the right) are presented in Figure 4.6(the 3Dplots of all the other samples are reported in Appendix). Both of them show the main α-relaxation process followed by cold-crystallization in the quenched sample. As expected, the α-relaxation process is less intense in the sample crystallized from the glassy state which clearly indicates the presence of a significant crystalline fraction. Moreover, the α-relaxation process appears broadened and shifted to higher temperatures which can be attributed to the presence of a rigid amorphous fraction [5, 7]

Figure 4.7 displays the relaxation map ($Log_{10}[\tau_{max}] = f(1000/T)$), obtained from DRS measurements in the glass transition temperature range for the samples submitted to *Quenching*.

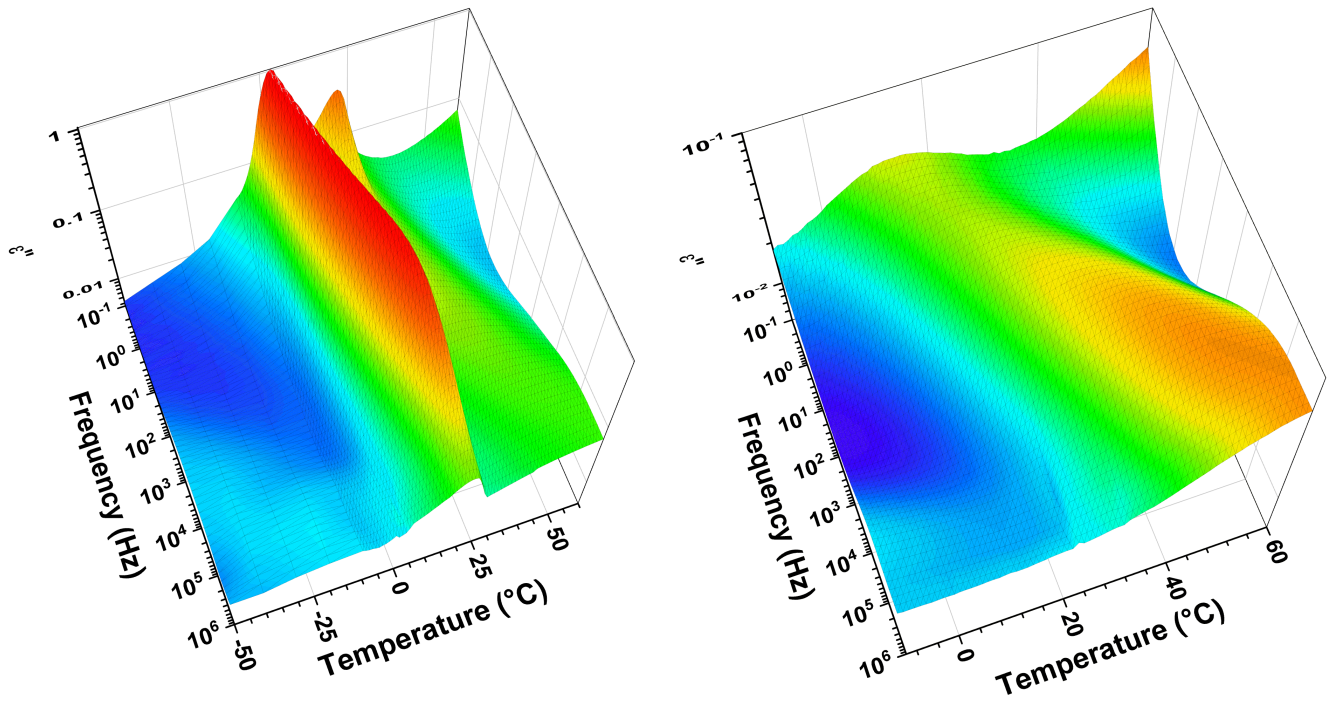

Figure 4.6: Imaginary part of the complex dielectric permittivity vs frequency and temperature for PHB after Quenching (on the left) and Crystallization from the glass (on the right).The 3Dplots of all the other samples are reported in Appendix .

As expected, all the samples show a non-linear dependence of the relaxation times with temperature. As reported in Chapter 1 (section 1.2.3), the Vogel-Tamman-Fulcher (VTF) law was used to fit the plots:

$$\tau_{max} = \tau_0 * exp\left(\frac{DT_0}{T - T_0}\right) \tag{4.3}$$

Where τ_0 is a pre-exponential factor, D is a dimensionless parameter related to the slope variation (a.k.a. "steepness strength"), and T_0 is a reference temperature. The fragility index m was then determined using the equation introduced by Angell [34]:

$$m = \left[\frac{d(log\tau)}{d(\frac{T_g}{T})}\right]_{T=T_g} \tag{4.4}$$

Where T_g is know as the "dielectric glass transition temperature", i.e. the temperature at which a relaxation time of 100s is observed. The values of both T_g(100s) and m are reported in Table **??**. According to Angell's fragility concept [34], small values of m indicate that the temperature dependence of the α-relaxation process follows an Arrhenius-like behavior. The glass-forming liquid is then considered as a "strong" supercooled liquid. Otherwise, when the α-relaxation process follows a non-linear temperature dependence, the glass-forming liquid is considered as "fragile" and the corresponding m value increases. In the literature it has been shown that the fragility index is an important parameter to study the relaxation dynamics of the amorphous phase, as it is strongly influenced by the molecular arrangement of the macro-

molecules [23, 26, 35, 36, 37, 38].

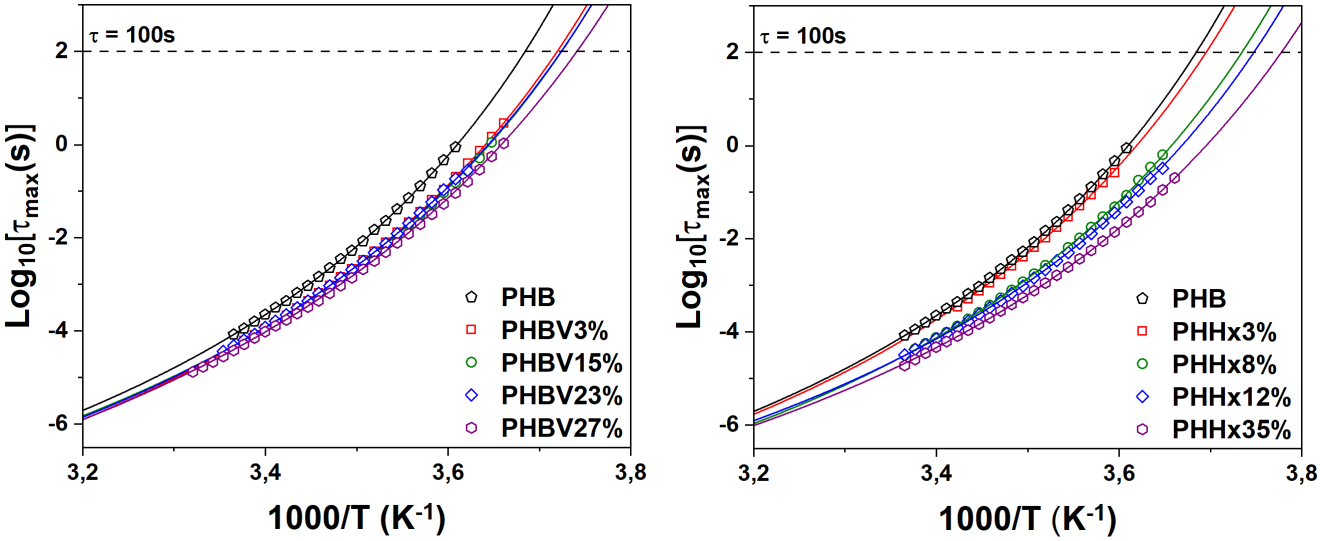

Figure 4.7: Relaxation maps obtained on (HB-*co*-HV) and (HB-*co*-HHx) copolymers after *Quenching*. The solid lines represent the best fit using VFT equation. The fitting curves have been extrapolated to $\tau = 100$s in order to estimate the temperature at which a relaxation time of 100s is observed (T_g (100s)).

The values reported in Table **??** show that, in quenched (HB-*co*-HV) and (HB-*co*-HHx) copolymers, the increase in the co-monomer content results in a decrease in the value of T_g (100s). In particular, for quenched (HB-*co*-HV) copolymers, the dielectric glass transition temperature decreases by only 3°C when the content of HV repeating units is multiplied by 10; however, in the case of quenched (HB-*co*-HHx) copolymers, the dielectric glass transition temperature decreases by 7°C when the amount of HHx repeating units increases by 10. This finding suggests that increasing the amount of HHx repeating units has a slightly stronger effect on the value of T_g (100s) as compared to the HV repeating units.

As pointed out in recent studies, the fragility index is a key parameter to assess the molecular arrangement and the relaxation dynamics of amorphous phases [23, 26, 36]. Indeed, fragility index is supposed to be mainly dependent on the packing efficiency of the amorphous chains [39, 40, 41] as well as on the stiffness of their backbone [22, 36, 37, 42].

In a study done on a wide range of polymers with different side-groups and backbone structures, Kunal et al. [36] showed that the backbone flexibility is one of the most important factor controlling fragility in polymers. In particular, their study revealed that polymers with very stiff backbones, such as polycarbonate (PC) and poly(ethylene terephthalate)(PET), are the most fragile (high values of m) while the polymers with very flexible backbones and no side groups, such as poly(ethylene)(PE), are the strongest (low values of m). The fragility index can then be used to compare the backbone flexibility in different polymer systems.

Dudowicz et al. [39] proposed a model to correlate the fragility index to the chemical structure of polymers. According to this description, three different categories were identified : (1) poly-

Table 4.3: Values of dielectric glass transition temperature T_g (100s) and fragility index m obtained on (HB-*co*-HV) and (HB-*co*-HHx) copolymers submitted to *Quenching* and *Crystallization from the glassy state* thermal treatments.

	Quenching		Cryst from the glass	
SAMPLE	$T_g(\tau$**=100s)** ±1[°C]	m ±10	$T_g(\tau$**=100s)** ±1[°C]	m ±10
PHB	-2	113	5	80
PHBV3%	-4	107	5	85
PHBV15%	-5.5	104	-3	98
PHBV23%	-5.5	104	-3	98
PHBV27%	-7	102	-2	87
PHHx3%	-2	98	5	99
PHHx8%	-5	91	-4	82
PHHx12%	-6	88	-7	82
PHHx35%	-9	92	-10	93

mers with flexible backbone and flexible side-group (F-F), (2) polymers with flexible backbone and stiff side-group (F-S), (3) polymers with stiff backbone and flexible side-group (S-F). In their work, they attributed the greater relative value of fragility index of the (F-S) polymers to their lower packing efficiency in the melt. It also appeared that fragility tends to decrease with an increase in the packing efficiency in the melt and vice versa.

In this work, the m values obtained for the quenched samples do not significantly depend on the content of either HV or HHx repeating units. It appears that, on a whole, the fragility index m is not really impacted by a change in the co-monomer content, at least in quenched samples. This finding indicates that in PHA copolymers, the backbone flexibility as well as the packing efficiency of the macromolecular chains remains constant independently of the co-monomer content. Another possible explanation could be that changes in backbone flexibility and chain packing efficiency are compensating each other which in turn results in an overall constant fragility index.

As for the effect of the nature of the co-monomer unit, Figure 4.9 shows that, in quenched samples, the values of T_g (100s) and m are not sensitive to the presence of an extra carbon atom in the side-chains (possible comparisons: HV 3 mol% vs. HHx 3 mol%; HV 15 mol% vs. HHx 12 mol HV 27 mol% vs. HHx 35 mol%). Yet, a slight decrease of the fragility value is observed between the (HB-*co*-HV) and (HB-*co*-HHx) copolymers which could be due to either a change in the backbone flexibility and/or in the amorphous chains packing efficiency.

Figure 4.8 shows the relaxation maps obtained on the samples submitted to the *Crystallization from the glassy state* protocol. Again, all the samples show a non-linear dependence of the relaxation times with temperature, and therefore the VTF law was used to fit the plots (the fitting parameters are reported in Table **??**). In both (HB-*co*-HV) and (HB-*co*-HHx) copolymers, the crystallization from the glassy state results in an overall increase in the glass transition

temperature, accompanied by a decrease in the m value as reported in Table ?? and Figure 4.9. The increase in the glass transition temperature due to an increase in crystallinity has already been reported in the literature and explained by the dynamic heterogeneities due to the formation of RAF [5, 7].

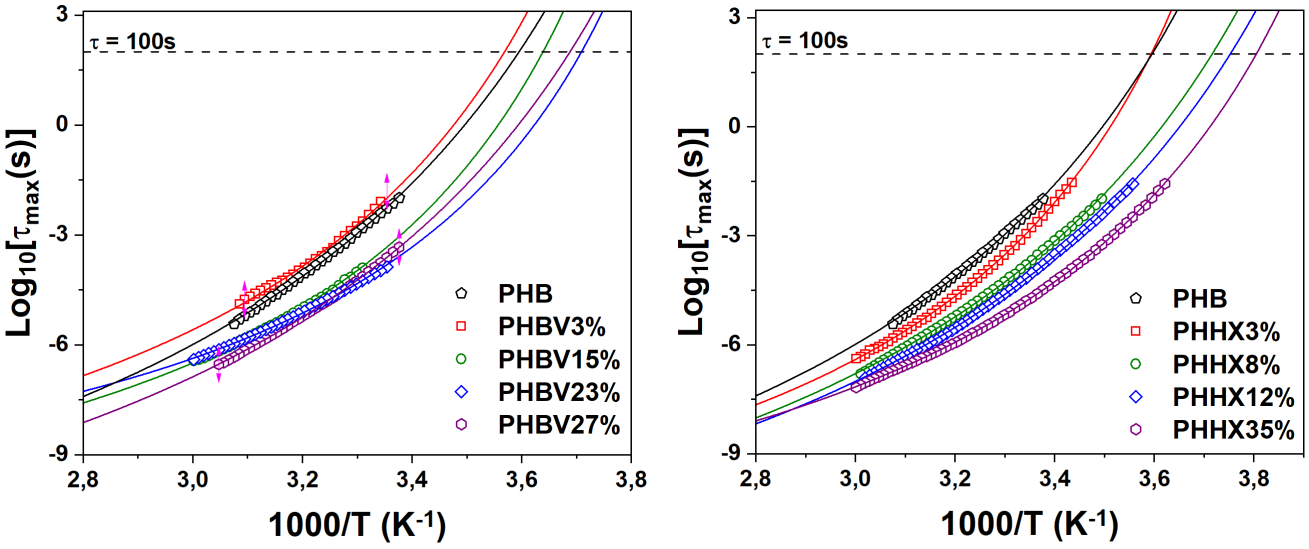

Figure 4.8: Relaxation maps obtained on (HB-*co*-HV) and (HB-*co*-HHx) copolymers after *Crystallization from the glassy state*. The solid lines represent the best fit using VFT equation. The fitting curves have been extrapolated to τ = 100s in order to estimate the temperature at which a relaxation time of 100s is observed (T_g (100s)).

Regarding the changes in the m value, no universal law has been established so far because the variations of m with the crystallization conditions also depends on the considered polymer. Some studies have shown that after crystallization the fragility index m remains the same as the one measured on the fully amorphous state [43]. Recently, some authors correlated the changes in the m value to the formation of RAF [44]. A few studies also suggested that the less flexible is the polymer backbone, the more the m value is affected by the confinement of the amorphous phase due to the presence of crystals [35, 45].

Earlier in this chapter it has been shown that non-negligible amounts of RAF are formed in both (HB-*co*-HV) and (HB-*co*-HHx) copolymers after cold crystallization. However, the changes in both the T_g and m values are more or less important depending on the molecular structure of the sample. Indeed, different amounts of RAF are formed depending on the amount and nature of the co-monomer units introduced in the copolymers. Figure 4.9 shows that two different behaviors can be identified regarding the changes in the m values after cold crystallization. In the (HB-*co*-HV) copolymers, the decrease in the m value is more important for either very low (HV 3 mol%) or very high (HV 27 mol%) amounts of HV repeating units with respect to the intermediate compositions (HV 15 mol% and HV 23 mol%). The opposite trend is observed for the (HB-*co*-HHx) copolymers, where the strongest decrease in the m value is observed for the intermediate compositions (HHx 8 mol% and HHx 12 mol%) as compared to the extremes of the series (HHx 3 mol% and HHx 35 mol%).

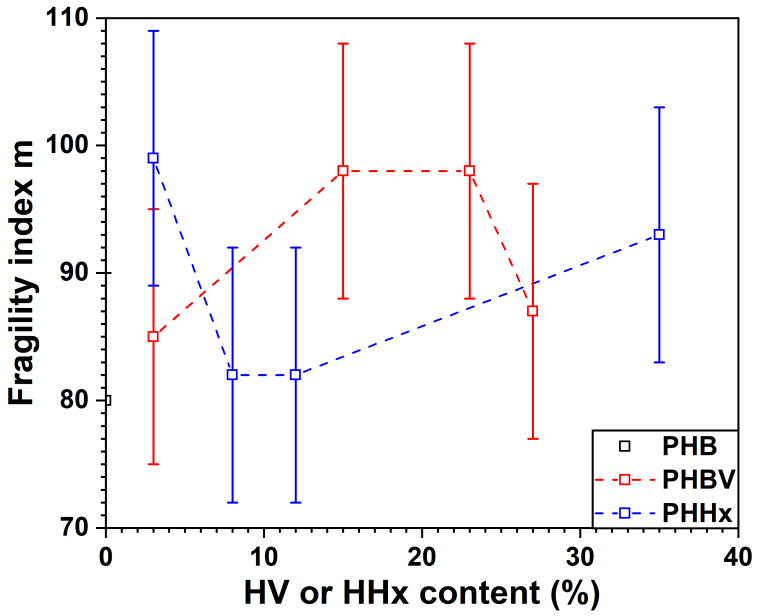

Figure 4.9: Fragility index as a function of the co-monomer unit content measured on the PHA copolymers crystallized from the glassy state. Dashed lines have been added as a guide for the eye.

Figure 4.10 shows the evolution of the dielectric strength ($\Delta\varepsilon$) associated with the α relaxation process as a function of temperature for all the considered samples after *Quenching* and *Crystallization from the glassy state*. A decrease in the overall $\Delta\varepsilon$ value is observed for both the (HB-*co*-HV) and (HB-*co*-HHx) copolymers. The value of $\Delta\varepsilon$ is usually expressed using the Kirkwood-Fröhlich equation:

$$\Delta\varepsilon = \frac{1}{3\varepsilon_0} g_K \frac{\mu^2}{k_B T} \frac{N}{V} \tag{4.5}$$

Where ε_0 is the vacuum permittivity, g_K is the Kirkwood correlation factor, μ is the average dipole moment of the relaxing units in vacuum, k_B is the Boltzmann's constant, and $\frac{N}{V}$ is the volume density of dipoles involved in the relaxation process. This equation proves that, for a given polymer, the dielectric strength ($\Delta\varepsilon$) is directly related to the number of dipoles in the amorphous phase of the sample. When comparing a crystallized sample to its amorphous counterpart, the decrease observed in the $\Delta\varepsilon$ value can be attributed to a decrease in the volume density of the dipoles involved in the relaxation process; it appears that $\frac{N}{V}$ decreases as the content of co-monomer units increases.

As shown in Figure 4.10, the dielectric strength ($\Delta\varepsilon$) is rather low for the samples submitted to the *Crystallization from the glassy state* protocol compared to the ones submitted to the *Quenching* protocol. Given that $\Delta\varepsilon$ is directly proportional to the fraction of amorphous phase in the sample, its evolution can be used to estimate the crystallizability of the samples. The largest decrease of $\Delta\varepsilon$ is observed for the samples containing small amounts of HV and HHx repeating units. This results confirms that the introduction of either HV or HHx co-monomer

units reduces the ability of the samples to crystallize. The amount of RAF is directly related to the quantity and regularity/perfection of the crystalline phase [46, 47]; therefore, an increase in the amount of HV or HHx co-monomer units, which leads to a decrease in the amount of crystals, should also reduce the amount of RAF. This means that the incorporation of controlled amounts of either HV or HHx co-monomer units during the biosynthesis can be used as an effective strategy to adjust the amounts of the different fractions in semi-crystalline PHAs.

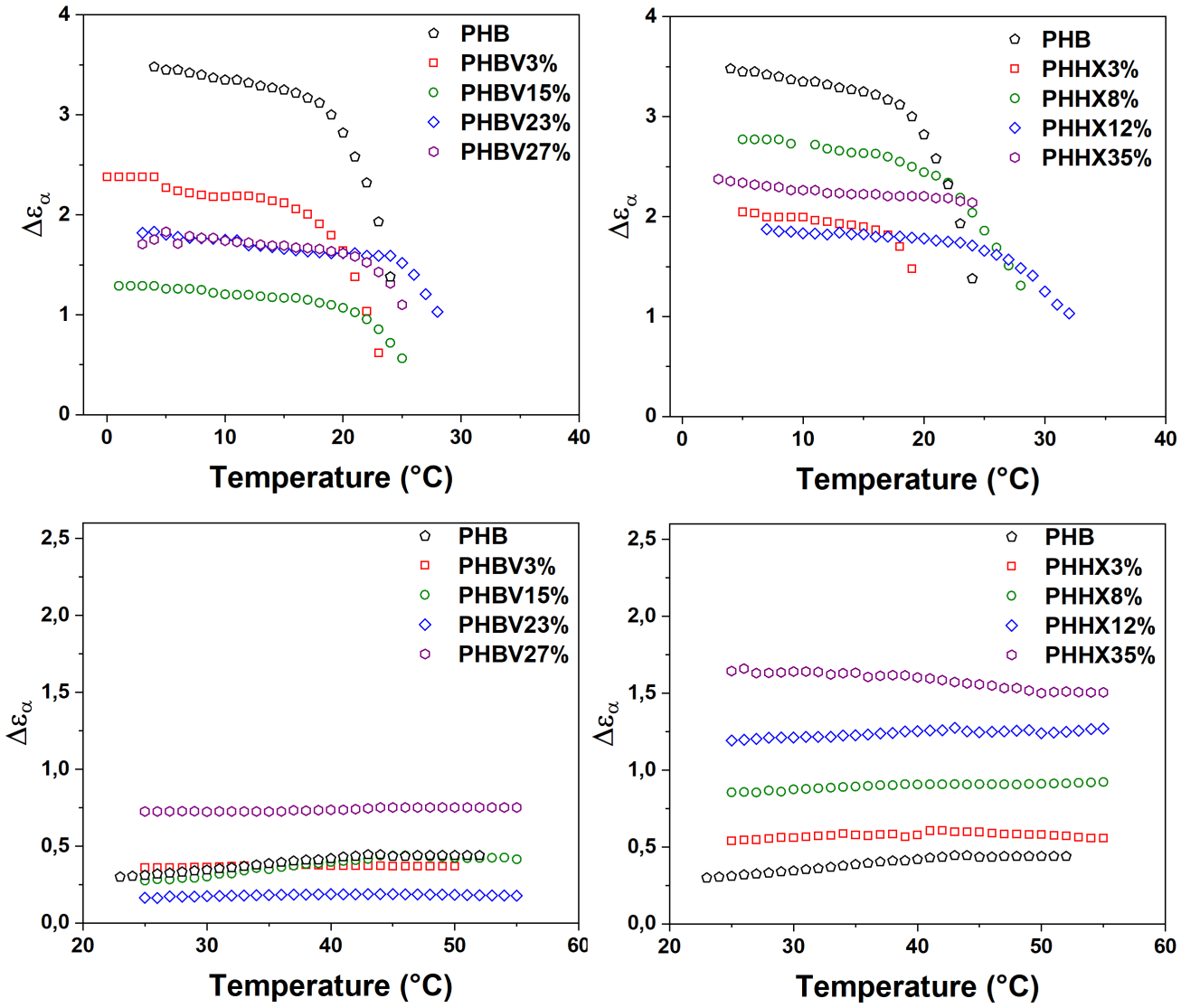

Figure 4.10: Dielectric strength ($\Delta\varepsilon$) expressed as a function of temperature for both (HB-*co*-HV) and (HB-*co*-HHx) copolymers after *Quenching* (top) and *Crystallization from the glassy state* (bottom).

4.2.3 Influence of copolymerization on the molecular spacing

As previously mentioned, some attempts have been made to evidence a link between the CRR size as defined by Adam and Gibbs [21] and the fragility index introduced by Angell [34]. Hong et al. [22] investigated a wide range of glass-forming liquids including polymers but no correlations was found between the cooperativity length and the fragility index. As a

consequence, they proposed to split fragility into two main contributions, respectively called the "isochoric fragility" (m_v) and the "isobaric fragility" ($m - m_v$). These two values can be expressed as follows:

$$m = (m - m_v) + m_v = \frac{\Delta V^{\#}}{ln(10)k_B}\frac{\alpha_\tau}{\kappa} + m_v \tag{4.6}$$

Where α_τ is the thermal expansion coefficient of the supercooled liquid at the glass transition temperature, κ is the compressibility, and $\Delta V^{\#}$ is a sort of "activation volume" (approximately equal to 4% of the cooperativity volume). The literature reports that, for a wide range of glass-forming liquids including polymers, $\frac{\alpha_\tau}{\kappa}$ ranges between 0.5 and 3 $MPa.s^{-1}$ [48, 49]. According to this equation, only the parameter $(m - m_v)$ is assumed to be straightly correlated to the cooperativity at the glass transition temperature; therefore, fragility and cooperativity are expected to be correlated only when m_v remains constant.

In a recent study on interpenetrated polymer networks (IPNs), Araujo et al. [42] reported that $(m - m_v)$ is mainly dependent on the interchain interactions (as for the CRR size) whereas m_v mainly depends on the backbone stiffness. A concomitant evolution of the cooperativity length and the fragility index should then be observed on systems in which the intermolecular interactions are changed without impacting the backbone stiffness. In a more recent study on plasticized polylactic acid (PLA) [25], a correlated variation of the cooperativity length and the fragility index has been observed. This observation supports the assumption that $(m - m_v)$ is mainly dependent on the intermolecular interactions while m_v depends on other parameters, such as the backbone stiffness and the intra-molecular interactions.

This chapter is focused on two series of PHA copolymers containing different amounts of either HV or HHx repeating units introduced in polymer backbones mainly composed of HB repeating units. Table 4.4 reports the values of cooperativity length ξ [nm], fragility index m, isobaric fragility $(m - m_v)$ and isochoric fragility m_v determined respectively with the experimental approached proposed by Donth [18], Angell [34] and Hong [22], respectively.

Table 4.4: Values of cooperativity length ξ, fragility index m, isobaric fragility $m - m_v$ and isochoric fragility m_v obtained on (HB-*co*-HV) and (HB-*co*-HHx) copolymers submitted to the *Quenching* protocol.

SAMPLE	ξ ± 0.1[nm]	m	$m - m_v$	m_v
PHB	4.1	113	87	26
PHBV3%	3.7	107	64	43
PHBV15%	3.4	104	49	55
PHBV23%	3	104	34	70
PHBV27%	3.4	102	49	54
PHHx3%	3.6	98	59	39
PHHx8%	3.8	91	69	22
PHHx12%	3.5	88	54	34
PHHx35%	3.1	92	38	54

An increase in the amount of the co-monomer units, or a change in their composition, result in an overall decrease of both the cooperativity length and the fragility index. However, the cooperativity length decrease independently on the type of co-monomer unit, whereas the decrease in the fragility index seems to be more pronounced in the (HB-*co*-HHx) copolymers as compared to the (HB-*co*-HV) copolymers.

Figure 4.11 displays the values of m_v and $m - m_v$ plotted against the content of co-monomer units for both (HB-*co*-HV) and (HB-*co*-HHx) copolymers. The $m - m_v$ value decreases as the amount of co-monomer units increases. This decrease has been reported for other polymeric systems [22, 23, 25, 42] and has been linked to the changes in cooperativity resulting from a decrease in the intermolecular interactions. The decrease in the $m - m_v$ value is accompanied by an increase in the m_v value, which indicates that the cooperativity length and the fragility index are not correlated in either the (HB-*co*-HV) or the (HB-*co*-HHx) copolymers. In the literature [42], the increase in the m_v value has been attributed to an increase in the polymer backbone stiffness. Yet, an increase in the co-monomer content should lead to a significant increase in the glass transition temperature as reported for other polymeric systems [50, 51], but as previously reported in this chapter the glass transition is slightly decreasing as the co-monomer content increases which has been attributed to a loss of intermolecular interactions. Thus, an increase in the backbone stiffness do not seem to be a possible explanation of the increase in the m_v value. According to the literature [39, 40, 41], fragility index depends mainly on (1) the backbone flexibility, (2) the chain packing efficiency. Therefore, it appears that an increase in the co-monomer content leads to a significant decrease in the chain packing efficiency.

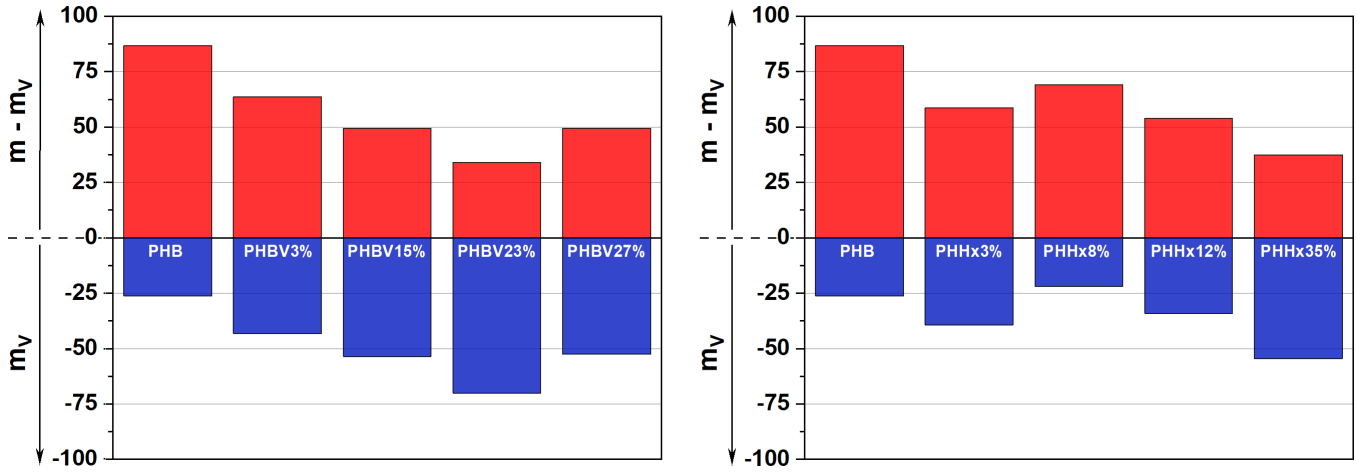

Figure 4.11: Isobaric (red) and isobchoric (blue) fragilities as a function of the co-monomer content of (HB-co-HV) copolymers and (HB-co-HHx) copolymers.

4.3 Three-phase model: rigid amorphous fraction

Figures 4.4 and 4.12 were used to discuss the molecular mobility at $T > T_g$ in terms of coupling between phases (amorphous and crystalline). Semi-crystalline polymers do not always develop

large amounts of RAF, but whenever present, the RAF can be considered as an intermediate "buffer zone" between the crystalline domains (where only local mobility is allowed) and the mobile amorphous fraction (where bigger portions of polymer chains are able to rearrange). Therefore, the higher is X_{RAF}, the lower is expected to be the molecular mobility at $T > T_g$. Esposito et al. [5] recently gave a new point of the view about the molecular mobility of the RAF, as they evaluated the time dependence of its devitrification. In particular, they showed that the polymer chains with the lowest molecular mobility (i.e. the ones that fold in the crystal domains) affect their closest neighbors, which in turns affect the surrounding volume, until reaching the polymer chains with the highest molecular mobility (i.e. the ones that relax at the glass transition temperature). Such microstructural depiction of semi-crystalline polymers was called "continuum of mobility" and found to be particularly suitable to describe polymer systems with a strong coupling between phases.

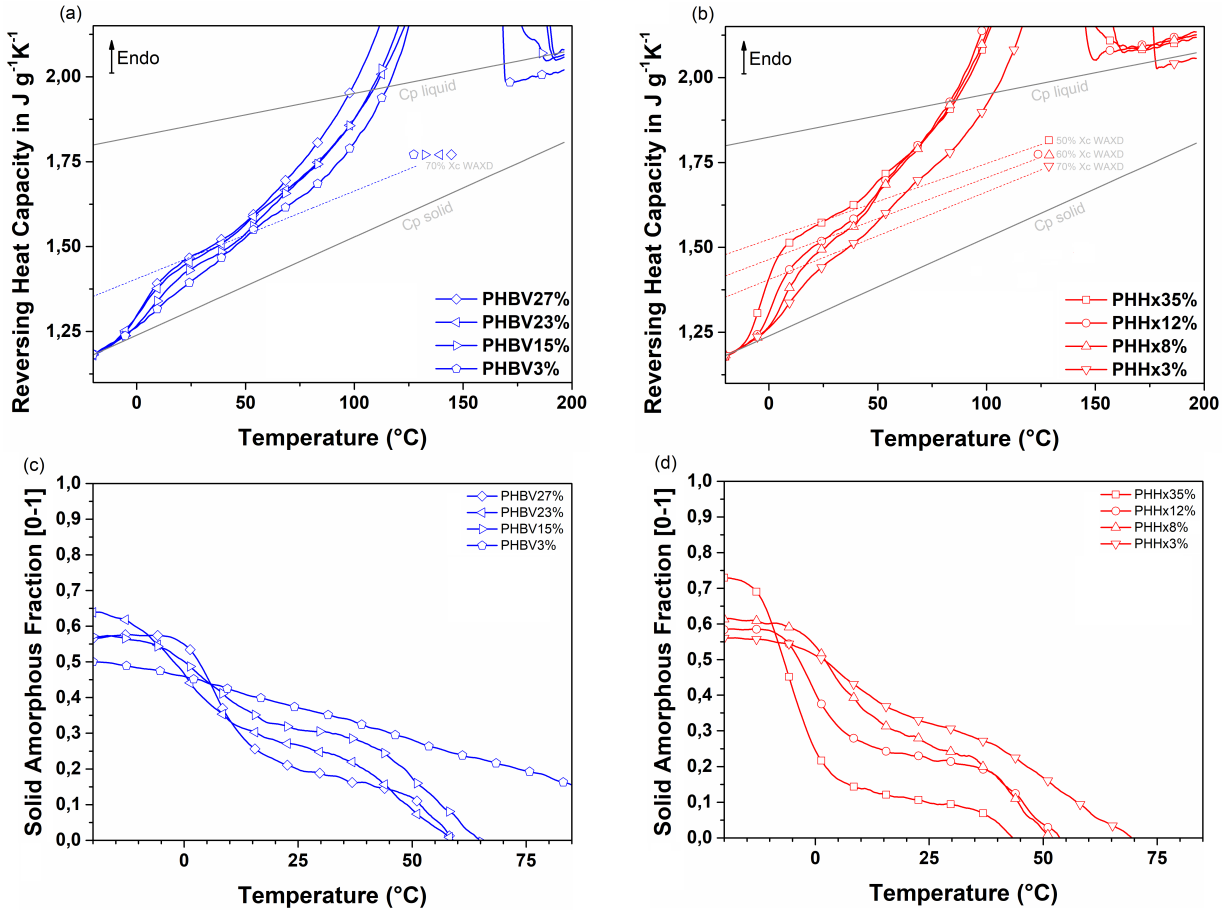

Figure 4.12: Reversing Heat Capacity extracted from MT-DSC signals recorded in Heat-Iso conditions on (a) (HB-*co*-HV) copolymers with 3, 15, 23 and 27 mol% HV and (b) (HB-*co*-HHx) copolymers with 3, 8, 12 and 35 mol% HHx after *Crystallization from the glassy state*. The reference values of specific heat capacity in the solid and liquid states for the hopolymer PHB are reported from the literature [8] and used to predict the repartition of crystalline and mobile amorphous fractions expected on the basis of a two-phase model (dotted lines). Temperature dependence of the Solid Amorphous Fraction $(X_{MAF} + X_{RAF})_{solid}$ obtained from the MT-DSC curves (a) and (b) over the temperature range going from the glassy to the rubbery states for (c) the (HB-*co*-HV) copolymers and (d) the (HB-*co*-HHx) copolymers, respectively. At $T < Tg$, X_C is the highest possible, X_{RAF} and X_{MAF} are not coupled with the exception of PHBV 3 mol% ("continuum of mobility" [5]). In the (HB-*co*-HHx) copolymers, X_{RAF} and X_{MAF} are the less and less coupled as the degree of copolymerization increases.

Under the assumption of equal heat capacities for crystalline and glassy polymers below the glass transition temperature, and because heat capacities are additive in the absence of thermodynamic excesses [6], equation 4.1 can also be used to discuss the expression of molecular mobility in semi-crystalline polymers in terms of repartition of the amorphous phase into mobile and rigid. Figures 4.12 (a) and (b) show the Reversing Heat Capacity (RevC_p) signals recorded by MT-DSC respectively on (HB-*co*-HV) and (HB-*co*-HHx) copolymers after *Crystallization from the glassy state* for t_c = 1440 minutes. The reference values of specific heat capacity in the solid and liquid states for the homopolymer PHB are reported from the literature [8], along with the heat capacity repartition of crystalline and amorphous fractions expected on the basis of the degree of crystallinity measured by WAXD (Table 4.1) under the assumption of a two-phase model obtained as a simple mixing rule (dotted lines). All the samples show only a partial alignment between the experimental C_p values and the expectation based on the two-phase model. The experimental values of RevC_p(T) shown in Figures 6 (a) and (b) can be injected in equation 4.1, along with the value of $X_{c,WAXD}$ selected according to Table 4.1 and the reference data for heat capacity ($C_{p,solid}$(T) and $C_{p,liquid}$(T)) obtained experimentally by extrapolating the RevC_p(T) curves from the high temperature to $T < T_g$ and from low temperature to $T > T_g$, respectively. Esposito et al. [5] recently investigated the microstructure of PHBV 3 mol% after cold crystallization from the glassy state, and found that the lowest endotherm on the Total Heat Capacity signal was detected at 47°C. They also proved by Flash DSC that cold-crystallized PHBV 3 mol% started melting around 80°C. If the assumption is made that an excess heat capacity for (HB-*co*-HV) and (HB-*co*-HHx) copolymers builds up approximately in the same temperature range, it seems quite reasonable to use the same temperature upper limit to discuss the devitrification of the RAF without the influence of thermodynamic excesses. As a consequence, the expression of molecular mobility as a function of temperature in Figure 4.12 (c) and (d) can be rigorously made only up to 50°C, i.e. in the temperature range where no reversing melting occurs.

The curves $(X_{MAF} + X_{RAF})_{solid} = f(T)$ obtained for the semi-crystalline samples are useful to evaluate the influence of the degree of copolymerization on the microstructure, i.e. how the fractions of polymer chains that did not fold and organize in crystalline domains are distributed into mobile and rigid, and how coupled they are to each other (as well as to the surface of the crystals). Figure 4.12 (c) shows that the copolymerization of HB and HV repeating units leads to a progressive decrease of the coupling between the mobile and rigid amorphous fractions. Coming from the glassy state, as temperature increases through and above the glass transition temperature, the expression of the molecular mobility proceeds gradually in PHBV 3 mol% cold-crystallized to the maximum extent ($X_{C,WAXD}$ = 0.50, Table 4.1). On the other hand, a neat repartition of the amorphous phase in mobile (X_{MAF} = 0.42) and rigid (X_{RAF} = 0.15) is observed for PHBV 27 mol% cold-crystallized in the same conditions ($X_{C,WAXD}$ = 0.43, Table 4.1). The distinction between glass transition (i.e. relaxation of the mobile amorphous fraction)

and devitrification (i.e. relaxation of the rigid amorphous fraction) becomes easier and clearer as the content of HV repeating units increases. The fraction of rigid amorphous chains also decreases with the degree of copolymerization both in the (HB-*co*-HV) and in the (HB-*co*-HHx) systems, but this decrease is more pronounced in the (HB-*co*-HV) copolymers. Figure 4.12 (c) shows that, for (HB-*co*-HV) samples, the degree of copolymerization significantly affects both the amount of RAF developed during cold crystallization (going from $X_{RAF} = 0.45$ in PHBV 3 mol% to $X_{RAF} = 0.15$ in PHBV 27 mol%) and the coupling between the mobile and rigid fractions of amorphous polymer chains.

The fact that the amount of RAF developed during the crystallization process decreases as the co-monomer content increases can be directly related to the changes in crystallizability induced by the degree of copolymerization (crystalline disruption). In the case of PHHx 3 mol%, the crystallinity reaches a value of $X_{C,WAXD} = 44\%$. Thus, the amorphous fraction is highly constrained by the important amount of crystals, which results in the development of a relatively large amount of rigid amorphous fraction at the expense of the unconstrained mobile amorphous fraction. The different fractions are then strongly coupled and the continuum of mobility should be used to describe the resulting microstructure not from a quantitative point of view but with a keener attention to the molecular mobility, as described by Esposito et al. [5]. On the other hand, in PHHx 35 mol%, the amount of crystals is lower than for PHHx 3 mol% ($X_{C,WAXD} = 27\%$), which leads to a less constrained environment of the amorphous chains and therefore a weaker confinement effects. The amount of rigid amorphous fraction is then much lower and the phases appears more decoupled. The classical three-phase model is, in this case, more suitable to describe the semi-crystalline microstructure, at least from a quantitative point of view. In any case, it clearly appears that increasing the amount of co-monomer units is a good strategy not only to disrupt crystallinity, but also to concomitanly reduce the coupling between phases and the formation of a rigid amorphous fraction. As such, the choice of specific co-monomer units to be introduced in controlled amounts into a polymer backbone can be considered an excellent pathway to tune the microstructure of semi-crystalline polymers, and therefore adjust their final properties.

4.4 Conclusion

In this chapter, the effects of the co-monomer content and nature on the semi-crystalline microstructures of PHA copolymers have been investigated and discussed. First of all, the aptitude to crystallize of the initially amorphous samples has been evaluated through modulated temperature differential scanning calorimetry (MT-DSC) and wide-angle X-ray diffraction (WAXD). It appears that the progressive incorporation of either HV or HHx units leads to a slowing down of the crystallization process as well as to a significant disruption of the crystalline phase.

In a second part, the impact of the copolymerization on the relaxation processes in the amor-

phous phase has been studied using the concepts of CRR and fragility. For both series of copolymers, a decrease in the CRR size has been observed with an increase in the co-monomer content, which was attributed to a loss of intermolecular interactions. The fragility index of the amorphous samples does not significantly depend on the co-monomer content. This finding indicates that in PHA copolymers the backbone flexibility as well as the packing efficiency remain unchanged independently of the co-monomer content. Another possible explanation would have been that the variations in the backbone flexibility and packing efficiency are compensating each other, which leads to an overall constant fragility index. On the other hand, a slight decrease in the fragility index has been observed between the (HB-*co*-HV) and (HB-*co*-HHx) copolymers, which has been attributed to either a change in the backbone flexibility and/or a change in the chain packing efficiency. Hong's approach has been used to discuss the correlation between the CRR size and the fragility index. However, no direct correlation has been observed, which has been explained by a decrease in the chain packing efficiency as the co-monomer content increases. Therefore, it appears that an increase in the co-monomer content can significantly impact the packing efficiency of the amorphous chains as well as the intermolecular interactions strength.

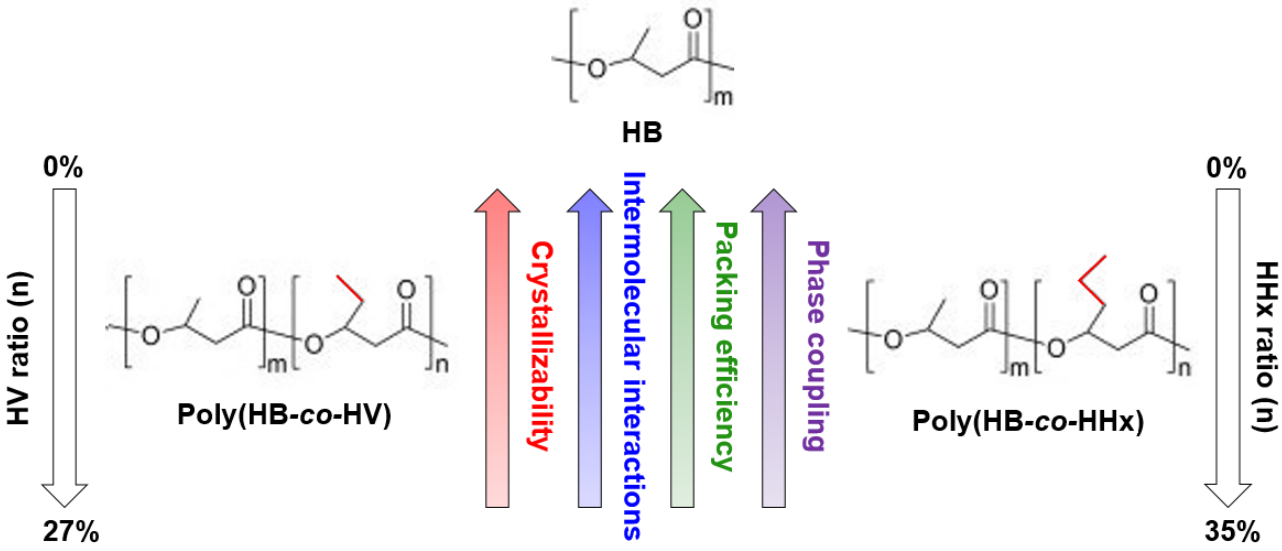

Figure 4.13: Schematic depiction of the effects of the co-monomer unit content/nature on the properties of PHA copolymers.

Finally, the semi-crystalline microstructures of PHA samples crystallized from the glassy state were characterized and described according to the three-phase model. The copolymerization of HB and HV (or HHx) repeating units leads to a progressive decrease in phase coupling. Moreover, the degree of copolymerization significantly affects the amount of RAF formed during the crystallization process. These findings were attributed to the change in crystallizability induced by the incorporation of different repeating units (disruption of the crystalline phase). Because, the different fractions are strongly coupled to each other, the concept of continuum of mobility introduced by Esposito et al. [5] should be used to describe the microstructure.

On the other hand, the amount of crystals in the copolymers containing a higher co-monomer content is lower, which leads to a less constrained environment of the amorphous phase. As a consequence, the mobile and rigid amorphous fractions appear more decoupled, and the classical three-phase model is more suitable to describe the microstructure.

From all the results presented in this work, and as graphically summarized in Figure 4.13, it clearly appears that a change in the co-monomer unit content/nature strongly affects the properties and the semi-crystalline microstructures of PHA copolymers. Therefore, it appears possible to tune the semi-crystalline microstructures of PHA samples by changing the co-monomer nature and content, which *in fine* allows to adjust their final properties thus expanding the range of possible applications.

References

[1] Z. Li, J. Yang, and X. J. Loh, "Polyhydroxyalkanoates: opening doors for a sustainable future," *NPG Asia Materials*, vol. 8, pp. e265–e265, Apr. 2016.

[2] B. S. Kushwah, A. V. S. Kushwah, and V. Singh, "RETRACTED ARTICLE: Towards understanding polyhydroxyalkanoates and their use," *Journal of Polymer Research*, vol. 23, p. 153, Aug. 2016.

[3] J. A. S. Puente, A. Esposito, F. Chivrac, and E. Dargent, "Effect of boron nitride as a nucleating agent on the crystallization of bacterial poly(3-hydroxybutyrate)," *Journal of Applied Polymer Science*, vol. 128, pp. 2586–2594, June 2013.

[4] P. Scherrer *Göttinger Nachrichten Gesell*, vol. 2.

[5] A. Esposito, N. Delpouve, V. Causin, A. Dhotel, L. Delbreilh, and E. Dargent, "From a Three-Phase Model to a Continuous Description of Molecular Mobility in Semicrystalline Poly(hydroxybutyrate- *co* -hydroxyvalerate)," *Macromolecules*, vol. 49, pp. 4850–4861, July 2016.

[6] C. Schick, A. Wurm, and A. Mohamed, "Vitrification and devitrification of the rigid amorphous fraction of semicrystalline polymers revealed from frequency-dependent heat capacity," *Colloid & Polymer Science*, vol. 279, pp. 800–806, Aug. 2001.

[7] I. Okazaki and B. Wunderlich, "Modulated differential scanning calorimetry in the glass transition region, V. activation energies and relaxation times of poly(ethylene terephthalate)s," *Journal of Polymer Science Part B: Polymer Physics*, vol. 34, pp. 2941–2952, Dec. 1996.

[8] A. Czerniecka, A. Magoń, J. Schliesser, B. Woodfield, and M. Pyda, "Heat capacity of poly(3-hydroxybutyrate)," *The Journal of Chemical Thermodynamics*, vol. 73, pp. 76–84, June 2014.

[9] C. Schick, A. Wurm, and A. Mohammed, "Formation and disappearance of the rigid amorphous fraction in semicrystalline polymers revealed from frequency dependent heat capacity," *Thermochimica Acta*, vol. 396, pp. 119–132, Feb. 2003.

[10] P. J. Barham, A. Keller, E. L. Otun, and P. A. Holmes, "Crystallization and morphology of a bacterial thermoplastic: poly-3-hydroxybutyrate," *Journal of Materials Science*, vol. 19, pp. 2781–2794, Sept. 1984.

[11] M. Martínez-Sanz, A. A. Vicente, N. Gontard, A. Lopez-Rubio, and J. M. Lagaron, "On the extraction of cellulose nanowhiskers from food by-products and their comparative reinforcing effect on a polyhydroxybutyrate-co-valerate polymer," *Cellulose*, vol. 22, pp. 535–551, Feb. 2015.

[12] D. Jonnalagadda and T. Kuboki, "Effect of natural flours on crystallization behaviors of poly(3-hydroxybutyrate- *co* -3-hydroxyhexanoate)," *Journal of Applied Polymer Science*, vol. 133, July 2016.

[13] S. Nakamura, Y. Doi, and M. Scandola, "Microbial synthesis and characterization of poly(3-hydroxybutyrate-co-4-hydroxybutyrate)," *Macromolecules*, vol. 25, pp. 4237–4241, Aug. 1992.

[14] M. Yokouchi, Y. Chatani, H. Tadokoro, K. Teranishi, and H. Tani, "Structural studies of polyesters: 5. Molecular and crystal structures of optically active and racemic poly (beta-hydroxybutyrate)," *Polymer*, vol. 14, pp. 267–272, June 1973.

[15] N. Yoshie, M. Sakurai, Y. Inoue, and R. Chujo, "Cocrystallization of isothermally crystallized poly(3-hydroxybutyrate-co-3-hydroxyvalerate)," *Macromolecules*, vol. 25, pp. 2046–2048, Mar. 1992.

[16] N. Kamiya, M. Sakurai, Y. Inoue, R. Chujo, and Y. Doi, "Study of cocrystallization of poly(3-hydroxybutyrate-co-3-hydroxyvalerate) by solid-state high-resolution carbon-13 NMR spectroscopy and differential scanning calorimetry," *Macromolecules*, vol. 24, pp. 2178–2182, Apr. 1991.

[17] E. Hempel, G. Hempel, A. Hensel, C. Schick, and E. Donth, "Characteristic Length of Dynamic Glass Transition near T_g for a Wide Assortment of Glass-Forming Substances," *The Journal of Physical Chemistry B*, vol. 104, pp. 2460–2466, Mar. 2000.

[18] E. Donth, "The size of cooperatively rearranging regions at the glass transition," *Journal of Non-Crystalline Solids*, vol. 53, pp. 325–330, Dec. 1982.

[19] E. Donth, "Characteristic length of the glass transition," *Journal of Polymer Science Part B: Polymer Physics*, vol. 34, pp. 2881–2892, Dec. 1996.

[20] E. Donth, H. Huth, and M. Beiner, "Characteristic length of the glass transition," *Journal of Physics: Condensed Matter*, vol. 13, pp. L451–L462, June 2001.

[21] G. Adam and J. H. Gibbs, "On the Temperature Dependence of Cooperative Relaxation Properties in Glass-Forming Liquids," *The Journal of Chemical Physics*, vol. 43, pp. 139–146, July 1965.

[22] L. Hong, V. Novikov, and A. Sokolov, "Is there a connection between fragility of glass forming systems and dynamic heterogeneity/cooperativity?," *Journal of Non-Crystalline Solids*, vol. 357, pp. 351–356, Jan. 2011.

[23] J. Puente, B. Rijal, L. Delbreilh, K. Fatyeyeva, A. Saiter, and E. Dargent, "Segmental mobility and glass transition of poly(ethylene-vinyl acetate) copolymers: Is there a continuum in the dynamic glass transitions from PVAc to PE?," *Polymer*, vol. 76, pp. 213–219, Oct. 2015.

[24] X. Monnier, N. Delpouve, N. Basson, A. Guinault, S. Domenek, A. Saiter, P. Mallon, and E. Dargent, "Molecular dynamics in electrospun amorphous plasticized polylactide fibers," *Polymer*, vol. 73, pp. 68–78, Sept. 2015.

[25] S. Araujo, N. Delpouve, S. Domenek, A. Guinault, R. Golovchak, R. Szatanik, A. Ingram, C. Fauchard, L. Delbreilh, and E. Dargent, "Cooperativity Scaling and Free Volume in Plasticized Polylactide," *Macromolecules*, vol. 52, pp. 6107–6115, Aug. 2019.

[26] K. Arabeche, L. Delbreilh, J.-M. Saiter, G. Michler, R. Adhikari, and E. Baer, "Fragility and molecular mobility in micro- and nano-layered PC/PMMA films," *Polymer*, vol. 55, pp. 1546–1551, Mar. 2014.

[27] C. Zhang, Y. Guo, and R. D. Priestley, "Characteristic Length of the Glass Transition in Isochorically Confined Polymer Glasses," *ACS Macro Letters*, vol. 3, pp. 501–505, June 2014.

[28] S. F. Nassar, S. Domenek, A. Guinault, G. Stoclet, N. Delpouve, and C. Sollogoub, "Structural and Dynamic Heterogeneity in the Amorphous Phase of Poly(l , l -lactide) Confined at the Nanoscale by the Coextrusion Process," *Macromolecules*, vol. 51, pp. 128–136, Jan. 2018.

[29] A. Saiter, D. Prevosto, E. Passaglia, H. Couderc, L. Delbreilh, and J. M. Saiter, "Cooperativity length scale in nanocomposites: Interfacial and confinement effects," *Physical Review E*, vol. 88, p. 042605, Oct. 2013.

[30] M. Nakanishi and R. Nozaki, "Model of the cooperative rearranging region for polyhydric alcohols," *Physical Review E*, vol. 84, p. 011503, July 2011.

[31] N. Varol, N. Delpouve, S. Araujo, S. Domenek, A. Guinault, R. Golovchak, A. Ingram, L. Delbreilh, and E. Dargent, "Amorphous rigidification and cooperativity drop in semicrystalline plasticized polylactide," *Polymer*, vol. 194, p. 122373, Apr. 2020.

[32] C. Schick and E. Donth, "Characteristic length of glass transition: experimental evidence," *Physica Scripta*, vol. 43, pp. 423–429, Apr. 1991.

[33] B. Wunderlich, "Reversible crystallization and the rigid–amorphous phase in semicrystalline macromolecules," *Progress in Polymer Science*, vol. 28, pp. 383–450, Mar. 2003.

[34] C. Angell, "Spectroscopy simulation and scattering, and the medium range order problem in glass," *Journal of Non-Crystalline Solids*, vol. 73, pp. 1–17, Aug. 1985.

[35] S. Napolitano and M. Wübbenhorst, "Effect of a Reduced Mobility Layer on the Interplay between Molecular Relaxations and Diffusion-Limited Crystallization Rate in Ultrathin Polymer Films," *The Journal of Physical Chemistry B*, vol. 111, pp. 5775–5780, May 2007.

[36] K. Kunal, C. G. Robertson, S. Pawlus, S. F. Hahn, and A. P. Sokolov, "Role of Chemical Structure in Fragility of Polymers: A Qualitative Picture," *Macromolecules*, vol. 41, pp. 7232–7238, Oct. 2008.

[37] R. Kumar, M. Goswami, B. G. Sumpter, V. N. Novikov, and A. P. Sokolov, "Effects of backbone rigidity on the local structure and dynamics in polymer melts and glasses," *Physical Chemistry Chemical Physics*, vol. 15, no. 13, p. 4604, 2013.

[38] E. Bouthegourd, A. Esposito, D. Lourdin, A. Saiter, and J. Saiter, "Size of the cooperative rearranging regions vs. fragility in complex glassy systems: Influence of the structure and the molecular interactions," *Physica B: Condensed Matter*, vol. 425, pp. 83–89, Sept. 2013.

[39] J. Dudowicz, K. F. Freed, and J. F. Douglas, "Fragility of glass-forming polymer liquids," *The Journal of Physical Chemistry B*, vol. 109, no. 45, pp. 21350–21356, 2005. PMID: 16853769.

[40] J. Dudowicz, K. F. Freed, and J. F. Douglas, "The glass transition temperature of polymer melts," *The Journal of Physical Chemistry B*, vol. 109, no. 45, pp. 21285–21292, 2005.

[41] J. Wu, G. Huang, L. Qu, and J. Zheng, "Correlations between dynamic fragility and dynamic mechanical properties of several amorphous polymers," *Journal of Non-Crystalline Solids*, vol. 355, no. 34, pp. 1755 – 1759, 2009.

[42] S. Araujo, F. Batteux, W. Li, L. Butterfield, N. Delpouve, A. Esposito, L. Tan, J.-M. Saiter, and M. Negahban, "A structural interpretation of the two components governing the kinetic fragility from the example of interpenetrated polymer networks: A Structural Interpretation of the Two Components Governing the Kinetic Fragility from the Example of Interpenetrated Polymer Networks," *Journal of Polymer Science Part B: Polymer Physics*, vol. 56, pp. 1393–1403, Oct. 2018.

[43] K. L. Ngai and C. M. Roland, "Intermolecular cooperativity and the temperature dependence of segmental relaxation in semicrystalline polymers," *Macromolecules*, vol. 26, pp. 2688–2690, May 1993.

[44] A. R. Brás, J. P. Noronha, A. M. M. Antunes, M. M. Cardoso, A. Schönhals, F. Affouard, M. Dionísio, and N. T. Correia, "Molecular Motions in Amorphous Ibuprofen As Studied by Broadband Dielectric Spectroscopy," *The Journal of Physical Chemistry B*, vol. 112, pp. 11087–11099, Sept. 2008.

[45] T. Lan and J. M. Torkelson, "Fragility-Confinement Effects: Apparent Universality as a Function of Scaled Thickness in Films of Freely Deposited, Linear Polymer and Its Absence in Densely Grafted Brushes," *Macromolecules*, vol. 49, pp. 1331–1343, Feb. 2016.

[46] B. Wunderlich and A. Mehta, "Macromolecular nucleation," *Journal of Polymer Science: Polymer Physics Edition*, vol. 12, pp. 255–263, Feb. 1974.

[47] R. Androsch and B. Wunderlich, "The link between rigid amorphous fraction and crystal perfection in cold-crystallized poly(ethylene terephthalate)," *Polymer*, vol. 46, pp. 12556–12566, Dec. 2005.

[48] U. Buchenau and A. Wischnewski, "Fragility and compressibility at the glass transition," *Physical Review B*, vol. 70, p. 092201, Sept. 2004.

[49] J. E. Mark, ed., *Physical Properties of Polymers Handbook*. New York, NY: Springer New York, 2007.

[50] G. Papamokos, T. Dimitriadis, D. N. Bikiaris, G. Z. Papageorgiou, and G. Floudas, "Chain Conformation, Molecular Dynamics, and Thermal Properties of Poly(n -methylene 2,5-furanoates) as a Function of Methylene Unit Sequence Length," *Macromolecules*, vol. 52, pp. 6533–6546, Sept. 2019.

[51] J. Örtegren, J. Tidlund, M. Nykvist, P. Busson, A. Hult, S. Sen, R. Boyd, and U. Gedde, "Dielectric relaxation of liquid crystalline dendrimers and liquid crystalline polymers with pendant nitro groups," *Polymer*, vol. 42, pp. 10027–10033, Dec. 2001.

Chapter 5

Glycolic subunit length effect onto the properties of furan-based polyesters

Contents

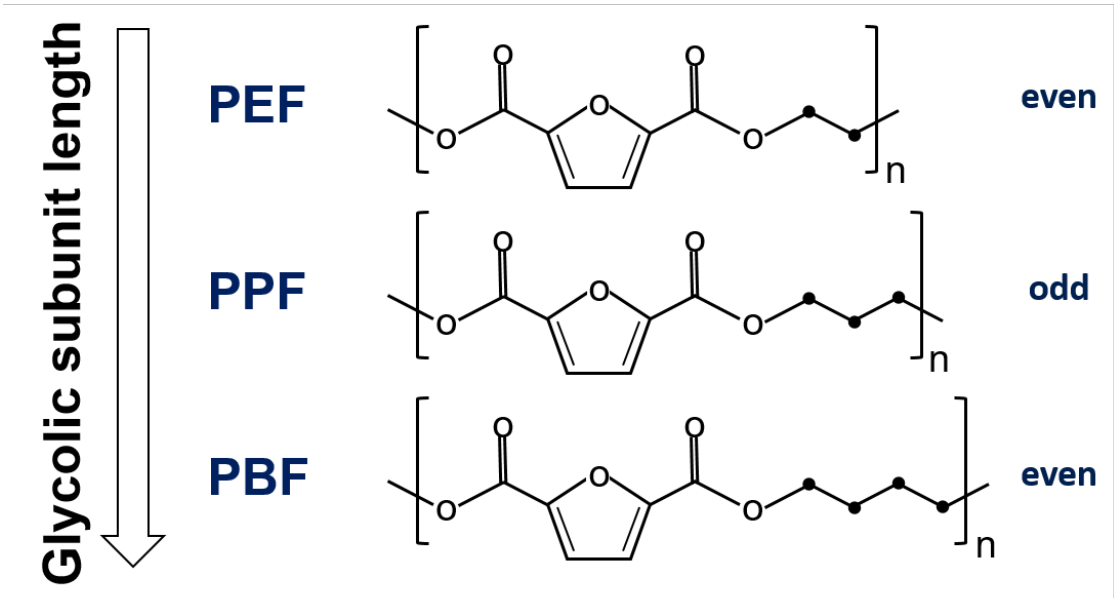

Figure 5.1: Schematic representation of the furanoate polymers investigated in this work. Three different polymers with increasing glycolic sub-unit length were characterized

As pointed out in section 1.5 of Chapter 1, new polymers are constantly being synthesized from sustainable resources to replace fossil-based materials. Polyesters are one of the largest family of biobased polymers; they can be obtained from different combination of an acid and a diol, that can be both extracted from sustainable resource. One of the most promising family of biopolyesters is the one synthesized using furandicarboxylic acid (FDCA), produced from vegetable feedstock. Due to its chemical structure, FDCA exists in the form of three different position isomers; the most commonly used is 2,5-FDCA. As shown in Figure 5.1, another interesting feature of furanoate polymers is that they can be synthesized with different diols, which provides polymers with different glycolic sub-unit lengths. Currently, the most studied furanoate-based polymer is 2,5-PEF due to its interesting mechanical and barrier properties, which makes it a good alternative to poly(ethylene terephthalate)(PET) for packaging applications. Among furanoate-based polyesters, 2,5-PPF and 2,5-PBF are also being studied, as they are promising surrogate to their petroleum-based homologues, poly(trimethylene terephthalate)(PTT) and poly(butylene terephthalate)(PBT), respectively. As a consequence, it is of uppermost importance to study the properties of these promising materials and particularly their semi-crystalline microstructures. Indeed, as shown in the literature, the presence of a rigid amorphous fraction has a strong effect on the mechanical and barrier properties[1, 2, 3, 4] of semi-crystalline polymers.

The focus of this chapter is to study the effect of the glycolic sub-unit length on the properties of a series of three furanoate-based polyesters: 2,5(PEF), 2,5(PPF), and 2,5(PBF). In a first part, the crystallization and melting behaviours of these materials will be studied to get a deeper insight into their crystallization mechanisms. Then, a study of the segmental mobility in the amorphous phase will be presented to evaluate the impact of the glycolic subunit length

on the relaxation processes. Finally, the analysis of microstructures generated on purpose to contain different amounts of RAF will be made to better understand how the glycolic subunit length impacts the formation of RAF.

5.1 Crystallization and melting behaviors

The first characterizations were done on the samples in their fully amorphous state, i.e. after melt quenching in liquid nitrogen, to evaluate their aptitude to crystallize upon heating. Figure 5.2 displays the total heat flow measured by MT-DSC with a heating rate of 2 $K.min^{-1}$. All the samples shows a clear glass transition step followed by a cold-crystallization exothermic peak and a subsequent melting peak. As reported in table 5.1, the difference between the cold-crystallization and melting enthalpies is negligible which confirms that all the samples were initially amorphous. The endothermic peak observed upon heating can then be attributed to the melting of the crystals formed by cold-crystallization during the heating ramp.

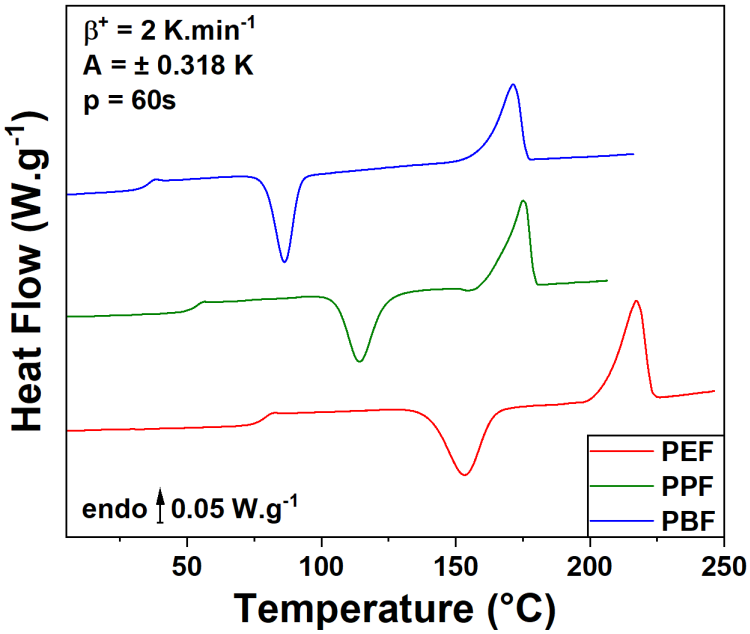

Figure 5.2: Heat flow curves obtained on amorphous samples through MT-DSC using a Heat-only protocol with an heating rate of $\beta^+ = 2\ K.min^{-1}$, a modulation amplitude of a = ± 0.318°C and a period of p = 60s.

The information extracted from Figure 5.2 are reported in Table 5.1. According to the literature [5, 6, 7, 8], at least two crystalline phases have been identified in furan-based polymers. The first crystalline phase has been attributed to less perfect α' crystals that grow at low crystallization temperatures and reorganize into the more perfect α crystals as temperature increases [6]. In the case of PPF, a third crystalline form has been identified and denoted as the β crystalline form [8, 9]. According to the literature, the cold-crystallization temperatures listed in Table 5.1 all correspond to the temperatures at which the less perfect α' crystals grow [5, 6, 7, 8]; furthermore, the melting temperatures measured upon heating at $\beta^+ = 2\ K.min^{-1}$ corresponds to the melting temperatures reported in the literature [5, 6, 7, 8] for the melting

of α crystals. This finding indicates that at heating rates as low as the ones used for DSC and MT-DSC experiments, the α' crystals can grown and then reorganize into the more perfect α crystalline phase. Extensive reorganization processes occur during the heating ramp and therefore the enthalpies of melting are measured with significant uncertainties that should be taken into account.

Table 5.1: Thermal parameters extracted from the results displayed on Figure 5.2, T_g is the glass transition temperature, T_{cc} is the cold-crystallization temperature, δT_{cc} is the width of the cold-crystallization peak, T_m is the melting temperature.

SAMPLE	ΔH_m-ΔH_{cc} ± 1 $[J.g^{-1}]$	T_g ± 1 [°C]	T_{cc} ± 1 [°C]	δT_{cc} ± 1 [°C]	T_m ± 1 [°C]
PEF	2.2	83	153	24	217
PPF	2.4	57	114	22	175
PBF	3.3	38	86	15	171

According to the values reported in Table 5.1, an increase in the length of the glycolic subunit results in a decrease in the glass transition temperature, as well as a decrease in both the cold crystallization and the melting temperature. The literature reports that the decrease observed in the characteristic temperatures as a consequence of an increase in the glycolic subunit's length can be attributed to the increased flexibility of the polymer chains [10, 11]. This trend has already been observed in other polymeric systems, including terephthalic-based polymers [12]. An increased chain flexibility can also explain the reduction of the temperature range for cold crystallization (width of the cold-crystallization peak). The broadness of the cold-crystallization peak is somehow related to how fast the crystallization process occurs, therefore an increase in the glycolic subunit's length should correlate with an increase in the crystallization rate of the sample.

In polyesters whose acidic subunit is terephthalic [12] or alicyclic [13], an increase in the glycolic subunit's length produces a sort of "even-odd effect" on the melting temperatures, as shown by the grey symbols in Figure 5.3 extracted from [12]. This effect has been explained by the fact that the melting temperature depends not only on the flexibility of the polymer chains, but also on their conformation and on the crystalline structure [13]. An even-odd dependence of the melting temperature has been recently observed by Papamokos et al. [10] on polyesters with a furanic acidic subunit (purple symbols in Figure 5.3). According to these results, starting from a "critical" length of the glycolic subunit's length, only the samples with an even number of methylene units in the glycolic subunit are able to crystallize, at least in the conditions experienced during a heating ramp at 10 $K.min^{-1}$ after melt quenching. These results clearly indicates that furan-based polyesters have different aptitudes to crystallize depending on the number of methylene groups in the glycolic subunit: odd numbers suppress crystallization, even numbers allow it.

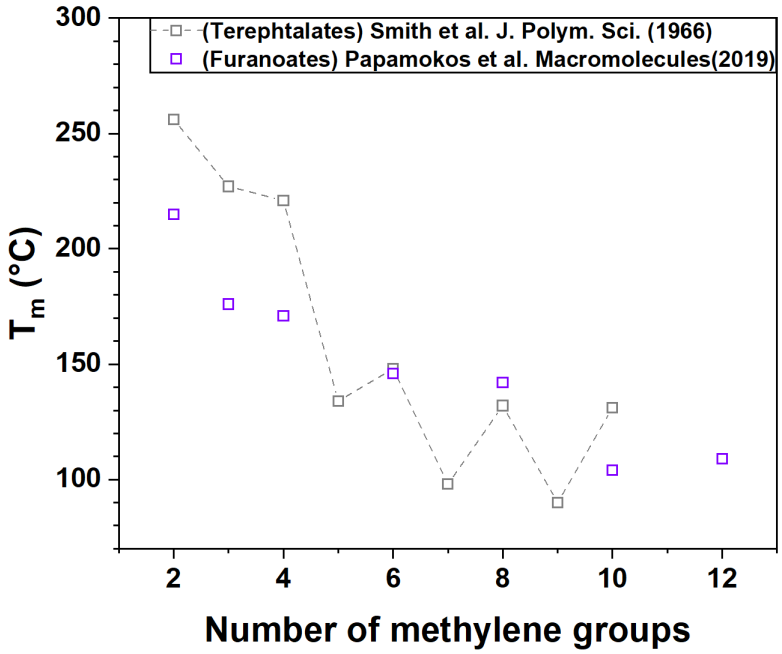

Figure 5.3: Melting temperature as a function of the number of methylene groups in the glycolic sub-unit. Purple open squares are the results obtained in the work of Papamokos et al. [10] on a wide range of poly(n-methylene furanoate) samples and the grey point are the results obtained by Smith et al. [12] on a study of poly(n-methylene terephtalate) samples. The grey dashed line is a guide for the eye.

5.2 Glycolic sub-unit's length effect on the molecular mobility of the amorphous phase

5.2.1 Effects on the molecular mobility in the glass transition temperature range

Figure 5.4 shows the Reversing Heat Capacity signals measured by MT-DSC in the glass transition region on the considered furanoate samples (and their terephthalate counterpart for comparison purposes) after melt quenching. All the samples were successfully quenched to a fully amorphous state, except PBT. The thermal properties extracted from Figure 5.4 are reported in Table 5.2.

Table 5.2 shows that, for both furanoate and terephthalate samples, an increase in the glycolic subunit's length leads to a decrease in the glass transition temperature (measured as the midpoint of the glass transition) that can be attributed to the increased flexibility of the polymer chains (see section 4.2). It also appears that the furanoate samples tend to have higher glass transition temperatures with respect to their terephthalate counterparts, except when the number of methylene groups is equal to 4. These findings suggest that the furanoate samples have a less flexible backbone and/or develop stronger intermolecular interactions with respect to the terephthalate samples. In a recent study comparing the chain motions in PEF and PET, Burgess et al. [14] showed that the furan ring-flipping motions are highly suppressed due to the non-linear axis of ring rotation in addition to a strong ring polarity, which is not the case of the phenyl ring-flipping motions in PET. This is consistent with the fact that PEF has a

less flexible backbone with respect to PET.

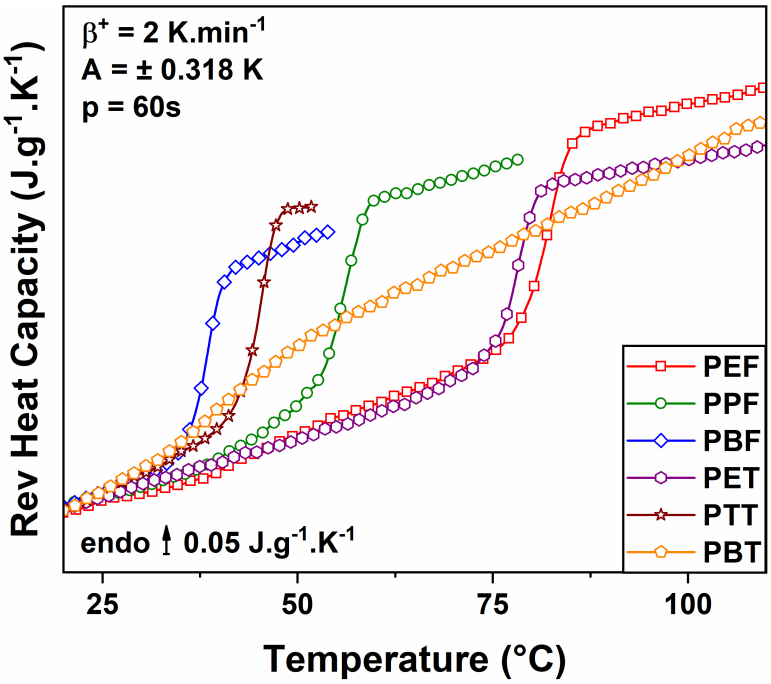

Figure 5.4: Reversing heat capacity curves of amorphous poly(n-methylene furanoate) and poly(n-methylene terephtalate) samples except for PBT sample for which no amorphous sample was obtained.

The cooperativity length was estimated for all the samples according to Donth's model (section 1.2.4). From the literature and as reported in Chapter 4, variations of CRR size in a system are generally attributed to: (1) chemical and/or physical modifications of the intermolecular interactions [15, 16, 17, 18, 19]; (2) confinement effects [20, 21, 22, 23].

Table 5.2: Thermal parameters extracted from the MT-DSC curves. T_g is the glass transition temperature, T_c and T_m are respectively the cold crystallization and melting temperatures measured at the maximum of the peak. δT_{cc} is the width of the cold crystallization peak measured as the difference between the onset and endset temperatures of the cold crystallization peak. ΔT_g and ΔC_p^0 are the width of the glass transition and the Heat Capacity step change at the glass transition temperature estimated from the Reversing Heat Capacity signal using the 16-84% method by Hempel et al. [15]. T_α and δT_g are respectively the temperature and the width of the α-relaxation peak observed on the Non-Reversing Heat Capacity signal. ξ is the characteristic length of dynamic glass transition estimated according to the Donth model[24, 25].

SAMPLE	T_g ±1 [°C]	ΔT_g ±1 [°C]	ΔC_p^0 ±0.01 $[J.g^{-1}.°C^{-1}]$	T_α ±1 [°C]	δT_g ±1 [°C]	ξ_α ±0.1 [nm]
PEF	83	6.8	0.39	82	2.8	3.4
PPF	57	7.7	0.37	56	2.6	2.7
PBF	38	4.3	0.33	38	2.6	2.8
PET	80	4.7	0.32	79	2.1	3.5
PPT	47	3.9	0.36	44	2.1	3.3
PBT	43	13.5	n.d	41	4.7	2.4

Regarding the sample analyzed in this work, Table 5.2 shows that the CRR size decreases as the glycolic subunit's length increases in both furanoate and terephtalate based polymers. Regarding the PBT sample, the CRR size value is much lower than the PET and PPT ones,

this finding could be attributed to the fact that the PBT sample used in this work is semi-crystalline. Indeed, it has been shown that the cooperativity length is highly impacted by confinement effects, such as the ones introduced by the crystallization process [26, 27].

Concerning the other samples, confinement effects do not seems to be a possible explanation of the CRR size decrease since all the samples were measured in their fully amorphous state. This behavior could then be attributed to a change in intermolecular interactions as a result of the introduction of a longer glycolic sub-unit. Indeed, an increase of the glycolic sub-unit length leads to a decrease of the dipole density which thus leads to a decrease in intermolecular interactions strength as reported for other polymeric systems [17, 19]. In the case of the terephthalate samples, the increase in the glycolic subunit's length seems to have a less significant effect on the intermolecular interactions. The loss of inter-chain interactions related to the increase in the glycolic subunit's length is more pronounced in the case of the furanoate samples; however, an effect is observed only when the number of methylene groups increases from $n = 2$ to $n = 3$, because the presence of an additional methylene ($n = 4$) has no influence on the value of ξ. In the future it would be interesting to investigate a longer series of samples ($n > 4$) to confirm the existence of a "cooperativity threshold" at $n = 3$, beyond which the inter-chain interactions are not significantly affected by a further increase in the glycolic subunit's length.

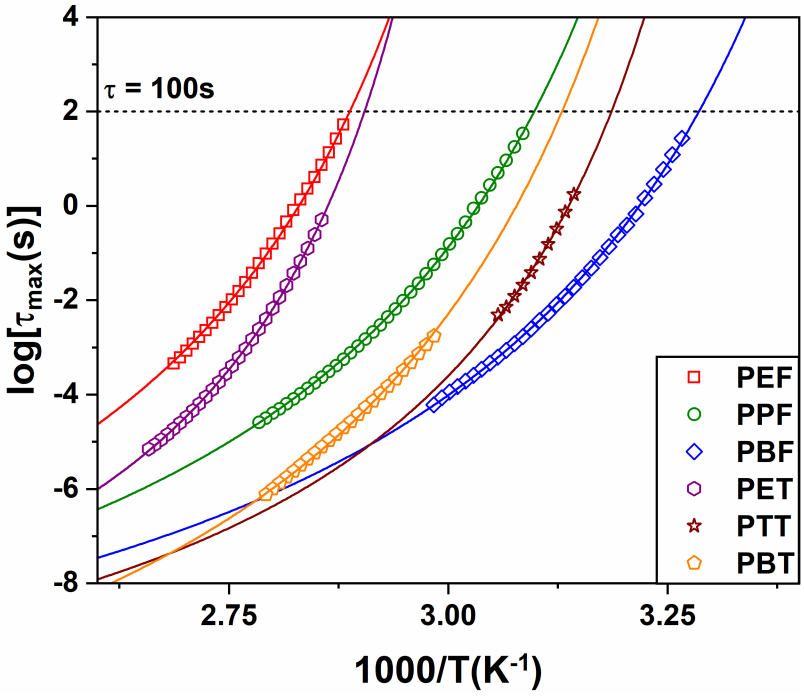

Figure 5.5: Relaxation map of amorphous poly(n-methylene furanoate) and poly(n-methylene terephtalate) samples except for PBT for which no amorphous sample was obtained. Solid lines are in every case the line of best fit using the VTF equation.

The relaxation maps (i.e. Log10 [τ_{max}] as a function of 1000/T), obtained by dielectric relaxation spectroscopy measurements (DRS) on the fully amorphous samples (except for PBT

sample), are reported in Figure 5.5. All the samples show a non-linear dependence of the α-relaxation time with temperature. The Vogel-Tamman-Fulcher (VTF) law was used to fit the experimental data in the α-relaxation temperature range. The VTF fitting procedure provided the information reported in Table 5.3, i.e. the dielectric glass transition temperature $T_g(100s)$ along with the fragility index m calculated according to Angell's equation (equation 1.4).

The value of m is not significantly impacted by the increase in the glycolic subunit's length, only the value of $T_g(100s)$ decreases. Besides, the values of dielectric glass transition temperature are similar to the values of calorimetric glass transition temperature determined by MT-DSC (Table 5.2), whose decrease has been attributed to the increased flexibility of the polymer chains as a consequence of the increased glycolic subunit's length. As pointed out in recent studies and as discussed in Chapter 4, the fragility index is supposed to be mainly dependent on the packing efficiency of the amorphous chains [28, 29, 30] as well as on the stiffness of their backbone [16, 31, 32, 33].

Therefore, if the backbone flexibility actually increased as a consequence of longer glycolic subunits as it has been reported for other polymeric systems [34, 35], a decrease in the fragility index should have been observed in both the furanoate and terephthalate samples. However, the fragility index of the furanoate samples is constant independently of the glycolic subunit's length. The same trend has been observed by Papamokos et al. [10] for a wider range of furanoate samples; they showed that the fragility index does not depend on the glycolic subunit's length. This is consistent with the conclusions previously drawn by Soccio et al. [36] about PBF, asserting that fragility is mainly correlated to the molecular motions of the acidic moiety. However, the literature reports that in systems allowing π-staking, an increase in the glycolic subunit's can lead to a poorer packing efficiency [37]. It is possible to assume that the increase in chain flexibility is compensated by a decrease in packing efficiency, which can eventually explain the overall constant fragility index observed for all the furanoate samples. On the other hand, in the terephthalate samples, a slight decrease in the fragility index is observed as the glycolic subunit's length increases, likely explained by an overall increase in chain flexibility accompanied by a slight decrease in the packing efficiency.

The values of fragility index obtained on furanoate samples have then been compared to the ones obtained on terephthalic samples (Table 5.3). Furanoate samples tend to have lower values of m as compared to terephthalic samples, which indicates that they are more flexible and/or have a better chain packing efficiency, according to the litterature [16, 31]. However, in this work it has been previously showed that terephthalic samples tend to have a higher backbone flexibility as compared to furanoate samples [14], which in turns indicates that furanoate samples have a higher chain packing efficiency as compared to their terephthalic counterparts. This difference in packing efficiency could be due to the fact that the furan ring allows π-stacking in a more efficient way than the terephthalic ring, probably because of the strong dipolar moment

born by the furanic heterocycle [38].

Table 5.3: Parameters obtained from the VTF fitting procedure applied to the DRS experimental curves. T_g (τ=100s) is the dielectric glass transition temperature, i.e. the temperature at which a relaxation time of 100s is observed, m is the fragility index, $m - m_v$ and m_v are the isobaric and the isochoric fragilities, respectively.

SAMPLE	T_g**(100s)**[°C]	**m**	$\mathbf{m - m_v}$	$\mathbf{m_v}$
PEF	73	116	74	42
PPF	58	111	37	74
PBF	37	111	41	70
PET	71	160	81	79
PPT	40	150	68	82
PBT	46	135	26	109

Figure 5.6 reports the values of fragility index vs. the values of cooperativity for all the samples investigated in this work, as well as for other samples whose values were found in the literature. The theoretical domain of the volume contribution (grey area) was determined according to Hong's equation [16] and superimposed on the experimental and literature data. For a given value of α_T/κ, if the change in fragility is only induced by the variations of cooperativity, then the evolution of m correlated to the cooperativity length ξ_α should follow a linear trend. This statement is verified here in the case of terephthalate samples. Their behavior is similar to the one observed in PLA samples with different contents of plasticizer in a study by Araujo et al. [19]. In terephthalate samples, fragility and cooperativity are correlated, which means that the isochoric fragility m_v is expected to remain constant as the glycolic subunit's length increases.

However, as shown by the red (PEF), blue (PPF) and green (PBF) dots in Figure 5.6 this behavior is not observed in the case of furanoate samples, since fragility remains constant in spite of a change in cooperativity. A similar trend has also been reported in the case of poly(ethylene-vinyl acetate) (EVA) copolymer systems by Soto et al. [17]. In their work, they studied the segmental mobility of amorphous EVA copolymers with different vinyl acetate (VAc) contents and showed that : (1) the cooperativity decrease as the VAc content decreases (which was attributed to a decrease in intermolecular interactions) (2) the fragility does remain quite constant whatever the VAc content. As a consequence, no direct correlation between the fragility and the cooperativity was evidenced.

The results shown in Figure 5.6 indicates that the isochoric fragility m_v does not remain constant as the glycolic subunit's length increases. Figure 5.7 reports the isobaric and isochoric contributions to the fragility index obtained with Hong's equation, and gives a better illustration of the variation of $m - m_v$ and m_v in both furanoate and terephthalate samples. As previously observed, the isochoric fragility m_v of terephthalate samples is not dependent on the glycolic subunit's length, except in PBT where the increase observed in the isochoric fragility is due to the presence of crystals. In the case of furanoate samples, the volume contribution significantly decreases as the length of the glycolic subunit increases, which can be explained

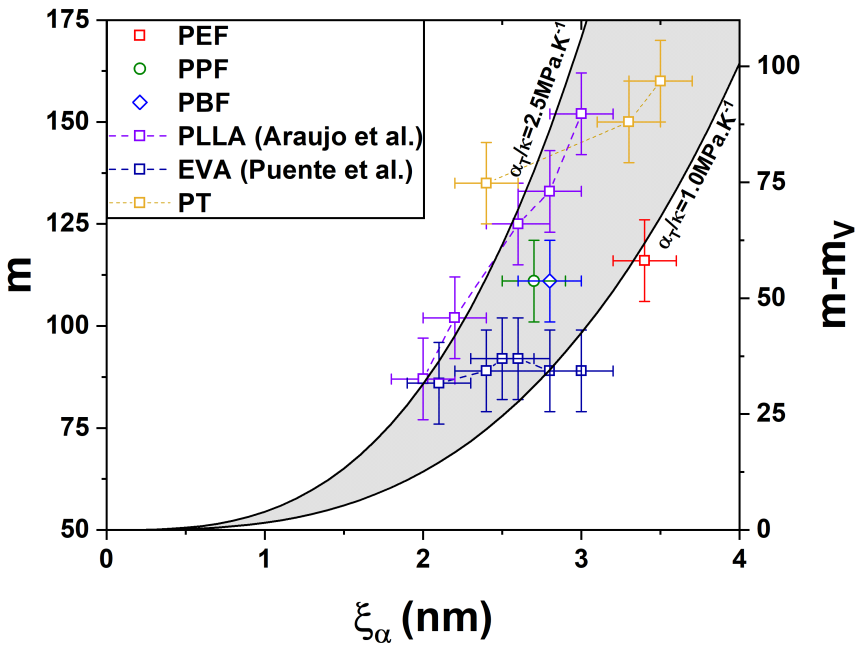

Figure 5.6: Fragility index plot against cooperativity length for different polymers. The data for poly(L-lactic acid) (PLLA) and poly(ethylene-vinyl acetate) (EVA) copolymers were extracted from the works by Araujo et al. [19] and Soto Puente et al. [17]. The data for poly(ethylene furanoate) (PEF), poly(propylene furanoate) (PPF), poly(butylene furanoate) (PBF) and poly(n-methylene terephthalate) (PT) were obtained experimentally in this work. Dashed lines are added as a guide for the eye. The black solid lines are the theoretical $m - m_v$ curves obtained using α_T/κ ratios of 1.0 and 2.5 $MPa.K^{-1}$ respectively, and the grey area represents the theoretical domain of the volume contribution $m - m_v$.

by a decrease in cooperativity. This decrease in the volume contribution is accompanied by a significant increase in the isochoric fragility. However, as shown in Figure 5.7, this trend is only observed when the number of methylene groups is increased from $n = 2$ to $n = 3$, whereafter changes in the number of methylene groups has no significant effect on both the volume and isochoric contributions. Figure 5.7 clearly shows that PEF and PET samples have similar volume contributions to the fragility index, which is expected to correlate with similar cooperativity length. However, PET shows a significantly higher isochoric fragility with respect to PEF.

According to Hong et al. [16], isochoric fragility is mainly dependent on the chemical structure such as the type of intermolecular interactions (hydrogen-bonding, ionic or Van der Waals interactions) as well as intramolecular degrees of freedom (rotational energy barriers in the case of polymers). In their study, Hong et al. showed that an increase in chain flexibility leads to a decrease in m_v value. Literature also reports that the two main parameters affecting the fragility index value are the backbone stiffness and the packing efficiency [16, 31, 32]. Since PEF and PET samples shows similar volume contributions it is possible to assume that isochoric fragility is impacted not only by backbone stiffness but also by the packing efficiency of the material. As previously mentioned, PET has a greater chain flexibility than PEF so differences observed in m_v values might be attributed to strong differences in chain packing efficiency. As shown in the literature [10], PEF has a good packing efficiency of the amorphous phase through

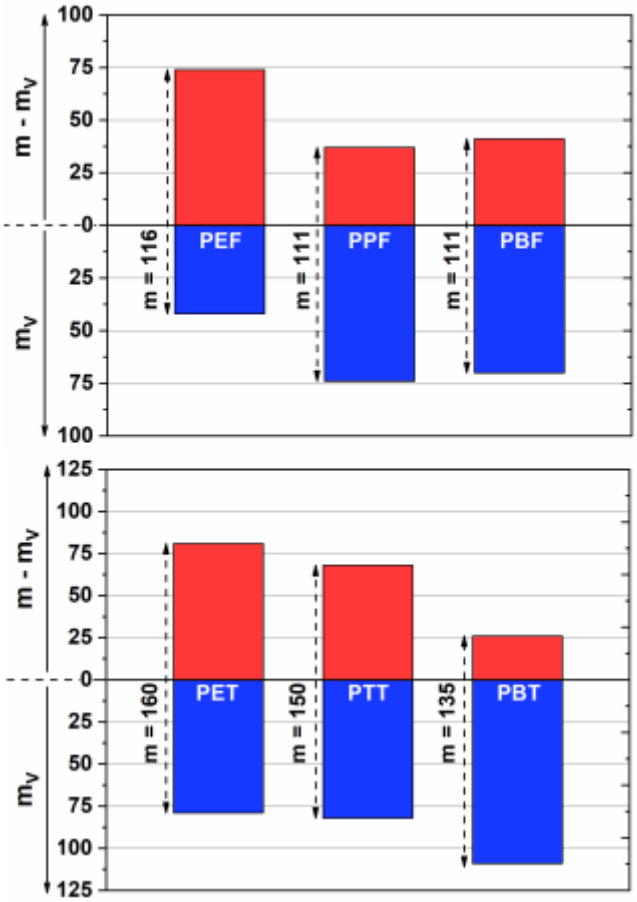

Figure 5.7: Isobaric (red) and isobchoric (blue) fragilities as a function of the number of mehtylene units in the glycolic sub-unit of poly(n-methylene furanoate) samples.

pi-stacking of the aromatic rings. This finding indicates that an increase in packing efficiency leads to a significant decrease in the isochoric fragility value. This assumption is supported by the differences observed between PEF, PPF and PBF isochoric fragilities. The lower isochoric fragility of PEF being due to its greater chain packing efficiency as compared to PPF and PBF. From Figure 5.7, it is possible to notice that PPF and PTT have different volume contribution as an effect of cooperativity differences that are not observed between PEF and PET. However, they show similar values of isochoric fragility which can be attributed to differences of backbone stiffness and chain packing efficiency that are compensating with PPF having a stiffer backbone but a better chain packing efficiency. As shown in Figure 5.7, PBT shows a high value of isochoric fragility as compared to all the other samples. This difference could be due to the poor chain packing efficiency of PBT as a result of its semi-crystalline behavior.

5.2.2 Effect on the dynamics of the local relaxation processes

Figure 5.8 displays the imaginary component of the dielectric permittivity measured in the low-temperature region, which are the expression of local molecular dynamics. These signals

were fitted with the following Cole-Cole function:

$$\varepsilon^*(\omega) = \varepsilon_\infty + \frac{\Delta\varepsilon}{1 + [i\omega\tau_{cc}]^b} \tag{5.1}$$

Where ε_∞ is the high-frequency limit of the real component of the dielectric permittivity, $\Delta\varepsilon$ is the dielectric strength, τ_{cc} is the relaxation time and b is a shape parameter. As previously reported in the literature [13, 36, 39, 40], two Cole-Cole functions are sometimes necessary to give a proper description of the local molecular motions in poly(propylene furanoate) and poly(butylene furanoate). The faster contribution (β_1) was attributed to the rotation of the bond linking the ester function to the oxygen between the acidic and the aliphatic subunits; the slower contribution (β_2) was associated with the motion of the ester function with respect to the aromatic ring in the acidic subunit. The literature [38, 41] showed that in the case of PEF a single contribution may be enough to fit the experimental data; according to Soccio et al. [36], it could be due to the concomitant presence of a highly rigid ring unit linked to a short aliphatic unit that are relaxing at similar energy levels. However, in some other polyesters including poly(ethylene terephthalate) [13, 39, 42], the literature clearly reports the presence of at least two local relaxation processes. It is therefore natural to wonder whether the β relaxation process in PEF can be deconvoluted into two partially overlapping contributions, as already reported for PPF and PBF [36, 40]. To this purpose, the experimental data were fitted with a single contribution and two Cole-Cole functions.

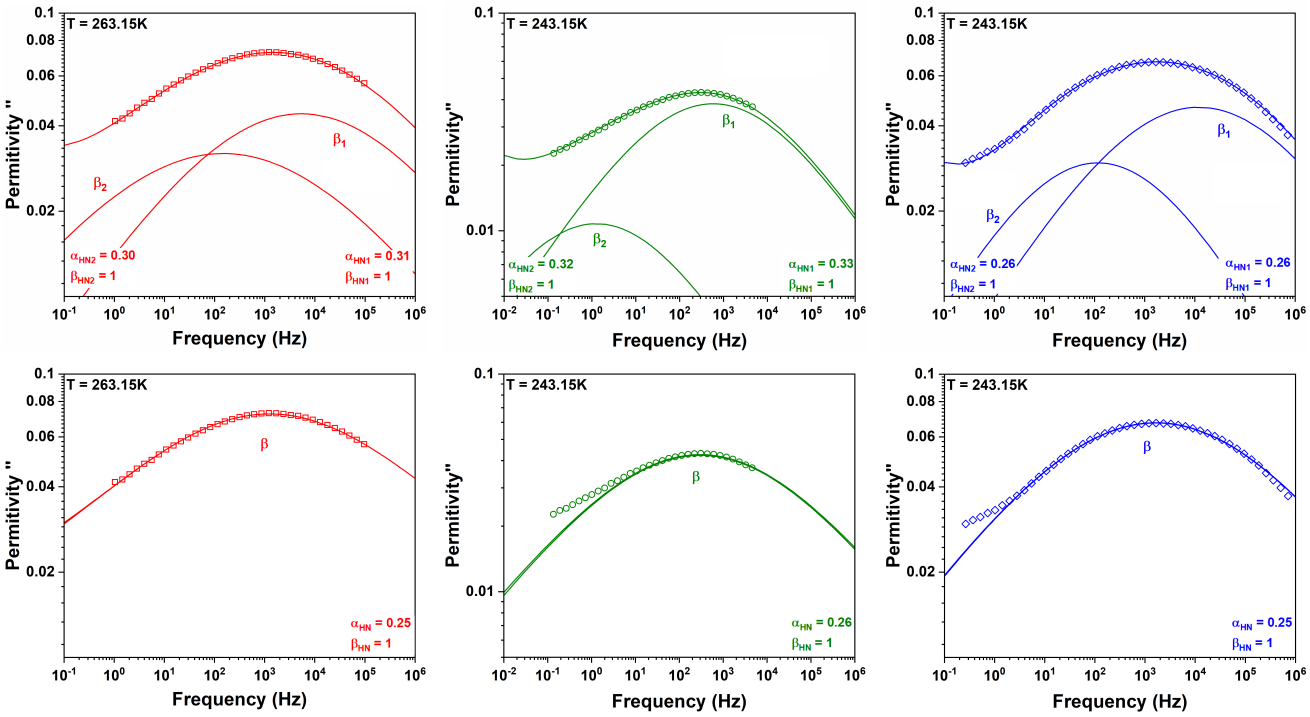

Figure 5.8: Imaginary components of the dielectric response of PEF (in red), PPF (in green) and PBF (in blue) measured by DRS at the indicated temperature. The colored dots are the experimental results and the solid lines are the lines of best fit using Cole-Cole functions for the β_1 and β_2 relaxation processes (top figures) and a single β relaxation process (bottom figures) with α_{HN} and β_{HN} being the fit parameters.

Figure 5.8 shows that all the experimental data are well described using two Cole-Cole contributions, which supports the results previously reported by Soccio et al. [36, 40]. Moreover, it appears that using a single contribution do not allow an efficient fitting of the PPF and PBF experimental curves. However, in the case of PEF a single contribution seems to be sufficient to provide a good fitting of the experimental results which in turn does not allow to assume that two Cole-Cole functions should be used to fit the PEF experimental curve. The temperature dependence of both the β_1 and β_2 relaxations were then described using the following Arrhenius law:

$$\tau = \tau_{0,A} exp(\frac{E_a}{RT}) \tag{5.2}$$

Where $\tau_{0,A}$ is a pre-exponential factor, R is the gas constant and E_a is the activation energy of the β relaxation process. The results of this fitting process are illustrated in Figure 5.9; the corresponding activation energies are reported in Table 5.4, along with the results found in the literature for the terephthalate counterparts of the investigated samples.

As shown in Figure 5.9 and as reported in the literature [36, 39], the β_2-relaxation process progressively merges with the β_1 relaxation process as the temperature increases; after this merging, the local dynamics can be described using a single relaxation process that follows the temperature dependency of the β_1 relaxation. Moreover, it appears that the activation energy of the β_1 process is very close to the activation energy of the β process obtained using a single contribution fit. Therefore, it appears that a single contribution fitting procedure is suitable to fit the experimental data in the high temperature region as the β_2 and β_1 process are hardly distinguished. Yet, in the low temperature region a fitting procedure using two Cole-Cole functions gives a more rigorous description of the local processes dynamics.

The activation energies of both the β_1 and β_2 relaxation processes for PPF and PBF are in close agreement with the values reported in the literature Table 5.4. For the terephthalate samples, the literature reports that the activation energy of the faster β_1 relaxation process increases as the glycolic subunit's length increases, whereas the activation energy of the slower β_2 relaxation process remains constant [43]. This trend is not observed in the case of the furanoate samples.

In agreement with the literature [40], no clear dependency of the activation energy of the faster β_1 relaxation process is observed with respect to the glycolic subunit's length in the furanoate samples. An even-odd dependency of the activation energy of the β_1 relaxation process could be assumed; however, this requires investigating a longer series of furanoate samples (number of methylene groups larger than 4) for confirmation. Indeed, further measurements are required to reinforce the statistics of these results, and to determine whether the differences observed as a function of the number of methylene groups are significant or due to measurement uncertainties. Anyway, it appears that the activation energy of the β_1 process in PEF is smaller compared to PPF and PBF, whose values are equals within experimental errors. This

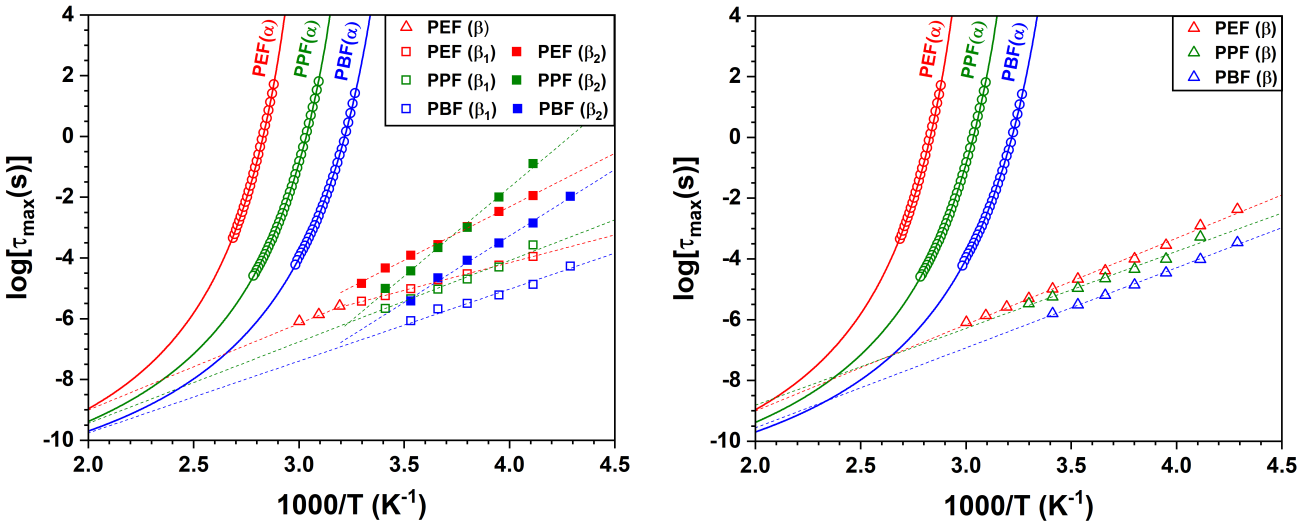

Figure 5.9: Relaxation map measured on amorphous poly(n-methylene furnaoate) samples. On the left, empty squares corresponds to the relaxation times associated to the β_1 process and the solid dots are the relaxation times of the β_2 process. Dashed lines are the lines of best fit using the Arrhenius equation (equation 5.2) from which activation energies have been determined. Empty dots are the relaxation times associated with the α-relaxation and the solid lines are the lines of best fit using the VTF equation. On the right, empty triangles corresponds to the relaxation times associated to the β relaxation using a single contribution.

finding indicates that, as reported for the terephthalate samples, the energy barrier associated with the rotation of the bond linking the ester function to the oxygen between the acidic and the aliphatic subunit is dependent on the glycolic subunit's length [43]. The previous assertion seems to be verified only for a number of methylene groups up to n = 3, whereafter no more increase in the activation energy of the β_1 relaxation process is observed, which is in good agreement with the results reported by Soccio et al. [40].

Table 5.4: Activation energies E_a of the local molecular dynamics of furanoate and terephthalate samples containing different glycolic subunits.

SAMPLE	PEF	PPF	PBF	PET	PTT	PBT
$\mathbf{E_a}(\beta_1)$ $\pm 10 kJ.mol^{-1}$	35	55 / 52 [40]	42 / 50 [36]	17 [44]	23 [43]	43 [39]
$\mathbf{E_a}(\beta_2)$ $\pm 10 kJ.mol^{-1}$	67	113 / 112 [40]	84 / 89 [36]	48 [44]	49 [43]	62 [39]

On the other hand, the activation energies of the β_2 relaxation process seem to follow an even-odd effect. Soccio et al. [40] reported that the β_2 relaxation process originates from the motions of the ester group with respect to the furan ring; as a consequence, one may conclude that having an odd number of methylene groups in the glycolic subunit is the most effective configuration to hinder the ring-flipping motions in the acidic subunit. It is also worth noticing that the activation energy of the β_2 relaxation process in PBF is significantly higher compared to PEF. This result can be attributed to a difference in the interchain interactions (dipolar interactions and π-stacking) that can also contribute to hinder the furan ring-flipping motions [40].

When compared to their terephthalic counterparts, the activation energies of the β_1 and β_2 relaxation processes of furanoate samples are in all cases higher. This result has been previously observed by comparing PBF and PBT [36] and has been attributed to the difference in backbone flexibility. The intrinsically higher stiffness of furan-based materials inhibites the ring-flipping motions as a result of lower bond angles and higher polarity of the furanoic acid as compared to the terephthalic acid [36].

5.3 Application of the three-phase model

The results reported so far are about the molecular mobility and dynamics in the amorphous phase, and are not only interesting to compare and predict the properties of the samples in their fully amorphous state, but also to help understanding how the molecular segments behave in the presence of crystals and what are the connections between the crystalline and the amorphous phases (the so-called "phase coupling"). MT-DSC is a powerful tool to unveil even the smallest differences in the thermal behavior of semi-crystalline samples with different microstructures, because it allows separating the total signal into Reversing and Non-Reversing components and provides a good estimation of the temperature dependence of the heat capacity.

Figure 5.10 shows the signals corresponding to the Total Heat Capacity (green), the Reversing Heat Capacity (blue) and the Non-Reversing Heat Capacity (red) measured by MT-DSC on furanoate samples crystallized from the glassy state (on the left) and from the melt (on the right) according to the protocols reported in Chapter 2. The green curves show that all the samples (whether they are crystallized from the glassy state or from the melt) experience a complex endothermic process that appears to proceed through a sequence of more or less overlapping phenomena, i.e. a sort of "multiple melting peaks". The fact that furanoate samples have a complex melting behaviour has already been widely discussed in the literature [6, 8, 45] and the following hypotheses have been made to explain the origin of this complex situation: (1) more than one crystallographic form develop during the crystallization process (polymorphism) and eventually coexist; (2) the crystalline form developed during the crystallization process is defective, therefore melting/recrystallization processes occurr during the heating ramp; (3) the "multiple melting peak" is a consequence of a broad and inhomogeneous crystal size distribution resulting from more than one crystallization process (primary, secondary...) and/or from heterogeneity in the molecular weight distribution [46, 47].

Regarding the samples crystallized from the glassy state at T_c=125°C (Figure 5.10 on the left), a distinction can be made between the samples containing an even and an odd number of methylene groups in the glycolic subunit. In the case of PEF and PBF (which contain $n = 2$ and $n = 4$ of methylene groups respectively), two endothermic peaks can be identified on both the Total Heat Capacity (green line) and on the Non-Reversing Heat Capacity signals (red line), and a significant exothermic peak is observed in between on the Non-Reversing Heat Capacity

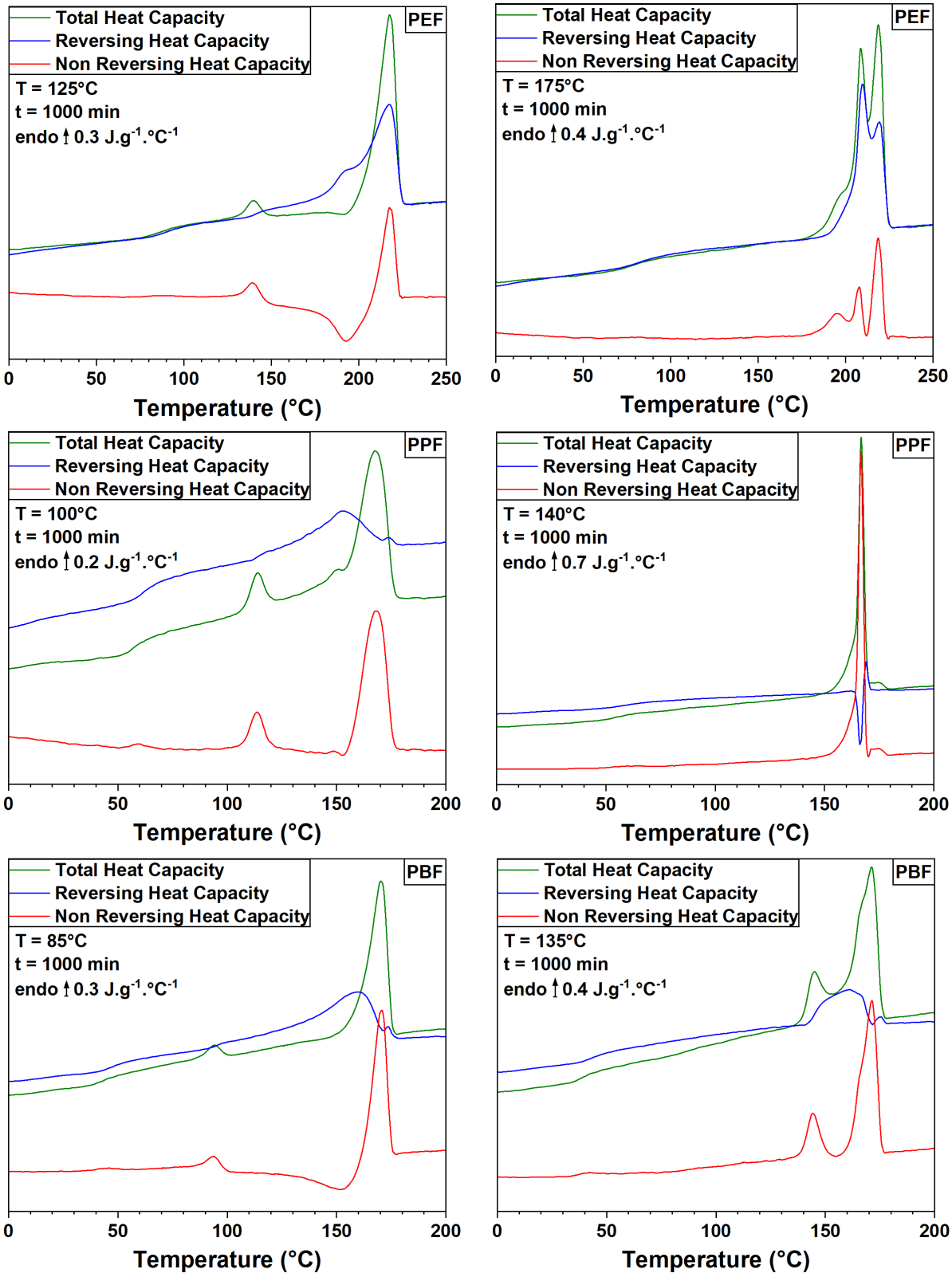

Figure 5.10: Total (green), Reversing (blue) and Non-reversing (red) heat capacity curves obtained through MT-DSC measurements (a = ±0.32K, β^{+}=$2K.min^{-1}$ and p =60s), on samples crystallized from the glass (on the left) and crystallized from the melt (on the right).

signal; this exothermic peak is accompanied by a broad endothermic peak on the Reversing Heat Capacity signal (blue line). This observation confirms that furanoate samples are generally prone to non-negligible melting/recrystallization processes upon heating at low heating rates [6, 8]. The extent of such processes as well seems to be dependent on the number of methylene groups in the glycolic subunit, and may eventually follow an odd-even effect, because the MT-DSC curves obtained for PPF (which contains $n = 3$ of methylene groups) are slightly different compared to the curves obtained for PEF and PBF. The Total Heat Capacity signal for PPF (green line) displays two endothermic peaks as well; the main difference with the samples containing an even number of methylene groups is observed on the Non-Reversing Heat Capacity signal (red line), which contains no exothermic peaks. No signs of melting/recrystallization processes upon heating at standard heating rates are visible on the MT-DSC curves recorded for PPF, or maybe these processes are concealed by concomitant endothermic signals that are difficult to separate. The latter assumption is however more in agreement with the literature, since melting/recrystallization processes have already been reported in PPF samples crystallized at low temperature and heated at low heating rate [8]. This is also consistent with the presence of a broad endothermic peak, as displayed on the Total Heat Capacity signal (green line) of the PPF sample; this indicates that the crystalline fraction is highly defective and has a broad distribution of crystal sizes, as one should expect from a sample crystallized at a low temperature from the glassy state.

The samples crystallized from the molten state (Figure 5.10 on the right) display a significantly different behaviour as compared to those crystallized from the glassy state. The common point is that, once again, a clear distinction can be made between the samples containing an even number of methylene groups (PEF and PBF) and the sample containing an odd number of methylene groups (PPF). Indeed, PEF and PBF exhibit a broad melting process that seems to proceed through three partially overlapping endothermic phenomena, while PPF displays a sharp melting peak with a small wing on the low-temperature side. Contrarily to the samples crystallized from the glassy state, no exothermic processes are observed prior to the final melting, which indicates that no melting/recrystallization processes are clearly evidenced at low heating rates in this peculiar crystallization conditions. However, once again, it is not possible to exclude that melting/recrystallization processes occur and are just hidden by the concomitant melting process. Clearly, the existence of melting/recrystallization processes is not a sufficient explanation for the multiple-peak behaviour displayed by furanoate samples on DSC and MT-DSC curves.

Things are made complex also by the fact that different crystallographic forms have been evidenced in furanoate samples [5, 6, 7, 8], as already mentioned in section (4.2), which could be a good/additional explanation for the complex melting behavior observed in Figure 5.10. Yet, it has been shown that the crystallographic forms reported for PEF and PBF are not really due to polymorphism, but to the possibility of having a highly defective α' crystalline

form and a more perfect α crystalline phase. The temperatures used for the crystallization protocols in this work were in all cases set at values where only the defective α' or the more perfect α crystalline phase is formed. Maybe the complex melting behaviour observed for PEF and PBF crystallized from the glassy state is due to the reorganisation of the α' crystals into α crystals. This possibility, however, does not explain the presence of the small endothermic peak at low temperatures, which is visible in all the investigated samples.

The literature reports [8] that, additionally to the α and α' crystalline forms, a third crystalline form called β can develop in PPF. This form has been evidenced after isothermal crystallization from the melt at crystallization temperatures higher than T_c = 140 °C and is supposed to develop concomitantly with the α crystalline form at crystallization temperatures up to T_c = 155 °C. The coexistence of α and β crystals with similar thermal stability is thus a good explanation of the complex melting processes displayed by PPF crystallized from the melt. Moreover, as it is the case for PEF and PBF, the complex melting behaviour displayed by PPF crystallized from the glassy state is most probably due to the reorganization of the α' crystals into α crystals upon heating.

Another possible explanation is that the multiple melting peak behaviour originates from the presence of a large distribution of crystal sizes in the sample. This hypothesis seems to be reasonable in the case of PPF, whose melting peak is broad but not made of sparse and distant overlapping contributions. Indeed, in PEF, the difference in the melting temperatures of the first small peak and the second peak is too big. Thus, crystal size distribution due to heterogeneity in the molar weight distribution does not seem to be a likely explanation of the multiple endothermic peak shown by the furanoate samples. Regarding the presence of the small endothermic peak at temperatures close to the crystallization temperature, the same feature has already been observed in the literature for other polymers, and is often referred to as an "annealing peak" that originates from the melting of highly defective crystals formed during the secondary crystallization process [8, 45, 48, 49]. An annealing peak was recorded for all the furanoate samples, independently on the crystallization path. When crystallized from the glassy state, the annealing peak looks like a single endothermic peak well separate from the following thermal transitions; when crystallized from the melt, it appears as a single endothermic peak for PBF and an endothermic wing on the low-temperature side of the melting peak in PEF and PPF.

In fact, the complex melting processes displayed by the furanoate samples could originate from a combination of all the three hypothesis previously made. In order to assess the previous assumptions, the results obtained by MT-DSC were compared to the ones obtained by FSC on PEF, already presented and exploited in Chapter 3 and reproduced here for comparison purposes on Figure 5.11.

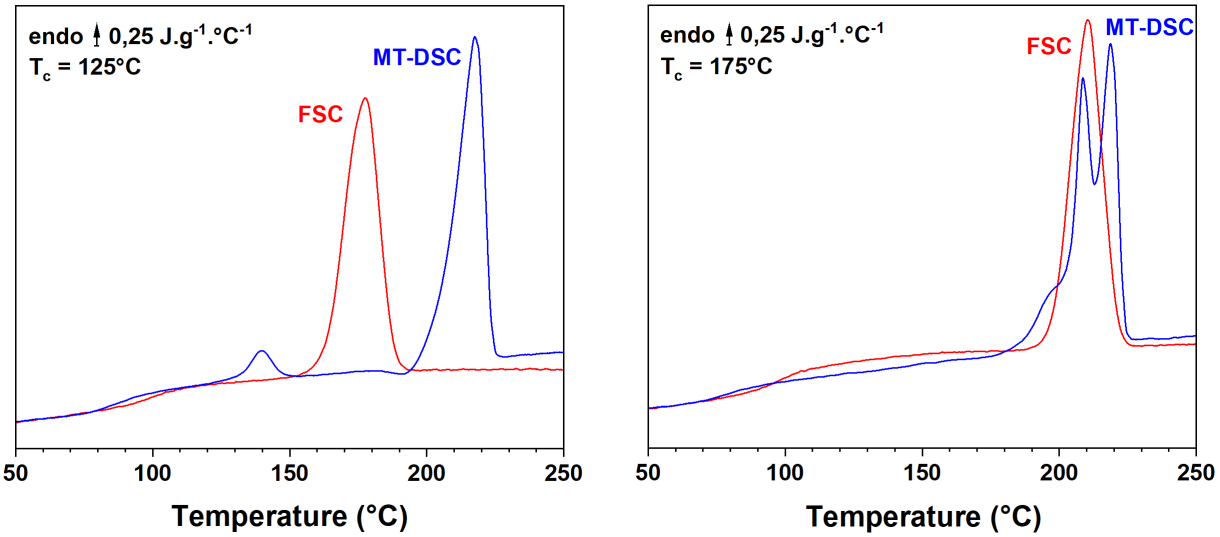

Figure 5.11: Total heat capacity recorded on a PEF sample through MT-DSC (blue) and FSC (red) after crystallization at T_c = 125°C (on the left) and T_c=175°C (on the right)

It is important to note that, for the crystallization at T_c = 125 °C (Figure 5.11, on the left), the MT-DSC sample was heated up from the glassy state whereas the FSC sample was cooled down from the melt; even if the subsequent isothermal crystallization was performed at the same temperature, this difference is likely to introduce uncertainties that should not be neglected (see section 1.3.2 of Chapter 1). For this reason, it is more reliable to compare the results obtained on the samples that have been both crystallized from the melt at the crystallization temperature of T_c = 175 °C (Figure 5.11, on the right). The multiple melting peak behaviour observed on the MT-DSC curve of PEF is replaced by a simple melting process in FSC. A good explanation for this discrepancy should consider a combination of two factors : (1) the multiple melting peak behaviour revealed by MT-DSC measurements is caused by a significant melting/recrystallization process that is suppressed using the high scanning rates allowed by FSC [50, 51, 52, 53], and (2) the sample crystallized in MT-DSC has probably undergone a secondary crystallization process, whereas the sample crystallized in FSC has not.

To summarize, furanoate samples have very complex melting processes due to the presence of primary and secondary crystals that are progressively melting and reorganizing in a more perfect crystalline phase upon heating. Moreover, some features of furanoate samples appear to be dependent on the number of methylene groups contained in the glycolic subunit, e.g. the number of methylene groups plays an important role on the crystallization mechanisms. It is then of great interest, and obviously a challenge, to evidence and quantify all the fractions in the microstructure of semi-crystalline furanoate samples. The three-phase model was then applied using the experimental data shown in Figure 5.10; the results are reported in Table 5.5.

Figure 5.12 shows the Reversing Heat Capacity curves measured on the furanoate samples crystallized from the glassy state (blue) and from the melt (red). Since the reference data for

Table 5.5: Amounts of the different fractions present in the sample crystallized from the glass and from the melt. X_c is the crystalline fraction, X_{MAF} is the mobile amorphous fraction and X_{RAF} is the rigid amorphous fraction.

	Cryst from the glass				Cryst from the melt			
SAMPLE	T_g ±1 [°C]	X_c [%]	X_{MAF} [%]	X_{RAF} [%]	T_g ±1 [°C]	X_c [%]	X_{MAF} [%]	X_{RAF} [%]
PEF	96	48	30	22	85	55	38	7
PPF	65	29	43	28	62	35	47	18
PBF	48	45	36	19	44	52	35	13

the temperature dependence of the specific heat capacity were not available in the literature, they were measured on an fully amorphous sample according to the procedure reported by Schick et al. [54]. The heat capacity of the liquid $C_{p_{liquid}}$ was obtained by a linear extrapolation of the baseline recorded in the region from above the glass transition up to the melt. Such a linear extrapolation is a reasonable fit of the experimental data and provides an accurate estimation of the temperature dependence of the heat capacity in the melt and in the supercooled liquid. The solid specific heat capacity $C_{p_{solid}}$ was obtained by a linear extrapolation of the baseline recorded below the glass transition, under the assumption that the heat capacity of a polymer in the glassy state is the same, whether it is amorphous or semi-crystalline. By the way, the same line was obtained on the semi-crystalline samples, which supports the assumption of equal heat capacities for semi-crystalline and amorphous arrangements of the same polymer in the glassy state.

In the absence of excess thermodynamics quantities, heat capacities are additive [54, 55], which allows to determine the baseline heat capacity from a simple mixing rule, as shown by equation (4.1):

$$C_p(T,t) = X_{crystal}(T,t) * C_{p,crystal}(T) + [1 - X_{crystal}(T,t)] * C_{p,liquid}(T) \tag{5.3}$$

Where $C_{p,crystal}$ is the specific heat capacity of the crystal (assumed to be equal to the specific heat capacity in the solid state $C_{p,solid}$), $C_{p,liquid}$ is the specific heat capacity in the liquid state, and $X_{crystal}$ is the crystalline fraction estimated according to the procedure by Mathot [56], i.e from the ratio between the measured melting enthalpy and the equilibrium melting enthalpy. The baseline heat capacities were estimated for each sample according to equation 5.3 and superimposed to the experimental data in Figure 5.12. For PEF and PPF, the experimental Reversing Heat Capacity curves at the end of the glass transition do not reach the baseline heat capacity estimated from the two-phase model, which clearly indicates the presence of RAF [54, 55]. In the case of PBF, signs of a significant excess of thermodynamic quantities is observed between the glass transition and the melting, which does not allow the discussion of the vitrification and devitrification of the rigid amorphous fraction based on the mixing rule applied to the heat capacities [54, 57]. For this reason, in this work the devitrification of the RAF will be discussed only for PEF and PPF.

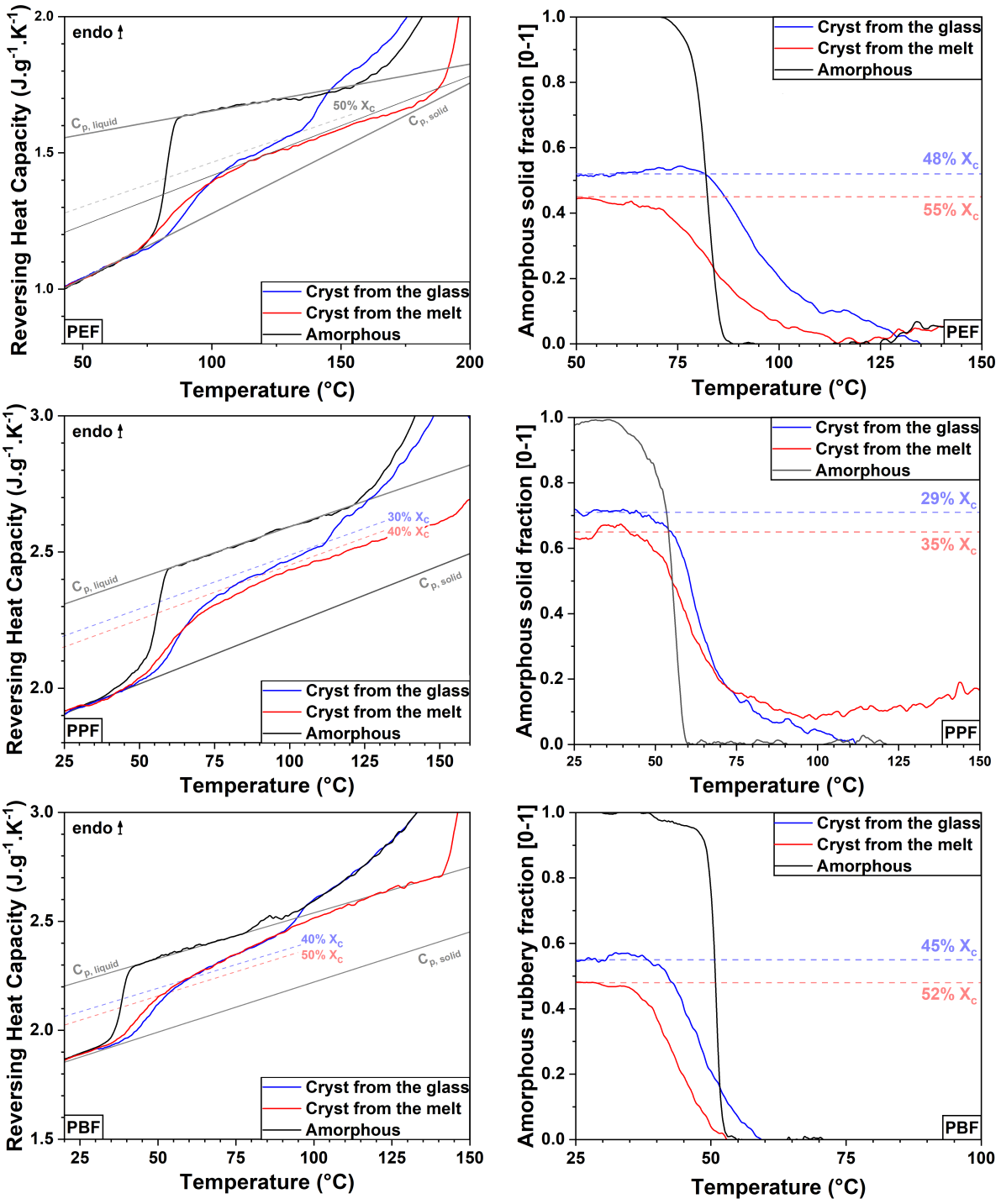

Figure 5.12: Reversing heat capacity signals (on the left) measured on the amorphous (black), crystallized from the glass (blue) and crystallized from the melt (red) samples through MT-DSC. The specific heat capacity of the liquid and solid state were determined experimentally according to the procedure reported by Schick et al. [54] and the baseline heat capacity lines were determined using equation (4.1) and the crystalline degrees reported in Table 5.5. The amorphous solid fraction temperature dependence (on the right) was obtained from equation (4.2) by computing the experimental datas obtained by MT-DSC. The crystalline degree lines displayed in the figure have been obtained using the crystalline degree reported in Table 5.5.

A better depiction of the devitrification of the RAF is obtained by representing the behaviour of the total amorphous solid fraction as a function of temperature (Figure 5.12, right side),

which can be estimated with the following equation:

$$(X_{MA} + X_{RA})_{solid} = 1 - X_{crystal} - \frac{RevC_p(T) - C_{p,solid}(T)}{C_{p,liquid}(T) - C_{p,solid}(T)} \tag{5.4}$$

Where $RevC_p(T)$ is the Reversing Heat Capacity extracted from the experimental curves. Figure 5.12 shows how the amorphous fraction goes from solid (glassy) to liquid as temperature increases, and can therefore be used to distinguish (when possible) the mobile from the rigid amorphous fraction. The dotted lines indicates the crystallinity determined from the experimental data (Table 5.5), and are assumed to be constant in the temperature range between glass transition and melting. Obviously, this assumption is true only for samples crystallized to the maximum extent (i.e. in the absence of cold-crystallization) and undergoing no melting/recrystallization processes (i.e. in the absence of excess thermodynamic quantitities). As an example, Schick and coworkers [54, 57] showed that no heat capacity excess is detected for semi-crystalline polymers such as poly(hydroxybutyrate) (PHB) at temperatures above the glass transition and below the lowest endotherm observed on the Total Heat Capacity signal. Similar considerations should be done for any other semi-crystalline polymer, especially when it is prone to grow complex microstructures. As a consequence, in this work the temperature limits for the furanoate samples were selected based on the Total Heat Capacity signals in Figure 5.11, i.e. by taking the onset melting temperature of the lowest endotherm as previously done by Schick and coworkers for PHB [54, 57]

The crystallization processes from the glassy state and from the melt are expected to induce a different repartition of the amorphous phase into mobile and rigid amorphous fractions. However, in this work it appears that the samples crystallized from the glassy state and from the melt have very similar temperature dependence of the total amorphous solid fraction (Figure 5.12, right side). In particular, the observed dependence is typical of semi-crystalline polymers, with a glass transition that is broader and shifted to higher temperatures (see Table 5.5) as compared to the fully amorphous sample (see Table 5.3) [55, 58, 59, 60, 61]. The literature reports that high-temperature crystallization is supposed to reduce crystal nucleation, favouring the formation of highly perfected crystal and reducing the coupling between the crystalline and amorphous phases, thus reducing the formation of RAF [55, 62, 63, 64]. In most cases, RAF originates from spherulite impingement or from any other kind of geometrical constraints that are hindering a proper organization of the macromolecular chains [65].

Figure 5.12 shows that this assertion is verified for PEF, since the amount of RAF is significantly low in the sample crystallized from the molten state (less than 10%) as compared to the sample crystallized from the glassy state (about 20%). Moreover, the devitrification of the RAF in the sample crystallized from the glassy state is observed over a temperature range of about 25°C, whereas it is not clearly observed in the sample crystallized from the melt.

Ma and coworkers [66] submitted a sample of poly(trimethylene terephtalate) (PTT) to a specific temperature protocol to induce a gradient of microstructural heterogeneity. Then they used the three-phase model to describe the microstructure, thus formed as a discrete structure composed of multiple layers of RAF with different molecular mobility. Later on, Esposito et al. [55] investigated the molecular mobility in a sample of poly(hydroxybutyrate-*co*-hydroxyvalerate) (PHBV) crystallized to the maximum extent from the glassy state, and observed the gradual devitrification of the constrained amorphous fraction rather as a continue distribution of relaxation times, that they described as a "continuum of mobility" (from the crystalline phase, where the mobility is the lowest, through the rigid amorphous fraction, and finally to the mobile amorphous fraction, where the mobility is the highest). This microstructural description of semicrystalline polymers is more subtle than a conventional three-phase model, especially when it comes to microstructures in which the amorphous fractions (mobile and rigid) are strongly coupled to each other, to the point that they cannot be clearly distinguished. As a counterexample, they observed a better decoupling of the phases in a sample of the same polymer crystallized from the melt. Their study showed that the crystallization conditions do not only have an effect on the crystalline phase, but play also a significant role on the mobility landscape within the amorphous phase.

In Figure 5.12, the devitrification of the RAF in PEF starts at temperatures right above the glass transition, and is completed before the temperature range where reversible melting occurs is reached, i.e. before the beginning of the melting/recrystallization processes. This result is in good agreement with the observations made about other semi-crystalline polymers, such as poly(ethylene terephtalate) (PET). The literature reports that two different behaviors can be observed: (1) RAF forms all along the crystallization process [67, 68], or (2) RAF forms after the completion of primary crystallization [54, 67, 69], concomitantly with secondary crystallization, or during the subsequent cooling step. PEF is frequently compared to PET because these two polyesters have similar molecular structures; in PET, the vitrification of the RAF has been observed after the completion of the primary crystallization process, and its devitrification occurs upon heating at temperatures above the glass transition until the melting process starts [69]. The behavior reported in this work for PEF is very similar.

In PPF, the RAF develops with similar mechanisms but in higher amounts, both in the samples crystallized from the glassy state (about 28%) and from the melt (about 20%). Its devitrification in PPF is analogous to the one observed in PEF, i.e. a gradual devitrification occurs starting from the end of glass transition up to the beginning of melting in the sample crystallized from the glassy state. On the other hand, no clear devitrification of the RAF was observed in the sample crystallized from the melt, which could be due to a fast devitrification of the RAF right after MAF devitrification.

5.4 Conclusion

The crystallization and melting behaviors of three different furanoate-based polymers (2,5-PEF, 2,5-PPF and 2,5-PBF) have been studied by differential scanning calorimetry (DSC). When heated from the glassy amorphous state, the sample follow a cold crystallization process in which an imperfect α' crystalline phase is formed. Cold crystallization is then followed by complex melting/recrystallization processes leading to the reorganization of the α' crystalline phase into the more stable α crystalline phase. As a consequence, furanoate samples display complex melting behaviors and the melting enthalpies are measured with significant uncertainties that have to be taken into account. As expected from the results obtained on similar polymeric systems, an increase in the glycolic subunit length in furanoate-based polymers leads to an increase in chain flexibility. This increase is accompanied by the appearance of a so-called "even-odd" effect on the melting temperatures.

The effects of the glycolic subunit length on the molecular mobility in the amorphous phase have then been discussed using the concepts of cooperativity (based on MT-DSC measurements) and fragility (based on DRS measurements). The CRR size in both the furanoate-based and terephthalate-based series of sample decreases as the glycolic subunit length increases, which was attributed to a loss of interchain interactions. However, in furanoate-based polymers this effect is only observed when the number of methylene groups increases from $n = 2$ to $n = 3$, afterwhat a threshold seems to appear. It would thus be of great interest to continue this investigation on a wider series of furanoate polymers (n>4) to confirm the existence of a "cooperativity threshold" at $n = 3$. Regarding the fragility index m, no dependence has been evidenced with the length of the glycolic subunit in furanoate-based polymers, while an overall decrease of the fragility index was observed in terephthalate-based polymers. This finding was attributed to the superposition of two different behaviors : (1) a decrease in the fragility index as a result of an increase in the backbone flexibility; (2) an increase in the fragility index due to a decrease in the chain packing efficiency in the amorphous phase. Using Hong's equation, the isochoric and isobaric components of the fragility index were estimated and it appears that isochoric fragility does not remain constant as the glycolic subunit length increases. This behavior is similar to the one reported in the literature for EVA copolymers, which was attributed in this case to a direct correlation between the isochoric fragility and the chain packing efficiency in the amorphous phase. Lastly, the effects of the glycolic subunit length on the local relaxation processes were discussed and the activation energies of these processes were estimated using an Arrhenius law. The local relaxation processes in furanoate-based polymers can be deconvoluted in two distinct subglass processes, as it has been previously reported for similar polymeric systems. An even-odd dependency of the faster β_1 process was assumed, but investigations on a wider series of sample is needed to confirm this finding. On the other hand, a clear even-odd dependency of the slower β_2 process was observed, and was attributed to an hindering effect on the ring-flipping motions that is stronger in samples containing an odd number of methylene

units.

The samples were then crystallized according to the two thermal protocols reported in Chapter 2, i.e. crystallization from the glassy state and crystallization from the molten state. The crystallized samples were then analyzed using MT-DSC and displayed complex melting behaviors that were attributed to the presence of primary and secondary crystals that are progressively melting and reorganizing in a more perfect crystalline phase upon heating. It also appeared that the number of methylene groups has a significant effect on the crystallization mechanisms of furanoate polyesters. The microstructures were described using the three-phase model to get a deeper insight into the formation of the rigid amorphous fraction. As expected, the samples crystallized from the molten state contain a reduced amount of RAF as compared to the ones crystallized from the glassy state. Moreover, the devitrification of the RAF in the samples crystallized from the glassy state was observed on a wide temperature range, while it was not clearly observed in the samples crystallized from the molten state. The vitrification and devitrification of the RAF in PEF and PPF samples are very similar to the one reported in PET, i.e. the vitrification occurs after the completion of the primary crystallization process and the devitrification is observed upon heating at temperatures above the glass transition temperature until the melting process starts.

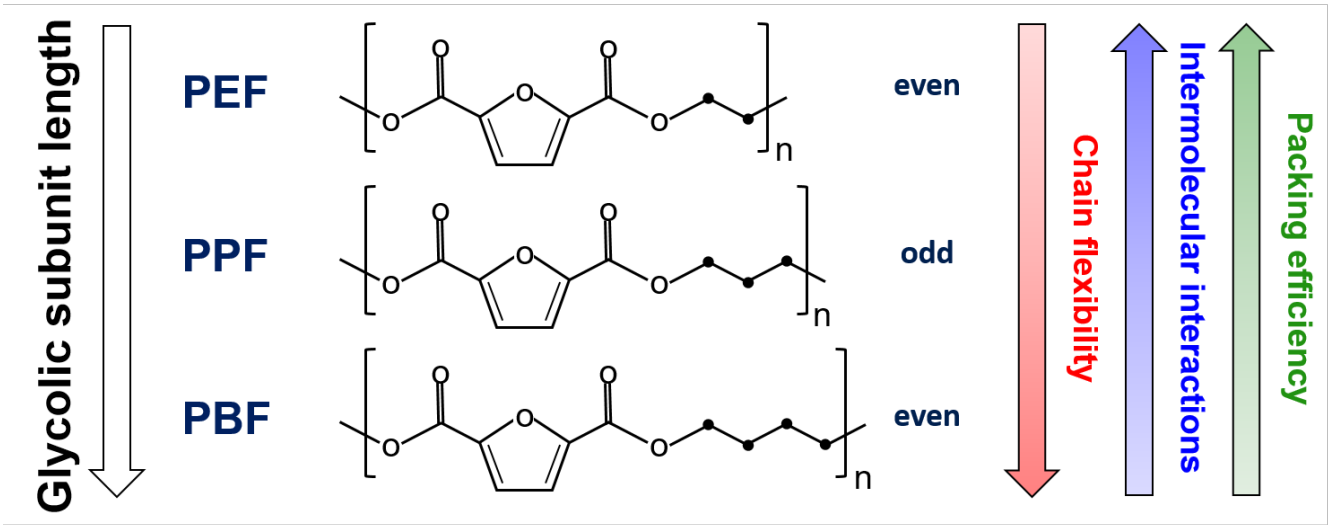

Figure 5.13: Schematic representation of the effect of the glycolic sub-unit length on the properties of the furanoate polymers investigated in this work.

In this work, the glycolic subunit length has been proven to strongly impact the microstructural properties of furanoate-based polymers. A schematic illustration of these effects is provided in Figure 5.13. It would be interesting to continue this study on a wider range of furanoate samples (number of methylene units higher than $n = 4$) to fully apprehend the properties of these very promising materials.

References

[1] I. Kolesov and R. Androsch, "The rigid amorphous fraction of cold-crystallized polyamide 6," *Polymer*, vol. 53, pp. 4770–4777, Sept. 2012.

[2] M. L. Di Lorenzo and M. C. Righetti, "The three-phase structure of isotactic poly(1-butene)," *Polymer*, vol. 49, pp. 1323–1331, Mar. 2008.

[3] B. G. Olson, J. Lin, S. Nazarenko, and A. M. Jamieson, "Positron Annihilation Lifetime Spectroscopy of Poly(ethylene terephthalate): Contributions from Rigid and Mobile Amorphous Fractions," *Macromolecules*, vol. 36, pp. 7618–7623, Oct. 2003.

[4] A. Guinault, C. Sollogoub, V. Ducruet, and S. Domenek, "Impact of crystallinity of poly(lactide) on helium and oxygen barrier properties," *European Polymer Journal*, vol. 48, pp. 779–788, Apr. 2012.

[5] J. Zhu, J. Cai, W. Xie, P.-H. Chen, M. Gazzano, M. Scandola, and R. A. Gross, "Poly(butylene 2,5-furan dicarboxylate), a Biobased Alternative to PBT: Synthesis, Physical Properties, and Crystal Structure," *Macromolecules*, vol. 46, pp. 796–804, Feb. 2013.

[6] G. Z. Papageorgiou, V. Tsanaktsis, D. G. Papageorgiou, S. Exarhopoulos, M. Papageorgiou, and D. N. Bikiaris, "Evaluation of polyesters from renewable resources as alternatives to the current fossil-based polymers. Phase transitions of poly(butylene 2,5-furandicarboxylate)," *Polymer*, vol. 55, pp. 3846–3858, Aug. 2014.

[7] L. Martino, N. Guigo, J. G. van Berkel, J. J. Kolstad, and N. Sbirrazzuoli, "Nucleation and Self-Nucleation of Bio-Based Poly(ethylene 2,5-furandicarboxylate) Probed by Fast Scanning Calorimetry," *Macromolecular Materials and Engineering*, vol. 301, pp. 586–596, May 2016.

[8] M. C. Righetti, P. Marchese, M. Vannini, A. Celli, F. Tricoli, and C. Lorenzetti, "Temperature-induced polymorphism in bio-based poly(propylene 2,5-furandicarboxylate)," *Thermochimica Acta*, vol. 677, pp. 186–193, July 2019.

[9] M. C. Righetti, P. Marchese, M. Vannini, A. Celli, C. Lorenzetti, D. Cavallo, C. Ocando, A. J. Müller, and R. Androsch, "Polymorphism and Multiple Melting Behavior of Bio-Based Poly(propylene 2,5-furandicarboxylate)," *Biomacromolecules*, p. acs.biomac.0c00039, Apr. 2020.

[10] G. Papamokos, T. Dimitriadis, D. N. Bikiaris, G. Z. Papageorgiou, and G. Floudas, "Chain Conformation, Molecular Dynamics, and Thermal Properties of Poly(n -methylene 2,5-furanoates) as a Function of Methylene Unit Sequence Length," *Macromolecules*, vol. 52, pp. 6533–6546, Sept. 2019.

[11] J. Örtegren, J. Tidlund, M. Nykvist, P. Busson, A. Hult, S. Sen, R. Boyd, and U. Gedde, "Dielectric relaxation of liquid crystalline dendrimers and liquid crystalline polymers with pendant nitro groups," *Polymer*, vol. 42, pp. 10027–10033, Dec. 2001.

[12] J. G. Smith, C. J. Kibler, and B. J. Sublett, "Preparation and properties of poly(methylene terephthalates)," *Journal of Polymer Science Part A-1: Polymer Chemistry*, vol. 4, pp. 1851–1859, July 1966.

[13] M. Soccio, N. Lotti, L. Finelli, M. Gazzano, and A. Munari, "Aliphatic poly(propylene dicarboxylate)s: Effect of chain length on thermal properties and crystallization kinetics," *Polymer*, vol. 48, pp. 3125–3136, May 2007.

[14] S. K. Burgess, J. E. Leisen, B. E. Kraftschik, C. R. Mubarak, R. M. Kriegel, and W. J. Koros, "Chain Mobility, Thermal, and Mechanical Properties of Poly(ethylene furanoate) Compared to Poly(ethylene terephthalate)," *Macromolecules*, vol. 47, pp. 1383–1391, Feb. 2014.

[15] E. Hempel, G. Hempel, A. Hensel, C. Schick, and E. Donth, "Characteristic Length of Dynamic Glass Transition near T_g for a Wide Assortment of Glass-Forming Substances," *The Journal of Physical Chemistry B*, vol. 104, pp. 2460–2466, Mar. 2000.

[16] L. Hong, V. Novikov, and A. Sokolov, "Is there a connection between fragility of glass forming systems and dynamic heterogeneity/cooperativity?," *Journal of Non-Crystalline Solids*, vol. 357, pp. 351–356, Jan. 2011.

[17] J. Puente, B. Rijal, L. Delbreilh, K. Fatyeyeva, A. Saiter, and E. Dargent, "Segmental mobility and glass transition of poly(ethylene-vinyl acetate) copolymers: Is there a continuum in the dynamic glass transitions from PVAc to PE?," *Polymer*, vol. 76, pp. 213–219, Oct. 2015.

[18] X. Monnier, N. Delpouve, N. Basson, A. Guinault, S. Domenek, A. Saiter, P. Mallon, and E. Dargent, "Molecular dynamics in electrospun amorphous plasticized polylactide fibers," *Polymer*, vol. 73, pp. 68–78, Sept. 2015.

[19] S. Araujo, N. Delpouve, S. Domenek, A. Guinault, R. Golovchak, R. Szatanik, A. Ingram, C. Fauchard, L. Delbreilh, and E. Dargent, "Cooperativity Scaling and Free Volume in Plasticized Polylactide," *Macromolecules*, vol. 52, pp. 6107–6115, Aug. 2019.

[20] K. Arabeche, L. Delbreilh, J.-M. Saiter, G. Michler, R. Adhikari, and E. Baer, "Fragility and molecular mobility in micro- and nano-layered PC/PMMA films," *Polymer*, vol. 55, pp. 1546–1551, Mar. 2014.

[21] C. Zhang, Y. Guo, and R. D. Priestley, "Characteristic Length of the Glass Transition in Isochorically Confined Polymer Glasses," *ACS Macro Letters*, vol. 3, pp. 501–505, June 2014.

[22] S. F. Nassar, S. Domenek, A. Guinault, G. Stoclet, N. Delpouve, and C. Sollogoub, "Structural and Dynamic Heterogeneity in the Amorphous Phase of Poly(l, l-lactide) Confined at the Nanoscale by the Coextrusion Process," *Macromolecules*, vol. 51, pp. 128–136, Jan. 2018.

[23] A. Saiter, D. Prevosto, E. Passaglia, H. Couderc, L. Delbreilh, and J. M. Saiter, "Cooperativity length scale in nanocomposites: Interfacial and confinement effects," *Physical Review E*, vol. 88, p. 042605, Oct. 2013.

[24] E. Donth, "The size of cooperatively rearranging regions at the glass transition," *Journal of Non-Crystalline Solids*, vol. 53, pp. 325–330, Dec. 1982.

[25] E. Donth, H. Huth, and M. Beiner, "Characteristic length of the glass transition," *Journal of Physics: Condensed Matter*, vol. 13, pp. L451–L462, June 2001.

[26] N. Varol, N. Delpouve, S. Araujo, S. Domenek, A. Guinault, R. Golovchak, A. Ingram, L. Delbreilh, and E. Dargent, "Amorphous rigidification and cooperativity drop in semi-crystalline plasticized polylactide," *Polymer*, vol. 194, p. 122373, Apr. 2020.

[27] C. Schick and E. Donth, "Characteristic length of glass transition: experimental evidence," *Physica Scripta*, vol. 43, pp. 423–429, Apr. 1991.

[28] J. Dudowicz, K. F. Freed, and J. F. Douglas, "Fragility of glass-forming polymer liquids," *The Journal of Physical Chemistry B*, vol. 109, no. 45, pp. 21350–21356, 2005. PMID: 16853769.

[29] J. Dudowicz, K. F. Freed, and J. F. Douglas, "The glass transition temperature of polymer melts," *The Journal of Physical Chemistry B*, vol. 109, no. 45, pp. 21285–21292, 2005.

[30] J. Wu, G. Huang, L. Qu, and J. Zheng, "Correlations between dynamic fragility and dynamic mechanical properties of several amorphous polymers," *Journal of Non-Crystalline Solids*, vol. 355, no. 34, pp. 1755 – 1759, 2009.

[31] K. Kunal, C. G. Robertson, S. Pawlus, S. F. Hahn, and A. P. Sokolov, "Role of Chemical Structure in Fragility of Polymers: A Qualitative Picture," *Macromolecules*, vol. 41, pp. 7232–7238, Oct. 2008.

[32] S. Araujo, F. Batteux, W. Li, L. Butterfield, N. Delpouve, A. Esposito, L. Tan, J.-M. Saiter, and M. Negahban, "A structural interpretation of the two components governing the kinetic fragility from the example of interpenetrated polymer networks: A Structural Interpretation of the Two Components Governing the Kinetic Fragility from the Example of Interpenetrated Polymer Networks," *Journal of Polymer Science Part B: Polymer Physics*, vol. 56, pp. 1393–1403, Oct. 2018.

[33] R. Kumar, M. Goswami, B. G. Sumpter, V. N. Novikov, and A. P. Sokolov, "Effects of backbone rigidity on the local structure and dynamics in polymer melts and glasses," *Physical Chemistry Chemical Physics*, vol. 15, no. 13, p. 4604, 2013.

[34] P. G. Santangelo and C. M. Roland, "Molecular weight dependence of fragility in polystyrene," *Macromolecules*, vol. 31, no. 14, pp. 4581–4585, 1998.

[35] M. L. Williams, R. F. Landel, and J. D. Ferry, "The Temperature Dependence of Relaxation Mechanisms in Amorphous Polymers and Other Glass-forming Liquids," *J. Am. Chem. Soc.*, vol. 77, pp. 3701–3707, July 1955.

[36] M. Soccio, D. E. Martínez-Tong, A. Alegría, A. Munari, and N. Lotti, "Molecular dynamics of fully biobased poly(butylene 2,5-furanoate) as revealed by broadband dielectric spectroscopy," *Polymer*, vol. 128, pp. 24–30, Oct. 2017.

[37] Z. Ma, H. Geng, D. Wang, and Z. Shuai, "Influence of alkyl side-chain length on the carrier mobility in organic semiconductors: herringbone vs. pi–pi stacking," *Journal of Materials Chemistry C*, vol. 4, no. 20, pp. 4546–4555, 2016.

[38] A. Bourdet, A. Esposito, S. Thiyagarajan, L. Delbreilh, F. Affouard, R. J. I. Knoop, and E. Dargent, "Molecular Mobility in Amorphous Biobased Poly(ethylene 2,5-furandicarboxylate) and Poly(ethylene 2,4-furandicarboxylate)," *Macromolecules*, vol. 51, pp. 1937–1945, Mar. 2018.

[39] A. Sanz, A. Nogales, N. Lotti, A. Munari, and T. Ezquerra, "Complex nature of the β relaxation and fragility in aromatic polyesters," *Journal of Non-Crystalline Solids*, vol. 353, pp. 3989–3995, Nov. 2007.

[40] M. Soccio, D. E. Martínez-Tong, G. Guidotti, B. Robles-Hernández, A. Munari, N. Lotti, and A. Alegria, "Broadband Dielectric Spectroscopy Study of Biobased Poly(alkylene 2,5-furanoate)s' Molecular Dynamics," *Polymers*, vol. 12, p. 1355, June 2020.

[41] T. Dimitriadis, D. N. Bikiaris, G. Z. Papageorgiou, and G. Floudas, "Molecular Dynamics of Poly(ethylene-2,5-furanoate) (PEF) as a Function of the Degree of Crystallinity by Dielectric Spectroscopy and Calorimetry," *Macromolecular Chemistry and Physics*, vol. 217, pp. 2056–2062, Sept. 2016.

[42] S. P. Bravard and R. H. Boyd, "Dielectric Relaxation in Amorphous Poly(ethylene terephthalate) and Poly(ethylene 2,6-naphthalene dicarboxylate) and Their Copolymers," *Macromolecules*, vol. 36, pp. 741–748, Feb. 2003.

[43] M. Soccio, A. Nogales, I. Martín-Fabiani, N. Lotti, A. Munari, and T. Ezquerra, "Relaxation dynamics and cold crystallization of poly(pentamethylene terephthalate) as revealed by dielectric spectroscopy," *Polymer*, vol. 55, pp. 1552–1559, Mar. 2014.

[44] A. Nogales, A. Sanz, and T. A. Ezquerra, "On the role of the β process as precursor of the α relaxation in aromatic polyesters," *Journal of Non-Crystalline Solids*, vol. 352, pp. 4649–4655, Nov. 2006.

[45] G. Z. Papageorgiou, V. Tsanaktsis, and D. N. Bikiaris, "Synthesis of poly(ethylene furandicarboxylate) polyester using monomers derived from renewable resources: thermal behavior comparison with PET and PEN," *Phys. Chem. Chem. Phys.*, vol. 16, no. 17, pp. 7946–7958, 2014.

[46] I. Okazaki and B. Wunderlich, "Reversible local melting in polymer crystals," *Macromolecular Rapid Communications*, vol. 18, pp. 313–318, Apr. 1997.

[47] F. Medellin-Rodriguez, P. Phillips, J. Lin, and R. Campos, "The triple melting behavior of poly(ethylene terephtalate): molecular weight effects," *Journal of Polymer Science Part B: Polymer Physics*, vol. 35, pp. 1757–1774, Dec. 1998.

[48] Y. Kong and J. Hay, "Multiple melting behaviour of poly(ethylene terephthalate)," *Polymer*, vol. 44, pp. 623–633, Jan. 2003.

[49] M. C. Righetti, M. L. Di Lorenzo, E. Tombari, and M. Angiuli, "The Low-Temperature Endotherm in Poly(ethylene terephthalate): Partial Melting and Rigid Amorphous Fraction Mobilization," *The Journal of Physical Chemistry B*, vol. 112, pp. 4233–4241, Apr. 2008.

[50] A. Toda, R. Androsch, and C. Schick, "Insights into polymer crystallization and melting from fast scanning chip calorimetry," *Polymer*, vol. 91, pp. 239–263, May 2016.

[51] A. A. Minakov, D. A. Mordvintsev, and C. Schick, "Melting and reorganization of poly(ethylene terephthalate) on fast heating (1000 K/s)," *Polymer*, vol. 45, pp. 3755–3763, May 2004.

[52] S. Adamovsky, A. Minakov, and C. Schick, "Scanning microcalorimetry at high cooling rate," *Thermochimica Acta*, vol. 403, pp. 55–63, June 2003.

[53] F. De Santis, S. Adamovsky, G. Titomanlio, and C. Schick, "Scanning Nanocalorimetry at High Cooling Rate of Isotactic Polypropylene," *Macromolecules*, vol. 39, pp. 2562–2567, Apr. 2006.

[54] C. Schick, A. Wurm, and A. Mohamed, "Vitrification and devitrification of the rigid amorphous fraction of semicrystalline polymers revealed from frequency-dependent heat capacity," *Colloid & Polymer Science*, vol. 279, pp. 800–806, Aug. 2001.

[55] A. Esposito, N. Delpouve, V. Causin, A. Dhotel, L. Delbreilh, and E. Dargent, "From a Three-Phase Model to a Continuous Description of Molecular Mobility in Semicrystalline Poly(hydroxybutyrate- *co* -hydroxyvalerate)," *Macromolecules*, vol. 49, pp. 4850–4861, July 2016.

[56] V. Mathot, "Temperature dependence of some thermodynamic functions for amorphous and semi-crystalline polymers," *Polymer*, vol. 25, pp. 579–599, May 1984.

[57] A. Wurm, M. Merzlyakov, and C. Schick, "Reversible melting during crystallization of polymers studied by temperature modulated techniques (TMDSC, TMDMA).," *Journal of Thermal Analysis and Calorimetry*, vol. 60, no. 3, pp. 807–820, 2000.

[58] I. Okazaki and B. Wunderlich, "Modulated differential scanning calorimetry in the glass transition region, V. activation energies and relaxation times of poly(ethylene terephthalate)s," *Journal of Polymer Science Part B: Polymer Physics*, vol. 34, pp. 2941–2952, Dec. 1996.

[59] M. Kattan, E. Dargent, and J. Grenet, "Three phase model in drawn thermoplastic polyesters: comparison of differential scanning calorimetry and thermally stimulated depolarisation current experiments," *Polymer*, vol. 43, pp. 1399–1405, Feb. 2002.

[60] M. Arnoult, E. Dargent, and J. Mano, "Mobile amorphous phase fragility in semicrystalline polymers: Comparison of PET and PLLA," *Polymer*, vol. 48, pp. 1012–1019, Feb. 2007.

[61] F. Hamonic, V. Miri, A. Saiter, and E. Dargent, "Rigid amorphous fraction versus oriented amorphous fraction in uniaxially drawn polyesters," *European Polymer Journal*, vol. 58, pp. 233–244, Sept. 2014.

[62] M. Pyda, A. Boller, J. Grebowicz, H. Chuah, B. V. Lebedev, and B. Wunderlich, "Heat capacity of poly(trimethylene terephthalate)," *Journal of Polymer Science Part B: Polymer Physics*, vol. 36, pp. 2499–2511, Oct. 1998.

[63] M. Pyda, R. Bopp, and B. Wunderlich, "Heat capacity of poly(lactic acid)," *The Journal of Chemical Thermodynamics*, vol. 36, pp. 731–742, Sept. 2004.

[64] M. L. Di Lorenzo, R. Androsch, and I. Stolte, "Tailoring the rigid amorphous fraction of isotactic polybutene-1 by ethylene chain defects," *Polymer*, vol. 55, no. 23, pp. 6132 – 6139, 2014. Shape Memory and Shape Morphing Polymers.

[65] M. C. Righetti and M. L. Di Lorenzo, "Melting temperature evolution of non-reorganized crystals. Poly(3-hydroxybutyrate)," *Thermochimica Acta*, vol. 512, pp. 59–66, Jan. 2011.

[66] Q. Ma, G. Georgiev, and P. Cebe, "Constraints in semicrystalline polymers: Using quasi-isothermal analysis to investigate the mechanisms of formation and loss of the rigid amorphous fraction," *Polymer*, vol. 52, pp. 4562–4570, Sept. 2011.

[67] C. Schick, A. Wurm, and A. Mohammed, "Formation and disappearance of the rigid amorphous fraction in semicrystalline polymers revealed from frequency dependent heat capacity," *Thermochimica Acta*, vol. 396, pp. 119–132, Feb. 2003.

[68] B. Wunderlich, "Reversible crystallization and the rigid–amorphous phase in semicrystalline macromolecules," *Progress in Polymer Science*, vol. 28, pp. 383–450, Mar. 2003.

[69] H. Chen and P. Cebe, "Vitrification and Devitrification of Rigid Amorphous Fraction of PET during Quasi-Isothermal Cooling and Heating," *Macromolecules*, vol. 42, pp. 288–292, Jan. 2009.

Conclusions and Prospects

In recent years, the influence of the chemical structure on the microstructure and the final properties of semi-crystalline polymers has been widely studied and discussed. This Phd work was carried out to understand how complex microstructures are formed as a consequence of given chemical compositions of the macromolecular chains, and how these microstructures should be described to consider all the subtle differences in the molecular arrangement that could eventually lead to dramatic differences in the final properties, for instance the aptitude to crystallize. For this reason, a large number of different polyesters have been screened and a selection was made to isolate interesting parameters, such as the flexibility of the backbone or the length of the pending groups. A particular attention was paid to the effect of the chemical structure of the repeating unit on the formation of the rigid amorphous fraction (RAF).

In the first part of the work, different methods allowing the determination of the equilibrium melting enthalpy have been presented and discussed. This reference quantity is specific to each material and allows the quantification of the crystalline phase from calorimetric measurements. Since the quantification of the rigid amorphous fraction requires an accurate quantification of both the crystalline and mobile amorphous fractions, it was of uppermost importance to determine an effective way to estimate the crystalline fraction from calorimetric analyses (in particular using Fast Scanning Calorimetry (FSC), which suppresses crystalline reorganization and the effects due to polymorphism). Using FSC, the impact of different experimental parameters (crystallization temperature, crystallization time, sample mass) on the formation of RAF in poly(ethylene furanoate)(PEF) has been discussed.

Investigations on the impact of the co-monomer content and nature on the properties of several polyhydroxyalkanoate (PHA) copolymers were also done, seeking for a possible connection between chemical composition, molecular arrangement, microstructure and therefore final properties. According to the results obtained by DSC, it appears that co-polymerization is significantly slowing down the cold-crystallization process (crystalline disruption). This finding is supported by the results obtained by WAXD, which confirmed the gradual disruption of the crystalline network as the degree of co-polymerization increases. The co-monomer content and nature plays a significant role on the crystalline phase of PHA copolymers. The investigations on the molecular dynamics of amorphous PHA samples were conducted using calorimetric and dielectric techniques. The results showed that an increase in the amount of the co-monomer units leads to an overall decrease in the intermolecular interactions in both (HB-co-HV) and (HB-co-HHx) copolymers. The semi-crystalline microstructures obtained for PHA copolymers crystallized from the glassy state were analyzed by MT-DSC to study the impact of the co-monomer content and nature on the formation and disappearance of the RAF. The results showed that co-polymerization leads to a progressive decrease of the coupling between phases, as well as to a decrease in the RAF amount. This decrease has been attributed to the changes

in the aptitude to crystallize induced by the copolymerization (crystalline disruption). On a whole, this study shows how the co-monomer content and nature affects the semi-crystalline microstructures of PHA copolymers, which in turns demonstrates that is possible to tune the final properties of a polyester by changing the co-monomer content and/or nature.

Then, the effects of the glycolic subunit's length on the microstructure and molecular mobility of a series of furan-based polyesters have been investigated and discussed. The results showed that crystallization and melting are strongly impacted by a change in the glycolic subunit's length, which was attributed to a change in the backbone flexibility. Different models (Donth, Hong...) were used to investigate the molecular mobility of the amorphous chains from both calorimetric and dielectric analysis. From these investigations, the length of the glycolic subunit has been proven to be a key parameter governing the intermolecular interactions and the packing efficiency of the amorphous chains in furan-based polyesters. The vitrification and devitrification of the RAF have been investigated from modulated-temperature DSC (MT-DSC) experiments. As expected, the samples crystallized from the molten state contained reduced amounts of RAF as compared to the samples crystallized from the glassy state. Furthermore, the devitrification of the RAF on the samples crystallized from the glassy state was observed on a wide temperature range (about 25°C), whereas it was not clearly observed on the samples crystallized from the molten state. Therefore, the vitrification and devitrification of the RAF in poly(ethylene furanoate) (PEF) and poly(propylene furanoate)(PPF) was shown to be similar to the one observed in poly(ethylene terephthalate)(PET). This work showed that the properties of furan-based materials are highly dependent on the length of the glycolic subunit , which is a proof of the wide panel of possible applications that can be triggered by a wise choice of the initial monomers for the synthesis of furan-based polyesters.

This research work shows how difficult it is to characterize (both quantitatively and qualitatively) the rigid amorphous fraction in a semi-crystalline polymer, and how many parameters can potentially affect its mechanisms of vitrification and devitrification. In particular, this work demonstrates how the chemical structure (composition and arrangement) of the macromolecular chains can impact the characteristics and behaviors of the different fractions in semi-crystalline polymers. As a perspective to the present work, it could be interesting to pursue the investigations on a wider range of polymeric systems to get a deeper insight into how the chemical structure can influence the microstructures of semi-crystalline polymers, and especially what are the mechanisms of appearance and disappearance of the RAF as a function of specific molecular parameters. It has been shown that the RAF has a major impact on the macroscopic properties of semi-crystalline polymers, therefore it is crucial to better understand the mechanisms governing its existence. By doing so, it will probably be possible to tune the polymer chemical structure in order to obtain the desired macroscopic properties, thus enhancing the range of possible application.

Scientific contributions

Publications

- C. Fosse, A. Bourdet, E. Ernault, A. Esposito, N. Delpouve, S. Thiyagarajan, R.J.I. Knoop, L. Delbreilh, E. Dargent; Determination of the equilibrium melting enthalpy of melting of two-phase semi-crystalline polymers by fast scanning calorimetry; Thermochimica Acta 677, 67-78,2019

Oral communications

- C. Fosse, A. Bourdet, A. Esposito, S. Thiyagarajan, R.J.I. Knoop, M. Soccio, N. Lotti, L. Delbreilh, E. Dargent; Investigation of a series of furan-based polyesters containing different glycolic subunits; Polychar 2019, Naples, Italy, 2019
- C. Fosse, A. Bourdet, E. Ernault, A. Esposito, N. Delpouve, S. Thiyagarajan, R.J.I. Knoop, L. Delbreilh, E. Dargent; Détermination de l'enthalpie de fusion théorique d'échantillons polymères semi-cristallins par fast scanning calorimetry, JCAT 50, Saint-Valéry en Caux, France, 2019
- A. Esposito, C. Fosse, N. Delpouve, L. Delbreilh, E. Dargent; On the use of thermal analysis to describe polymer microstructure from a three-phase model to a continuous description of molecular mobility in semi-crystalline poly(hydroxybutyrate-co-hydroxyvalerate); JCAT 50, Saint-Valéry en Caux, France, 2019
- A. Esposito, C. Fosse, N. Delpouve, L. Delbreilh, E. Dargent; On the use of thermal analysis to describe polymer microstructure: from a three-phase model to a continuous description of molecular mobility in semi-crystalline poly (hydroxybutyrate-co-hydroxyvalerate); XL National (Italian) Congress AICAT, Pise, Italy, 2018

Poster communications

- C. Fosse, A. Bourdet, A. Esposito, P. Lemechko, S. Bruzaud, Y. Suguma Salim, K. Sudesh, S. Thiyagarajan, R.J.I Knoop, M. Soccio, N. Lotti, E. Dargent ; Effect of molecular structure on microstructural properties of different biopolymers; Biopol 2019, Stockholm, Suède, 2019
- C. Fosse, A. Bourdet, A. Esposito, N. Delpouve, S. Thiyagarajan, R.J.I Knoop, L. Delbreilh, E. Dargent; Determination of the equilibrium melting enthalpy of melting of semi-crystalline polyesters using fast scanning calorimetry : a two-phase model approach; Lähnwitzseminar on Calorimetry 2018, Rostock, Germany, 2018
- C. Fosse, A. Esposito, V. Gaucher, P. Lemechko, S. Bruzaud, Y. Suguma Salim, K. Sudesh, E. Dargent; Effect of co-monomer nature and content on the microstructure of Polyhydroxyalkanoates investigated in MT-DSC; Lähnwitzseminar on Calorimetry 2018, Rostock, Germany, 2018

Appendix

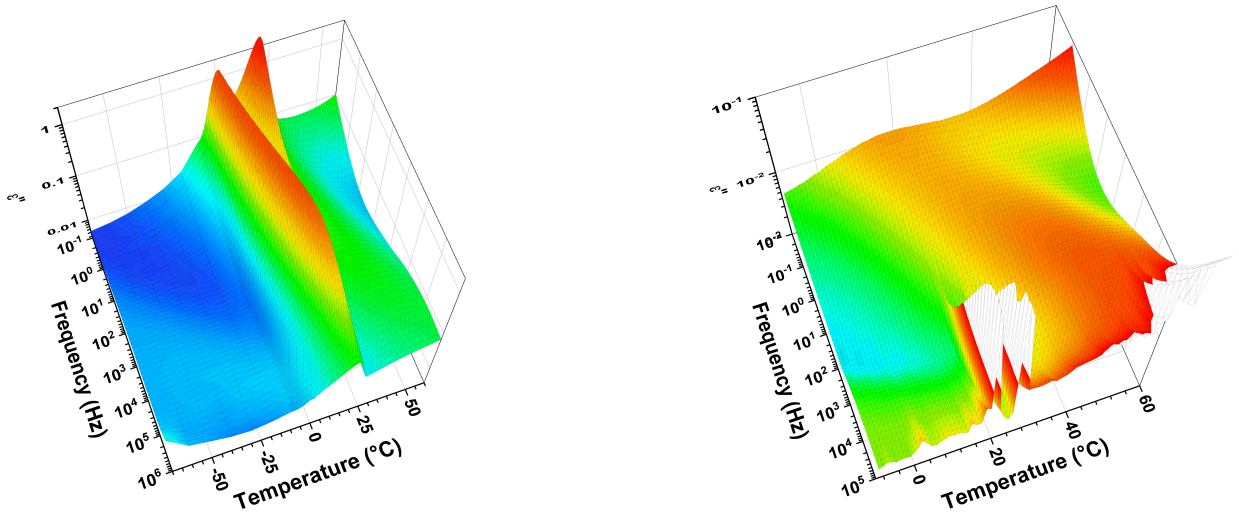

3D plots of the PHBV3% sample measured after Quenching (on the left) and after crystallization from the glassy state (on the right).

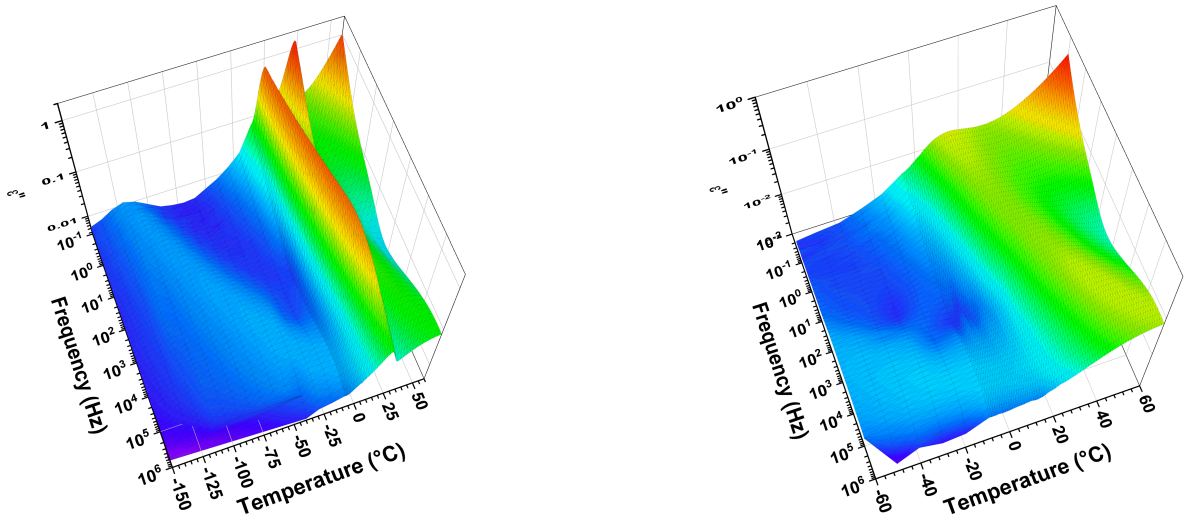

3D plots of the PHBV15% sample measured after Quenching (on the left) and after crystallization from the glassy state (on the right).

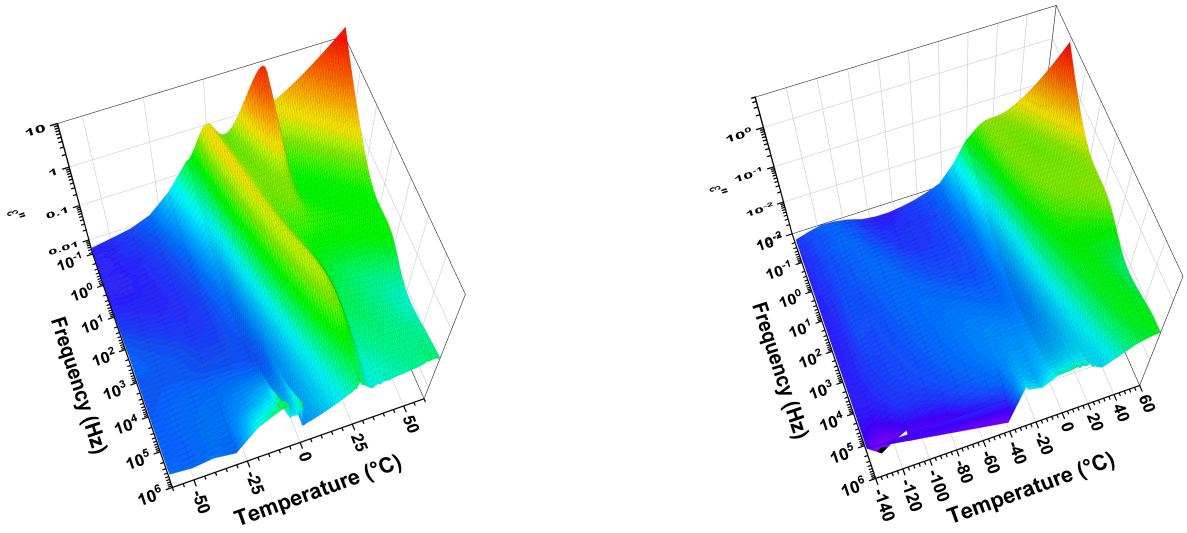

3D plots of the PHBV23% sample measured after Quenching (on the left) and after crystallization from the glassy state (on the right).

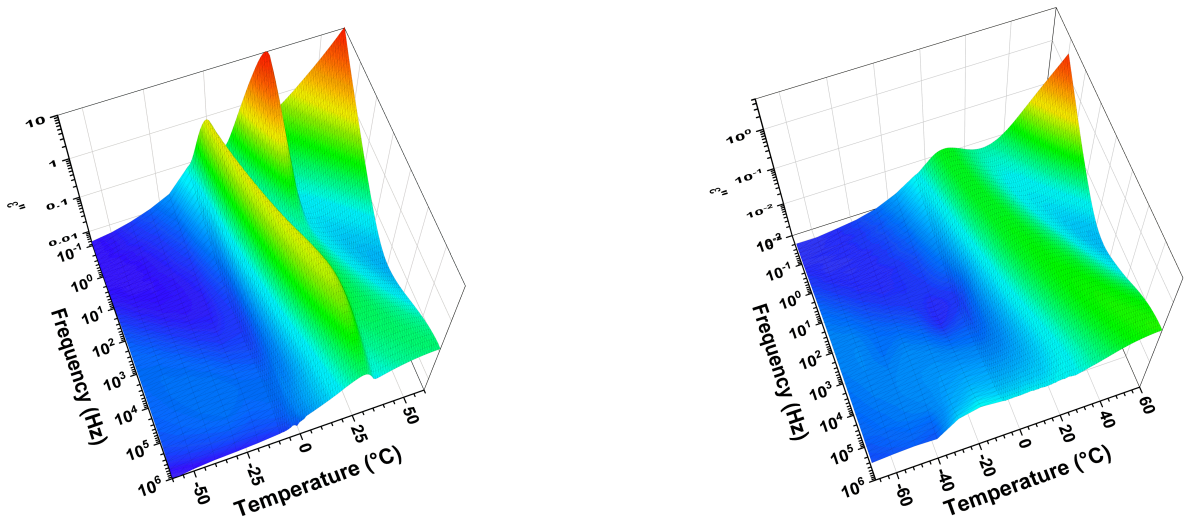

3D plots of the PHBV27% sample measured after Quenching (on the left) and after crystallization from the glassy state (on the right).

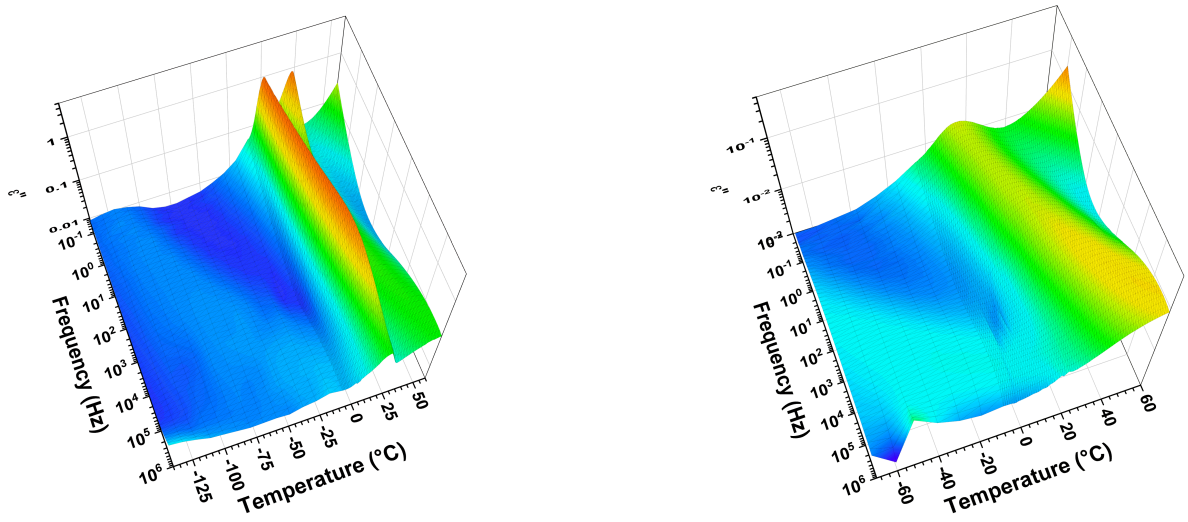

3D plots of the PHHx3% sample measured after Quenching (on the left) and after crystallization from the glassy state (on the right).

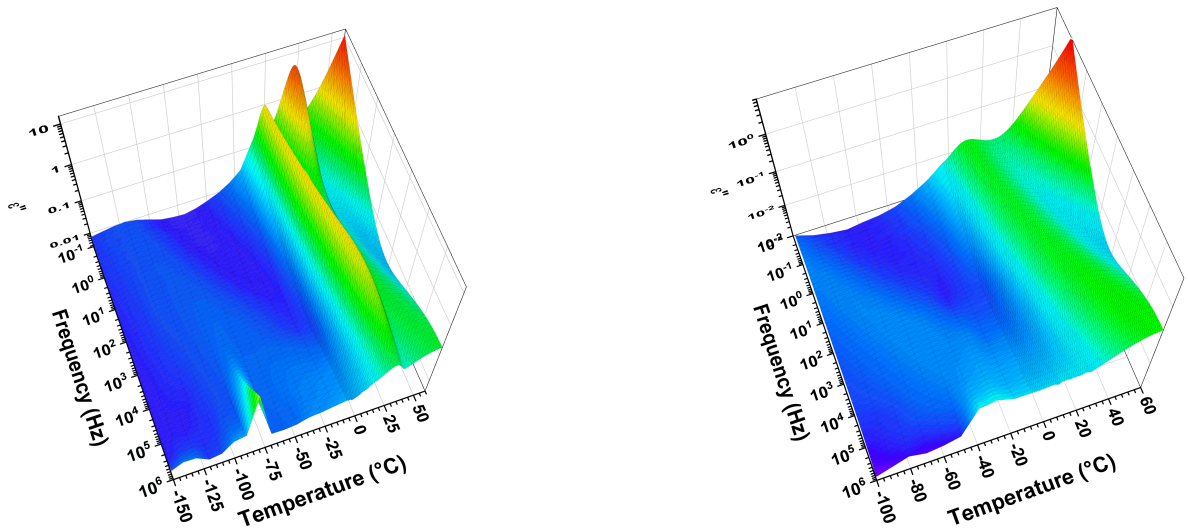

3D plots of the PHHx8% sample measured after Quenching (on the left) and after crystallization from the glassy state (on the right).

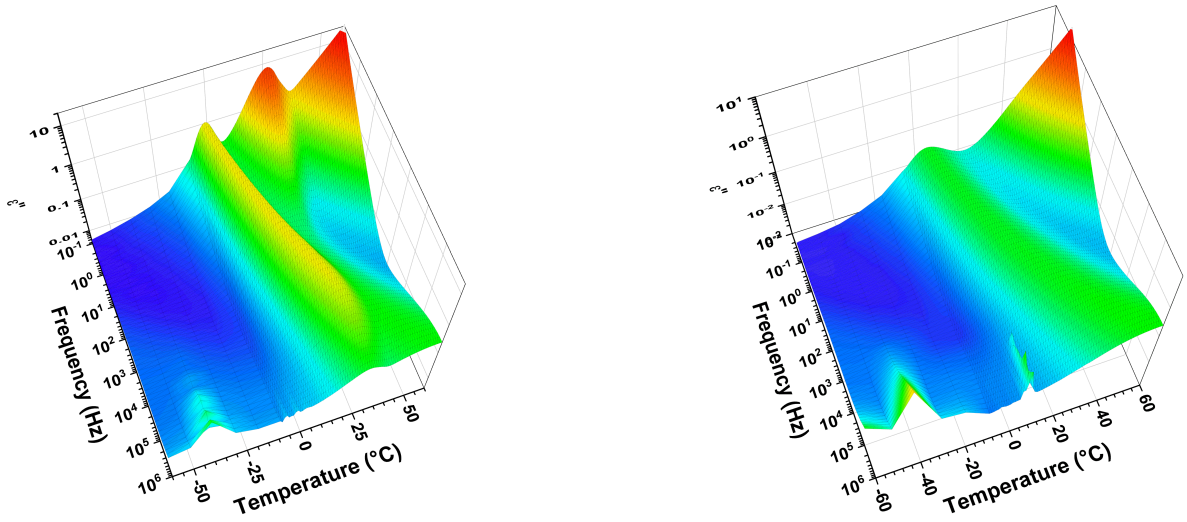

3D plots of the PHHx12% sample measured after Quenching (on the left) and after crystallization from the glassy state (on the right).

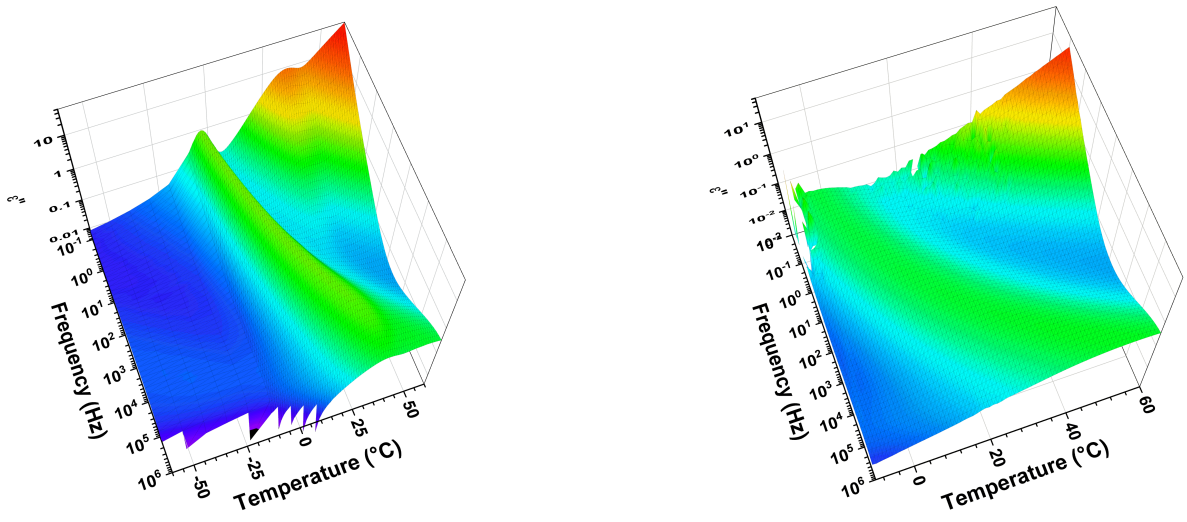

3D plots of the PHHx35% sample measured after Quenching (on the left) and after crystallization from the glassy state (on the right).

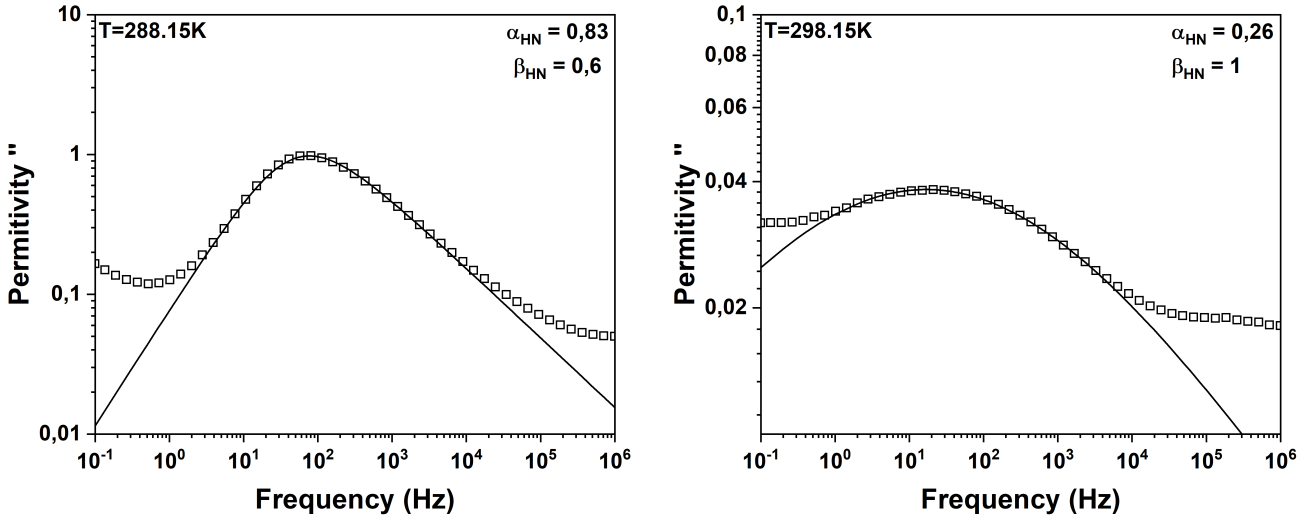

Imaginary part of the permitivity signal as a function of the frequency obtained on PHB samples after *Quenching* (on the left) and *Crystallization from the glassy state* (on the right). Black squares are the experimental data and the black solid line is the line of best fit, the shape parameters α_{HN} and β_{HN} are also reported.

Havriliak-Negami shape parameters (α_{HN} and β_{HN}) obtained on the PHA samples after *Quenching* (recorded in isothermal mode at T = 288.15K) and *Crystallization from the glassy state* (recorded in isothermal mode at T = 298.15K).

	Quenching		Crystallization from the glassy state	
SAMPLE	α_{HN}	β_{HN}	α_{HN}	β_{HN}
PHB	0.83	0.6	0.26	1
PHBV3%	0.81	0.59	0.30	1
PHBV15%	0.9	0.5	0.5	1
PHBV23%	0.87	0.47	0.47	1
PHBV27%	0.89	0.56	0.4	1
PHHx3%	0.86	0.42	0.37	1
PHHx8%	0.81	0.57	0.4	1
PHHx12%	0.84	0.55	0.44	1
PHHx35%	0.87	0.51	0.54	1

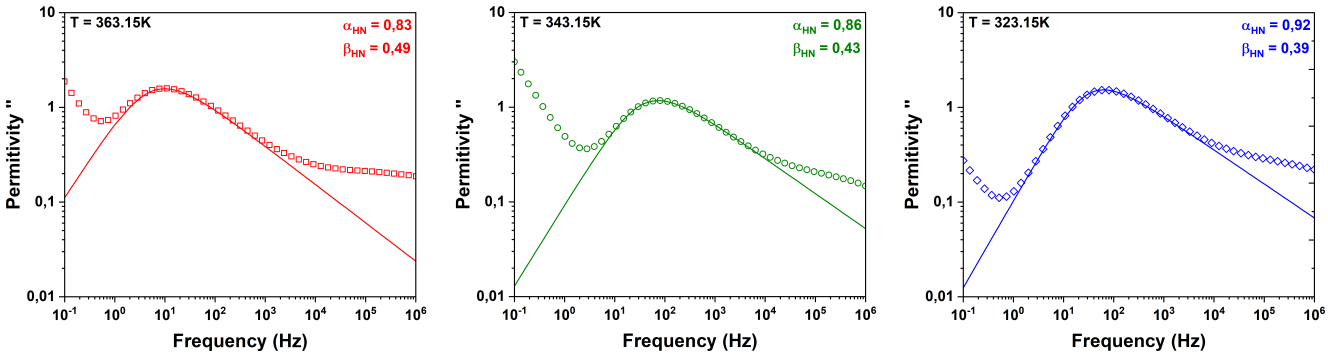

Imaginary part of the permitivity signal as a function of the frequency obtained on the different furanoate samples, respectively PEf, PPF and PBF. Open symbols are the experimental data and the solid lines are the line of best fit, the shape parameters α_{HN} and β_{HN} are also reported.

Abstract

The aim of this work was to investigate the mechanisms of appearance and disappearance of the rigid amorphous fraction as well as its effects on the molecular mobility in a large panel of polyesters. Microstructural were performed to evaluate the effects of different chemical compositions and structures on the appearance and disappearance of the rigid amorphous fraction. These studies were carried out using different experimental techniques : modulated-temperature differential scanning calorimetry (MT-DSC), fast scanning calorimetry (FSC), dielectric relaxation spectroscopy (DRS) and X-ray diffraction (XRD). Fast scanning calorimetry proved to be a very efficient technique to obtain the temperature dependence of the melting enthalpy of the fully crystalline material, which then allows to get a better estimation of the rigid amorphous fraction in semi-crystalline samples. The microstructural studies showed that the chemical composition and structure have a strong effect on the appearance and disappearance of the rigid amorphous fraction. The whole set of experimental results also proved that by adjusting the chemical composition and structure,as well as the crystallization protocol, it is possible to obtain microstructures with different properties, which gives access to a wide range of applications.
Keywords: Rigid amorphous fraction, polyesters, biopolymers, crystallization, molecular mobility, fast scanning calorimetry.

Résumé

L'objectif de ce travail était d'étudier les mécanismes de formation et de disparition de la fraction amorphe rigide ainsi que son impact sur la mobilité moléculaire d'un large panel de polyesters. Des études microstructurales ont été réalisées afin d'investiger les effets de la composition et de la structure chimique sur la formation et la disparition de la fraction amorphe rigide dans différents systèmes polymères. Ces études ont été réalisées à l'aide de différentes techniques d'analyses : calorimétrie différentielle à balayage avec modulation en température (MT-DSC), calorimétrie à balayage rapide (FSC), spectroscopie diélectrique relaxationelle (DRS) et diffraction des rayons X (DRX). La calorimétrie à balayage rapide s'est montrée particulièrement intéressante pour étudier la dépendance en température de l'enthalpie de fusion des échantillons 100% cristallins, ce qui permet ensuite, d'obtenir une meilleure estimation de la quantité de fraction amorphe rigide dans les échantillons semi-cristallins. Les études microstructurales sur les différents polyesters ont ensuite montrés que la composition et la structure chimique du polymère ont un effet significatif sur la formation et la disparition de la fraction amorphe rigide. Elles ont également prouvé qu'en ajustant la composition et la structure chimique, ainsi que le protocole de cristallisation, il est possible de créer des microstructures avec des propriétés diverses et variées augmentant ainsi le nombre d'applications.
Mots-clés: Fraction amorphe rigide, polyesters, biopolymères, cristallisation, mobilité moléculaire , calorimétrie à balayage rapide.